Universität der Bundeswehr München
Fakultät für Luft- und Raumfahrttechnik
Institut für Raumfahrttechnik und Weltraumnutzung

Orbit and Uncertainty Propagation for Space Object Catalogue Maintenance

Srinivas Janardhana Setty

Vollständiger Abdruck der von der Fakultät für Luft- und Raumfahrttechnik der Universität der Bundeswehr München zur Erlangung des akademischen Grades eines

Doktor-Ingenieur (Dr.-Ing.)

genehmigten Dissertation.

Vorsitzender:	Prof. Dr.-Ing. Roger Förstner
1. Gutachter:	Prof. Dr.-Ing. Felix Huber
2. Gutachter:	Prof. Dr. phil. nat. Thomas Schildknecht

Die Dissertation wurde am 01. October 2019 bei der Universiät der Bundeswehr München eingereicht und durch die Fakultät für Luft- und Raumfahrttechnik am 16. Juni 2020 angenommen. Die mündliche Prüfung fand am 22. Juli 2020 statt.

ABSTRACT

Space Situational Awareness (SSA) requires a catalogue comprised of information for all the Earth orbiting objects. Operational satellite collisions with an object that is not in the catalogue are unacceptable. The increased demand for using space based services for a wide range of applications has significantly increased the number of known objects around the Earth. Observing, cataloguing, and maintaining all of these Earth orbiting objects is not a trivial task.

Catalogue maintenance for SSA demands accurate and computationally lean orbit propagation and orbit determination techniques. These techniques are required for space resource operations, and for dealing with the large number of space objects created in past decades and anticipated in future decades. Multiple satellite theories were examined in order to establish the basis for recommending a viable alternative to the standard numerical propagator. Propagation accuracy and computational load testing methods are established, and the Draper Semi-analytical Satellite Theory (DSST) is investigated for its performance. A separate study was conducted to establish a least squares orbit determination process which uses the DSST partial derivatives. This process estimates the mean equinoctial elements and the dynamical parameters. Exhaustive simulated data test cases show that including the DSST in the orbit determination program is advantageous, specifically when processing observation data that is representative of SSA scenarios.

Catalogue maintenance and its applications require an understanding of the uncertainties associated with the states of the catalogued objects. The majority of the objects in the current space debris environment are in Low Earth Orbit (LEO). Here, atmospheric drag is the major contributor to the orbit prediction errors, as it is the most uncertain force to model. A stochastic approach is developed to estimate the orbit prediction error statistics due to uncertainties in the density model. The method is tested with available real data, and the results are discussed. The uncertainty estimation method is combined with a standard covariance propagation method to showcase the applicability to the catalogue maintenance system.

Keywords:

space debris, orbit propagation, orbit determination, catalogue maintenance, atmospheric density uncertainty

ACKNOWLEDGEMENTS

First and foremost, my greatest gratitude is to my supervisor Dr. Oliver Montenbruck. Thank you for taking me by hand and teaching me just not the technical aspects of orbital mechanics, but also to think and state a scientific problem in a clear manner. I cannot thank enough for the patience Dr. Montenbruck have shown in making sure I got the fundamentals right, and for the time and patience put during the preparation of this thesis. Second, I would like to thank Dr. Hauke Fidler for giving the opportunity to work in Space Situational Awareness group at GSOC, for the valuable discussions and for the support, and for proof reading the thesis. Also, I would like to thank Dr. Paul Cefola, who unofficially supervised me through out this work, from explaining the math concepts to helping in scientific writing and introducing to the astrodynamics community. Dr. Cefola provided not only the technical expertise, but also huge opportunity for personal and professional development. I am humbled and extremely honoured to have been given the opportunity to work with all three. Any number of thanking words would not justify the time and effort they have given me.

I want to thank Prof. Dr. Felix Huber for being my Doktorvater, at the Bundeswehr University Munich, for constructive comments during the graduate seminars at GSOC and for the careful reading of my thesis. I would like to thank my former colleagues Johannes Herzog, Sonya Spiridonova, Mauricio Andres, and specially to Jan Siminski and Andreas Hinze. Thank you all for the fruitful discussions, assists, and support during this thesis work at GSOC and later. Being associated with this group has been enjoyable, greatly fruitful, and has culminated in a strong sense of fulfilment.

I would like to convey my thanks to Prof. Juan Felix San Juan for his unconditional support and reviewing the thesis, and to Mr. David Vallado for thoroughly reading the thesis and providing the constructive comments.

The work in this thesis was supported by Munich Aerospace funding, I would like to thank all involved in providing the scholarship.

The final and largest thank-you is to my parents and family, I would have never made it without your support and patience through the years.

TABLE OF CONTENTS

CHAPTER 1

INTRODUCTION

This research work focuses on the selection, development and testing of orbit prediction and orbit determination methods: the selection is carried out for the purpose of space object catalogue maintenance. Approximations in the selected propagator method and uncertainties in the selected force models are studied. Methods for uncertainty propagation are investigated.

The first objective of this study is to find a propagation method that can be used for several cataloguing tasks, and will offer a favourable trade-off between accuracy and computational effort. The selected propagation method should be a computationally lean alternative to the more common numerical orbit propagation techniques. As a second objective, efforts were concentrated in characterising the model uncertainties and in formulating a method to capture these uncertainties within the propagated covariances.

1.1 Motivation

The space age began with the launch of the world's first artificial satellite, Sputnik-1, from the former Soviet Union on October 4, 1957. Four months later, Sputnik-1 was followed by the U.S. satellite Explorer-1. Since then satellites have been used to improve human lifestyle with applications in the fields of safety, science, communication, navigation, weather, land-stewardship, entertainment, etc. According to the NASA-ODPO (2016), up to January 2016 there were over 5,160 launches worldwide. Since 1965, approximately 150 satellites have been launched every year by different nations (Jakhu et al., 2018). Figure 1.1 shows the annual launches across the globe. As of June 2017, the U.S. Space Surveillance Network was tracking about 4,495 orbiting payloads together with 14,145 rocket bodies and debris objects. The space objects (SO) currently tracked by the U.S. Space Surveillance Network vary in size from a smart phone (nano satellites) to a football ground (International Space Station).

With advancements in launch technology and increased demand for space applications, the number of payloads released into orbit is increasing. On February 15, 2017 a record 104 satellites were deployed by a single Indian PSLV launcher. Companies such as OneWeb, SpaceX, and Google are all developing mega-constellations comprising 600 to 4,000 satellites for low Earth orbit communication systems[1]. The forecast of the planned missions together with the current usage of space suggests a steep increase in the artificial satellite population (Jenkin et al., 2015).

[1] Similar to the early internet in the sky concepts such as Teledesic

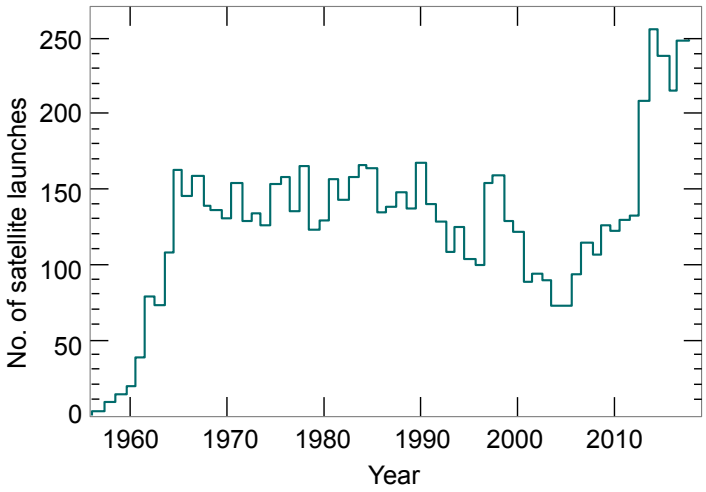

Fig. 1.1 Total number of satellites launched each year by all the space bearing nations. Plot is adapted from the data published by Jakhu et al. (2018)

Many orbiting satellites are no longer operational. They have become uncontrollable defunct SOs. "Space debris" also includes launcher upper stages, fragments from break-ups and other SOs which are not steerable (Goericke, 1999). There are instances where debris, and defunct objects collide among themselves, or with an operational satellite, posing a threat to valuable infrastructure and creating more debris. To avoid the collision of operational satellites with orbiting debris, the space operator needs precise data. Knowledge of the space environment provides this necessary information to space operators in order to preserve the integrity of the space assets.[2]

Awareness of the space environment can be imparted either by a statistical modelling approach or by a deterministic approach. The statistical description of the distribution of SOs is known as space debris modelling. These models provide statistical approximations for the distribution of objects in terms of flux, physical characteristics of objects, regarding size, mass, density, etc (Klinkrad, 2006). Nazarenko (2014) also presents a method for predicting the evolution of space debris based on spatial distribution. This type of model is useful for risk and damage assessments, prediction of debris detection and mission planning. Space debris models are helpful while performing long-term analysis and forming an effective space debris mitigation concept.

The second approach to gaining knowledge on SOs addresses the problem using the methods of classical astrodynamics. Here, observations are performed making use of available Space Surveillance and Tracking networks; thus detected objects are maintained in a catalogue defining their precise orbital information. This catalogue provides the required information concerning orbital ephemerides more accurately than a debris model. Also, such a catalogue plays a crucial role in day-to-day space operations, in terms of estimating collision probability and collision avoidance manoeuvre planning. Hence such a catalogue is effective for short-term applications.

The increasing number of objects in orbit poses an increasing challenge to the cataloguing of SOs. As of June 2017, 18,640 in-orbit objects were tracked by the U.S. Space Surveillance Network and maintained in the US Space Object Catalogue. This number will inevitably increase due to further launches and unavoidable collisions. Flegel et al. (2010) estimated

[2] A space object catalogue serves both civilian and military applications.

that the number of objects with a diameter of 1 cm or greater exceeds 700,000. A report from IADC (2011) presents the total number of estimated fragments orbiting the Earth to be in excess of 100 million. The problem of space debris and its distribution in the orbital space is discussed further in the Section 2.2.

Out of the total SO population, objects of the sizes ≥ 10 cm are considered to be hazardous (US General Accounting Office, 1997). The collision of an active spacecraft with an object of a greater size than 5 cm to 10 cm can induce enough damage to the spacecraft to render it unusable. A space operator has to be aware of all objects that could be hazardous to his/her mission. The unclassified part of the catalogue maintained by the US Strategic Command office is distributed publicly in the form of Two Line Elements (TLE). However, TLEs are not suitable as a standalone database to perform space related operations, such as proximity monitoring and collision avoidance manoeuvre planning. This is due to the limited accuracy (Herriges, 1988), latency and lack of SO orbital information within the TLE catalogue. Also the TLE catalogue does not provide the complete information regarding the number of objects and the SOs' physical parameters. An accurate and complete space situational awareness requires a complete catalogue information.

Although objects greater than 10 cm in size are considered as hazardous, there are instances where 1 cm-size SOs debris can create a considerable amount of damage and render a satellite useless. Although reports of such collisions are rare, they have occurred. The first known collision damaged the small French military satellite Cerise in 1996. Cerise's gravity stabilisation boom was cut off by space debris, with an estimated size of between 1cm and 5cm (Alby et al., 1997). More recently, on August 23, 2017, Copernicus Sentinal-1A satellite's solar panel was hit by a millimetre-size particle which reduced the power generation at the spacecraft ESA (2016a). Current satellite observing technological limitations hinder the cataloguing of SOs smaller than certain sizes.

Moreover, space debris not only poses a threat to space operations and space sustainability, but also affects astronomical observations. During astronomical observations, the trails left from passing debris degrade the quality of the imaging, sometimes wasting valuable time and causing expensive experimental campaign resources to return without useful observations. This issue cannot be mitigated with a SOs catalogue. But, efforts are being made to remove the debris tracks from space observation images, and to incorporate the debris orbits within the ground based telescope planning systems.

Continuous monitoring of a specific object is not possible given the current observation technology. This restricts information relating to the estimation of the current location of an object and the prediction of the future trajectories. Limited availability of observational data requires the prediction of orbital states on the order of a few days into the future, allowing the ability to reacquire the object with follow-up observations. Since space dynamics is non-linear in nature and every estimated state is associated with its imminent uncertainty, long-term accurate prediction of space object motion poses a non-trivial task.

Maintaining a catalogue with a few hundred thousand objects requires a significant computational resource and an accurate representation of orbital motion around the Earth. Together with the orbit propagation techniques, it is necessary to have a good knowledge of orbit estimation and uncertainty propagation techniques. Figure 1.2 shows the different interconnected focal areas relevant for a precise space object catalogue maintenance system. Each topic is vast and difficult to cover under one single research title. This research work is thus concentrating on tacking the issue by evaluating the hatched area of the overall problem. This is carried out by analysing the available orbit propagation methods suitable for space

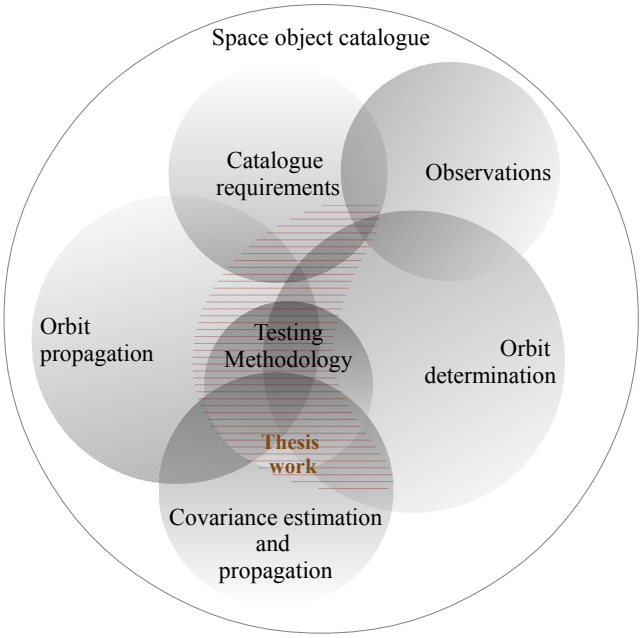

Fig. 1.2 This research brings together and builds upon work conducted by many others in the areas of orbit propagation methods, orbit determination methods, techniques for covariance propagation, and methods for estimating the uncertainty, while newly analysing the space object catalogue maintenance systems requirements and establishing some new methods for estimating the uncertainty in predictions due to an uncertain force model.

object catalogue maintenance in addition to extending them further to propose a method for realistic covariance estimation. The following section provides the main research objectives of this thesis.

1.2 Research Objective

Fundamentally, the trajectory of an artificial satellite in orbit around the Earth can be described by purely numerical techniques, as well as analytical theories of motion. While numerical methods offer high accuracy and can consider a wide variety of perturbing forces, they require step-by-step integration from given initial conditions and may demand great computational effort when applied over long intervals. Cataloguing based on numerical techniques provides highly accurate solutions at the expense of high computational costs coupled with the difficulty in maintaining the catalogue in a non-linear dynamical position and velocity space. The previous statement is presented under the assumption that a numerical propagator makes use of good quality high-fidelity force models. If a numerical propagator is making use of an imperfect drag model or improper spacecraft model, prediction accuracies are not necessarily better than those of analytical methods.

Although there are several agencies (Boikov et al., 2009; Morton and Roberts, 2011; Oltrogge and Alfano, 2015) already maintaining a precise SOs catalogue, the details are not available for open research platforms. Thus, the first objective of the present thesis is defined as:

1. Establish the requirements for an orbital theory, that is to be employed in a catalogue maintenance system.

Establishing such a requirement considers the information flowing to the catalogue maintenance system, operations or tasks to be handled within the catalogue, and the application of the catalogue. The requirements will be established in terms of characteristics of the orbital theory, prediction accuracy of the theory and computational runtime.

2. Develop a generic test methodology for evaluating the performance of an orbit propagation method for the various orbital regions.

The limited availability of real satellite observations hinders the testing of a satellite theory and its suitability in all Earth-bound orbital regions. Hence, it is crucial to develop an alternative test method allowing the evaluation of a propagation method, while providing insights into the dynamics of the orbital dynamics.

3. Study, evaluate, and propose a suitable satellite theory for the catalogue maintenance system. Extend the selected theory to make it suitable, in case of close match.

For a first step, reference models for numerical and analytical orbit propagations will be established, taking into account applicable categories of orbits. Existing analytical and semi-analytical theories will be reviewed and compared regarding short-term and long-term accuracy, as well as computational load, to assess their use in space object cataloguing for the various categories of orbits. Before the theory is analysed for the purpose of fulfilling the requirements, a theoretical study of available methods provides the necessary background to make an informed decision.

4. Optimize computation of partial derivatives to allow use of the selected orbit propagator in a differential correction (i.e. orbit determination) process to assist the catalogue maintenance system.

This should also include quantifying the factors affecting the performance of an orbit determination system. The analysis should also recommend additional factors for cataloguing system in terms of fit length of orbital arc, observations accuracy requirement, and initial orbit determinations accuracy. Each of these studies can be elaborated to a independent research topic, here it is aimed to provide a method for quantifying different factors' influence on orbit determination system.

5. Develop a method for estimating orbit prediction uncertainty due to the most uncertain force model, and a method for realistic covariance propagation.

For a catalogue, it is vital to provide orbits with a realistic accuracy information. Along with the assessment of orbit propagation uncertainties, methods for a realistic prediction of orbital uncertainties will be examined, taking into account initial state uncertainties, force model uncertainties, and model specific simplifications. The linearity region for covariance propagation and possible deformations of the initial uncertainty ellipsoids will be characterised as a function of the prediction interval and the respective orbit type. Specifically a method for estimating the model uncertainty in orbit propagation due to atmospheric densities is developed.

Based on the above objectives, the research was conducted to tackle certain issues of the catalogue maintenance system. During the period of research, the results were presented in a journal publication (Setty et al., 2016b), and at several conferences (Setty et al., 2016a, 2014, 2013). This thesis will present the details of the problem and obtained results. The below section presents the organisation of the topics.

1.3 Organization of the Dissertation

The structure of the thesis is presented in Figure 1.3. To reach the first objective and to establish the performance requirements of an orbit propagator, preliminary chapters are dedicated to understanding the space debris situation and its future increase, followed by the available sensor data for a catalogue maintenance system, together with the available orbit propagation and determination methods. After acquiring the theoretical knowledge on different flavours of propagation techniques a specific propagator, namely the Draper Semianalytical Satellite Theory (DSST), was selected. This selected method was tested extensively to check if it met the accuracy and computational requirements. The last parts of the thesis present the developed method to capture the prediction uncertainty caused due to un-modelled fluctuations in the atmospheric densities. It is evaluated for its correctness and the results are discussed. A list of chapters with short description of their contents is presented:

Chapter 2 *Space Surveillance and Tracking* establishes the required background concerning the current problem, its characteristics, available technologies to gain the information for a catalogue maintenance system and the method for general precision catalogue maintenance. This is followed by, a brief discussion on the high level architecture of a precise space object catalogue maintenance system. At the end, the propagator requirements within the scope of catalogue maintenance are derived making use of the gathered information.

Chapter 3 *Astrodynamical Methods for Catalogue Maintenance* discusses the required astrodynamical techniques, which are relevant for the catalogue maintenance system. This is carried out while presenting state-of-the-art orbit propagation, orbit determination, and uncertainty propagation methodologies. The chapter is concluded by presenting the selection of the propagator for catalogue maintenance system.

Chapter 4 *Draper Semi-analytical Satellite Theory* provides the theory and software development associated with the selected semi-analytical orbit propagator. The improvements conducted regarding the method to improve its orbit prediction accuracy are then discussed. Later, the method for estimating the mean elements used within DSST, which is implemented as DSST-OD, is presented.

Chapter 5 *Evaluating Orbit Propagation and Orbit Determination Methods* provides the unique testing methodology developed to quantify an orbital theory, together with the application of the methodology to extensively test the DSST. The results are then discussed.

Chapter 6 *Atmospheric Density Model: Uncertainty Estimation* deals with the quantification of model uncertainty specifically for the atmospheric density and its influence on the uncertainty in predictions. After the derivations, the adaptation of the method to

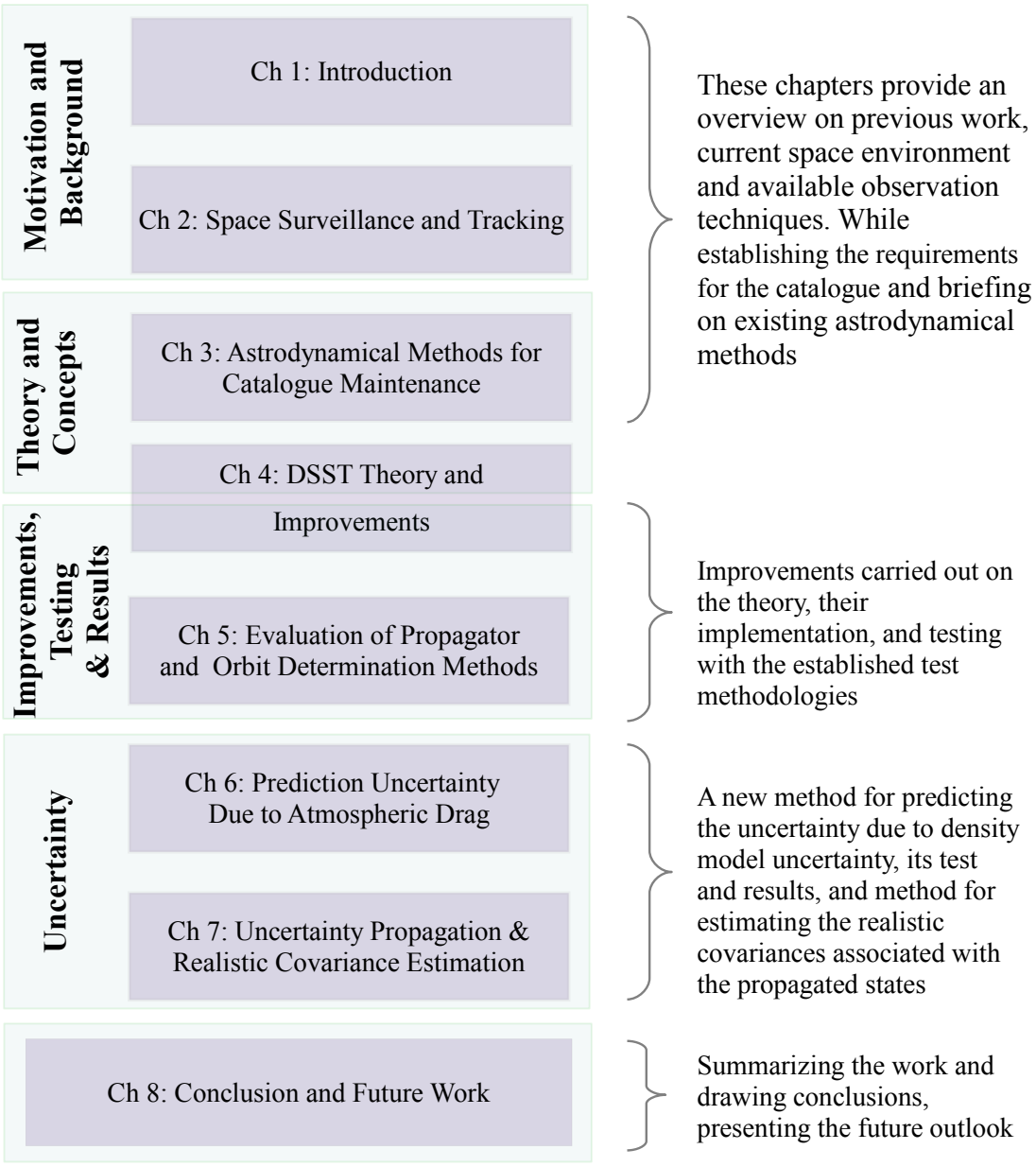

Fig. 1.3 Structure of the thesis together with the individual chapters and relevance

catalogue maintenance system is discussed. At the end of the chapter, test results from comparison of the real precise orbital data are showcased.

Chapter 7 *Uncertainty Propagation Quantification* presents the method for realistic covariance estimation for the catalogue maintenance system, making use of the mean element set, and including the model uncertainty within the propagated uncertainty. A calibration methodology is also discussed, in short, making use of the results from previous chapters. Finally, the obtained results are compared against Monte-Carlo simulation test cases to check the accuracy of the propagated covariances.

Chapter 8 *Conclusion and Future Work* discusses the research while summarising the work. To conclude, open questions related to the catalogue maintenance system and future works are discussed.

CHAPTER 2

SPACE SURVEILLANCE AND TRACKING

This chapter introduces the definitions and information required to understand the issues within Space Surveillance and Tracking, together with the issues related to a space object catalogue maintenance system. A brief picture of the space object population is discussed together with the main observing techniques employed within the space surveillance and tracking community. The main objective of this chapter is to establish the required information and to recognize the issues regarding orbit propagation, orbit determination, and uncertainty quantification for the purpose of SOs cataloguing.

2.1 Orbital Classes

A satellite's mission usually dictates its orbit around the Earth. Typical orbits of SO range from a couple of hundred kilometres above the ground (the International Space Station at 340 km) to graveyard orbits for dead geostationary satellites above 36,000 km. Although the useful orbits for current space applications can be divided into a few altitude ranges, debris from collisions and uncontrolled objects is scattered into all possible altitude ranges. Another aspect of orbits is their eccentricities. Due to satellites' intended application and unintended incidents, such as collisions and explosions, it is possible to find man-made objects from near circular ($e \approx 0$) to the most eccentric orbits ($e \approx 0.8$).

For ease of analysis and understanding the dynamics of the Earth bound orbits, they are broadly classified into four orbital regimes.

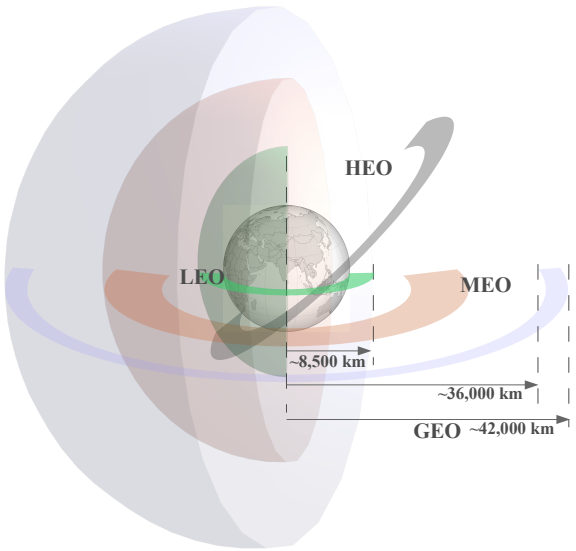

Fig. 2.1 Schematic representation of orbits around the Earth

LEO – Low Earth Orbits **MEO** – Medium Earth Orbits
HEO – Highly Eccentric Orbits **GEO** – Geostationary and geosynchronous Orbits

The above classification is based on the orbit shape parameters [Semi-major axis (a) and Eccentricity (e)] and Inclination (i), without considering the angle parameters [Right-ascension (Ω), Argument of perigee (ω), and Mean-anomaly (M)]. The regions are summarised in Table 2.1 and Figure 2.1 shows a pictorial representation of the classified orbits.

Table 2.1 Summary of orbital class definitions

Parameter	LEO	MEO	HEO	GEO
Semi-major [km]	$< 8,500$	$8,500 \leq a < 36,000$	$\leq 36,000$	$36,000 \leq a < 44,000$
Eccentricity	< 0.2	< 0.2	$0.2 \leq e < 0.9$	< 0.2
Inclination	$0^\circ \leq i \leq 180^\circ$	$0^\circ \leq i \leq 180^\circ$	$0^\circ \leq i \leq 90^\circ$	$0^\circ \leq i \leq 30^\circ$

The classification in Table 2.1 is defined for the purpose of orientation and analysing the propagation effects. The defined orbital regions cover 99.2% of the NORAD catalogue as of March 2018. The missions with newer applications and certain specific orbits are not considered within this classification, such as retrograde HEOs, highly inclined GEOs, and two-day orbits.

2.2 Current Space Object Population

Understanding the evolution and distribution of man-made space objects serves two purposes. First, it allows extrapolation of the number of trackable space objects in the future catalogue by understanding the quantity of past satellite missions and occurrence of collision between the objects. Second, it permits estimation of the computational burden on the catalogue maintenance system by estimating the number of observations that will be processed. Also, understanding the frequency at which an object could be re-observed with the current technology and number of observation sites will give an approximate interval over which the propagator needs to predict the satellites' orbits. Altogether, the gathered information will assist in deriving the requirements in terms of orbital regimes in which the selected propagator will be applied and the computational load that is allowed within the system.

Figure 2.2 presents the time evolution of the total number of space objects in orbit around the Earth, including the mission-related wastes, debris, and fragmented objects. The total number of SOs represented in the graph is based on the satellite catalogue (SAT-CAT) maintained by Celestrak (Vallado, 2018). In the Figure 2.2, the number of satellites shows a linear trend over the years, along with rocket bodies and mission-related debris. In contrast, the total number of SO shows several jumps and noisy character, that are caused by collisions and fragmentations. Out of all the objects in the NORAD catalogue, approximately 35% of the SO originated from ten collisions or breakups (NASA-ODPO, 2016), which are listed in Table

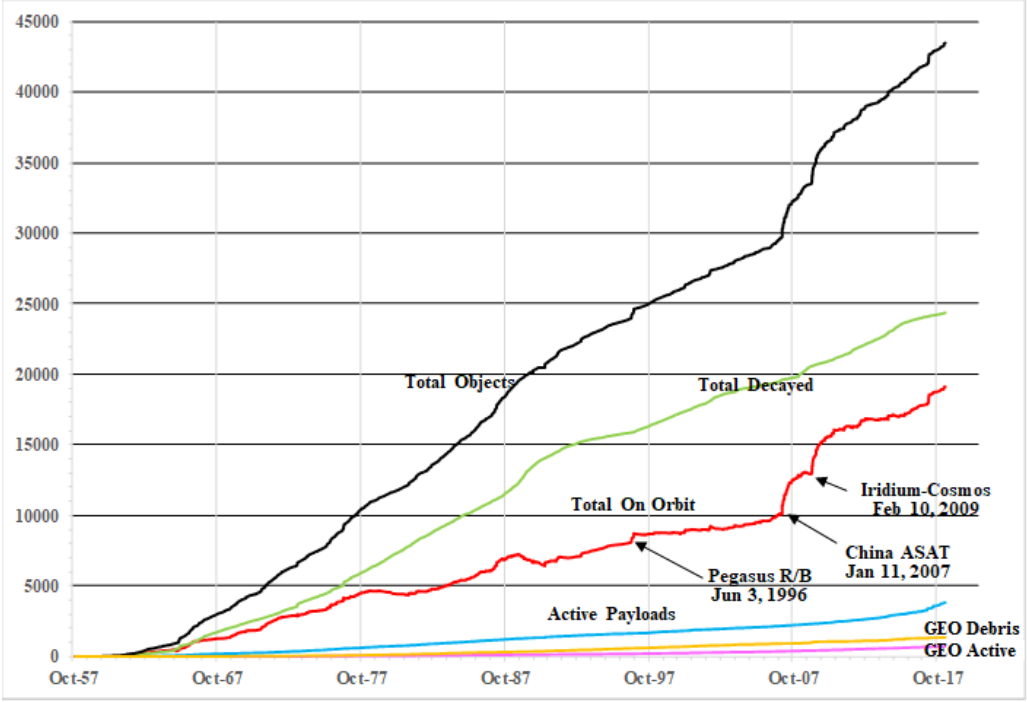

Fig. 2.2 Evolution of catalogued objects in Earth orbit by object types until October 2017. Data and plot courtesy Vallado (2018).

2.2. Although two-thirds of the fragments have de-orbited, 5,059 are still present in the LEO region.

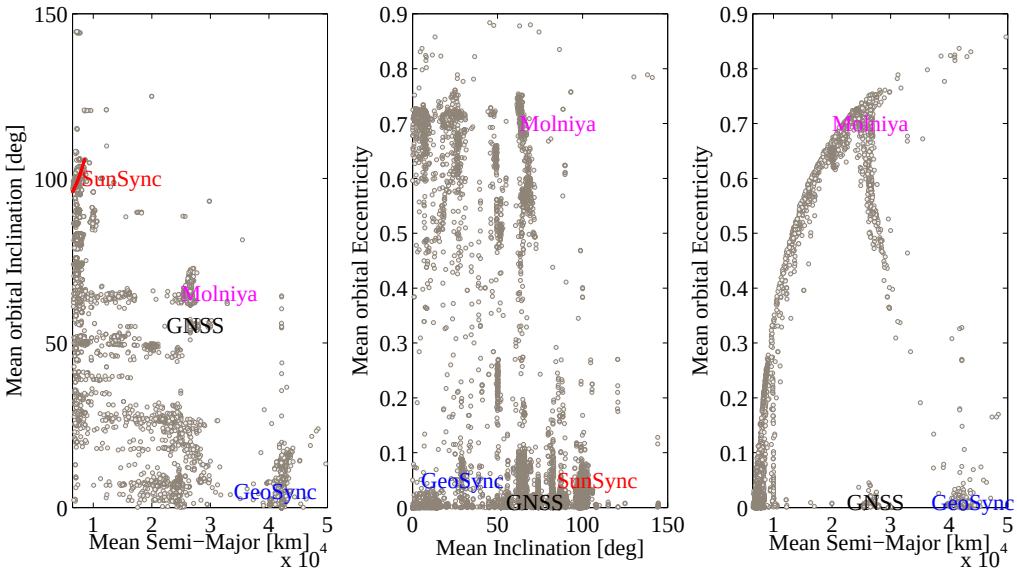

Fig. 2.3 Space object distribution from NORAD catalogue, dated 01-May-2016, in $(a-e-i)$ orbital space. Main application orbits are highlighted

Figure 2.3 shows semi-major axis, inclinations and eccentricities of 17,255 catalogued objects. Figure 2.4 presents the number of objects in each of the classified orbital regimes. Nearly 70% of the listed satellites and fragments are in LEO. The reason is that this kind

Table 2.2 Top ten collisions and breakups along with the amount of debris created from the event NASA-ODPO (2016)

Nr.	Name	Year of Breakup	Catalogued Debris	Debris in Orbit	Cause of Breakup
1	Fengyun-1c	2007	3428	2880	intentional collision
2	Cosmos 2251	2009	1668	1141	accidental collision
3	STEP-2 Rocket Body	1996	754	84	accidental explosion
4	Iridium 33	2009	628	364	accidental collision
5	Cosmos 2421	2008	509	0	unknown
6	SPOT-1 Rocket Body	1986	498	32	accidental explosion
7	LCS 2 Rocket Body	1965	473	33	accidental explosion
8	SACI 1 Rocket Body	2000	431	210	accidental explosion
9	Nimbus4 Rocket Body	1970	376	235	accidental explosion
10	TES Rocket Body	2001	372	80	accidental explosion
		total	9137	5059	

of orbit is the most suitable for atmospheric sciences, remote sensing, ocean monitoring, Earth observation, military surveillance, and communication purposes. From the Figure 2.3 it can be observed that in LEO objects occupy most of the inclination space. But more specifically a cloud of objects can be found between the inclinations $95° - 113°$, due to the special characteristics of these orbits of being 'sun-synchronous'.

Satellites in GEO regime are communication, broadcasting, meteorological, and a few navigation satellites. Because the period of a GEO orbit is equal to Earth's rotation, it is ideal for information broadcasting over a wide area on Earth for the whole day. Currently about 8% of all tracked objects, within the NORAD catalogue, are between the semi-major of $42,164 \pm 2000$ km and inclinations between $0° - 30°$.

Most satellites contributing to Global Navigation Satellite Systems are placed in MEO region, with a period of 11 hours to 14 hours. Russian communication satellites, GEO transfer vehicles, and other objects that have higher eccentricity larger than 0.2 constitute 13% of objects catalogued as HEOs.

Space utilization and space debris will only increase as barriers to access space become lower, and the number of governmental and commercial space actors continue to grow. New developments in space applications and technological advancements are giving rise to "mega-constellations" such as the OneWeb constellation, which is planned to have over 600 satellites in the LEO regime (Space News, 2015). This is one of several future constellations planned for providing internet service from LEO.

Taking the number of further launches, possible collisions, and statistical approximation of break-ups into account, the effective number of space objects, ≥ 10 cm in size, orbiting around the Earth is estimated to be over 20,000 in LEO alone by the year 2050 (Liou and Johnson, 2007). This also makes an optimistic assumption of no cascading effects of further collisions. Lin et al. (2007) provide simulated prediction using the ORDEM2000 model of space debris evolution for all orbital regimes. On the order of 10^5 objects with sizes greater than 10 cm are anticipated. These studies give a perspective on the future growth. There are several factors which influence the prediction of orbital debris, such as launch rate in following years, orbital class utilisation and technological advancements, collisions and breakups, international policy towards space sustainability, etc., which at present cannot be addressed with certainty.

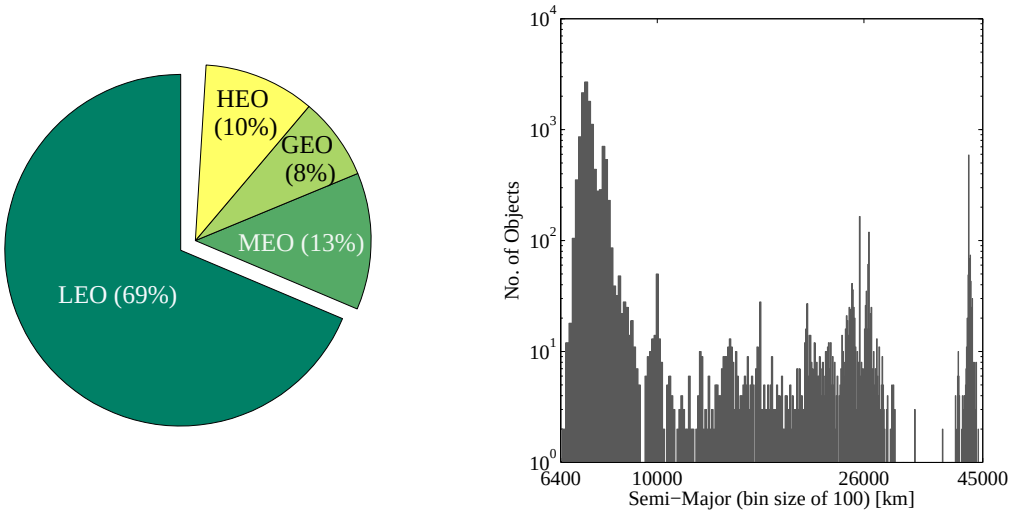

Fig. 2.4 Left: Percentage of SOs in different orbital regimes within the NORAD catalogue. Right: Distribution of number of NORAD objects over semi-major axis

Following the estimates from above literatures the number of objects in future catalogue can be realistically assumed to be between the orders of 10^5 and 10^7. From analysing the currently available information, it is seen that the SOs are spread over all possible orbital regimes. This constraints the selection of orbit propagation method which must be able to propagate orbits in all possible Earth bound orbits. That is with semi-major axis ranging from 6,550 km to 44,000 km, inclinations from 0° to 180° ($i > 90°$, are also called as retrograde orbits), and with eccentricities between $0 - 0.8$.

With the current observation technologies an organization is able to track objects down to sizes of ≥ 1 cm (Liou, 2018). Considering the application, limitation, and the detection capabilities, space objects with size of 5 cm are planned to be included in the future catalogue. This will escalate the number of catalogued objects to the order of 10^5 SO. Hence, the propagation method must be computationally compatible with the catalogue maintenance system's capabilities.

The next section describes the observation methods employed at different orbital regimes, accuracies achieved by individual techniques, and their limitations.

2.3 Observation Methods

As per the definition from the European Space Agency (ESA, 2016b), 'Space Surveillance and Tracking is the ability to detect and predict the movement of space debris in orbit around the Earth'.

The first part of the space surveillance and tracking system, the detection of space debris, is achieved by using three basic types of sensors: optical, radar, and space-based sensors. In this classification, it is assumed that the first two sensor types are ground-based and the latter can be either optical, infrared, or radar based sensors orbiting in space. Figure 2.5 shows the schematic representation of different satellite observation methods in use. Other means of tracking satellites includes Global Positioning System (GPS) measurements and Satellite Laser Ranging (SLR). The latter two are possible if the satellite carries a GPS receiver

or a retroreflectors on board which limits the detection of new debris and adjunct satellites. Recent efforts presented by Sproll et al. (2016) are trying to adapt the SLR in debris tracking mode, and improve the orbital knowledge of SOs without retroreflectors. In this method the laser ranging relies on the objects' body reflection. Irrespectively, if the observations are available from GPS or SLR measurements, they are used within the maintenance of a catalogue. Even if GPS and SLR data do not make it into the catalogue maintenance system, they might be used to evaluate the accuracy of the catalogue; to calibrate the propagation and determination subsystems. Table 2.3 provides the capabilities of different sensors and their operational orbital regimes.

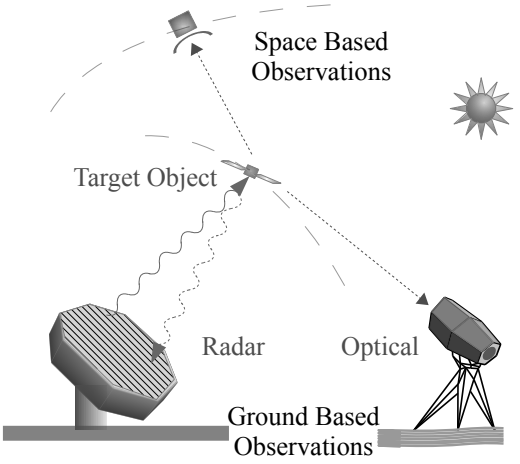

Fig. 2.5 Schematic representation of general space object observation methods

Currently, optical and radar systems are employed for space surveillance. Optical sensors measure the visible energy emitted or reflected by objects, and radar sensors measure high-frequency radio waves reflected by objects. Space-based sensors use infrared and visible spectrum for detection and tracking.

Observation campaigns are performed in two modes: detection mode and tracking mode. In detection mode, also known as survey mode, sensors are used to scan a certain part of space and detect new objects. The observations are correlated with the existing objects within the catalogue. If no match is found, then a new object profile is created for that set of observations. In tracking mode sensors are pointed to observe specific SO, to reinforce the already existing objects' orbital information. Space object catalogue, database of SO orbital information, constitutes the latter part of the space surveillance and tracking system.

For this research, it is vital to understand the 'quality and quantity' of observation data that flows into the space object cataloguing system. The number and distribution of sensors that provide the re-tracking or re-observing capabilities will enable us to set the requirements for selecting a suitable orbit propagation method.

Table 2.3 Possible observation methods from different bases for tracking and detecting space objects in LEO (L), MEO (M), and GEO (G) regions for tracking and detecting space objects. Darker boxes indicate currently used methods.

Sensor base	Sensor type		
	Optical	Radar	Infrared
Ground	M G	L M	–
	L	G	
Space	L M G	–	L M

Figure 2.6 gives the optical and radar sensor locations worldwide dedicated to space surveillance along with the contributing sensors.

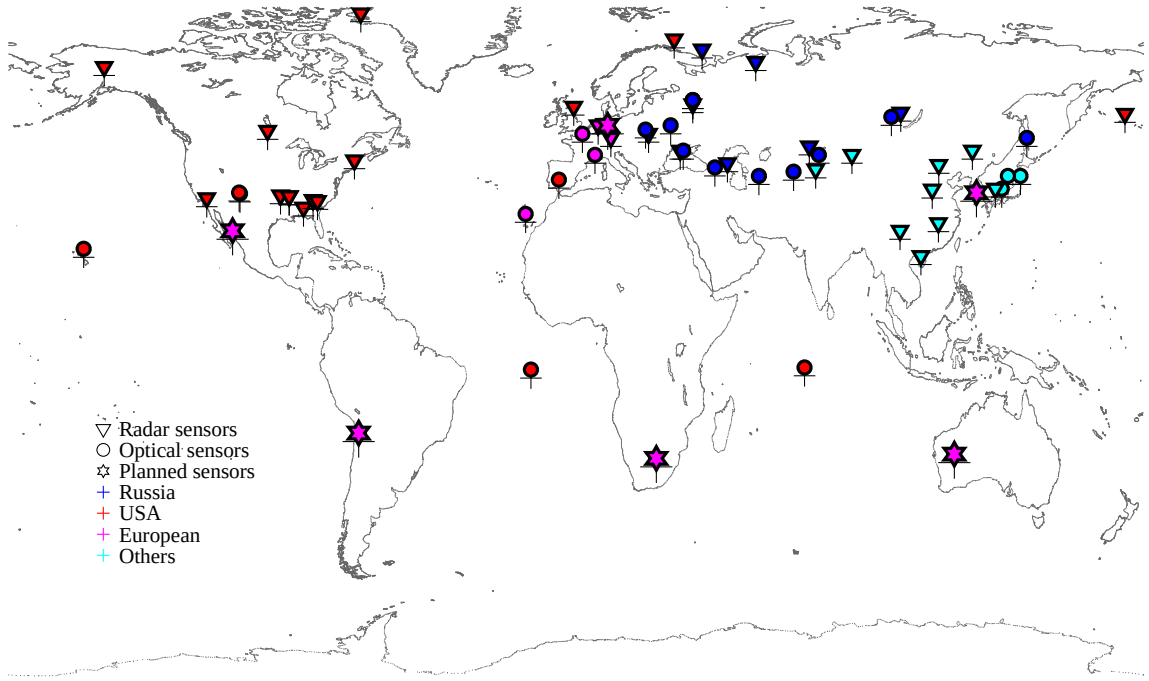

Fig. 2.6 Dedicated, contributing, and planned sensor locations from different space surveillance programs. The above data is compiled using publicly available sources.

Different observing methods are briefly discussed regarding operations with more emphasis on sensors' accuracy and capabilities. Detailed descriptions regarding sensor types, usages, and their limits can be found in Klinkrad (2006), Molotov et al. (2008), Walsh (2013), and Vallado (1997).

Radar sensors

The system transmits a beam of electromagnetic energy towards a target from the antenna. Depending on the physical characteristics of the target, the energy will be absorbed, reflected, or some combination of both will occur. If any energy is reflected, then the reflected beam will be sensed by a receiver, that will measure the direction and time-of-flight of the received signal. This provides the base of radar observations in the form of azimuth(α), elevation(β), range(ρ), and Doppler measurements. Furthermore, angle-rates($\dot{\alpha}, \dot{\beta}$) and range-rates ($\dot{\rho}$) can be deduced with post-processing techniques (Khutorovsky, 2004).

Radars are used for imaging, tracking, and detecting space objects and ballistic objects. Currently, there are two general classification of radars used for observing Earth-orbiting objects: phased array radars and conventional radars (Mehrholz et al., 2002). Phased-array radars can maintain tracks on multiple satellites simultaneously and scan large areas in short time intervals. This is due to their ability to steer the beam electronically. Conventional radars use movable tracking antennas to detect and track the satellites, which are generally used for tracking individual objects. Skolnik (1981) and Minihold and Bues (2012) provide the details on development and operation of both radar types for different applications.

Table 2.4 Radar measurement errors for openly available radars when they are in maximum sensitivity mode (SNR = 10dB) (Walsh, 2013)

	Range error [m]	Angle error [deg]
FPS-85 (Florida, USA.)	33.0	0.180
Haystack (Massachusetts, USA)	0.03	0.008
HAX (Massachusetts, USA)	0.02	0.014
TIRA (Wachtberg, Germany)	0.50	0.070
DON-2N (Moscow, Russia)	10.0	0.037

Characteristics of Radar Measurements

Ground-based radar stations can observe an object when it is having a flyover within the radar's field of view. Re-tracking of an object thus also depends on the ground track repeatability of the orbit. A usual radar observation arc length varies in the range of 50 to 1,000 seconds (1-16 minutes) depending on the altitude and phase of the ground track with respect to the observing station. Some high-power radar stations can stretch their orbital reach up to GEO altitudes.

Radars are the backbone of space surveillance and tracking systems (Berger et al., 1992). To establish the requirements, in this study phased-array radars are analysed for their accuracies. The radars being evaluated here measure range and angles. The standard deviation of the radar range measurement error σ_ρ is defined as the Root Mean Square(RMS) of the three error components as in equation 2.1 (Curry (2005): chapter 8)

$$\sigma_\rho = \sqrt{\sigma_{\rho N}^2 + \sigma_{\rho F}^2 + \sigma_{\rho B}^2} \tag{2.1}$$

where the noise range error is defined with $\sigma_{\rho N} = \Delta R/\sqrt{2 \cdot SNR}$. The SNR is the signal-to-noise ratio, and ΔR is the radar range resolution, which is equal to the speed of light divided by twice the signal bandwidth. $\sigma_{\rho F}$ is the fixed random error due to random noise in the receiver and is commonly of similar magnitude as the noise range error at a signal-to-noise ratio of 20dB. $\sigma_{\rho B}$ is the range bias error.

Similar to range measurement errors, each angular measurement ($A = \{\alpha, \beta\}$) is characterized by RMS errors of the three components, as in equation 2.2

$$\sigma_{A_i} = \sqrt{\sigma_{A_i N}^2 + \sigma_{A_i F}^2 + \sigma_{A_i B}^2} \tag{2.2}$$

where the angle noise $\sigma_{A_i N} = B_w/(1.6 \cdot \sqrt{2 \cdot SNR})$, B_w is the radar beam-width, and σ_{AF} is the fixed random error which will limit angular accuracy.

The usual operational SNR and B_w levels for radars detecting or tracking a space object with the size greater than 10 cm (area greater than $10^{-2} m^2$) and at an altitude of 500 km are 10 dB and 0.05° (Walsh, 2013). Using the information in Equations 2.1 and 2.2, the range error is calculated to be $15m$, and angle errors are 0.01°. Walsh (2013) provides the σ_ρ and σ_A for five radar observatories within the USA and Europe which are presented in Table 2.4.

Since most of the radar operational data are not available publicly, for this research the average of σ_ρ = 10m and $\sigma_A = 0.0028°$ (= $10'' = 4.85 \times 10^{-5}$rad) is considered as the nominal quality of radar observations for debris tracking and surveying.

Optical sensors

An optical sensor (telescope) tracks satellites across the sky by recording the right ascension and declination. The sensor is composed of a detector (Charge Coupled Device (CCD)), optics, and a gimbal. The gimbal is a mounting device that stabilizes the sensor and provides control of the tracking motion.

Detection and tracking from optical sensors rely on the reflected sunlight from the space objects. Images captured from CCD sensors are processed to extract astrometric observations in terms of angles. The accuracy of the derived quantities depends on several factors (Herzog, 2013). A list of the common error sources in optical measurements is presented below, and Table 2.5 provides the magnitude of three telescopes around the globe.

1. Pixel size and number of pixels on a sensor
    - Describes the area of the sky scanned by a single pixel.
    - First order of approximation for accuracy computation: field of view divided by the number of pixels (representative value of $3''$ is considered).
2. Seeing
    - Describes the effect of the air turbulences on the measured position.
    - After exposure time, light from stars and/or objects is detected not by a single pixel, but distorted into a two dimensional Gaussian distribution with seeing as standard deviation.
3. Tracking mode
    - Tracking error is dependent on the tracking velocity. An error in tracking velocity makes stars or objects appear as streaks rather than point-like, which induces inaccuracies in deducing angle measurements.
    - Leads to elongated two dimensional Gaussian distribution convoluted with near linear tracking errors, which is in turn quantified as white noise within measurements.
4. Pointing accuracy
    - Dependent on the accuracy of the mount and the line-of-sight direction.
5. Atmospheric corrections
    - Refraction due to atmosphere can lead to wrong angular measurements. Hence, the line of sight vectors are corrected using atmospheric models.
    - Incorrectly applied atmospheric model leads to deviation of extracted quantities.
    - Given the sophistications adapted in reducing the atmospheric effects, the error induced due to this effect is assumed to be zero.
6. Gimbal
    - Vibrations induced due to the motion of the mount lead to errors in measurements.

- For well balanced telescopes, decay time of the vibrations is small (in the order of a few seconds). Taking advantage of this stabilization, telescopes are pointed at planned directions ahead of exposure times. Hence, this error source can be ignored, assuming the practice of telescope operations.

7. Time stamp of the epoch

   - Is in the order of several arc-seconds, if not well calibrated. Many sensors are tested and the timing bias is introduced to overcome the error source.

Table 2.5 Operating accuracies of three different telescopes and mounts that are parts of the ZimSMART network (Herzog, 2013)

Telescope	Mount	Pixel scale	Seeing	Tracking accuracy	Pointing Accuracy
Takahashi	Paramount	$3.6''$	$2''$	$1''-7''$	$10''-30''$
ASA	ASA	$1.8''$	$2''$	$0.35''-1''$	$\leq 12''$
Takahashi	ASA	$3.6''$	$2''$	$0.35''-1''$	$\leq 12''$

Using the average values from Table 2.5, and computing the RMS value of all uncertainties, $\sim 12''$ is assumed to be an average error in angular measurements from optical sensors.

Given the operational principles and mechanical limitations of a gimbal, ground-based optical telescopes are presently used to detect and monitor MEO and GEO objects. An uncertainty of $12''$ in azimuth translates to $50-1,200$ [m] in along-track direction, and a similar range of error in normal direction is considered for further analysis[1].

Fiedler et al. (2015) give details of DLR's planned telescope network, along with the constraints and time lengths of observing durations that could be achieved with optical telescopes. Kubo-oka et al. (2015) present their experience in surveying GEO satellites using optical telescopes.

Space-based sensors

These sensors operate under visible or infrared wave-lengths. Generally these sensors are coupled with optics to take advantage of the absence of atmosphere and the ability to observe in multiple wavelengths simultaneously. Space-based sensors can detect debris, satellites, and other natural objects orbiting the Earth without being influenced by weather or atmospheric conditions. They also have an advantage of higher resolution because of the potentially smaller distance between the observer and the object for LEO-to-LEO observing sensors. While the errors are reduced for LEO-to-GEO observations due to the absence of strong atmospheric effects. Deducing the observables and pointing a space based sensor are more complex than ground based sensors due to the orbital motion of the observer (Vallado et al., 2016). It is a prerequisite to know the precise orbital position of the observer with respect to Earth in order to accurately measure other SOs.

The Midcourse Space Experiment (operational from 1996 - 2006) was an early space mission dedicated to observing space debris (Egan et al., 2003). It used an optical sensor to

[1]The error in normal direction is more influenced by the geographic distribution of the optical sites and number of distributed sensors, which is not investigated to evaluate the magnitude of error and the quantity is assumed for the present study.

detect small to mid-sized debris in the GEO region. The costs of space-based sensors are in general higher than those of ground-based sensors which limits their use. As an alternative to having a dedicated mission of space based sensor for SSA, Boyle et al. (2006) have suggested the use of star-trackers for the purpose of observing SOs. Widespread use of space based sensors is not yet routine. Therefore, these sensors are left out of the detailed analysis for their error sources.

2.4 Space Object Catalogue and Its Maintenance

The space object catalogue is a database of the characteristics of the orbital population along with the collection of orbital elements (or states) that have been derived from measurements or records (Goericke, 1999). Space objects' states are regularly updated with observations from a space surveillance network. Once an object is brought into the database, its orbit information has to be updated based on re-observations which is known as 'catalogue maintenance'.

Several space agencies maintain their own databases for operational and research purposes. The USA maintains a SO catalogue that is frequently updated by observations by the Air Force Space Command. The Russian Federation maintains its own space object catalogue through the Main Space Intelligence Centre. The European Space Agency uses information from these databases and archives it in the Database and Information System Characterising Objects in Space (DISCOS). Presently, these catalogues and details of complete maintenance procedures are not publicly available. The only openly distributed catalogue is in the form of Two Line Elements (TLEs) provided by the Joint Space Operation Center (JSpOC) maintained catalogue. But the publicly available TLE catalogue has limitations in terms of its accuracy, update latency, and completeness in terms of number of objects, which alone disqualifies it for accurate space operations.

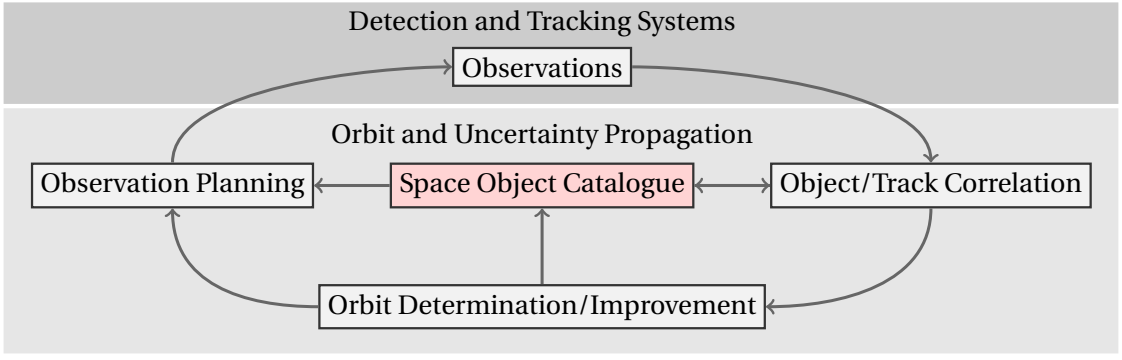

Fig. 2.7 Different elements of space object catalogue maintenance system, along with the subsystems in which orbit and uncertainty propagation methods play a role

One of the main objectives of this research is to provide a suitable orbit and uncertainty propagation method for maintaining a space object catalogue. In this, the first step is to identify the applications of orbit propagation and determination methods and their accuracy requirements within a maintenance system. Figure 2.7 shows high the level information flow of a space object catalogue maintenance system. Typical SSA tasks that involve orbit determination and/or orbit predictions are listed below:

- observation processing: object correlation, track association and updating of catalogued objects (orbit determination);
- object manoeuvre detection and manoeuvre processing;
- object conjunction assessment: covariance propagation and uncertainty propagation;
- sensor tasking; and
- lifetime predictions.

The first three tasks typically demand an accurate orbit propagation technique, whereas a statistical assessment of approximate predictions is sufficient for lifetime predictions. Less accurate propagations will also suffice for sensor tasking. Methods for sensor tasking and lifetime predictions are presented in Miller (2007), Goodliff et al. (2006) and Dell'Elce et al. (2015). Orbit propagation and determination methods supporting the maintenance tasks of a catalogue system are within the focus of the present study.

2.5 Propagation Requirement for Catalogue Maintenance

Finding an orbit propagation method that can be used for all cataloguing tasks requires that an OP method offers a favourable trade-off between accuracy and computational effort. Thus precise constraints and requirements are to be defined to support the selection of a suitable satellite theory for the mentioned purpose. The previous Section 2.4 discussed the role of a propagator in SO catalogue maintenance and supporting space situational awareness. These roles impose constrains on the accuracy together with the information flowing into a maintenance system.

Several existing orbital theories have been established for specific purpose and applications. An overview of various satellite theories are discussed in chapter 3. There are several advantages in having a common propagation method together with a common data model to be employed for a complete space object catalogue. Commonality reduces redundancy and provides structure to support reliable decision making by the space authorities. Therefore, we consider using a single satellite theory for the entire orbital regime. Before deriving the requirements in terms of accuracy and computational times, the following functionalities of the propagator are observed to be essential:

1. Force modelling for different orbital regimes: the theory should be based on non-singular orbital elements and capable of handling both conservative and non- conservative perturbations.
2. Flexibility of choosing force models at run time: having this option to propagate orbits with different spacecraft area to mass ratios and altitudes facilitates orbits in different regions.
3. Ability to incorporate current Earth Orientation Parameters (EOP) and space weather data.
4. Facilitate modular implementation: the theory should provide flexibility to update or upgrade the constants and models used within the propagator.

5. Fast and accurate state transition matrix computation: the theory should be capable of providing means to support orbit determination methods and covariance propagation.

6. Ability to generate closely spaced ephemerides without increasing the computational effort: to have an interpolation procedure in order to process dense and closely spaced observations.

Applications of the orbit propagator and the orbit determination methods are the driving factors in deriving accuracy requirements. To be reasonable in setting up the requirements, it is preferred to define an average propagation time length during which the propagator is expected to perform. The propagation length depends on the time lengths between re-observations or also known as the length of the update interval. The quantity, length of update interval, is a topic which deserves a dedicated research for understanding and considering all the aspects of a cataloguing system. For evaluation and testing purposes within this study, the average propagation length required for the future catalogue is assumed to be seven days ($T_L = 7$).

Naka et al. (1997) state that, to make use of available sensor information it is required to model orbits with a precision compatible with the observation accuracies. That is to say that the selected orbit propagation should have prediction accuracy for the arc length of seven days with the same quality as available observations. In the previous section the performances of different sensors employed in SST are studied and nominal accuracies for different sensors are defined. Translating the angular uncertainty of optical sensors to tangential distances at the observing altitudes in MEO and GEO orbits, the optical sensors uncertainty is assumed to be in the range of 60 to 1200 meters in along-track direction. The typical range observation accuracy from a radar sensor will be on the order of 10 meters. Hence from the SO catalogue's input perspective 10 meters, in radial direction, can be considered as the best available information.

On the application end of the SO catalogue's perspective US General Accounting Office (1997)(GAO) technical report states that: *NASA's requirements specifically call for sensor tracking to an orbital 'semi-major axis' uncertainty of 5 meters or less. The purpose of this requirement is to better predict possible collisions and better decide on the need for collision avoidance manoeuvres.* The GAO report also suggests that objects 1 cm to 10 cm in size be tracked and included in the future catalogue. Reaching the recommended requirements is restricted by the present tracking and observation processing capabilities. For near circular orbits, it can safely be assumed that, the difference between the uncertainty in semi-major axis and the uncertainty in radial direction is negligible.

If there is ~5 m uncertainty in radial direction, by rule of thumb, the uncertainty in along-track direction grows by a factor of 10 for each orbital revolution. That is to say that for a GEO satellite, after seven days of propagation, the uncertainty in along-track direction will be approximately ~350 m for initial 5 m radial uncertainty. Quantifying the propagators' actual prediction capabilities requires continuous stream of observations from different orbital regions and from different time periods. The main focus of the present research work is to find an alternative to the existing numerical propagator. The selected propagator needs to be performing as close as possible to the numerical method to meet the GAO recommendations and to make up for unknown factors.

Using the above assumptions and information for the present study the maximum allowed position inaccuracy for the arc length of seven days is set to be ≤ 50 meters, with radial uncertainty ≤ 10 meters. Although the radial uncertainty is twice the limit set from GAO

report, it is assumed that the post processing can be performed on the catalogued information to meet the operational needs.

The future catalogue is expected to include on the order of 10^6 space objects (discussed in Chapter 2; GAO report). Morton and Roberts (2011) estimate that the US Joint Space Operation Centre (JSpOC) performs about 40,000 track and object correlations per day to maintain their catalogue and provide collision warnings. This system requires a few hundred thousand orbit predictions and determination runs per day. Also, Boikov et al. (2009) states that the Russian Space Surveillance Centre performs about ten million orbits propagations every day to preserve their catalogue. In order to perform 10^5 to 10^7 orbit predictions per day and to process the observations within the same day, the computing system should be able to complete each prediction in $\frac{1}{100}^{th}$ of a second [2]. The present numerical propagator consumes computational time in the order of a few (1 to 10) seconds for seven days of prediction, depending on various factors. The present state-of-the art computing machines are supplied with multi-core processors and increasing the computational resource is not expensive for a SO catalogue maintaining facility. Considering these factors, realistically we set the requirement on the computational runtime of the propagator to be an order of magnitude lower than that of a conventional precision/numerical propagation methods, that is the preferred propagator should be ten times faster than the numerical propagator. Which translates to be in the range of 0.1 to 1 second per seven days of propagation.

Together with the six points mentioned at the beginning of this section, the Table 2.6 summarizes the accuracy and computational load requirements set for the orbit propagator to be used in the catalogue maintenance system.

Table 2.6 Accuracy and computational load requirements for the propagator within a precision SO catalogue maintenance system

Prediction accuracy for 7 day prediction	$\sigma_{pos} \leq 50m$ $\sigma_R \leq 10m$
Relative computational load for 7 day propagation w.r.t. numerical propagator	≤ 0.1

[2] The definition of the time consumed by computing machine varies depending on the available number of cores within the processing unit, and the program paradigm employed for the catalogue maintenance.

CHAPTER 3

ASTRODYNAMICAL METHODS FOR CATALOGUE MAINTENANCE

The following chapter discusses the general astrodynamical methods which are required within a SO catalogue maintenance system including orbit propagation, orbit determination/estimation, and uncertainty propagation methods.

3.1 Orbit Propagation Methods

The space object is usually assumed to be influenced by a variety of external forces including irregular gravity fields ($\boldsymbol{a}_H$), atmospheric drag ($\boldsymbol{a}_D$), solar radiation pressure ($\boldsymbol{a}_R$), third-body perturbations ($\boldsymbol{a}_L$), Earth tidal effects ($\boldsymbol{a}_T$), and general relativity in addition to satellite propulsive manoeuvres. Excluding intentional manoeuvres, the above terms are commonly referred as perturbing accelerations. Figure 3.1 shows the schematic representation of forces acting on a spacecraft orbiting the Earth. These forces result in a non-linear set of dynamical equations of motion. Furthermore, the lack of detailed knowledge of the physics of the environment, especially for non-conservative forces, [1] through which the space object travels is limiting the accuracy with which the state of the object can be predicted at any given time.

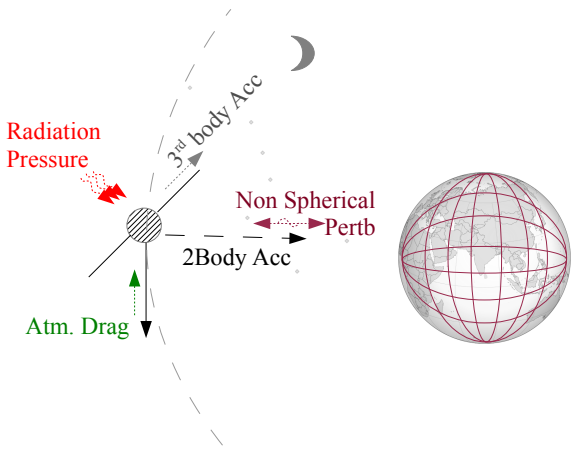

Fig. 3.1 Schematic representation of forces and their directions acting on an Earth orbiting object

If $\boldsymbol{y}$ denotes the orbital state vector of an object consisting of position and velocities ($\boldsymbol{y} = [\boldsymbol{r},\ \dot{\boldsymbol{r}}]^\top$), the differential equation governing the orbital motion is given by Equation 3.1.

$$\ddot{\boldsymbol{r}} = \boldsymbol{F}(t, \boldsymbol{y}) = -\frac{\mu}{||\boldsymbol{r}||^3}\boldsymbol{r} + \boldsymbol{a}_H + \boldsymbol{a}_L + \boldsymbol{a}_D + \boldsymbol{a}_R + ... \tag{3.1}$$

[1] The physical environment becomes more important specifically for non-conservative forces. For atmospheric forces, the limited knowledge (and predictability) of the environment together with the incomplete knowledge of the atmosphere-satellite surface interaction and the uncertainties in the optical properties for radiation pressure are compounding problems.

where $\boldsymbol{F}(t, \boldsymbol{y})$ is the acceleration on orbiting object and μ is the product of the central-body's mass and its gravitational constant. This is the sum of the central body acceleration and all the perturbing accelerations. The fidelity of the modelling terms in Equation 3.1 influences the accuracy of orbit predictions.

Orbit propagation techniques can be classified into three main categories (Vallado, 1997). If the solution is achieved using a numerical integrator, then the method is called numerical propagator or Special Perturbation (SP) theory. If the solution is obtained with analytical approximations, then it is known as General Perturbation (GP) or analytical method. One can also use a combination of analytical and numerical techniques to solve the Equation 3.1; these are termed as Semi-analytical Satellite Theories (SST). Each technique comes with its own advantages and disadvantages. The formulation and description of different orbit propagation methods can be found in many of the standard celestial-mechanics textbooks (Battin, 1999; Beutler et al., 2005; Montenbruck and Gill, 2001; Vallado, 1997).

Perturbing Accelerations

An orbit under the influence of the central body's gravitational force field alone is commonly referred to as a Keplerian motion or a Keplerian orbit. Perturbations are the small disturbances ($\boldsymbol{a}_i$ terms in Equation 3.1) acting on the SO which makes the object deviate from the Keplerian orbit. For Earth orbiting objects, the magnitude of the perturbing acceleration is always an order magnitude lower than that of the central body effect. Figure 3.2 shows the magnitudes of perturbations acting on SO in different orbital regimes. The figure is the adaptation from the original concept from Montenbruck (2001), and makes use of the approximated solutions provided by Milani et al. (1987) (Table 2.1 from the text book) for computing the relation between perturbing forces and altitude.

Details of the individual forces and modelling them will not be discussed further. Various force models, their implementations, and influences of the accuracies are presented in a plethora of openly available literature.

The main purpose of discussing perturbation forces is to decide what forces should be included in the orbit propagation methods to achieve the required accuracies. By neglecting certain perturbations, it is possible to foresee that errors roughly proportional to the magnitude of the perturbational acceleration will be induced in the propagated states. This provides an insight to simplify or to optimise the equation, by not including certain accelerating terms during the propagation. This in turn results in gaining computational efficiency during OP and OD.

As it can been seen in Figure 3.2, for LEO orbits most of the known perturbing forces will play a crucial role for the accuracy of the prediction $\boldsymbol{y}(t)$. The third body perturbations are a few orders of magnitude lower than the first order Zonal term ($J_{2,0}$: equatorial bulge). In GEOs, $J_{2,0}$ has a similar order of magnitude as the third body perturbations. An other important feature of GEOs is the presence of pronounced tesseral resonance terms. Resonance effects are prominent where there is exact commensurability between Earth rotation and orbit period Gedeon (1969). All the tesseral terms in the spherical harmonic expansion contribute to either shallow or deep resonances.

3.1.1 Special Perturbation Theories

Various methods exist to perform numerical integration, and many are commonly used in orbit propagation. Integrators fall into various categories (Hairer et al., 2009): single-step

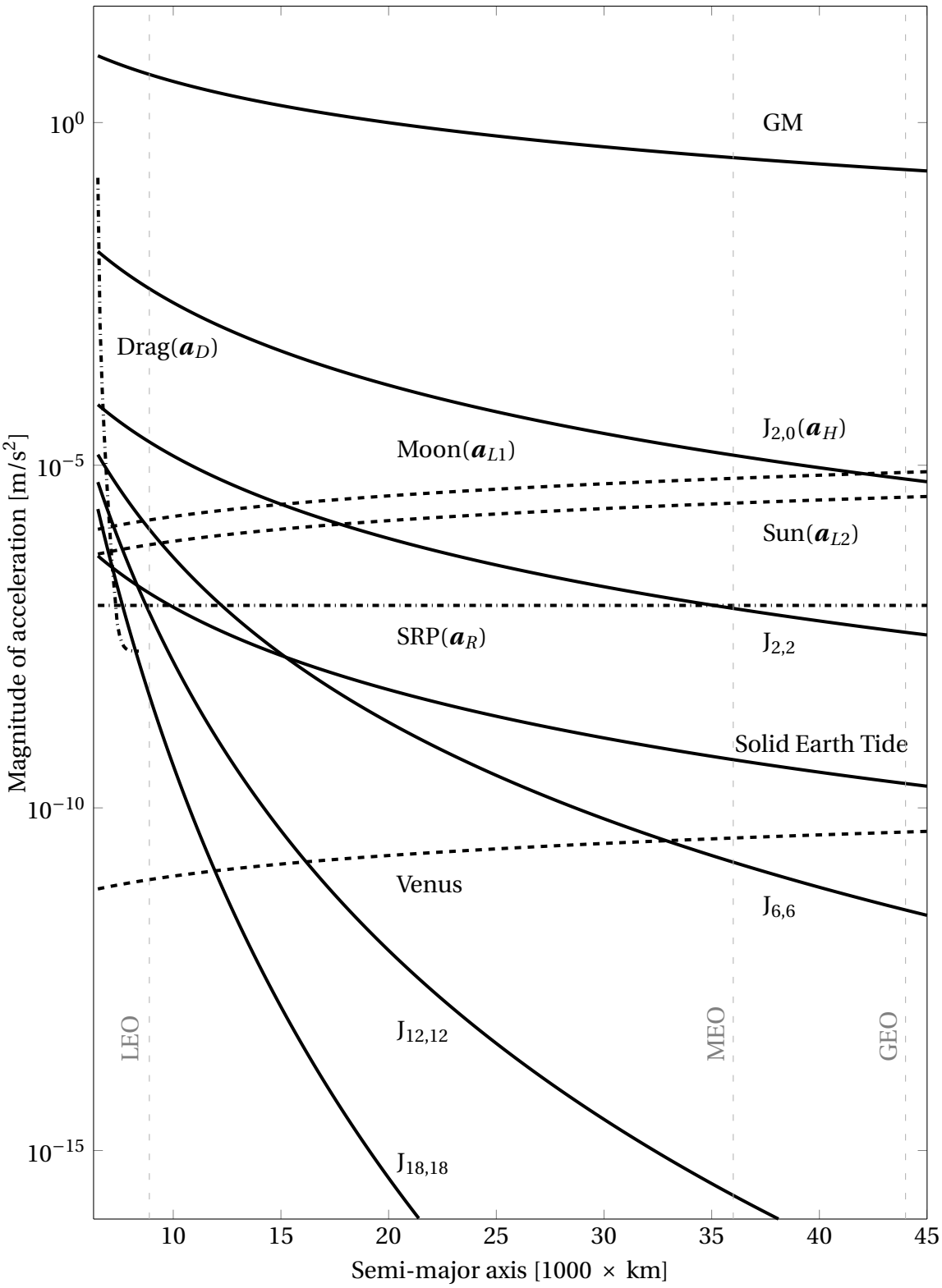

Fig. 3.2 Magnitude of different perturbing accelerations at different altitudes for an Earth orbiting object, calculations are based on relations from Milani et al. (1987)

or multi-step, fixed step-size or variable step-size, summed or non-summed, and single or double integrators. Berry (2004) provides an exhaustive list of different integrator methods, their description, limitations of individual methods, and evaluation of their accuracy for the application of orbit prediction. Along with the comprehensive set of force models (accelerations constituting the right hand side of Equation 3.1) numerical integrators provide the most precise orbital states for computing short arcs of satellite orbits (Tapley et al., 2003). A SP method is the most suited when precision is a key factor. Most geodetic applications call for centimetre level accuracy in orbit predictions, which could be achieved only through SP techniques.

Generally, the SP method makes use of a state vector representation of orbits

$$\boldsymbol{y} = \begin{pmatrix} \boldsymbol{r} \\ \dot{\boldsymbol{r}} \end{pmatrix} = \begin{pmatrix} \boldsymbol{r} \\ \boldsymbol{v} \end{pmatrix} \tag{3.2}$$

differentiating the above equation with respect to time, gives

$$\dot{\boldsymbol{y}} = \boldsymbol{f}(t, \boldsymbol{y}) = \begin{pmatrix} \boldsymbol{v} \\ \boldsymbol{a}(t, \boldsymbol{r}, \boldsymbol{v}) \end{pmatrix} \tag{3.3}$$

A numerical integrator forms the solution to the above equation 3.3 by increments of short steps (h), and it is assumed that the step size is equal to the propagation time. Multiple integration steps are required for predicting orbits for $t > h$. Numerical integrators make use of the series expansions with truncation up to certain order, or use intermediate slopes within the integration time interval. This causes any numerical integrator to have an inherent truncation error. The required accuracy within the propagation along with the truncation error of the selected integrator, and magnitude of the acceleration acting on the space object, restricts the maximum length of the step-size used within SP. Depending on the characteristics of the integrator for orbit predictions, step-sizes can vary between typical values of 100 s (for a LEO object) to 5,000 s (for a GEO object) (Zadunaisky, 1976).

Advantages of the SP methods with respect to its application in space object catalogue maintenance are:

- It is flexible to accommodate comprehensive force models and to include selected accelerations.
- It can produce centimetre level accuracies in orbit determinations[2].
- It is capable of handling the full range of altitudes, eccentricities, and inclinations.
- It is able to handle reinitialization of the orbit propagator with reasonable computational effort. The cost is also dependent on the method of numerical integrator. Reinitialization of integrators are required while handling the transition between sun-light and shadow regions as well as the inclusion of manoeuvres.

Even with the above advantages the following properties hinder the use of SP methods for the purpose of cataloguing:

[2] Centimeter level accuracy in orbit determination is achieved when using numerical integrator with high fidelity force models and empirical corrections.

- It does not provide the insight into the orbital mechanics of the SO. Although this does not have direct influence on the catalogue maintenance system, it limits the understanding of the evolution of the debris model and has certain implications in the covariance propagation and analysis.
- It is computationally very expensive to perform $10^5 - 10^7$ orbit predictions per day.
- It commonly propagates the orbits in position and velocity space. Uncertainty propagation in position and velocity space is highly non-linear, which in turn affects the error propagation and other SSA related tasks (Folcik et al., 2011).
- Long-time predictions of orbits are erroneous due to build-up of local truncation error and numerical error when propagation times are of the order of weeks or months. Although the issue remains for the short arc propagations as well, it is assumed that the model induced errors are orders of magnitude larger than that of the integrator errors in the short prediction lengths.

Due to these reasons, the current research was aimed at finding an alternative to the SP method for the purpose of catalogue maintenance.

Although SP methods have limitations, their high accuracy lets them to be used as a standard against which other propagation methods are compared. In the context of this thesis work the Orbit Determination for Extended Maneuvers (ODEM) software is used as a standard numerical prediction and determination method. Section 3.4 provides the details of ODEM's formulation and the implemented software.

3.1.2 General Perturbation Theories

If Equation 3.1 is solved analytically, then the procedure is known as General Perturbations (GP) method. Analytical theories are formulated by separating different effects of perturbations in terms of long periodic, short periodic, and secular terms (Brouwer, 1959; Kozai, 1959; Vinti, 1961). These effects are then modelled up to a certain order with transformations, series expansions or polynomial approximations (Hori, 1971). Thus the accuracy of an analytical theory is linked to the order in its formulation (Vinti, 1961).

Operational GP theories may be constrained in their application due to the problems of singularity, resonances and high-eccentricities, as well as non-conservative perturbations; however they are extensively used as a tool in elucidating the dynamical characteristics of an orbiting object (Finkleman and Cefola, 2012). Depending on the accuracy needed, an analytical theory of motion that includes a given model of forces acting on the satellite is required. With an accuracy requirement of a few meters in prediction accuracy, analytical formulations not only have to include a complex force model but also expand the formulations which includes more than first order approximations.

Unlike the SP theories where state vector representations are commonly used for propagation, GP theories are generally formulated in element space (Keplerian, Equinoctial, Canonical, etc.). The element space may provide more linearity than the state space (Folcik et al., 2011). GP theories make use of a 'mean element' set to separate long term (secular and long periodic) and short-periodic variations. Osculating elements represent the instantaneous position of an object in the orbit, while mean elements are a form of orbital representations deduced from different methods of averaging on the osculating elements. For the rest of the thesis $\boldsymbol{c}_k$, with $k = 1...6$, represents osculating elements, and $\bar{\boldsymbol{c}}_k$ represents mean element set. In

GP theories, periodic and secular variations are separated and treated individually. This is carried out by using analytical transformations on variation of parameter equations (VOP).

With the objective of maintaining the appropriate level of accuracy in orbital calculations, the proper transformation from osculating to mean orbital elements, and vice-versa is needed. The transformation from mean to osculating elements is usually realized by the application of the corresponding analytical theory of satellite motion. An inverse transformation is not so simple, consequently iterative processes are often used for the purpose (Wnuk, 2002). If multiple set of osculating elements are provided, precise mean element conversion is possible by means of least squares fit of a theory to osculating elements sets.

Before the selection of a propagation method a theoretical study of the available GP theories was made. A partial list of the previously formulated and used theories is given below.

SGP (**S**implified **G**eneral **P**erturbations) This theory uses the simplified version of Kozai's gravitational theory (Kozai, 1959). SGP makes use of the mean Keplerian elements for modelling and propagation. The theory includes the primary perturbations due to Earth's non-uniform mass distribution and atmospheric drag without a density model. Due to its formulation in Keplerian elements, the solutions have singularities for an orbit whose eccentricity or inclination is close to zero.

SGP4 (**S**implified **G**eneral **P**erturbations **4**) A modified form of Brouwer's theory was implemented as SGP4 (Brouwer and Hori, 1961; Lane, 1965), and a version which includes perturbations for deep space objects (orbital periods greater than 225 minutes) is available as SDP4 (Hujsak, 1979). Hoots and Roehrich (1980) provide the implementation routines. Further extensions of these methods were presented by the SGP8/SDP8 analytical propagators. SGP4 along with SDP4 is the theory on which the NORAD catalogue is maintained. A validated implementation of the theory is distributed by Vallado et al. (2006)

ANODE (**AN**alytical **O**rbit **DE**termination system) Sridharan and Seniw (1980) developed an analytical theory analogous to SGP4/SDP4 at MIT, Lincoln laboratory. The development was motivated to support realtime and analytical orbit estimation program. ANODE is the extension of SDP4 to be used on low inclination half-synchronous and synchronous orbits.

HANDE (Hoot's analytical theory) Hoots and France (1984, 1987) applied the method of averaging to Brouwer's theory to formulate HANDE. It was one of the first analytical propagation methods to incorporate empirical atmospheric density models, which allowed better accuracy in propagating LEO objects. A sixth order polynomial is fitted for the densities as a function of time. These polynomial coefficients are used to evaluate the acceleration due to atmospheric drag. HANDE computes atmospheric density from the Jacchia 1970 model. For the gravitational model, HANDE includes the zonal harmonics, J_2, of the first order, and J_3 and J_4, of second order. Additionally, the theory includes 12 hours and 24 hours resonances to model MEO and GEO orbits.

ASOP (**A**nalytical **S**atellite **P**redictor) Morrison (1965) presented a complete analytical first order satellite theory intended for low Earth orbits. This formulation makes use of the canonical elements. This theory included short period, long period, and secular effects of J_2 and all higher zonal harmonics; secular and quadratic effects of atmospheric drag;

and the average mean motion for all harmonics of the geopotential terms (Mueller et al., 1979).

AOPP (**A**nalytical **O**rbit **P**rediction **P**rogram) This program was designed to compute ephemerides automatically and efficiently for different applications (Coffey and Alfriend, 1984). The theory consists of first- and second-order coordinate transformations along with the secular terms through the third order. Coffey and Deprit (1982) developed the underlying theory for the program. The theory solves the zonal harmonics $J_2 - J_4$, and it was the first analytical theory that provides a range of options allowing the user to select relevant parts of the theory to fit a particular application in LEO.

A & AP (**A**nalytical **&** analytical prediction with **A**dvanced **P**erturbations) Analytical prediction algorithm (A) and analytical perdiction algorithm with enhanced accuracy (AP) are the subsets of the Russian prediction algorithm packages (Boikov et al., 2009). Both prediction algorithms account for perturbations from the zonal harmonics (C_{20},C_{30},C_{40},C_{50}, and C_{60}); the second sectoral harmonics (C_{22}, and S_{22}); atmospheric drag. The AP additionally include the major perturbations from the zonal and tesseral hamonics up to the eighth order based on Kaula's formulations (Kaula, 1966).

Kamel Theory Kamel (1982, 1983) developed a solution in modified equinoctial element sets dedicated for geo-stationary objects, with $i \approx 0$ and $e \approx 0$. The solution includes tesseral harmonics up to C_{33} coefficients, and luni-solar perturbations. The development of the theory was intended towards the station keeping applications.

AEGS (**A**nalytical **E**phemeris solution for **G**eostationary **S**atellties) Lee et al. (1997) also developed an analytical formulation for propagator dedicated to GEO regime and based on equinoctial elements. Lee's solution included fifth order tesseral harmonics, luni-solar attractions, and solar radiation pressure.

Others Several other GP formulations exist which were not studied within the current scope of research. For further information, readers are directed to formulations from: Wnuk (2002), Eckstein et al. (1966), Danielson et al. (1990), Crawford (1991), No and Jung (2005) etc.

Advantages of the GP methods with respect to the application in space object catalogue maintenance are:

- It provides insight into the orbital dynamics and thus facilitates the understanding of the effects from different forces.
- It propagates orbits in a less dynamic mean element space, which allows the uncertainty to be linear for longer time lengths than in state space.
- It is computational lean, which includes solving a set of algebraic equations during propagation. This is due to making use of analytically solved/approximated solutions for predictions. The major advantage lies in the fact that the computational cost does not depend on the propagation interval.

Intuitively with the above advantages GP theories have several disadvantages:

- They are not flexible enough to allow modularity in force model selections. Each of the current formulations is dictated by its application region.
- Generally, prediction accuracies are limited on the order of kilometres (for propagation arcs of $1-10$ days). With a few exceptions where Boikov et al. (2009) claim that the AP theory has a prediction accuracy in sub-metre levels, and Lee et al. (1997) present the semi-major accuracy for his GP theory for a geo-stationary object to be ≤ 35 metres for the propagation duration of three months, and ≤ 10 metres for the propagation duration of a week.
- Conversion of osculating to mean elements set is not straight forward and requires additional computation through an iterative process.
- Re-initialisation of propagator is required for restarting the propagator, limiting the application of GP theory in sequential filters.
- Availability of algorithm description and software are restricted. Only few institutions make their theories and associated code publicly available.

3.1.3 Semi-analytical Satellite Theories

As mentioned in the description of GP methods within a perturbation approach, the highest frequencies are removed using analytical transformations on VOP equations. The averaged equations of motions depend only on long period angles (McClain, 1977), these can either be solved analytically or using a numerical integrator to obtain the solution. Using averaged equations of motion with an integrator allows the integration to be performed with large step-sizes, on the order of days. Due to slow variability of the mean elements, numerical integrators are able to handle the step-sizes of days without compromising on the accuracy of the integrated elements. The system, which makes use of both SP and GP techniques, is known as Semi-analytical Satellite Theory (SST). Within SST the short-period effects, if required, can be recovered at any step of the integration by the simple evaluation of the analytical expressions of the averaged transformations. However, it is often the case that the algorithm must perform an osculating to mean conversion before analysis/propagation may commence. The major difference between a GP and a SST is that the GP theories form approximate solution to mean element propagation while the SSTs make use of numerical integrators to evaluate mean VOP. The evaluation of short-periodic terms remain similar in both approaches.

The averaging transformation can be performed directly over the variation of parameter equations using different approaches such as the generalised method of averaging (McClain, 1977), the Hamiltonian function using the canonical form of perturbations (Mersman, 1970), the Lie transformation method (Hori, 1971), the Poincarè method (Collins, 1981), the von Zeipel-Brouwer variant (Zeis, 1977), or recent developments which make use of the multiple scales (O'Brien and Sang, 2004).

Based on the averaging technique used, many different SSTs have been formulated. Below are the descriptions of preferential theories which were studied before the propagator selection for the catalogue maintenance.

Kaufman SST Kaufman (1981) included secular and long periodic terms due to third body perturbations. The resulting equations of motion are numerically integrated to obtain a

mean elements set. The theory is used to recover the short periodic terms due to third body effects and zonal harmonics.

DSST (**D**raper **S**emi-analytical **S**atellite **T**heory) was developed for a wide range of applications, which includes comprehensive set of force modelling for both gravitational and non-gravitational perturbations. DSST also includes precise osculating to mean equinoctial elements transformations (Cefola et al., 1974) allowing the recovery of osculating position and velocity states.

USM (**U**niversal **S**emi-analytical **M**odel) Details of the theory are presented by Yurasov (1996). It follows the separation of short and long periodic motion using transformations of variable similar to DSST. The theory was developed to support the Russian Space Surveillance Program.

SALT (**S**emi **A**nalytical **L**iu **T**heory) This theory was developed for the purpose of estimating lifetime or orbital decay of close Earth satellites (Liu and Alford, 1980). The theory includes perturbations due to atmospheric drag, oblateness of the Earth, and spherical harmonics (J_2, J_3, and J_4). The general perturbation theory, namely the method of averaging, is employed for the mean to osculating element transformation (Liu and Alford, 1979)

NAP (**N**umerical **A**nalytical **P**rogram) is a Russian theory which was developed subsequent to USM (Boikov et al., 2009). All predictions account for perturbation from the zonal harmonics C_{20}, C_{30}, C_{40}, C_{50}, and C_{60}, the second sectoral harmonics C_{22} and D_{22}, and atmospheric drag. The theory is based upon the Kaula's formulation for obtaining the VOPs in mean element space.

STOAG (**S**emi-analytic **T**heory with **A**ir drag and **G**ravitational perturbations) is one of the more recently developed theories for the application of long-term evolution analysis of LEO objects. The theory includes atmospheric drag with the analytical TD88 density model, the zonal harmonics up to J_9 cofficients and third body perturbations (Bezděk and Vokrouhlický, 2004).

THEONA is another theory designed for wide range of applications from lifetime predictions to statistical estimation of orbits (Golikov, 2012). The theory considers the perturbations caused by the following effects: the inhomogeneity of the gravity field of the primary planet, the gravity effects of other celestial bodies, the solar radiation pressure (with shadowing effect), and the air drag (Akim and Golikov, 1993). THEONA is capable of propagating orbits around different planets of the solar system and is not just limited to Earth orbiting SOs.

Others Following is the list of a few other existing SST methods: Multiple scales method by O'Brien and Sang (2004), SST dedicated for launcher designing purposes introduced by Correia Da Costa et al. (2012), SST for propagating GEO objects by Valk et al. (2008, 2009), Semi-analytical Tool for End of Life Analysis - STELA from CNES (Fraysse et al., 2011), HEOSAT a SST for propagating highly eccentric orbits from Lara et al. (2018), etc.

By taking the advantages of both SP and GP techniques SST offers the following benefits:

- Even with the additional initialization requirement, the consumption of computational resources is usually less than SP methods.

- Due to numerical integration of averaged equations of motions in SST, it does not inherit the series approximation errors. Series approximations are generally used for obtaining analytical solutions of the averaged equations in GP methods. This, in general, provides better accuracy than GP methods.
- Interpolators can be employed in between the large integration time steps to evaluate the mean elements at required epochs. This is feasible because mean elements behave like linear oscillators, and the variations can easily be captured from low order polynomial approximations without loosing the orbital accuracy. Also, interpolators can be employed for obtaining the series coefficients, which are used for mean to osculating conversions. This further contributes to the computational efficiency of a SST propagator.
- The averaged equations within the formulation of SST are derived in a modular fashion. It does not couple different perturbing forces in order to obtain complete analytical solution. This type of formulation allows a SST to be implemented in a modular way, which in turn provides the option to include or exclude the force models during the time of predictions.
- Formulating the averaged VOPs provide insight into the orbital dynamics, and having the propagation carried out in mean elements, a SST has the benefits of longer linear covariance propagation time intervals as in GP methods.

Along with the above advantages SST carries some disadvantages such as:

- Transformation of mean to osculating element conversion is carried out by using analytical expressions, and the accuracy of the transformation is dependent on the order of series expansions employed. Considering that the use of higher order series evaluation is cumbersome on both fronts: to formulate and to evaluate, one has to carefully chose the trade-off between the both.
- Requirement of re-initialization of mean element propagator hinders it from direct application within sequential filters. This could be overcome by the method proposed by Taylor (1982).
- Due to the required initialization steps and interpolation steps the computational runtime is better than SP method with reduced accuracy and after certain prediction arc lengths.

3.2 Orbit Determination Methods

The previous section presented different orbit propagation methods. In principle, if it were possible to exactly model the forces acting on a space object together with the exact initial conditions, there would be no need for further re-observations of an identified or observed SOs. That is to say, after the initial orbit determination or identification of the object, shown as the process flow in Figure 2.7, there would be no requirement for further orbit improvement. Since modelling of the forces suffer from limited accuracy, orbit determination plays a vital role in a catalogue maintenance system. This is especially important for the Earth orbiting SOs which are under the influence of non-gravitational forces.

Using a set of observations, the Orbit Determination (OD) process estimates an orbit in the form of orbital state or elements at epoch, or at the current time. An OD process involves system models, measurements, and estimation techniques. Section 2.3 provided the required information on measurements. This section is dedicated to a review of the state-of-the-art orbit determination procedures, and their merits and limitations with respect to a cataloguing system.

Orbit determination methods are organized into three categories based on their operation principle and application:

- Initial Orbit Determination (IOD)
- Batch Least-Squares differential correction (LS)
- Sequential Filters (SF)

Using the information from a few observations along with the locations of the sensors, IOD estimates the orbit ($\hat{\boldsymbol{y}}$ - estimated position and velocity vector or $\hat{\boldsymbol{c}}$ - estimated six orbital elements set). The method is intended to provide the initial guess of a spacecraft's orbit, hence it does not make use of any a-priori information for the computation. Different methods of IOD are discussed by Vallado (1997). He discusses the different types of observation processing for the different measurement categories. In terms of catalogue maintenance, IOD is required when a new object or track is being observed. IOD plays a crucial role while populating a SO catalogue. New objects without any a-priori values and the observations gathered in a survey mode require IOD. This thesis does not examine IOD methods further. To adhere to the research objective the current work assumes observations are provided from the tracking sensors and catalogue is populated with all possible observable SO. Hence, further examinations will concentrate on orbit determination/estimation methods.

3.2.1 Least Squares Orbit determination

A Least Squares Orbit determination (LS) technique is the most widely used method within current catalogue maintenance systems (Vetter, 2007). A batch least-squares differential correction method takes all the available observations, $\{\boldsymbol{x}_{\boldsymbol{t_0}}, \boldsymbol{x}_{\boldsymbol{t_1}} \ldots \boldsymbol{x}_{\boldsymbol{t_n}}\}$, over an arc (time span t_n) and determines the best fit orbit at the epoch for a given system model by reducing the sum of the squares of the residuals. Due to the non-linearity of the orbital system and the measurement models, rather than directly estimating $\hat{\boldsymbol{y}}$ the problem is formulated in a linearised form. That is, $\delta\hat{\boldsymbol{y}}$, is the correction to the a-priori values obtained by minimizing the sum of the squares of the residuals between observations and the model. The required a-priories are assumed to be available from IODs or previously stored states. This section provides the general mechanism of a LS method.

Following the assumptions from Tapley et al. (2004), the orbit dynamics can be modelled in a differential equation of the form

$$\dot{\boldsymbol{y}}_{\boldsymbol{t}} = \boldsymbol{f}(t, \boldsymbol{y}_t) \tag{3.4}$$

where $\boldsymbol{y}_t$ is the orbital state vector of a spacecraft at given time 't', which is generated with the initial condition $\boldsymbol{y}_t = \boldsymbol{y}_0; t = 0$. Again, assuming the dynamics are deterministic, linearisation of the dynamics about a reference trajectory $\tilde{\boldsymbol{y}}$

$$\delta\boldsymbol{y}_t = \boldsymbol{\Phi}(t, t_0)\delta\boldsymbol{y}_0 \tag{3.5}$$

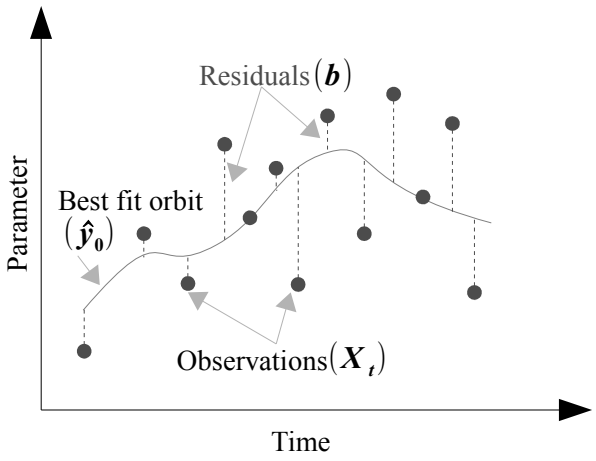

Fig. 3.3 Schematic representation of principle of least-squares adjustment

should be valid. The reference trajectory $\tilde{\boldsymbol{y}}$ is expected to be close to the actual trajectory $\boldsymbol{y}$. Here, $\delta\boldsymbol{y}$ is the amount which takes the reference trajectory into the closest estimate, $\bar{\boldsymbol{y}}$, of the actual orbit $\boldsymbol{y}$. In the above Equation 3.5, the partial derivative matrix $\boldsymbol{\Phi}(t, t_i)$ is the state transition matrix (STM), given by

$$\boldsymbol{\Phi}(t, t_i) = \frac{\partial \boldsymbol{y}_t}{\partial \boldsymbol{y}_{t_i}} \tag{3.6}$$

which maps deviations in the state vector from time epoch t_i to another epoch t.

If H represents the observation matrix mapping the observation space to orbital state space, it is expressed in the partial derivative form as in Equation 3.7.

$$\boldsymbol{H} = \frac{\partial \boldsymbol{x}_t}{\partial \boldsymbol{y}_t} \tag{3.7}$$

where $\boldsymbol{x}_t$ is the observation at time t. If it was possible to perfectly model an orbit and all the associated observation noise, it would be possible to generate true state $\boldsymbol{y}_t$ and generate the actual observation $\boldsymbol{x}_t$, thus estimating the actual trajectory of a SO. The residuals $\boldsymbol{b}$ in observation space is

$$\boldsymbol{b} = \boldsymbol{x}_t - \tilde{\boldsymbol{x}}_t \tag{3.8}$$

where $\tilde{\boldsymbol{x}}_t$ is the estimate of the observation from models using $\tilde{\boldsymbol{y}}_t$. From the Equations 3.7 and 3.8

$$\begin{aligned} \boldsymbol{b} &= \boldsymbol{H}\boldsymbol{y}_t - \boldsymbol{H}\tilde{\boldsymbol{y}}_t \\ &= \boldsymbol{H}\left(\boldsymbol{y}_t - \tilde{\boldsymbol{y}}_t\right) \\ &= \boldsymbol{H}\delta\boldsymbol{y}_t \end{aligned} \tag{3.9}$$

substituting the Equation 3.5 in 3.9, we get

$$\boldsymbol{b} = \boldsymbol{H}\boldsymbol{\Phi}(t, t_0)\delta\boldsymbol{y}_0 \tag{3.10}$$

Having a matrix $\boldsymbol{A} = \boldsymbol{H\Phi}$ representing the cumulative partial derivative matrix. The above system of equations can be represented in the form of a linear equation

$$\delta \boldsymbol{y}_0 = (\boldsymbol{A}^\top \boldsymbol{A})^{-1} \boldsymbol{A}^\top \boldsymbol{b} \tag{3.11}$$

which is the solution for the non-linear least squares estimation.

If $\boldsymbol{W}$ is a diagonal matrix with its components being the inverse of variances of observations ($1/\sigma_{\boldsymbol{x}}^2$), then the above equation can be weighted according to observations' confidence in the form weighted least square estimator as given below

$$\delta \boldsymbol{y}_0 = (\boldsymbol{A}^\top \boldsymbol{W} \boldsymbol{A})^{-1} \boldsymbol{A}^\top \boldsymbol{W} \boldsymbol{b} \tag{3.12}$$

The accuracy of the estimated orbital elements through a least-square orbit determination process is represented in the form of covariance matrix ($\boldsymbol{P}$), which is the component of the Equation 3.12

$$\boldsymbol{P} = (\boldsymbol{A}^\top \boldsymbol{W} \boldsymbol{A})^{-1} \tag{3.13}$$

From the above equation it can be observed that the confidence of the estimated parameters is dependent on the partial derivative matrix, and measurement standard deviations entering through the weighting matrix. As one could intuitively imagine, the actual noise in measurements does not affect the computation of the covariance matrix. Hence it is understood that $\boldsymbol{P}$ is not an indication of observation accuracy. Some of the other relevant characteristics of least squares orbit determination methods are listed below:

- The LS should be solved by an iterative method. The number of iterations depend on the reference trajectory, quality of the partial derivatives ($\boldsymbol{A}$), initial a-priori ($\tilde{\boldsymbol{y}}_0$), and the orbital element space in which the orbit is estimated.
- Since the process is based on the Newton-Raphson method, having too far away a-priori might lead to divergence in the solution. Using the Levenberg-Marquardt algorithm for updating within the iterations provides the robustness towards a wide range of starting values.
- The iterative process is terminated for a specified set of observations with a convergence criteria. For example, $||\boldsymbol{b}_{n-1,n}||$ is smaller than ϵ.

The curve fitting in general sense can pose issues when long periods (orbital arc lengths) are considered or in stressing cases like re-entry scenarios.

3.2.2 Sequential Orbit Estimation

Although the LS method has been used as a standard in most of the cataloguing maintenance system, it is slowly being supplemented with sequential estimation methods. There exists Sequential Processing and Sequential Filtering (SF) observations processing methods. Sequential processing methods are distinguished from LS processing methods in that batches of data are considered sequentially, collecting a set of observations over a specified time interval and batch-processing one interval after the next. This can be thought of as a moving time window whose contents are captured and processed at intervals, independent of previously

processed batches of data. The analysis does not include process noise inputs and calculations. Filter methods output refined state estimates sequentially at each observation time. The filter time update propagates the state estimate forward, and the filter measurement update incorporates the next measurement. The search for sequential processing was begun by Wiener, Kalman, Bucy, and others (Vetter, 2007).

Kalman filters are a form of sequential filters; Kalman Filters adapted for a nonlinear system are being implemented for the purpose of determining the orbits (Vallado, 1997). SFs enable more comprehensive treatment of errors in the dynamics of equations of motions. The method makes use of prediction and correction steps to determine $\boldsymbol{y}_t$, when an observation is available at time t. Two widely used flavours of Kalman filters are: the Extended Kalman Filter (EKF) and the Unscented Kalman Filter (UKF).

The prediction stage of the EKF makes use of an orbit propagator for moving the mean, and implements differential equations, using the STM, for the time evolution of the covariance, together with the process noise $\boldsymbol{Q}$, as given below

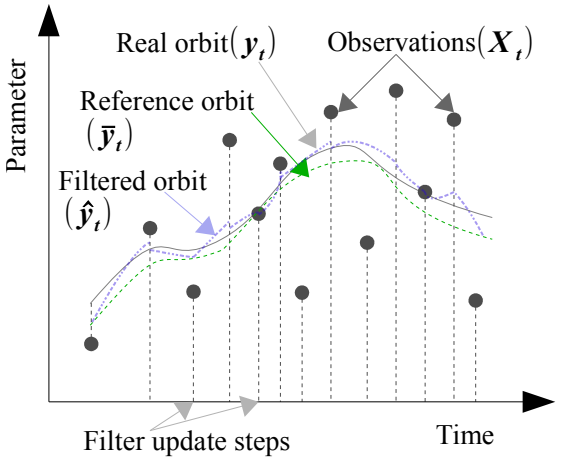

Fig. 3.4 Schematic representation of sequential filtering techniques

$$\begin{aligned} \boldsymbol{\delta}\tilde{\boldsymbol{y}}_{t_n} &= \boldsymbol{\Phi}(t_n, t_{n-1})\delta\hat{\boldsymbol{y}}_{t_{n-1}} \\ \tilde{\boldsymbol{P}}_{t_n} &= \boldsymbol{\Phi}(t_n, t_{n-1})\boldsymbol{P}_{n-1}\boldsymbol{\Phi}^T(t_n, t_{n-1}) + \boldsymbol{Q} \end{aligned} \tag{3.14}$$

If an observation is available at time t_n, then the information is made available to improve the predicted state and covariance through Kalman gain ($\boldsymbol{K}_{t_n}$), which considers the measurement noise $\boldsymbol{R}$

$$\boldsymbol{K}_{t_n} = \tilde{\boldsymbol{P}}_{t_n}\boldsymbol{A}^\top[\boldsymbol{A}\tilde{\boldsymbol{P}}_{t_n}\boldsymbol{A}^\top + \boldsymbol{R}_{t_n}]^{-1} \tag{3.15}$$

Thus corrected orbital state update and covariance are given by

$$\delta\hat{\boldsymbol{y}}_{t_n} = \delta\tilde{\boldsymbol{y}}_{t_n} + \boldsymbol{K}_{t_n}\left(\tilde{\boldsymbol{b}}_{t_n} - \boldsymbol{A}^\top\boldsymbol{\delta}\tilde{\boldsymbol{y}}_{t_n}\right) \tag{3.16}$$

$$\begin{aligned} \hat{\boldsymbol{y}}_{t_n} &= \bar{\boldsymbol{y}}_{t_n} + \delta\hat{\boldsymbol{y}}_{t_n} \\ \hat{\boldsymbol{P}}_{t_n} &= [1 - \boldsymbol{K}_{t_n}\boldsymbol{A}]\tilde{\boldsymbol{P}}_{t_n} \end{aligned} \tag{3.17}$$

Steps comprising the evaluation of Equations 3.14 are called prediction steps, and the steps involving the Equations 3.15 and 3.16 are referred as correction step.

The point to be observed is that the prediction step for EKF is solely dependent on the linearity assumption between previous known state and observation times (t_{n-1} and t_n). That is, EKF demands to estimate variance such that the first two moments are rightly represented. If the observations are not available for an object within the assumed linearity region of prediction, then the filter diverges from the true state leading to an incorrect state estimation.

This is one of the major limitation factor for using sequential filters within a SOs catalogue system, as a frequent observation of all SO are highly resource demanding. Resources in terms of available sensor systems and the policies on observational data sharing might be the driving factors to make use of SF in future cataloguing systems.

The limitation from the absence of observations within the linearity region can be overcome by the proper mathematical formation of process noise. Seago et al. (2011) demonstrate the processing of sparse data using SF.

To extend the operability of Kalman filter with non-linear systems, UKF predicts the mean and covariances at observation times using "unscented" transforms, hence the name Unscented Kalman Filter. Julier and Uhlmann (2004) proposed the idea of unscented transforms and UKF. Instead of making use of state transition matrices for propagating the initial orbital state and covariance, a set of $2D+1$ simga points ($\boldsymbol{z}^{(k)}$) is used, this method of obtaining the variances of states are termed as unscented transformation. Here D is the number of dimensions in the system. This set of sigma points is propagated using an orbit propagator in turn estimating the mean and the covariance at the observation times. The weighted estimation of the propagated mean and covariance using unscented transformation are given as below.

$$\begin{aligned} \tilde{\boldsymbol{y}}_{t_n} &= \sum_{k=1}^{2D+1} W^{(k)} \boldsymbol{z}_{t_n}^{(k)} \\ \tilde{\boldsymbol{P}}_{t_n} &= \sum_{k=1}^{2D+1} W^{(k)} \left\{ \boldsymbol{z}_{t_n}^{(k)} - \tilde{\boldsymbol{y}}_{t_n} \right\} \left\{ \boldsymbol{z}_{t_n}^{(k)} - \tilde{\boldsymbol{y}}_{t_n} \right\}^T \end{aligned} \tag{3.18}$$

These equations form the corrector step for UKF. From analysing the predicted covariances over different time lengths within the UKF, Horwood et al. (2014) state that the standard UKF resolves to better covariance of the propagated uncertainty but predicted mean can be different from the mode of the true orbit. Though the UKF extends the usability arc lengths between previous known state and the future observation times it is still limited by the non-linearity of the system together with the frequency of observations.

Several research work has been carried out to extend the applicability of sequential filters by making use of different methods of covariance propagation. The Gaussian mixture filter splits the covariance matrix when it reaches a level of disagreement with a first-order prediction (DeMars, 2010). The propagation of multiple covariance matrices is carried out until the next disagreement, where the covariances are further split to represent the true system. Another method suggested by Fujimoto and Scheeres (2012) tries to approach the non-linearity problem by evaluating the analytical solution of the Fokker-Planck Equation for a deterministic dynamical system.

As mentioned earlier in the section, within a catalogue maintenance system the availability of observations is typically quite sparse: due to a large number of orbiting objects and limited availability of observing sensors. This in turn hinders the use of sequential filters within a catalogue maintenance system. With betterment in spacecraft observing technology in the future and better cooperation between space fairing nations the situation could change the situation of data availability, and thus the application of SF in cataloguing system. Nevertheless SF provide several advantages in terms of understanding quality and accuracy of observations, uncertainty within the models, and assists in establishing and propagating the realistic covariances, and manoeuvre recovery and characterization.

3.3 Uncertainty Quantification and Propagation Methods

In the equation of motion the forces acting on the satellite are assumed to be deterministic and the initial condition ($\boldsymbol{y}_0$) is known with a complete confidence. But, in reality the above two quantities are uncertain and are known only with a certain confidence.

Estimating the covariances associated with the propagated states is generally termed as the orbit uncertainty quantification. The magnitude and orientation of uncertainty can be either estimated at each time step, or one can understand the dynamics of uncertainty propagation and use the model to propagate the initially estimated covariances to future states. The latter is known as uncertainty propagation.

For maintenance of the SOs catalogue, orbit uncertainty quantification and propagation play a major role. Orbit uncertainties are due to: initial state uncertainties, force model uncertainties, and model specific simplifications. Understanding the source and magnitude of the above uncertainties quantify the realistic covariance of an estimated or a propagated state. For non-linear orbital dynamics the evolution of the probability density function (PDF) will not retain its Gaussian nature. This occurs particularly during propagation arcs in the order of days. Due to this fact, one has to understand the length of propagation where Gaussian representation is valid or to have a method to propagate the higher moments representing the non-linear PDFs.

Orbital uncertainty or covariance plays an important role in both catalogue maintenance and applications of the SO catalogue. The most noticeable effects of unrealistic uncertainty which are previously studied are listed below:

- Impact on catalogue maintenance system
  - Tagging of uncorrelated observations or identifying previously untracked objects: the incorrect covariance might lead to miss associations or false tagging (Kragel et al., 2012).
  - Observation processing: with false correlations will further degenerate the covariance estimation.
  - Sensor tasking: optimistic covariance estimation can drive the information content based sensors scheduler to lose the object from the catalogue (Hill et al., 2010).
- Impact on the application of the space object catalogue
  - Incorrect or low confidence in the estimation of probability of collision: is very critical as one of the main objective of maintaining a space object catalogue is to assist space operations (Akella et al., 1998).
  - Manoeuvre detection: this will effect both maintenance and application.
  - Higher uncertainty in the lifetime predictions: especially in the low Earth orbiters (Goodliff et al., 2006).
  - Incorrect position uncertainty leads to dilution regions when estimating the conjunction probabilities (Alfano, 2003).

3.3.1 Uncertainty Quantification

By understanding the orbital propagation methods, the uncertainty associated with $\boldsymbol{y}_t$ is from three main sources. Figure 3.5 shows the structure of most prominent sources which influences the uncertainties in the propagated states.

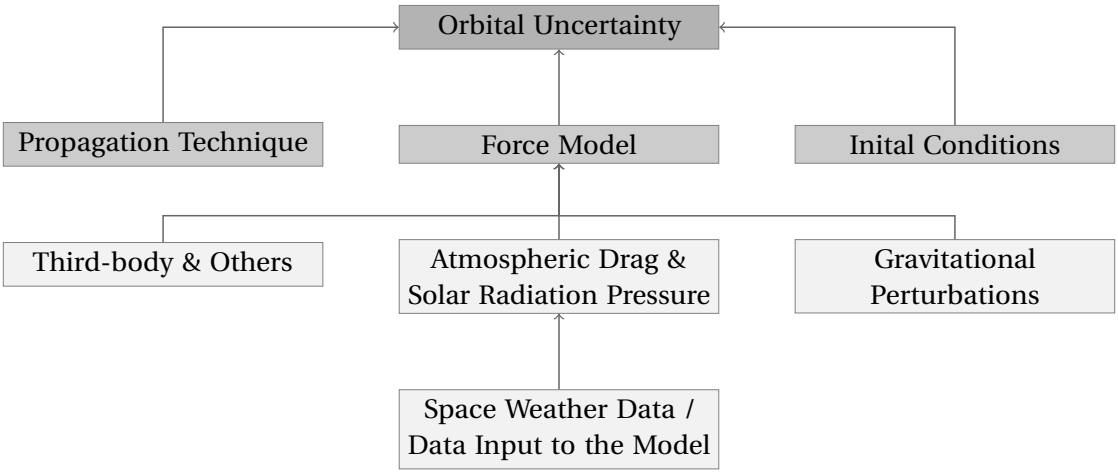

Fig. 3.5 Different sources of uncertainty which affects the quantification of orbital covariances

Uncertainty in the initial condition is described by the a-priori covariance which is obtained through an OD process. At this point of time, it is assumed that an OD process is capturing all the observation noise and systematic errors. Intrinsically, within an OD, the uncertainty in $\boldsymbol{y}_0$ depends on the estimation method, the algorithm used for modelling the orbit, and force model uncertainty. Quantifying noise and bias in observations together with understanding the impact of orbit propagation errors on the state estimation will assist in estimating the right set of errors in initial conditions (Vetter, 2007).

In orbit propagation, the second uncertainty due to orbital theory is mainly due to the method of orbit modelling and propagation technique. A method for quantifying the prediction uncertainty due to orbital theory is one of the research objective of the present study and it will be detailed in later chapters.

The last and the largest contributor of uncertainty in the orbit predictions are the uncertainty within the force models. Tardioli and Vasile (2015) further classifies model uncertainties as the random variability in the environment which cannot be captured in a physical model, and the error due to lack of understanding in certain processes. Usually, certainty of the conservative perturbing forces can be increased by improving the knowledge on Earth's gravity field variation and the variability in forces due to third body variations. This is possible since the temporal variations of gravitational forces are low. Although the forces acting on a satellite vary rapidly due to satellites motion, Earth's rotation, and Sun and Moon motion with respect to Earth, it can be assumed in the present context the Earth gravitational field is essentially static in Earth fixed frame. Also, the time frames of the actual variations of the conservative forces are a few orders of magnitude smaller than compared to that of the non-conservative forces. The non-conservative perturbations, such as atmospheric drag and solar radiation pressure, are much harder to model. This in turn demands the physical models to capture both spatial and temporal fluctuations. Due to higher dynamics and limited physical knowledge on the factors influencing the non-conservative forces' variations, these are characterised as random variations.

3.3.2 Covariance Propagation

If the estimated uncertainties are sufficiently small together with the Gaussian approximation, the orbital uncertainties can be represented by an ellipsoid centred at the estimated states ($\boldsymbol{y}$). The volume and the orientation of the main axes of the ellipsoid are equal to the determinant and the eigenvectors of the covariance matrix $\boldsymbol{P} = E\{[\boldsymbol{y} - \tilde{\boldsymbol{y}}][\boldsymbol{y} - \tilde{\boldsymbol{y}}]^\top\}$. $\boldsymbol{P}$ contains the information in the form of variances and covariances between different orbital parameters. The state vector $\boldsymbol{y}$ represents the actual orbit, and $\tilde{\boldsymbol{y}}$ represents the estimated orbital states. The diagonal elements of the matrix represent the variances of the six components and the off-diagonal elements define the covariances between them. Under the linearity assumption the covariance matrix from the initial epoch ($\boldsymbol{P}_0$) is propagated to time t by using the state transition matrix ($\boldsymbol{\Phi}$), provided there is no process noise.

$$\boldsymbol{P}_t = \boldsymbol{\Phi}(t, t_0)\boldsymbol{P}_0\boldsymbol{\Phi}^\top(t, t_0) \tag{3.19}$$

For simplicity, application of the above Equation 3.19 is called as Extended Kalman filtering method of covariance propagation (EKF). Similar to the discussion presented for EKF-SF the propagation of covariance is valid for time lengths, where linearity holds good. Figure 3.6 schematically depicts the departing of orbital uncertainty from the linearity assumption. It is shown by representing the orbital uncertainties with a non-ellipsoid / non-Gaussian region after certain propagation times.

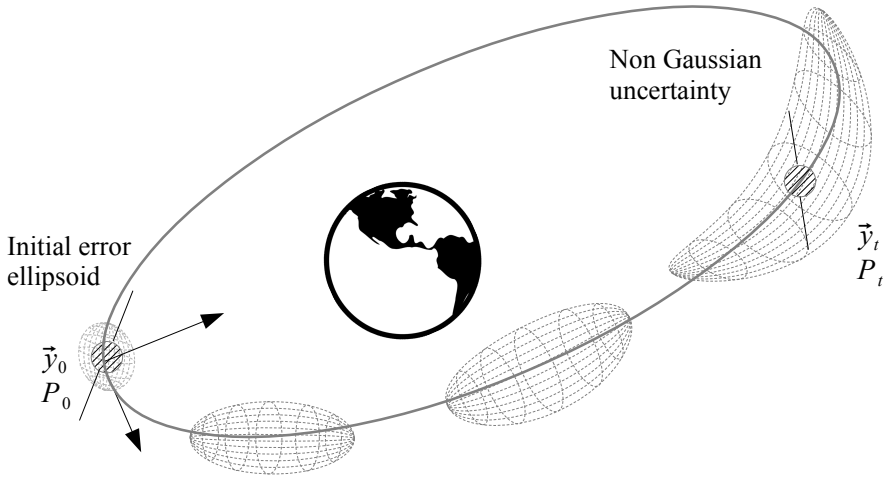

Fig. 3.6 Schematic representation of initial errors as a covariance ellipsoid and propagated covariances departing from the Gaussian assumption over a period of time

Methods which are employed in propagating uncertainties under linearity assumptions are:

Propagation using Extended Kalman Filtering is making use of the solution to the system represented by Ordinary Differential Equations (ODE) which governs orbit propagations. If the initial state is Gaussian distributed, $\boldsymbol{y}_0 \sim \mathcal{N}(\boldsymbol{\mu}_0, \boldsymbol{P}_0)$, with mean $\boldsymbol{\mu}_0$ and covariance $\boldsymbol{P}_0$, then $\boldsymbol{y}_t$ is approximately $\mathcal{N}(\boldsymbol{\mu}_t, \boldsymbol{P}_t)$ at propagated time t. Then the matrix $\boldsymbol{P}_t$ can be computed using the Equation 3.19.

The state transition matrix $[\boldsymbol{\Phi}(t, t_0)]$ is established by solving the variational equations

$$\boldsymbol{\Phi}'(t, t_0) = \boldsymbol{F}(\boldsymbol{y}_t, t)\boldsymbol{\Phi}(\boldsymbol{t}, \boldsymbol{t_0}) \text{ , with } \quad \boldsymbol{\Phi}(\boldsymbol{t_0}, \boldsymbol{t_0}) = \boldsymbol{I}_{6\times 6} \tag{3.20}$$

where the matrix $\boldsymbol{F}(\boldsymbol{y}_t, t)$ denotes the partial derivatives of forces acting upon the SO with respect to its state.

$$\boldsymbol{F}(y_t, t) = \frac{\partial \boldsymbol{f}(\boldsymbol{y}_t, t)}{\partial \boldsymbol{y}_t}$$

Some of the noticeable features of the EKF form of linear propagation technique are:

1. Considers the first two statistical moments for the propagation
2. The system of equations can be integrated using numerical methods
3. The integration of ODE when using high-fidelity models results in high computational costs
4. The propagated covariances can be overly optimistic (Jones et al., 2012). This is also dependent on the models which are included within the partial derivative matrix $\boldsymbol{F}(\boldsymbol{y}_t, t)$ and the specific formulation.
5. Stochastic differential equation formulation supports for the inclusion of process noise or model uncertainty.
6. Orbit propagation method employed in obtaining $\boldsymbol{\Phi}$ influences the accuracy and computational efficiency of the EKF
7. Selection of coordinate system plays a very important role for keeping the system under Gaussian assumption. Vallado and Alfano (2011) presents the advantages of choosing curvilinear coordinates over Cartesian coordinates for covariance propagation, and Folcik et al. (2011) presents the benefits of propagating covariance in equinoctial elements over position and velocity state vector. The point will be analysed in-detail within the chapter 7

Propagation using Unscented transformation also known as UKF, where the covariances are constructed from a deterministically chosen set of sigma points, as described for UKF-SF. The sigma points can be propagated by using the full non-linear force models to retrieve the uncertainties at given time t. The propagation equation is given by

$$\boldsymbol{P}_t = \sum_{k=1}^{2D+1} W^{(k)} \left\{\boldsymbol{y}_t^{(k)} - \boldsymbol{y}_t\right\} \left\{\boldsymbol{y}_t^{(k)} - \boldsymbol{y}_t\right\}^T \tag{3.21}$$

where $D = 6$ is the number of degrees of freedom for an orbit, $W^{(k)}$ are the weights for the sigma points, $\boldsymbol{y}_t^{(k)}$ are the state sigma points at time t, and $\boldsymbol{y}_t$ is the model propagated state vector.

In this method the assumptions remain similar to EKF method, i.e., the initial covariance is Gaussian in the considered coordinate reference frame. For propagating orbits we need a six-dimensional representation, thus UKF needs $2D+1 = 13$ sigma points. In case additional parameters are considered within the covariance propagation, such as drag or solar radiation coefficients,the number of sigma points are increased accordingly. Some relevant features of the UKF method are as follows:

1. UKF propagates the first two moments (mean and covariance)
2. Requires 13 sigma points to be propagated, which directly translates to 13× the computational effort used for propagation
3. The covariance propagation method uses an orbit propagation technique, hence it can be easily adapted to any satellite theory
4. The computed state estimate (mean) is the mean of the propagated probability distribution function, which can suffer from offsets from the true mean
5. UKF tries to capture the non-Gaussian part of the uncertainties by over estimating the ellipsoids, which might affect its application.

Propagation using Gauss von Mises filter makes use of the Gauss von Mises (GVM) distribution to represent the non-Gaussian covariances and higher moments of the noise are considered within the propagation. It is a joint distribution defined for by a normal distribution for five of six elements, and the sixth element (θ) is treated with von Mises distribution. Combining the both, the GVM distribution is defined to be the joint probability distribution as in

$$p(\boldsymbol{y},\theta) = \mathcal{GVM}(\boldsymbol{y},\theta,\boldsymbol{\mu},\boldsymbol{P},\alpha,\beta,\boldsymbol{\Gamma},\kappa) \equiv \mathcal{N}(\boldsymbol{y};\boldsymbol{\mu},\boldsymbol{P})\ \mathcal{VM}(\theta;\Theta(\boldsymbol{y}),\mathrm{k}) \tag{3.22}$$

where

$$\begin{aligned}\mathcal{N}(\boldsymbol{y};\boldsymbol{\mu},\boldsymbol{P}) &= \frac{1}{\sqrt{\det(2\pi\boldsymbol{P})}}\exp\left[-\frac{1}{2}\left(\boldsymbol{y}-\boldsymbol{\mu}\right)^{\mathsf{T}}\boldsymbol{P}^{-1}\left(\boldsymbol{y}-\boldsymbol{\mu}\right)\right],\\ \mathcal{VM}(\theta;\Theta(\boldsymbol{y}) &= \frac{1}{2\pi e^{-\kappa}I_0(\kappa)}\exp\left[-2\kappa\sin^2\frac{1}{2}\left(\theta-\Theta(\boldsymbol{y})\right)\right],\end{aligned}$$

and

$$\Theta(\boldsymbol{y}) = \alpha+\beta^{\mathsf{T}}\boldsymbol{z}+\frac{1}{2}\boldsymbol{z}^{\mathsf{T}}\boldsymbol{\Gamma}\boldsymbol{z},\quad \boldsymbol{z}=\boldsymbol{A}^{-1}\left(\boldsymbol{y}-\boldsymbol{\mu}\right),\quad \boldsymbol{P}=\boldsymbol{A}\boldsymbol{A}^{\mathsf{T}} \tag{3.23}$$

where $\mathcal{N}(\boldsymbol{\mu},\boldsymbol{P})$ is the Gaussian density function and $\mathcal{VM}(\boldsymbol{\Theta}(\boldsymbol{y}),\mathrm{k})$ is the von Mises density function with the parameter set $(\boldsymbol{\mu},\boldsymbol{P},\alpha,\beta,\boldsymbol{\Gamma},\kappa)$. The parameters β and $\boldsymbol{\Gamma}$ model correlation between $\boldsymbol{y}$ and θ. The parameter matrix $\boldsymbol{\Gamma}$ gives the $\mathcal{GVM}$ distribution their distinctive banana or boomerang shape. In the above $\mathcal{VM}$ distribution I_0 is the modified Bessel function of the first kind of order 0. The parameter α and κ are measures of location and concentration. For large κ, the von Mises distribution becomes concentrated about the able α and approaches a Gaussian distribution in θ with mean α and variance $1/\kappa$.

The description and method of establishing the parameter set $\boldsymbol{\Theta}(\boldsymbol{y}),\alpha,\beta,\kappa,\boldsymbol{\Gamma}$ can be found in (Horwood and Poore, 2014). The authors are the first to explore this particular probability density function for the application of astrodynamics, and detailed derivation and formulation of the methodology can be found in the same literature. According to the authors, the salient features of GVM method of covariance propagation are :

1. The GVM density function is defined over a cylindrical manifold. The GVM density function cannot be operated on Cartesian coordinates, rather it is designed to

treat the uncertainties in the fast moving position variable in element space in a different way.

2. GVM makes use of the same number of sigma points as in UKF, which requires 13 sigma points to be propagated.
3. When $\mathbf{\Gamma} \rightarrow 0$, and $k \rightarrow \infty$, GVM reduces to a Gaussian distribution.

Propagation using Gaussian Mixture Model (GMM) are a popularly used tool for density estimation, clustering, and un-supervised learning within a wide range of applications in Computer Science (Singer and Warmuth, 1998). The application of GMM has been evaluated quite extensively by DeMars (2010) for the purpose of Space Situational Awareness tasks. Within GMM a distance function based on the Entropy of the system is used. Once a threshold of the entropy is reached, a Gaussian PDF is split in such a way as to represent the original PDF by superposition of two or more Gaussian PDFs. These split PDFs are propagated further using any of the above described linear uncertainty propagation methods.

Propagation using Polynomial Chaos makes use of the non-restrictive nature of polynomials to represent any smooth non-linear functions. Nechak et al. (2010) make use of multi-dimensional Taylor series expansion to represent the time variation of the orbital state covariances. A reduced model is used to represent the time derivatives of the polynomial coefficients are tested and suggested to be suitable for short term statistics of the initial uncertainty propagation.

Propagation using State Transition Tensors makes use of analytic probability density functions. When the equation of motion is formulated as a system of stochastic differential equations (SDE), their time evolution in terms of mean and covariance are given by Fokker-Plank-Equations (Fujimoto and Scheeres, 2012). Solving this equations analytically or integrating them numerical yields an approximation for the uncertainty propagation. This is the traditional/rigorous way of handling of process noise in a Kalman filter. The major limitation is to capture model uncertainties and the difficulty in solving the complex SDE system.

The major issue with uncertainty propagation is to properly handle Gaussian error propagation. This in turn is highly influenced by the choice of orbital representation, and the behaviour of the selected element space. Many previous studies (DeMars, 2010; Folcik et al., 2011; Jones et al., 2012) have been dedicated to understanding the nature of uncertainties and their linearity. Hill et al. (2010) and Hill et al. (2012) have discussed non-Gaussian error propagation methods that can be employed for specific applications of track association and sensor tasking. Chapter 7 is dedicated for comparing the different propagation methods and choosing the right coordination system for the purpose of SOs catalogue system.

3.4 Reference Orbit Propagation Tool - ODEM

In order to characterise and compare the alternative propagator methods, a numerical orbit propagation and OD tool which is developed by the German Space Operations Center (GSOC) is employed. The Orbit Determination for Extended Manoeuvres (ODEM) program is a flight dynamics software tool used for space operation tasks at GSOC. The orbit propagation within

ODEM is based on a Adams-Bashforth-Moulton numerical integrator, which is a variable order and variable step-size integrator. The ODEM program uses fidelity force models for gravitational and non-gravitational forces acting on an Earth orbiting satellite. The force models implemented in ODEM includes:

- Earth's gravitational field using Cunningham's algorithm (up to 120 × 120)
- Atmospheric drag based on the Jacchia 71 model (Jacchia-Gill)
- Solar radiation pressure accounting for the shadow effect (umbra, penumbra and sunlit)
- Sun and Moon point mass forces based on analytical ephemeris
- Extended manoeuvres
- Impulsive manoeuvres

Orbit determination within ODEM is formulated as a batch least-squares estimator. Along with the following observation models:

- Radar range (2 way, 4 way, range differences)
- Average radar range-rates (2-way, 3-way)
- Gimbal angles (azimuth, elevation, X- & Y- angles)
- GPS receiver position (object position in Earth-fixed reference frame)
- Satellite Laser Ranging with light-time and atmospheric corrections

Mathematical descriptions of the software are provided in (Gill, 2005). The ODEM software is implemented in FORTRAN 90 programming language and it has been tested extensively for its accuracy and performance. It is being used within GSOC for routine flight dynamics activities and for the maintenance of the BACARDI catalogue (Weigel and Patyuchenko, 2011).

For the rest of the comparison study within this thesis, the performance of ODEM is used as the standard against which other theories' performance are compared. The following section presents the initial comparison study performed before proceeding to the detailed analysis of a selected propagation method.

3.5 Preliminary Selection of the Propagation Method

A preliminary comparison was performed to determine a candidate orbit propagation method, which could provide a proper base to meet the requirements.

Detailed literature studies upon the formulations of satellite theories revealed the theoretical prediction limitations of them. Previously Barker et al. (1995) analysed several GP and SST theories for their accuracy and computational efficiency. Theories such as: SGP, SGP4/SDP4, HANDE, SALT, and DSST are compared for prediction accuracies against a numerical method for a single space object in different orbital regimes. This particular study considered four representative SOs, each in LEO, MEO, HEO and GEO. The theories which contain the most complete models performed better in terms of accuracy, but took longer to compute the orbits. Figure 3.7 shows the performance of the studied orbital theories in comparison with

a numerical propagator for a single satellite in each orbital regime. Barker (1995) provides the specific force models employed within DSST in Table 3 of his paper. Figure 3.8 shows the runtime performance in terms of CPU time. Especially for the LEO regime where the drag is prominent, DSST and SALT performed better, in terms of accuracy, than strictly GP theories. Within the study conducted it is observed that SALT ran marginally faster than the DSST. But at the same time it was observed that DSST took three to four iterations fewer to converge when used within the least squares orbit determination routine.

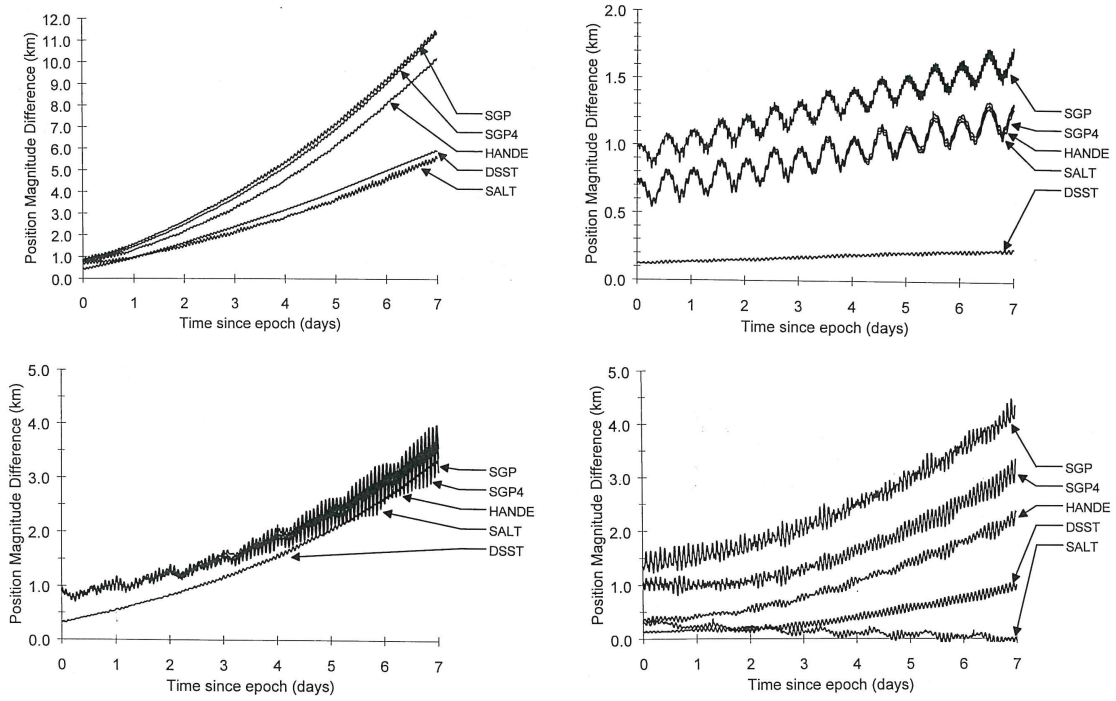

Fig. 3.7 Comparison of prediction accuracy of different propagators by Barker et al. (1995). Top left shows the accuracy for a LEO satellite prediction and top right is a MEO satellite; bottom left and bottom right are for a HEO and a GEO satellites respectively. [Reprinted from Barker et al. (1995)]

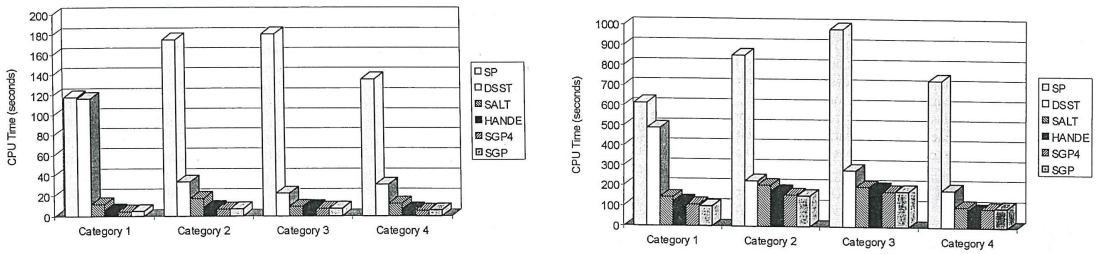

Fig. 3.8 Comparison of prediction and OD runtimes of different propagators by Barker et al. (1995). The left plot shows the OP performance in terms of CPU times and the right plot shows the OD performance for different theories. [Reprinted from Barker et al. (1995)]

Another independent study conducted by Fonte et al. (1995) examined a set of analytical and semi-analytical theories implemented within the Goddard Trajectory Determination

System (GTDS R & D). They analysed the OD and OP performance of the GTDS R& D theories using real observations in low altitude circular, high altitude circular, and high altitude eccentric Molniya orbits. The comparisons in this analysis are based against Cowell truth trajectory was established for each orbital test case, against which individual theories were fit. Root Mean Square value of the residuals from the differential correction procedure is used as comparison metric. Table 3.1 summarizes the comparison results. The detailed description of the test cases and particular orbits which are estimated can be found in (Fonte et al., 1995).

Table 3.1 GP, SP, and SST theories fit comparison against Cowell trajectories, from the study conducted by Fonte et al. (1995) (BL- Brower Lyndane)

Theory	Low circular RMS [m]		High circular RMS [m]		High eccentric RMS [m]	
	OD	OP	OD	OP	OD	OP
BL	50.3	197.2	24.6	185.3	-	-
Cowell	14.5	41.6	0.3	3.8	0.001	0.4
SGP	688.7	14701.0	773.9	6828.3	1721.2	105170.0
SGP4	53.9	934.0	19.9	358.5	-	-
DSST	34.9	47.3	19.4	31.8	34.8	174.4

GP theories proved efficient in terms of runtimes, but performed poorly in terms of accuracies. The studied semi-analytical method, DSST, demonstrated accuracy approaching those of SP technique at the speeds comparable to GP techniques.

During the course of the current research a comparative study concentrating on GEO regime was performed and presented in (Setty et al., 2013). The SDP4 analytical theory, Kamel's analytical theory, and a semi-analytical DSST are implemented and tested in comparison to numerical propagator (ODEM). Table 3.2 provides a comparison of force models included in these theories. The study focused on establishing different test cases to get a better picture on the behaviour of theories due to force models truncation. Combined with the intention of understanding the effects on orbital parameters as inclination and eccentricity, GEO orbits were subdivided into:

uGEO - "usual" operational range of geostationary orbits (zero inclination and geo-stationary altitude)

iGEO - inclined geosynchronous orbits

eGEO - eccentric orbits at geosynchronous altitudes

Selected methods are compared for their propagation accuracies against ODEM, and the results are presented in Table 3.3. The semi-analytical theory, which has the capability to include similar force models as that of the SP, performed better in comparison with analytical theories. The DSST performed with the position error RMS $\sim$ 250 meters when compared to ODEM in GEO regime. This error was associated with the lack of time dependent terms in the evaluated version, giving the hint for improvement without much modification within the core of the theory. The last column with Table 3.3 shows that the selected three methods consume $\leq$ 10.4% of the computational resources compared to the SP method.

Section 2.5 established the accuracy and computational requirements of a selected theory which will be used within the space object catalogue maintenance system. Among the characteristic requirements, the theory should be able to propagate all possible orbits around

Table 3.2 List of perturbations models included in the selected analytical and semi-analytical theories for GEO orbits

Perturbations	Theory		
	SDP4	Kamel	DSST
J_2	secular, long periodics, short periodics 0^{th} order in e	secular, long and short periodics	secular, first order long and short periodics
J_3	long periodics	secular, long and short periodics	secular, first order long and short periodics
J_4	secular effects	–	secular, first order long and short periodics
J_2^2	secular effects	secular, long and short periodics	secular, first order short periodics in e
Tesseral terms	J_{22}, J_{31}	J_{22}, J_{31}, J_{33}	up to degree and order 50×50
Third body	first (P2) term in the Legendre expansion	third order solar and lunar second order Lunar terms	general luni-solar long and short periodic
Radiation pressure	–	First order averaged terms	long and short periodic terms
Others	–	–	solid Earth tides and coupling terms

Section 5.2 provides the description of force models.

Table 3.3 Theories average accuracy comparison in different subclasses along with the average computational time as percentage of numerical method

Theory	Class	Fit RMS [m]			% ODEM runtime [s]
		R	T	N	
SDP4	uGEO	713.54	1159.59	1337.53	6.1
	iGEO	980.23	1246.67	2194.42	
	eGEO	1134.73	1974.89	3208.32	
Kamel	uGEO	651.76	929.87	973.62	6.7
	iGEO	–	–	–	
	eGEO	–	–	–	
DSST	uGEO	139.49	213.70	8.66	10.4
	iGEO	272.56	295.28	8.49	
	eGEO	371.51	254.13	9.86	

the Earth. During the selection phase of the work, this requirement was translated into looking for a theory which is derived in non-singular equinoctial element set. The preliminary test results and literature surveys suggest that the DSST has potential to be used within the catalogue maintenance system. Hence, DSST is selected as the candidate technique and analysed rigorously for its prediction and fit accuracies. The following chapter will discuss the formulation, the implementation, and the improvements carried out on the selected theory, the DSST.

CHAPTER 4

DRAPER SEMI-ANALYTICAL SATELLITE THEORY

The Draper Semi-analytical Satellite Theory (DSST) is a precision mean element satellite theory. It was developed at the Draper Laboratory and the Computer Sciences Corporation by a team led by Paul J. Cefola. DSST is a semi-analytical theory expressed in non-singular equinoctial elements. This chapter provides the mathematical overview of the DSST and its implementation as a standalone propagator, together with the refinements brought into the standalone propagator to meet the required propagation accuracy.

In this chapter, a brief mathematical description on the formulation of DSST is presented. Here, the differences between the short periodic and long periodic perturbations terms are discussed, and the models which are established in the context of DSST are presented. This is followed by the discussion on the standalone propagator, and improvements which are brought into DSST during the present research work. In the end, using DSST within a batch least squared procedure with semi-analytically computed partial derivative matrices is discussed.

4.1 Mathematical Summary

Semi-analytical theory is a compromise to overcome the drawbacks of numerical integrators and analytical propagators. In DSST, the perturbations are expressed in terms of the singularity free equinoctial elements, which consists of semi-major axis (a), eccentricity vector ($[h,k]$), inclination vector ($[p,q]$), and mean longitude (λ), the set is represented with $\boldsymbol{c}$ ($c_{k=1\ldots6} : [a,h,k,p,q,\lambda]$). The non-singular equinoctial variables can be expressed in terms of classical Keplerian elements $\{a,e,i,\omega,\Omega,M\}$ as

$$\begin{aligned} a &= a \\ h &= e\sin(\omega + I\Omega) \\ k &= e\cos(\omega + I\Omega) \\ p &= \left[\tan\left(\frac{i}{2}\right)\right]^I \sin(\Omega) \\ q &= \left[\tan\left(\frac{i}{2}\right)\right]^I \cos(\Omega) \end{aligned} \tag{4.1}$$

$$\begin{aligned} \lambda &= M + \omega + I\Omega \\ I &= \text{retrograde factor} = \begin{cases} +1: & 0 \le i \le \frac{\pi}{2} \\ -1: & \frac{\pi}{2} < i \le \pi \end{cases} \end{aligned}$$

Equation 4.1 applies exactly for the conversion of the osculating Keplerian elements to the osculating equinoctial elements. The term osculating is used to refer to the epoch-wise representation of the true orbit.

The unperturbed motion of a satellite, in DSST, uses the classical two-body solution. That is, at any time (t), there exists a Keplerian orbit such that the position and velocity of a satellite can be evaluated. In order to estimate the precise (or closer to real) orbits of an orbiting satellite, it is vital to include the disturbing accelerations acting upon it. These perturbing forces are included through the Variation Of Parameter (VOP) equations. The VOP equations of motion represent the osculating orbital element rates as a function of the osculating orbital elements and the time. If $\boldsymbol{c}_{1-5}$ represents the five orbital shape elements, and θ the position or angular parameter of a satellite, then with $n(\boldsymbol{c}_{1-5})$ as mean motion, the general form of VOP equations can be expressed as below.

$$\begin{aligned} \dot{\boldsymbol{c}}_{1-5} &= \epsilon \boldsymbol{f}(\boldsymbol{c}_{1-5}, \theta) \\ \dot{\theta} &= n(\boldsymbol{c}_{1-5}) + \epsilon g(\boldsymbol{c}_{1-5}, \theta) \end{aligned} \tag{4.2}$$

For simplicity, it is assumed that the motion depends only on one angular parameter (θ). The disturbing forces which are expressed in terms of single phase angle are: zonal harmonics of the central body and atmospheric drag. A second phase angle may be considered for modeling tesseral harmonic terms, third body perturbations, and solar radiation pressure. Then the vector for the above equation can be used to represent the VOP for $\dot{\boldsymbol{\theta}}$.

The two main forms of VOP equations which are used in modelling perturbed orbits are:

1. the Gaussian VOP equations:

$$\frac{dc_k}{dt} = \frac{\partial c_k}{\partial \dot{\boldsymbol{r}}} \cdot \boldsymbol{q} \;;\; k = 1...6 \tag{4.3}$$

   where $\boldsymbol{q}$ is the disturbing acceleration. This form is flexible since it may be used for including both conservative and non-conservative perturbations. It requires transformation from elements to position and velocities, as the disturbing accelerations $\boldsymbol{Q}$ will be expressed in terms of satellite positions and velocities.

2. the Lagrange VOP equations:

$$\frac{dc_k}{dt} = -\sum_{j=1}^{6} (c_k, c_j) \frac{\partial R}{\partial c_j} \;;\; k = 1...6 \tag{4.4}$$

   where R is the disturbing potential and quantities (c_k, c_j) are the Poisson brackets (McClain, 1977). Due to the fact that the potential representation of perturbing accelerations is used, this formulation is suitable for conservative forces.

The Lagrangian VOP equations of the form 4.5 is used within DSST, which evaluates the fast variable separately, to model the motion due to non-spherical gravitational perturbations and third body accelerations. The Gaussian VOP equations of the form 4.6 is employed to

model the motion due to non-conservative forces.

$$\frac{dc_k}{dt} = -\sum_{j=1}^{6}(c_k, c_j)\frac{\partial R}{\partial c_j} \;;\; k = 1,2,3,4,5 \tag{4.5}$$

$$\frac{dc_k}{dt} = \frac{\partial c_k}{\partial \dot{\boldsymbol{r}}} \cdot \boldsymbol{q} \;;\; k = 1,2,3,4,5 \tag{4.6}$$

The equation of motion for the rapidly varying phase angle, in equinoctial element space $\theta = \lambda$ (mean longitude of the satellite), is given by

$$\frac{d\lambda}{dt} = \frac{dc_6}{dt} = n - \sum_{j=1}^{6}(c_6, c_j)\frac{\partial R}{\partial c_j} + \frac{\partial c_6}{\partial \dot{\boldsymbol{r}}} \cdot \boldsymbol{q} \tag{4.7}$$

where

$c_{k=1\ldots6}$: $[a, h, k, p, q, \lambda]$ (osculating equinoctial elements)
(c_k, c_j) : Poisson brackets for the equinoctial elements
R : disturbing potential for the conservative forces
$\frac{\partial c_k}{\partial \dot{\boldsymbol{r}}}$: partial derivatives of the equinoctial elements w.r.t velocity (two-body partial derivatives)
$\boldsymbol{q}$: accelerations associated with the non-conservative perturbations
n : mean motion

DSST makes use of the Generalized Method of Averaging (GMA) to achieve the required prediction accuracy. The details on establishing averaged VOP equations, descriptions on GMA, and its application in formulating DSST are well documented by McClain (1978), Zeis (1977), Green (1979), Slutsky and McClain (1981), Taylor (1982), and Fonte et al. (1995). This satellite theory employs GMA to separate short-periodic motion from long-periodic and secular motions (McClain, 1977). In a single averaged semi-analytical theory, the averaging of the VOP differential equations is performed over the period of $0 \leq \lambda \leq 2\pi$, on satellite angle to obtain mean element rates. The short-period motion is defined in context to DSST as a variation with periods less than one orbital period, and long-period motion corresponds to periods greater than orbital revolution.

If the averaged equinoctial elements are represented with $\bar{c}_k$ (for $k = 1, \ldots, 6$) and osculating elements are represented with c_k, then the near identity transformations between averaged elements and osculating elements are given by Equation 4.8.

$$\begin{aligned} \boldsymbol{c} &= \bar{\boldsymbol{c}} + \epsilon\boldsymbol{\eta}(\bar{\boldsymbol{c}}, \bar{\lambda}) \\ \lambda &= \bar{\lambda} + \epsilon\eta_6(\bar{\boldsymbol{c}}, \bar{\lambda}) \end{aligned} \tag{4.8}$$

The mean element rates are given by the Equations 4.9 and 4.10, with $\epsilon\boldsymbol{\eta}$ being the truncated short periodic functions.

$$\frac{d\bar{c}_k}{dt} = \sum_{j=1}^{N} \epsilon^j A_{i,j}(\bar{c}_k) + \epsilon^{N+1} \quad k = 1...5 \tag{4.9}$$

$$\frac{d\bar{\lambda}}{dt} = \bar{n}(\bar{c}_1) + \sum_{j=1}^{N} \epsilon^j A_{6,j}(\bar{c}_k) + \mathrm{O}\left(\epsilon^{N+1}\right) \tag{4.10}$$

The short periodic functions and mean element rates are obtained by matching the first order in ϵ to the original VOP equations to differentiation of the near-identity transformations and substitution of mean element rates (Wagner, 1986). The short-periodic functions $\boldsymbol{\eta}$ are periodic and have zero mean over one period of the orbit. By integrating the matching condition, it is assumed that the dependencies on $\boldsymbol{\eta}$ is negligible over averaging period. This will be the main basis for finding the mean element dynamics.

Single-averaged values of the conservative disturbing forces' rates are computed by averaging the effects of all perturbations over the single orbital element for one complete orbital period [1]. If single averaging has to be applied over the perturbations which are dependent on additional phase angles, it is necessary to consider the role of the phase angles. Considering the variability of the second phase angle, the second angle is either held constant or treated as a weak dependency. One case in which weak dependent terms have to be considered are for third body perturbations. The same will be discussed in detail under section 4.3. The GMA is still applied for non-conservative perturbations and the averaging is obtained using numerical quadratures.

By using the generalized method of averaging both long-period and secular motions are retained within the averaged VOPs. First order $A_{i,j}$ functions are accounted for the periodic terms in the Fourier series in the fast variable. If $U_{k\sigma}$ and $V_{k\sigma}$ are the series coefficients then the approximations between the short-periodic functions and Fourier series are given by

$$\begin{aligned} \epsilon\boldsymbol{\eta}_{1-5}(\bar{\boldsymbol{c}},\bar{\lambda}) &= \sum_{\sigma=1}^{N} \epsilon\boldsymbol{U}_\sigma(\bar{\boldsymbol{c}})\sin(\sigma\bar{\lambda}) - \epsilon\boldsymbol{V}_\sigma(\bar{\boldsymbol{c}})\sin(\sigma\bar{\lambda}) \\ \epsilon\eta_6(\bar{\boldsymbol{c}},\bar{\lambda}) &= \sum_{\sigma=1}^{N} \epsilon U_{6,\sigma}(\bar{\boldsymbol{c}})\sin(\sigma\bar{\lambda}) - \epsilon V_{6,\sigma}(\bar{\boldsymbol{c}})\sin(\sigma\bar{\lambda}) \end{aligned} \tag{4.11}$$

$U_{k\sigma}$ and $V_{k\sigma}$ are computed for $\epsilon\boldsymbol{f}(\bar{\boldsymbol{c}},\bar{\lambda})$ and $\epsilon\boldsymbol{g}(\bar{\boldsymbol{c}},\bar{\lambda})$ of VOP equations. These coefficients depend on slowly varying mean equinoctial elements, thus coefficients themselves vary slowly. The behaviour is taken as an advantage through using an interpolator. Using an interpolator in computing the series coefficients further improves the computational efficiency of the semi-analytical theory.

The part of the semi-analytical theory which propagates the mean element motion is referred to as the Averaged Orbit Generator (AOG). To first order in the small parameters, the

[1] Note that this is the case in single averaging. However, additional averaging can be performed over another fast varying variable of the dynamic system otherwise known as double averaging

averaged equations of motion for the conservative perturbations are given by Equation 4.12

$$\frac{d\bar{c}_k}{dt} = -\sum_{j=1}^{6}(\bar{c}_k, \bar{c}_j)\frac{\partial \bar{R}}{\partial \bar{c}_j} \quad k = 1...5 \tag{4.12}$$

and the averaged equations of motion for the non-conservative perturbations are given by Equation 4.13

$$\frac{d\bar{c}_k}{dt} = \frac{1}{2\pi}\int_0^{2\pi}\frac{\partial \bar{c}_k}{\partial \dot{\boldsymbol{r}}}\cdot \boldsymbol{q}\, d\lambda \quad k = 1...5 \tag{4.13}$$

and the equation of motion for the mean phase angle is given by Equation 4.14

$$\frac{d\bar{\lambda}}{dt} = \frac{d\bar{c}_6}{dt} = \bar{n} - \sum_{j=1}^{6}(\bar{c}_6, \bar{c}_j)\frac{\partial \bar{R}}{\partial \bar{c}_j} + \frac{1}{2\pi}\int_0^{2\pi}\frac{\partial \bar{c}_6}{\partial \dot{\boldsymbol{r}}}\cdot \boldsymbol{q}\, d\lambda \tag{4.14}$$

where

$\bar{c}_{k=1...6}$: $[\bar{a}, \bar{h}, \bar{k}, \bar{p}, \bar{q}\bar{\lambda}]$ (mean equinoctial elements)

$\bar{R}$: averaged disturbing potential for the conservative forces

$\bar{n}$: mean mean-motion, which is a function of $\bar{a}$

Accurate solution of the VOP equations by a semi-analytical satellite theory is not complete without the recovery of short-periodic variations.The transformation from averaged elements ($\bar{c}_i$) to osculating elements (c_i) is computed by using Equation 4.15.

$$c_i = \bar{c}_i + \sum_{j=1}^{N}\epsilon^j \boldsymbol{\eta}\left(\bar{a}, \bar{\lambda}\right) + \mathrm{O}\left(\epsilon^{N+1}\right), k = 1,2,3,4,5,6 \tag{4.15}$$

The part of the propagator which deals with $\boldsymbol{\eta}$ is referred to as the Short Periodic Generator (SPG). Green (1979) developed the required expansions to achieve generality in the SPG models. Short-periodic variations are approximated with a Fourier series expansion in the mean-mean longitude ($\bar{\lambda}$) for central body perturbations, and Fourier series expansion in mean eccentric-longitude ($F = E + \omega + I\Omega$, where E is the eccentric anomaly) are used for the coupling terms and the third body perturbations terms. Equations 4.16 gives the analytical short-periodic coefficients for conservative disturbing forces

$$\begin{aligned}
\epsilon U_{ik} &= \frac{-1}{k\bar{n}}\sum_{j=1}^{5}(\bar{c}_i, \bar{c}_j)\frac{\partial\overline{[R\cos(k\bar{\lambda})]}}{\partial \bar{c}_j} - \frac{(\bar{c}_i, \bar{\lambda})}{\bar{n}}\overline{[R\sin(k\bar{\lambda})]} + \left(\frac{3\epsilon V_{1k}}{2k\bar{c}_1}\right)\delta_{i6} \\
\epsilon V_{ik} &= \frac{-1}{k\bar{n}}\sum_{j=1}^{5}(\bar{c}_i, \bar{c}_j)\frac{\partial\overline{[R\sin(k\bar{\lambda})]}}{\partial \bar{c}_j} - \frac{(\bar{c}_i, \bar{\lambda})}{\bar{n}}\overline{[R\cos(k\bar{\lambda})]} + \left(\frac{3\epsilon U_{1k}}{2k\bar{c}_1}\right)\delta_{i6}
\end{aligned} \tag{4.16}$$

The details of the short-periodic models are given for the zonal harmonics by Slutsky and McClain (1981), for the tesseral harmonics by Proulx et al. (1981), and for the lunar-solar point

masses by Slutsky and McClain (1981) and Slutsky (1983). Formulated DSST force models are summarized in the below Table 4.1

Table 4.1 Force model formulation for Draper Semi-analytical Satellite Theory

Mean element dynamics (Averaged VOP equations)	Short-periodic ($\boldsymbol{\eta}$) functions
Recursive, closed form zonal model and J_2^2 upto first order in eccentricity (e^1) *	Recursive, closed form zonals J_2^2 up to first order in eccentricity
Recursive, closed form tesseral resonance model (e^n, $n > 20$) up to 50×50 geopotential	Recursive, closed form tesseral m-dailies model
	Recursive tesseral linear combinations (e^n, $n > 20$) Recursive J_2 secular/ tesseral m-daily coupling in closed form
Recursive Solar-Lunar single averaged (Time Independent) in closed form	Recursive Solar-Lunar in closed form
Recursive Solar-Lunar double averaged	Recursive Solar-Lunar double averaged (Weak Time Dependent) in closed form
Solid Earth tide in closed form	
Atmospheric drag via numerical quadrature J_2 - drag coupling terms via numerical quadrature	Atmospheric drag numerical computation
Solar radiation pressure via numerical quadrature	Solar radiation pressure numerical computation

* A quadrature model for J_2^2 zonal terms for high eccentricity is presented by Folcik and Cefola (2012)

Formulation of DSST in its AOG and SPG form contributes to the efficiency gains through:

1. The analytical integration of SPG for all gravitational perturbations
2. Using numerical quadrature for integrating SPGs of drag and solar radiation pressure
3. The Fourier coefficients depend only on the slowly varying mean elements (see Equations 4.11)
4. Slowly varying variables allow extensive use of interpolators
5. The series converge quickly, and hence the approximation may be truncated to low orders (Taylor, 1982).

The main characteristics of the DSST can be summarized as below:

- Based on Generalized Method of Averaging perturbation theory
- Employs non-singular equinoctial orbital elements
- Makes use of numerical approximations for slowly varying quantities

- Facilitates different integration coordinate systems employed in the numerical solution of the mean element equations of motion
- Employs efficient interpolation strategies for estimating mean elements at the times of SPG evaluations
- Makes use of numerical quadratures for averaging non-conservative forces like drag and solar radiation pressure

4.2 Standalone Orbit Propagator

The Goddard Trajectory System (GTDS) served as a development platform for the FORTRAN 77 based implementation of the DSST semi-analytical satellite theory. This implementation's inital focus was to bring in mean element equations of motion due to conservative perturbations. Later at the Draper Laboratory the numerical quadrature of non-conservative forces, interpolation strategies, refinement of tesseral resonance models, and coupling terms for short-periodic motions were coded into the tool.

To provide easier accessibility to DSST for research and applications outside the Draper Laboratory, a standalone version was created in 1984 (Neelon et al., 1997). This DSST standalone orbit propagator package was developed to be a self-contained version of the DSST functions which existed within GTDS. The portable DSST standalone propagator is implemented in Fortran 77, and comprises of over 200 subroutines. Initially, the subroutines were designed under the common-blocks paradigm of functional programming. The standalone version has undergone numerous enhancements and improvements over the years of its use. In 2013, a copy of the standalone version was made available to DLR/GSOC. It served as starting point for this thesis and had the following characteristics:

- Common-block free functional programming paradigm was used. All the common blocks were moved into "header" files, which in turn will facilitate parallel execution, if required.
- Integration of the mean element equations of motion is implemented in modular structure allowing straightforward modification to different integration methods. Presently, a Runge-Kutta fourth order integrator is implemented.
- Output of mean elements, osculating elements, and position and velocity at an arbitrary request time.
- Ability to update the force models: geopotential terms, atmospheric density models, Solar/Lunar/Planetary (SLP) ephemeris, and timing coefficients. Table 4.2 provides the complete list of different force models included in the standalone propagator.
- Coordinate transformations between True-of-Date, mean of J2000, and Earth-Centred-Earth-Fixed coordinate frames.

Figure 4.1 presents the high-level architecture of the standalone propagator. The detailed usage procedures, available propagator settings, and associated files descriptions are presented in Appendix A.

Table 4.2 Specific force models available within the DSST standalone propagator before improvements (GSOC version in 2013)

Geopotential	GEM1, GGSM02, and WGS84 [1]
Atmospheric Density	Harris-Priester (static atmosphere), and Jacchia 71 (dynamic atmosphere; solar flux and geomagnetic indices). Spherical spacecraft model [2]
Solar Radiation Pressure	Cylindrical shadow model and a spherical spacecraft model
Third-body	Point mass approximations. JPL solar and lunar ephemerides are used

[1] Within GTDS the list includes geopotentials models from the families of WGS, JGM, GEM, etc.
[2] GTDS version includes extensive list of dynamic density models. Also, the recent developments, for GTDS, have made attempt to include extended spacecraft models for precise predictions

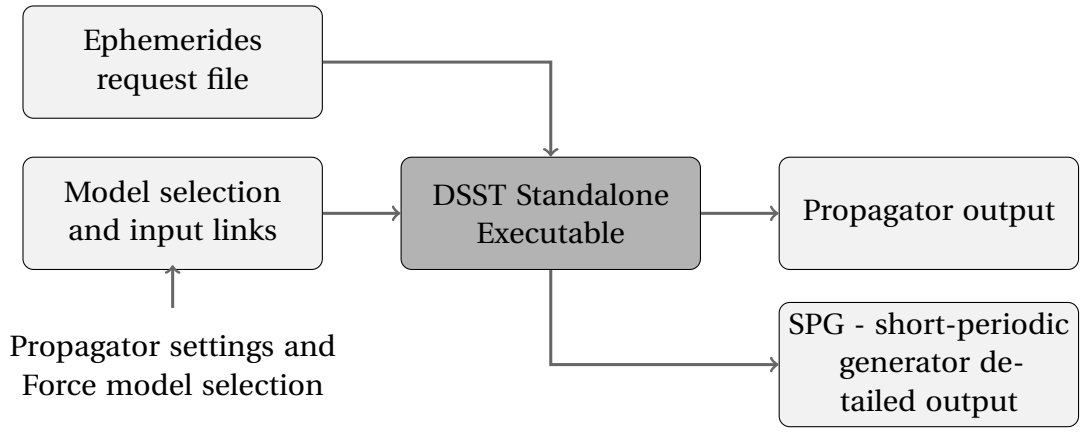

Fig. 4.1 DSST standalone propagator inputs and outputs

4.3 Improvements to the DSST Standalone Orbit Propagator

Initial examination of the DSST standalone propagator resulted in identification of several restrictions in terms of its performance. It was not able to achieve the accuracy in terms of orbit predictions which one would expect from its formulation and model inclusion. This discrepancy was also affirmed from the theory's performance in the GTDS R&D test cases. During the course of this study, several bug fixes and inclusion of missing or necessary short-periodic force models were performed. LEO and GEO test cases were used to identify the limitations of the standalone DSST by comparing the orbits against ODEM generated orbits. Table 4.3 presents the epoch time Keplerian elements for the two test cases. These orbits were propagated using the best available DSST settings (based on the previous study from Fonte and Sabol (1995))and the predicted ephemerides were compared against a numerical propagator to check for DSST's accuracy. Figures 4.2 and 4.3 show the differences between DSST orbits and Cowell orbits.

The test cases included 50×50 geopotential terms along with high accuracy settings available for both average and short-periodic generator. The equivalent force models were used to generate reference orbits against which the DSST generated orbits were compared. From test cases, the position error RMS for a LEO orbit is found to be 553 meters and for

Table 4.3 LEO and GEO test satellites' orbital mean elements at epoch 10 December 2012 00:00:00 hours

Elements	LEO test satellite	GEO test satellite
Semi-major axis [km]	6800.00	42000.00
Eccentricity	0.001	0.001
Inclination [deg]	60.00	5.00
Right ascension [deg]	0.00	0.00
Argument of perigee [deg]	0.00	0.00
Mean anomaly [deg]	0.00	0.00

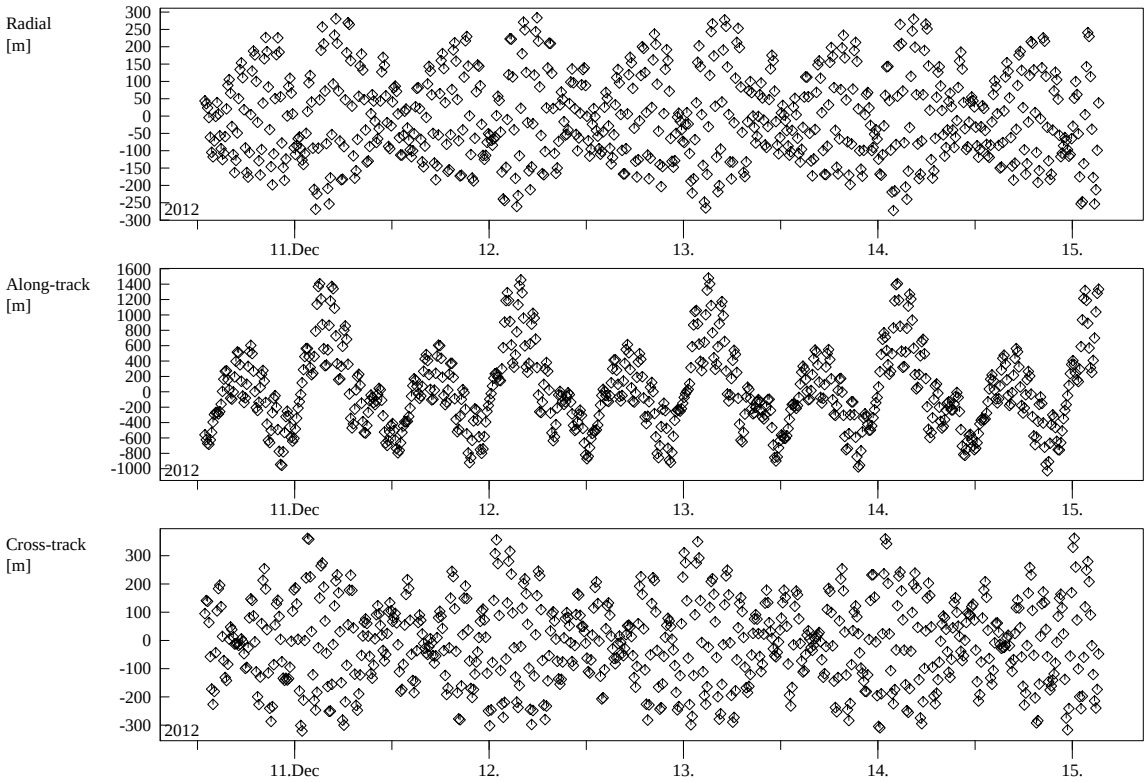

Fig. 4.2 DSST prediction for a LEO satellite (Table 4.3) compared against Cowell orbit

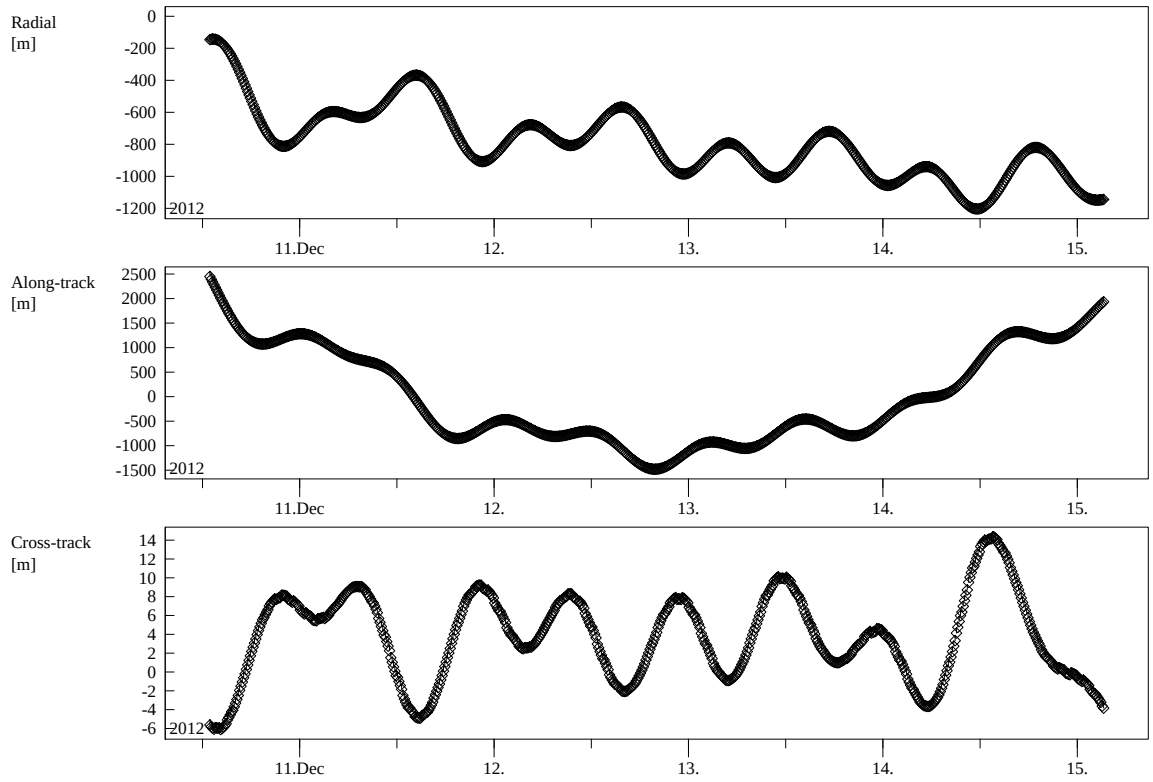

Fig. 4.3 DSST prediction for a GEO satellite (Table 4.3) compared against Cowell orbit

the selected GEO orbit it is close to 1.5 kilometers. The same cases were performed by generating the orbits using GTDS version of DSST. Here it was noticed that the GTDS version was performing with prediction accuracy two orders magnitude better than the standalone version.

With the brute-force testing and analysis for individual force modelling terms within both versions of DSST, the missing perturbation models in the standalone version were identified. This set of short-periodic models were adapted and implemented for GSOC's standalone DSST version.

To improve the conversion of mean elements to osculating elements, the Fourier coefficients for the series expansions are to be computed including higher order terms. That is, the coefficients U_{ik} and V_{ik} within the Equations 4.16 must include the prominent higher order terms, coupling terms, and time dependent variations when required. The descriptions of the identified three main SPG models are as follows:

J_2- squared short-periodic variations

This coupling term was identified to influence the prediction accuracy of highly eccentric orbits. A model for the J_2-squared terms has been developed by Folcik and Cefola (2012) which employs numerical quadrature for integrating the potential. Implementation of the coupling term following the Folcik and Cefola derivation is presented in Appendix C.

J_2- secular/tesseral m-daily coupling terms

The coupling terms in short-periodic modelling influences the LEO satellites. Based on Proulx (1982) derivations, the following equations are established:

$$U_{ik} = C_{ik} + \left[\frac{\partial \bar{c}_i}{\partial t} M_{ik} - \frac{\partial N_{ik}}{\partial t}\right] + \left[\frac{3n}{2\omega_E a}\delta_{i6}\frac{D_{1k}}{k}\right]$$
$$V_{ik} = D_{ik} + \left[\frac{\partial \bar{c}_i}{\partial t} N_{ik} - \frac{\partial M_{ik}}{\partial t}\right] + \left[\frac{3n}{2\omega_E a}\delta_{i6}\frac{C_{1k}}{k}\right] \tag{4.17}$$

where

$U_{ik}; V_{ik}$: SPG Fourier coefficients for J2– m-daily coupling terms
$C_{ik}; D_{ik}$: J2 short periodic Fourier coefficients
$M_{ik}; N_{ik}$: Tesseral M-Daily short periodic coefficients

Within the implementation, a two point finite differencing method is used to compute the required partial derivatives of the tesseral m-daily short periodic coefficients.

Weak Time Dependent (WTD) short-periodic corrections

Both the averaged element rates and the short-periodic functions due to the lunar-solar point masses are derived under the assumption that the third-body is held fixed during the averaging interval. However, a better assumption is that the osculating equations of motion for lunar-solar point masses are functions of two phase angles both of which have a periodic character. These are the satellite mean longitude and the mean longitude of the third body. To treat the two phase angle case Green (1979) modifies both the assumed form of the mean element equations and the assumed form of the near-identity transformation to include the second phase angle [Green (1979): Eqs. (2-63), (2-64) and (2-65)]. Green assumes the time-dependent short periodic functions are represented by a Fourier series in the mean longitude, where the coefficients are functions of the slowly varying mean equinoctial elements and the third-body mean longitude. Finally, the third body short-periodic motions are expressed as the time dependent coefficients in terms of Time-Independent(TI) coefficients, and first and second time derivatives of the TI coefficients. Thus the weak time dependent short-periodic motion can be viewed as the sum of the TI motion and the WTD corrections.

Slutsky (1983) developed an analytical form for the time-independent short-periodic functions as Fourier series in the eccentric longitude [Slutsky (1983): Eq.(4)]. This formulation has the advantage that it is in closed-form with respect to eccentricity. Also the Slutsky formulation is analytical. Given the eccentricity is small, the constant term in the Slutsky expansion becomes small and the Fourier coefficients in the Slutsky eccentric longitude expansion approach the Fourier coefficients in the Green mean longitude expansion.

In the DSST Standalone, we can (as an option) approximate the third body short-periodic motion as the sum of the Slutsky TI expansion plus an approximation of the WTD corrections. This approximation is obtained by substituting the partial derivatives of the Slutsky TI Fourier coefficients with respect to time into Green's equation. This approximation proved to be fast in computation and useful for small eccentricities ($e \leq 0.2$) [1]. Equations 4.18 presents the WTD Fourier coefficients derived in terms of mean eccentric longitude.

[1] From analysing the objects distribution in GEO and MEO region, it is observed that the majority ($\geq 90\%$) have eccentricities below 0.2

$$
\begin{aligned}
U_{ix} = C_{ix} &- \frac{1}{n}\left[G\left\{\frac{\partial D_{ix}}{\partial t}, \bar{h}, \bar{k}\right\} - \frac{3}{2a}\delta_{i6}H\left\{\frac{\partial C_{1x}}{\partial t}, \bar{h}, \bar{k}\right\}\right] \\
&+ \left(\frac{1}{n}\right)^2\left[G\left\{\frac{\partial^2 D_{ix}}{\partial t^2}, \bar{h}, \bar{k}\right\} - \frac{3}{a}\delta_{i6}H\left\{\frac{\partial^2 C_{1x}}{\partial t^2}, \bar{h}, \bar{k}\right\}\right] \\
V_{ix} = D_{ix} &- \frac{1}{n}\left[H\left\{\frac{\partial C_{ix}}{\partial t}, \bar{h}, \bar{k}\right\} - \frac{3}{2a}\delta_{i6}G\left\{\frac{\partial D_{1x}}{\partial t}, \bar{h}, \bar{k}\right\}\right] \\
&+ \left(\frac{1}{n}\right)^2\left[H\left\{\frac{\partial^2 C_{ix}}{\partial t^2}, \bar{h}, \bar{k}\right\} - \frac{3}{a}\delta_{i6}G\left\{\frac{\partial^2 D_{1x}}{\partial t^2}, \bar{h}, \bar{k}\right\}\right]
\end{aligned}
\tag{4.18}
$$

where

$U_{ix}; V_{ix}$: WTD Fourier coefficients for 3^{rd} body perturbations

$C_{ix}; D_{ix}$: TI short periodic coefficients for 3^{rd} body perturbations

$G_{ix}; H_{ix}$: Slutsky's correction functions for time independent terms in eccentric longitude

The Slutsky's terms make use of numerical quadrature methods to compute the corrections. Similar to the J_2-tesseral coupling terms, the implementation makes use of the numerical two point finite differencing method to compute the required partial derivatives of the coefficients. Figures 4.4 shows the differences in the Sine and Cosine terms computed which are mentioned in Equations 4.18. The following Figure 4.5 shows the influence of the weak time dependent terms on the prediction of orbit in Keplerian elements.

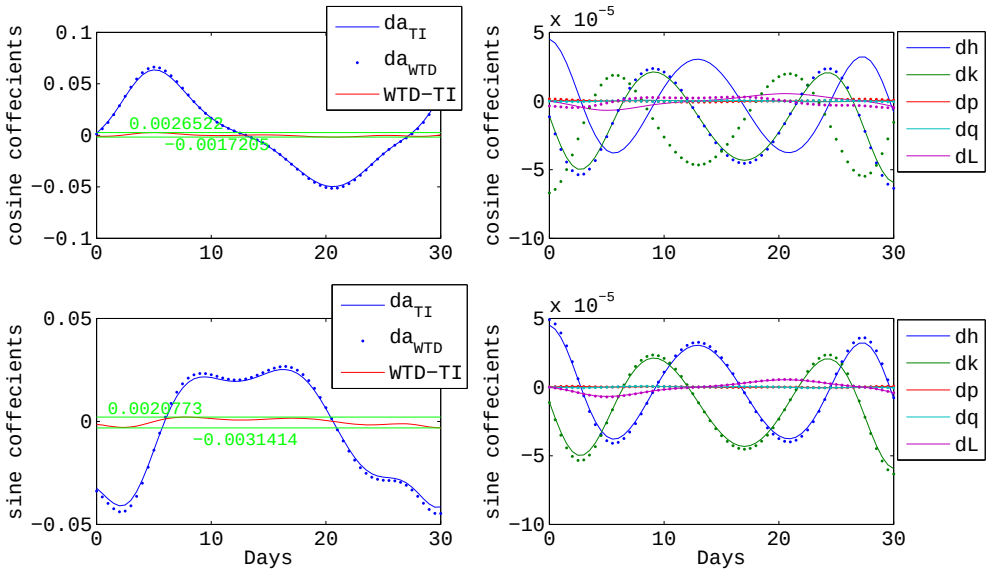

Fig. 4.4 Differences between time independent and weak time dependent sine and cosine Fourier coefficients which are used in approximating the third body forces on GEO satellites. Right hand plots show the difference for semi-major axis and the left hand side plots show the differences for the remaining five equinoctial elements (h,k,p,q, and λ or L)

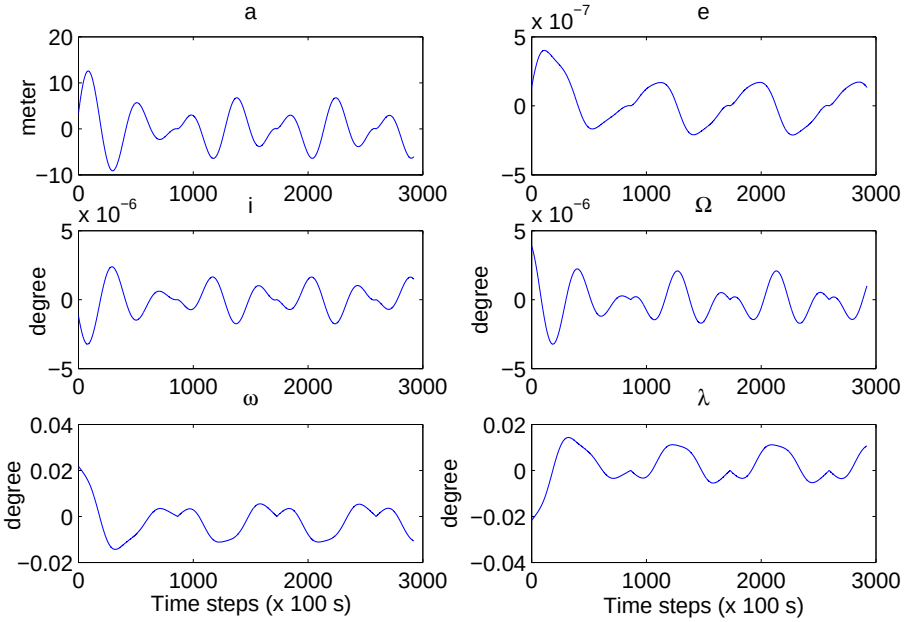

Fig. 4.5 Differences in Keplerian elements when propagating a GEO satellite (with near circular orbit and perfect geostationary altitude of 41260 km) with time independent third body perturbation forces and including the weak time dependent terms for approximating the third body perturbations

As seen in the Figure 4.4 the differences in the sine and cosine terms for da have a magnitude of 10^{-3} km/s. These divergences of the Moon and Sun coefficients induces orbit prediction errors of the order of 10^{-2} km in semi-major axis. The same can be observed in the Figure 4.5 which shows the differences in Keplerian elements for a seven days propagation interval. Since the requirement for catalogue maintenance the propagation accuracy was set to be below 10 m level, it is observed that the inclusion of weak time dependent terms is required.

After updating the standalone with new models, the current DSST version offers the following force models which can be included for the propagation and orbit determination procedures. Table 4.4 presents the complete summary of available averaged and short-periodic models within the standalone version of DSST at GSOC.

Figures 4.6 and 4.7 show the accuracy of improved DSST propagation runs for a LEO and a GEO orbit compared against Cowell orbits. For a LEO orbit the position accuracy was reduced to 185 meters and for a GEO orbit the prediction root mean square value came down to 7 meters. The large discrepancy is LEO was traced to the different atmospheric density models used within the DSST and ODEM. This forced the implementation of the Jacchia-Gill atmospheric density model within the DSST standalone version, for the purpose of comparison.

Mean Element Rates and Partial Derivatives

To facilitate the implementation of the mean element estimation procedure, computation of mean element rates and partial derivatives were implemented within the standalone DSST propagator. The code related to improvements is provided in Appendix C.

Table 4.4 Averaged and short periodic perturbations in the present DSST standalone version at GSOC

Perturbation factors	AOG formulations	SPG formulations
Zonal harmonics	Linear terms	First order terms in $\{a,h,k,p,q,\lambda\}$, treated via a closed-form expansion in true longitude
Second degree zonal-harmonic	Up to second-order terms without $J_2^2 \times e^2$ terms	Up to second-order terms in $\{a,h,k,p,q,\lambda\}$, expansion in mean longitude and without $J_2^2 \times e^2$ terms and higher
Geopotential tesseral harmonics ($2 < l < 50,\ l < m < 50$)	Linear terms and resonance effects in general form	m-dailies, linear-combination terms and J_2- tesseral- m-daily coupling terms
Solar and Lunar perturbations	Linear terms in general form	Linear terms in general form, closed form expansion in eccentric longitude and Weak time dependent terms
Atmosphere drag	Linear and cross coupling terms with J_2. Rates are evaluated via quadratures. Included models: Harris-Priester, Jacchia 71, Jacchia-Gill and MSISE-90	Linear terms via expansion in mean longitude. Coefficients are evaluated via quadratures
Solar radiation pressure	Linear terms. Cylindrical model for shadow	Linear terms via expansion in mean longitude. Coefficients are evaluated via quadratures
Solid Earth tides	Love number terms	–

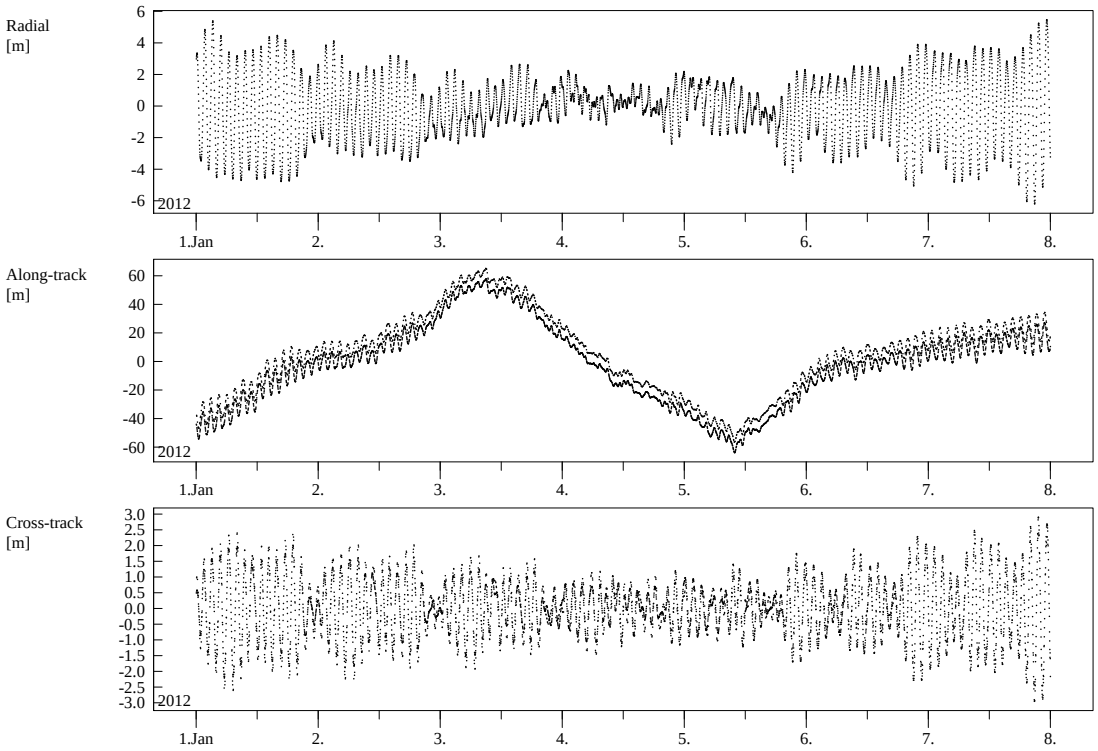

Fig. 4.6 DSST prediction for a LEO satellite (Table 4.3) compared against Cowell orbit after the inclusion of J_2^2 and J_2- secular/tesseral m-daily coupling terms within short-periodic modelling, and Jacchia-Gill density model in both propagators.

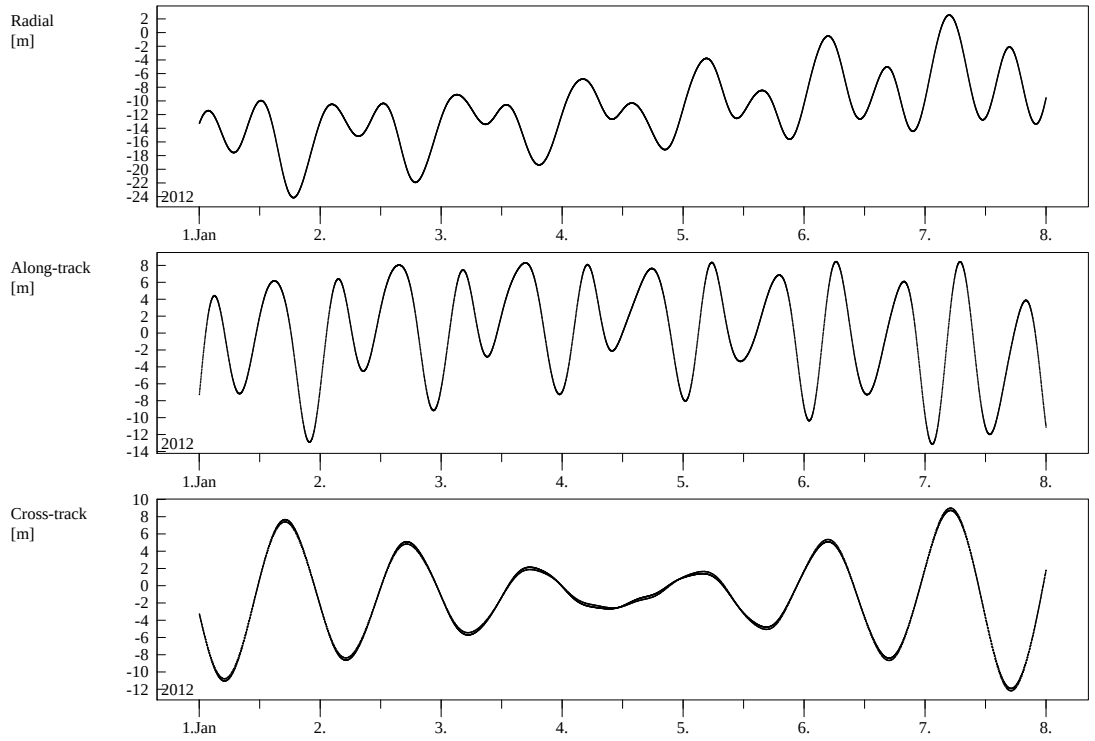

Fig. 4.7 DSST prediction for a GEO satellite (Table 4.3) compared against Cowell orbit after the inclusion of weak-time-dependent terms in third body short-periodic motion

4.4 Mean Element Based Differential Correction Process

The weighted Batch Least Squares (BLSQ) algorithm is the most widely used OD method within a SO catalogue maintenance system. The focus of this investigation is to reduce the computational effort in OD runs; for this purpose we coupled the selected SST with the BLSQ differential correction method.

A semi-analytical way of computing partial derivatives for a perturbed object which is compatible with the DSST was formulated by Green (1979). The working principle and characteristics of a BLSQ OD method are discussed in section 3.2.1. For a given initial condition of a space object, with state $\boldsymbol{Y}_{t_0}$ associated with covariance $\mathbf{P}_{t_0}$ and for the available arc of observations, BLSQ provides the best estimate at the epoch state, $\hat{\boldsymbol{y}}_{t_0} = \boldsymbol{y}_{t_0} + \delta \boldsymbol{y}_0$ with

$$\delta \mathbf{y}_0 = (\boldsymbol{A}^T W \boldsymbol{A})^{-1} \boldsymbol{A}^T W \mathbf{b} \tag{4.19}$$

where,

$$\boldsymbol{A} \;:\; \text{partial derivative matrix} \tag{4.20}$$

$$W \;:\; \text{weighting matrix} \tag{4.21}$$

$$\mathbf{b} \;:\; \text{residual vector} \tag{4.22}$$

The partial derivative matrix, $\boldsymbol{A}$, is usually composed of the observation matrix: $\boldsymbol{H}$ and the state transition matrix (STM): $\boldsymbol{\Phi}$.

$$\boldsymbol{A} = \frac{\partial \alpha(t)}{\partial \mathbf{y}(t)} \cdot \frac{\partial \mathbf{y}(t)}{\partial \mathbf{y}_{t_0}} = \boldsymbol{H}_{t,t} \cdot \boldsymbol{\Phi}_{t,0} \tag{4.23}$$

$\boldsymbol{\Phi}_{t,0}$ can be computed by finite differencing method or by integrating the variational equations. $\boldsymbol{\Phi}_{t,0}$ provides the slope and direction to the least squares system towards convergence. Computation of $\boldsymbol{\Phi}_{t,0}$ must include the major perturbing forces to reach convergence (best estimate) in a smaller number of iterations. Figure 4.8 shows the schematic diagram of the BLSQ differential correction process, together with the major parts of an OD process.

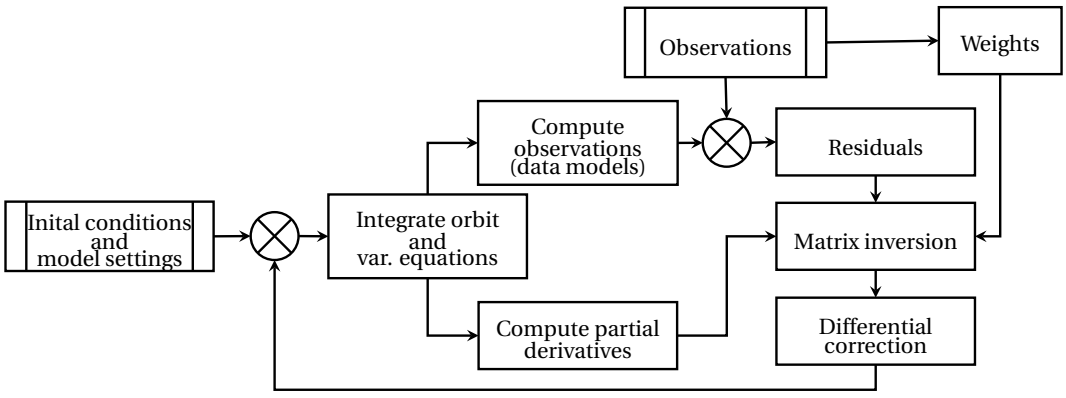

Fig. 4.8 Schematic diagram of a least squares orbit determination program

Runtime profiling of OD process components was carried-out, where the OD is integrating variational equations for computing the partial derivatives of observations with respect to

states. The computation of the STM is the most resource consuming part of the BLSQ system. When this profiling was carried out on a BLSQ program within ODEM, comparison with DSST orbit determination using finite differencing method (to establish partial derivatives) showed similar characteristics. Figure 4.9 shows the normalized times consumed by different parts, discussed in the previous flow chart, of the selected OD programs.

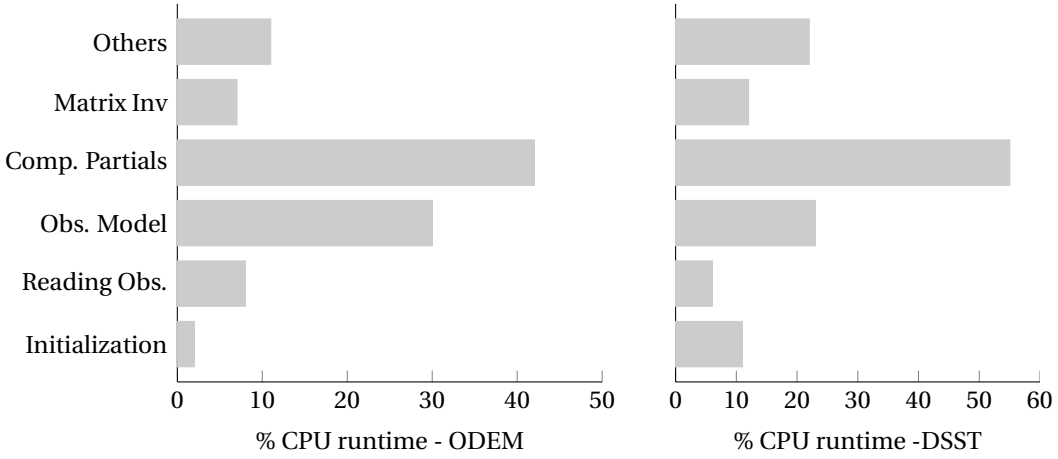

Fig. 4.9 Orbit determination program computational profile of different parts of the numerical and DSST orbit determination

The semi-analytical BLSQ computes the STM in a semi-analytical fashion, thereby reducing the computational load of the overall OD process. DSST employs propagation in mean element space while the observation modelling is based on the osculating state. To map the mean space to the osculating space, the STM is further divided into two components, as in Equation 4.24

$$\mathbf{\Phi} = \frac{\partial \mathbf{y}_t}{\partial \mathbf{c}(t)} \boldsymbol{G} \tag{4.24}$$

Here $\mathbf{y}_t$ represents the osculating positions and velocities, and $\boldsymbol{c}(t)$ represents the osculating equinoctial elements at an arbitrary time, t. $\boldsymbol{G}$ represents the perturbed partial derivatives which are expressed as

$$\boldsymbol{G} = \left[\left\{ \frac{\partial \boldsymbol{c}(t)}{\partial \bar{\mathbf{c}}_0} \right\} \middle| \left\{ \frac{\partial \boldsymbol{c}(t)}{\partial \boldsymbol{p}} \right\} \right] \tag{4.25}$$

with $\bar{\mathbf{c}}_0$ as the epoch mean equinoctial elements, and $\boldsymbol{p}$ as the vector composed of the dynamical parameters in the least squares estimation. In Equation 4.24, the first part of the right hand side, $\frac{\partial \boldsymbol{y}_t}{\partial \underline{\mathbf{c}}(t)}$, is the two-body partial derivatives, which maps the variations in the equinoctial elements to positions and velocities. Formulation and implementation of two body partials is straight forward and can be found in McClain (1977) and Vallado (1997).

Matrix $\boldsymbol{G}$ consists of $\boldsymbol{B}_{1...4}$ matrices, as given in Equation 4.26. Retaining the structure as below, allows the computation of $\boldsymbol{G}$ to be carried out in a modular way.

$$\boldsymbol{G} = [\boldsymbol{I} + \boldsymbol{B_1}][\boldsymbol{B_2}|\boldsymbol{B_3}] + [\mathbf{0}|\boldsymbol{B_4}] \tag{4.26}$$

with

$$\boldsymbol{B_1} = \left[\frac{\partial \varepsilon \boldsymbol{\eta}_1(\boldsymbol{c}_t)}{\partial \overline{\boldsymbol{c}}(t)}\right] \tag{4.27}$$

$$\boldsymbol{B_2} = \left[\frac{\partial \overline{\boldsymbol{c}}(t)}{\partial \overline{\boldsymbol{c}}_0}\right] \tag{4.28}$$

$$\boldsymbol{B_3} = \left[\frac{\partial \overline{\boldsymbol{c}}(t)}{\partial \boldsymbol{p}}\right] \tag{4.29}$$

$$\boldsymbol{B_4} = \left[\frac{\partial \varepsilon \boldsymbol{\eta}_1(\boldsymbol{c})}{\partial \boldsymbol{p}}\right] \tag{4.30}$$

The $\boldsymbol{B_2}$ and $\boldsymbol{B_3}$ matrices are the partial derivatives of the mean elements at an arbitrary time w.r.t epoch time mean elements and solve-for parameters, respectively. The $\boldsymbol{B_1}$ and $\boldsymbol{B_4}$ matrices represent the short periodic portion of the semi-analytical partial derivatives which are computed at observation time intervals.

The $\boldsymbol{B_2}$ and $\boldsymbol{B_3}$ matrices are governed by linear differential Equations 4.31 and 4.32, and are computed on the mean element integration time grid. For DSST, this is usually on the order of a half or one day step sizes.

$$\frac{d}{dt}\boldsymbol{B_2} = \boldsymbol{C} \times \boldsymbol{B_2} \quad ; [\boldsymbol{B_2}]_{t_0} = \boldsymbol{I} \tag{4.31}$$

$$\frac{d}{dt}\boldsymbol{B_3} = \boldsymbol{C} \times \boldsymbol{B_3} + \boldsymbol{D} \quad ; [\boldsymbol{B_3}]_{t_0} = [\boldsymbol{0}] \tag{4.32}$$

with

$$\boldsymbol{C} = \left\{\frac{\partial \left[d(\overline{\boldsymbol{c}})/dt\right]}{\partial \overline{\boldsymbol{c}}(t)}\right\} \tag{4.33}$$

$$\boldsymbol{D} = \left\{\frac{\partial \left[d(\overline{\boldsymbol{c}})/dt\right]}{\partial \boldsymbol{p}}\right\} \tag{4.34}$$

In Equations 4.34 the numerator of the right hand side stands for the VOP equations in mean equinoctial elements. These VOP equations are evaluated during propagation, and the same can be made use within the computation of $\boldsymbol{G}$ matrix and further reduce the computational burden on an OD system. The above described method has been implemented. The same state transition matrices are used within the covariance propagation routines. Implementation of both methods: orbit determination services and covariance propagation services, are briefly described below.

Implementation of the Standalone DSST OD

Figure 4.10 shows the flow chart for the implemented BLSQ orbit determination method making use of the DSST. For simplicity, this OD program will be referred as 'DSST-OD' in the rest of this paper. Figure 4.10 also shows the semi-analytical path of computing partial derivatives for observation processing, where the actual savings in computational load occurs. Building the DSST-OD program consisted of building the new main program

'orbit_determination_services'

and employing the DSST propagator and LAPACK (Linear Algebra PACKage) libraries.

Implementation of DSST-OD is included with the following observation models to be able to process different data:

- Radar observations: range, azimuth, and elevation (without atmospheric, station coordinate, and light time corrections)
- Optical observations: right ascension and declination
- GNSS observations: position and velocities in terrestrial reference frame
- State vectors: position and velocities in inertial celestial reference frame

Implementation of Covariance Propagation

To support the later part of the studies regarding uncertainty propagation, two covariance propagation routines which are based on the EKF and the UKF techniques are implemented. Making use of the semi-analytical partial derivative matrices covariances are propagated either in forward or backward in time as a EKF method. This method has the same computational advantages as the DSST-OD and follows the STM computation flow as in DSST-OD. The covariance propagator is capable of propagating uncertainties in position and velocity vectors, mean and osculating Keplerian elements, and mean and osculating equinoctial elements. This allowed to perform the covariance consistency tests in different element spaces for comparing their linearity regimes.

Multiple orbit propagations are employed to propagate sigma points, as described in UKF section 3.3.2. This method requires multiple initialisation of the propagator and is less computationally efficient than EKF method. Detailed analysis and comparison of both covariance propagation methods are carried out in chapter 7.

The following chapter presents detailed examination of DSST's performance in modelling orbits, predicting orbits, and determining orbits.

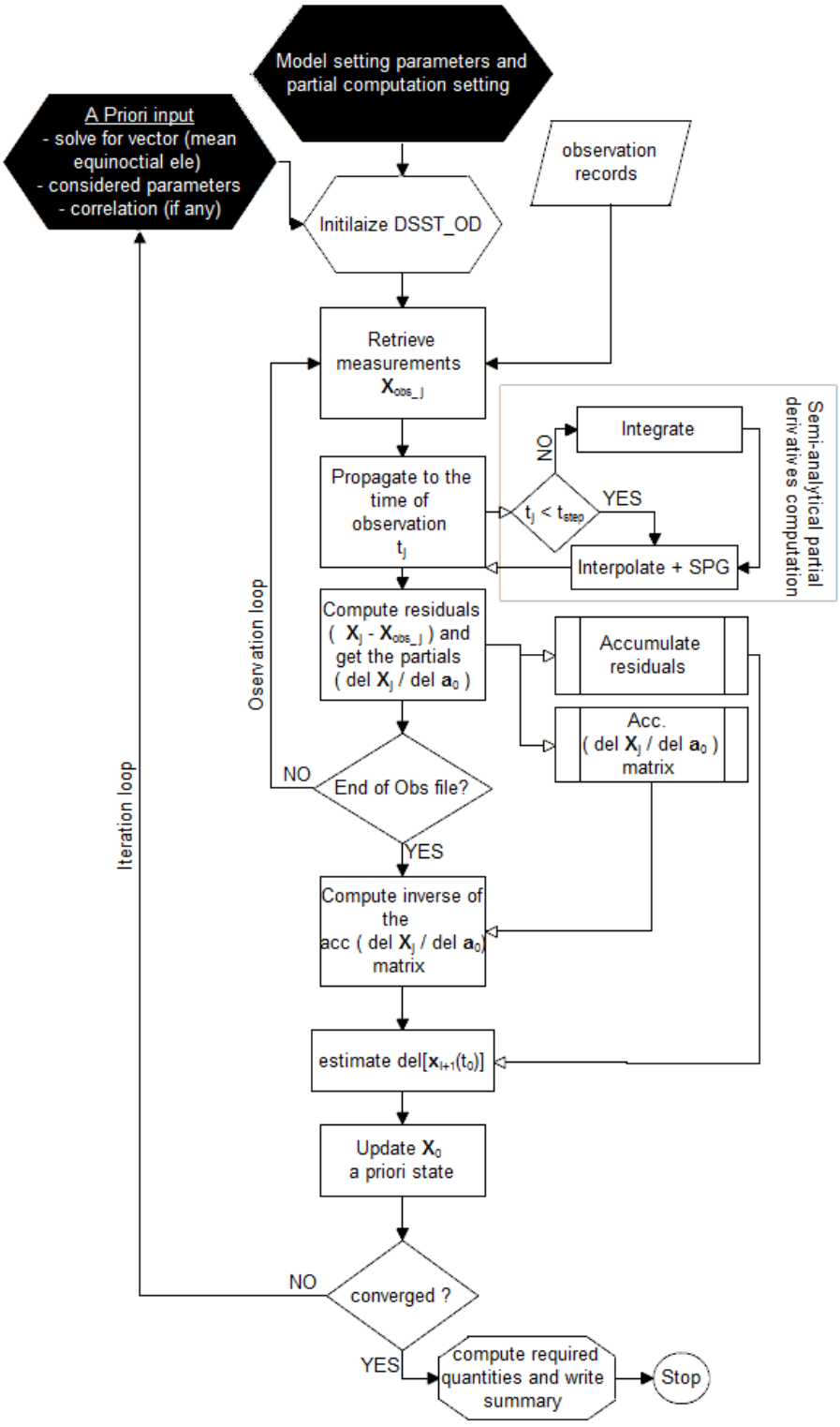

Fig. 4.10 Flowchart for the orbit determination routine in standalone DSST

CHAPTER 5

EVALUATING ORBIT PROPAGATION AND ORBIT DETERMINATION

The interlinked nature of the astrodynamics tools and techniques makes it hard to evaluate the performance of an orbital theory. The primary components within the SO cataloguing system are a set of measurements, an orbit determination routine, and an orbit propagator. Quantifying the performances, the accuracies, for each component is constrained by the links attached between them. The lack of a true representation of orbits make the quantification of orbital models more challenging. Although a true orbit does exist, it generally remains unknown. This is because of the inherent errors within the generated measurements or observations. Together, there are limitations in modelling the forces acting on the satellites. Orbits estimated using noisy observations will be the closest representation of the modelled orbit, rather than a true orbit. Figure 5.1 shows an overview of high level chain of components within a cataloguing system together with the leading factors affecting the performances of the main components.

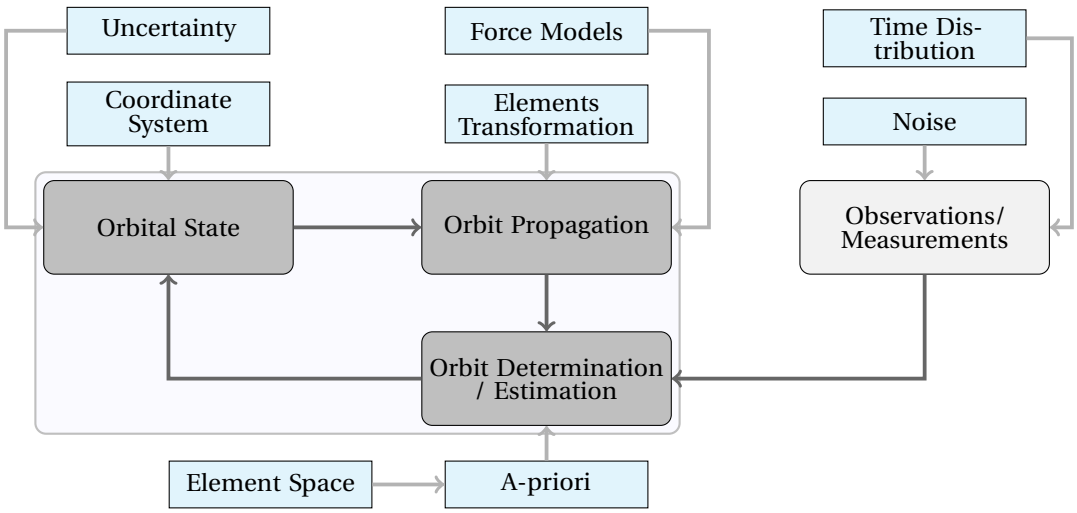

Fig. 5.1 Process flow within the astrodynamical problem. Blue blocks represents the factors influencing the performance of the main components in grey blocks. The outer grey box encompasses the strongly coupled components.

Irrespective of the theory used within the orbit propagation segment of the catalogue maintenance system, the accuracy of measurements flowing into the catalogue will remain decoupled from the satellite theory's accuracy. Making use of this characteristic, the selected semi-analytical theory is evaluated for its performance by comparing it to a numerical theory. Assuming that a numerical theory, together with a set of high fidelity force models, will provide

the most accurate representation of a true orbit, the evaluation of the selected theory is carried out. This comparison is also consistent with one of the main objective of the thesis, that is to suggest an alternative satellite theory to a numerical propagation technique. Hence evaluating DSST against a SP technique will provide its relative performance in propagating an orbit.

Satellite theories are the modelled representation of orbits. Comparing two orbital theories against each other is the task of understanding how well can one theory represent the other. As it can be seen in Figure 5.1 OD and OP are coupled and other factors such as: force models used within the propagator, element representation/coordinate system in which orbits are represented, and state space in which orbits are compared, will all influence the comparison results. To obtain the absolute accuracy from the propagation testing all the above factors are to be addressed.

On the other hand, the absolute accuracy of an orbit propagator is fundamentally limited by inaccurate models of the orbital dynamics. The other well-known error sources are truncation errors in the satellite theory, computational round-off errors, model simplification approximations, and errors associated with the implementation. These factors make it hard to test the absolute accuracy of any OP or OD method in a completely decoupled fashion. Especially, when one orbital theory is evaluated for its performance against another orbital theory.

All of the above mentioned factors involved within the propagation method and the comparison task are addressed with the intention to evaluate the theory for its applicability in a cataloguing system. Thorough testing will also facilitate in understanding the different sources of uncertainties within the propagated states and quantifying the magnitude of these uncertainties will assist in estimating realistic covariances. The final goal is to quantify the performance of the DSST in comparison to the SP method within ODEM. To achieve the same, the first step is to ensure that coordinate system, reference frame, and force models implemented within the two propagators are either identical. If not identical, it is required to quantify how similar they are. The second step is to ensure the epoch state representations used to initialise both the propagators are identically.

This chapter presents the systematic empirical evaluation of the selected theory, considering different factors shown in Figure 5.1. The first section 5.1 presents the employed testing methodology. In section 5.2, test cases for evaluating the influences of force models on propagation accuracies are presented. The results from section 5.2 are used to optimize the propagator settings for achieving the best possible prediction accuracy while reducing the computational efforts. Section 5.3 will discuss the results from orbit fit accuracy and orbit prediction accuracy tests. The orbit determination routine presented in section 4.4 is tested with both simulated and real data, results of which are discussed in section 5.4. To evaluate the computational loads, section 5.5 discusses the computational run-time comparisons between the two propagation and determination methods. At the end of the chapter, the results are summarized while presenting the overall performance of DSST in comparison to a numerical propagator.

5.1 Testing Methodology

For the purpose of SO catalogue maintenance system, an orbital theory must be tested for three major functions: orbit representation, orbit prediction/ propagation, and orbit

determination. The applicability of the DSST within the SO catalogue maintenance system is tested in the form of:

Orbit fit comparisons: This comparison is intended to reveal the modelling characteristics of an orbital theory. One orbit propagator is used to generate equally spaced observations within a certain arc, and another orbital theory is used to make an orbital fit using least squares estimation. The resulting residuals from the best possible fit reveals the frequencies due to missing or truncated force models, which are eventually contributing to the estimation of model induced errors. Understanding the magnitude of errors and their time dependencies facilitates realistic covariance estimation.

Orbit prediction tests: After estimating the best fit of the two orbital theories, the estimated epoch elements are propagated into future/past times to compare the differences between the two theories. These tests will contribute in the estimation of propagator induced uncertainties.

Testing orbit determination routine: If the selected theory is making use of complete force models within the estimation of partial derivatives, this step would be redundant to the fit comparisons. But, within the DSST-OD (presented in section 4.4) it is chosen to make use of selected force models and their analytical partial derivatives. Hence, it is important to check the established OD routine and computed partial derivative matrices are sufficient in estimating the epoch mean elements.

Results from the first and the second test methods are presented in section 5.3, and results from testing the DSST-OD routine is presented in section 5.4.

The schematic representation of fit and prediction test methods are depicted in Figure 5.2. If 'A' and 'B' are hypothetical orbit propagators, then the propagator 'A' is used to generate true states for the time length T for an assumed imaginary satellite. Later propagation method 'B' is used to get the best fit possible for the generated orbital arcs. The RMS of the fit residuals are used as metric to state the level of agreement between the two theories for the considered orbit of an imaginary satellite. This method of testing will remove the initial state uncertainties which are used to represent the same orbit by two different theories.

For catalogue maintenance it is important to get the understanding of the orbital theory's behaviour in all orbital regimes. A grid of imaginary satellites was chosen in the element space comprising of orbital shape parameters $[a, e, i]$. Figure 5.3 shows the assumed grid points in different orbital regions, and Table 5.1 gives the step size and range of evaluated orbital regimes. Variations in the selected three orbital elements $[a, e, i]$ should capture analytical averaging effects on forces acting on the satellites' remaining three angular elements $[\Omega, \omega, M]$. In the evaluated $[a, e, i]$ grid space 1776 imaginary satellites are included to compare the performance of orbit prediction and determination routines.

Sections 5.3 and 5.4 employs the following test methodology. For testing DSST for its propagator capabilities: DSST is set as theory 'A' and the ODEM's Cowell integrator as theory 'B'. To standardize the OD and prediction time spans, and keeping the objective of SOs catalogue maintenance system, an update interval of seven days was selected as the length for both fit and prediction intervals. The arc length of seven days was chosen by considering the present debris scenario together with the observation capabilities which are discussed in chapter 2.

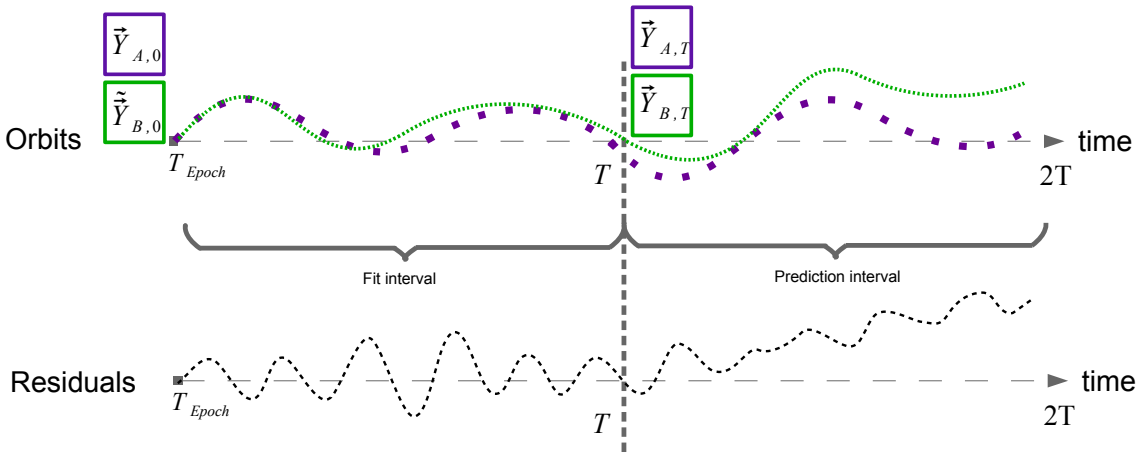

Fig. 5.2 Schematic diagram for orbit fit and orbit prediction comparisons for two different orbital theories 'A' and 'B'. Vectors with tilde represent the best orbital fit state vector for the theory 'B'

Table 5.1 Range and grid sizes of semi-major axis, eccentricity and inclination in LEO, MEO, HEO and GEO regions used within the testing of OP and OD

Orbit parameter		LEO		MEO		HEO		GEO	
		range	grid	range	grid	range	grid	range	grid
Semi-major (a)	[10^3km]	6.6 - 8.8	0.1	8.8 - 37	1	20 - 37	1	37 - 44.5	0.5
Eccentricity (e)	–	0.01	-	0.01	-	0 - 0.9	0.05	0 - 0.2	0.1
Inclination (i)	[deg]	0-90	5	0-90	5	60	-	0-90	5

The propagation performance of DSST was evaluated as following: for each satellite on the grid DSST generates a seven day orbital arc. This orbit is used as observation and an OD is performed using ODEM to estimate the epoch state osculating elements[1]. At each of the output time steps, the predicted orbit was compared to the reference orbit by calculating position and velocity residuals. This process was repeated for all the grid points. The OD solved for all six orbital elements and a model parameter depending on the altitude. The drag coefficient, C_D, was estimated for LEO satellites and the direct solar radiation pressure coefficient, C_R, was estimated for MEO and GEO satellites. For HEO satellites both C_D and C_R were adjusted. DSST was used with the settings specified in the Table 5.8 to generate reference orbits. A standard spacecraft area of 1m^2 and mass of 100 kg were used throughout the test cases. In addition, for the generation of reference orbits $C_D = 2.2$ and $C_R = 1.2$ were taken as surface characteristics of each imaginary spacecraft. From the simulations the data comprising the epoch and the end times, the estimated epoch elements, the orbital arc with 60 seconds spaced ephemerides, the OD fit outputs, and the CPU running times were saved for further analysis. Flowchart in the Figure 5.4 shows the test methodology employed for carrying out the simulation runs.

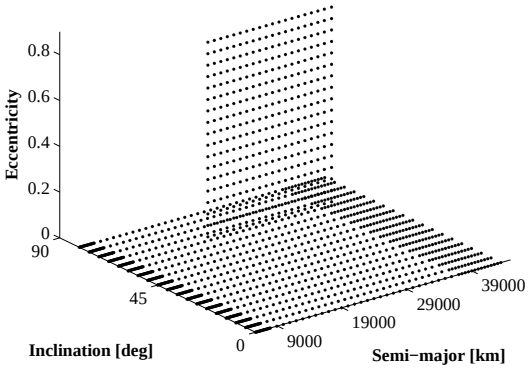

Fig. 5.3 Schematic representation of the assumed grid of imaginary satellites

Since DSST offers many different configurations for setting the force models, it is important to address the non-trivial task of selecting the optimal propagator input settings. To include the right set of averaged orbit and short-periodic motion generators to achieve the best possible prediction accuracy, the next section is dedicated for understanding the influence of different perturbation forces. The best possible accuracy with the least computational effort can be identified by assessing the magnitude of propagation inaccuracies induced by individual perturbing forces. To eliminate the effects of factors presented in figure 5.1 and to have pure DSST versus ODEM comparison, both propagators were aligned for the coordinate system, reference frame in which comparison is carried out, and force models used. The task of alignment is carried out on a test satellite together effects of perturbing forces are tested.

ODEM makes use of an osculating element set to initialize the propagator, whereas the DSST makes use of a mean element set for its initialization. This brings us to the non-trivial problem of estimating the $\bar{\boldsymbol{Y}}_0$ (mean element set) which corresponds to the $\boldsymbol{Y}_0$ (osculating element set) at epoch. To achieve this, a DSST trajectory ($\boldsymbol{Y}^{DSST}$) is generated using an initial condition $\bar{\boldsymbol{Y}}_0$. Then ODEM is used to fit a numerical trajectory to the generated DSST trajectory to estimate $\boldsymbol{Y}_0$ at the epoch. The outputs of both propagators were set to generate state vectors in the mean of J2000 reference frame. Both propagators used $M \times N$ geopotential terms. The estimated $\boldsymbol{Y}_0$ is assumed to give the best representation of $\bar{\boldsymbol{Y}}_0$ at the epoch.

For the purpose of propagator alignment, and further individual test cases, a representative satellite, Proba-V, is considered. The selection of this test satellite was influenced by PROBA-V's representative altitude, near circular eccentricity, and sun-synchronous inclina-

[1]The observation set is osculating position and velocity vectors, in terrestrial reference frame, at equally spaced time intervals. The weighting matrix within the OD routine assumes identity matrix.

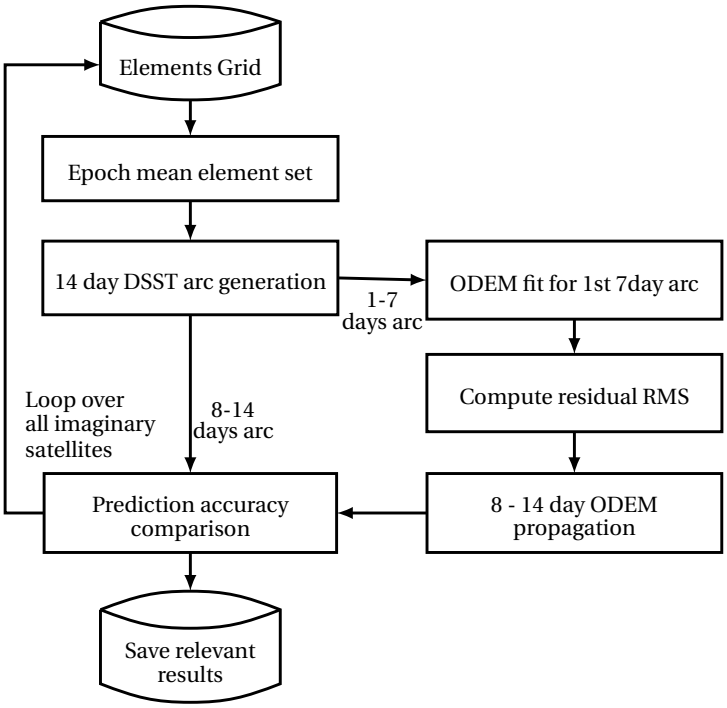

Fig. 5.4 Flowchart showing the test methodology for fit accuracy and prediction accuracy comparisons between DSST and ODEM

tion, for a large number of satellites and debris objects. It has a 98° inclination (retrograde orbit) and an altitude which admits effects from both drag and solar radiation pressure. Table 5.2 provides the epoch state mean Keplerian elements and the corresponding osculating elements.

Table 5.2 Assumed mean element set and equivalent osculating element set at Epoch 01-Jan-2014, 00:00:00.00. The same epoch state mean elements are used for all the individual test cases mentioned other wise

Keplerian Elements	Mean elements	Osculating elements
Semi-major [km]	7191.3512	7187.3041
Eccentricity[10^{-3}]	3.5885	1.1395
Inclination [deg]	98.7945	98.7936
Right Ascension [deg]	82.6675	82.6658
Arg. Perigee [deg]	132.3427	132.3454
Mean anomaly [deg]	286.4490	286.4508

Once the osculating and mean epoch elements are established, ephemerides were generated using both propagators over N days arc to generate n equally spaced observations. The estimated osculating and assumed mean element sets are provided in Table 5.2. The outputs ($\boldsymbol{Y}_i^{DSST}$ and $\boldsymbol{Y}_i^{ODEM}$) were then compared in terms of Root Mean Square (RMS) values of their position differences, as given in Equation 5.1 below.

$$\mathrm{RMS}_{pos} = \sqrt{\frac{\sum_{i=1}^{n}\left(\boldsymbol{Y}_{pos,i}^{DSST} - \boldsymbol{Y}_{pos,i}^{ODEM}\right)^2}{n}} \tag{5.1}$$

Before performing the grid based testing, the following section presents the individual test cases which are used to understand the influence of perturbing forces and at the same time align the force models used within ODEM and DSST.

5.2 Influence of Perturbing Models on Propagation Accuracy

Effects from conservative perturbing forces are analysed individually to evaluate the effects on orbit prediction accuracy. While preparing two orbit propagators to be compared against each other in section 5.3.

Influence of degree and order of Geo-potential model on propagation accuracy

Generally, non-spherical perturbations are represented in terms of deviation from two-body symmetry in terms of latitude [ϕ] (zonal harmonics), longitude [λ] (sectorial harmonics), and combination of ϕ and λ (tesseral harmonics). The potential function is represented using spherical harmonics as in the below Equation 5.2 (Montenbruck and Gill, 2001)

$$\psi = \frac{\mu}{r}\left[\sum_{m=0}^{\infty}\sum_{n=0}^{m}\left(\frac{R_e}{r}\right)P_{n,m}(\sin\phi)(C_{n,m}\cos(m\lambda)+S_{n,m}\sin(m\lambda))\right] \tag{5.2}$$

where μ is the gravitational constant, R_e and r are the radius of the Earth and the orbiting object respectively, $P_{n,m}$ is the associated Legendre polynomial, and [$C_{n,m}$, $S_{n,m}$] are the spherical harmonic coefficients. The subscripts n and m are the degree and order of the geopotential expansions. Depending on the values of n and m, the potentials are classified as in Table 5.3

Table 5.3 Harmonics conditions from degree and order of the potential function

Zonal harmonics	Sectorial harmonics	Tesseral harmonics
$m = 0$	$n = m$ $m \neq 0$	$n \neq m$ $m \neq 0$

One can select either 'square' ($m = n$) or 'non-square' ($n < m$) potential terms. Studies from Vallado (2005) and Sharifi and Seif (2011) have shown that the truncation in zonal harmonics has more impact on the prediction accuracy than truncation of the sectoral and tesseral harmonics.

Comparing geopotential terms within DSST

The influence of individual spherical harmonic coefficients on the prediction accuracy is tested by comparing the orbits generated with different geopotential degree and order. A reference orbit is generated using DSST with 50×50 geopotential terms. This reference orbit is compared with an orbit generated using $m \times n$ geopotential terms ($2 \leq n \leq 50$ and $2 \leq n \leq m$). Seven days orbital arcs are compared against each and the position root mean square values are computed.

Figure 5.5 shows the range of position errors, for seven day propagation arc, while truncating the sectorial and tesseral terms for PROBA-V for the prediction arc of seven days. From the plot it is seen that the exclusion of lower degree ($m \leq 4$) geopotential terms influences

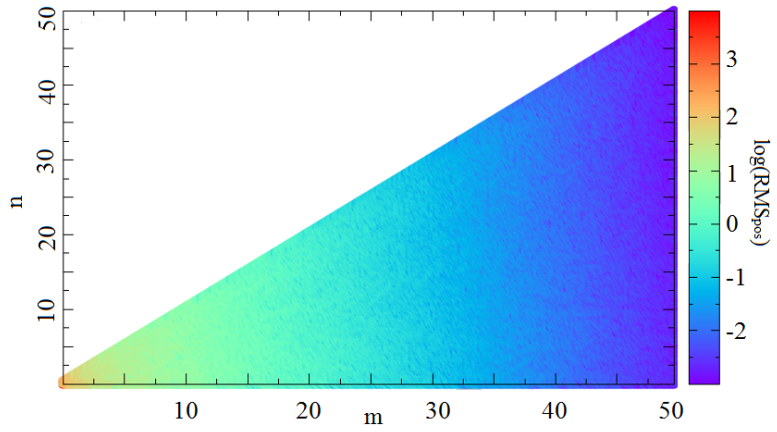

Fig. 5.5 Prediction error induced on the PROBA-V satellite due to truncation in specific degree and order of the spherical harmonics

the propgation accuracy in the order of thousand kilometres for the assumed propagation arc length. The geopotential terms beyond 28 × 28 has sub-metre level influence on the prediction accuracies. From similar simulations for a MEO satellite, it was observed that the influence of higher geopotential terms beyond 8 × 8 affects the prediction accuracy on the order of centimetre. This experiment provided an intuition for estimating the number of geopotential terms to be included within the propagator. For SO catalogue maintenance system, the requirement of 50 metres in position RMS, can be achieved neglecting the higher order spherical harmonics.

Comparing geopotential terms within DSST against ODEM

Two different sets of experiments were designed. The first set was to ascertain the level of agreement between DSST and ODEM. The second set is to compare where the truncation errors within the DSST overrides the geopotential errors. The GGM01S gravity model Tapley et al. (2003) was used in both propagators, and tests were carried out on the PROBA-V test satellite.

Table 5.4 presents the formulated test cases together with the comparison results between ODEM propagation and DSST propagation with geopotential terms only.

The magnitude of RMSpos provided insight into differences in force modeling. Initial results pin-pointed a deviation in physical constants, which were then aligned to the same values. These comparisons indicated that the two propagation programs, DSST and ODEM, agree to 15 meters level for the seven day prediction. In DSST, columns of geopotential terms were used during the propagation as explained in Case 4 of Table 5.4, this is the main source of deviation from ODEM while propagating with 50×50 gravity model.

To compare where the truncation errors within the DSST overrides the geopotential errors, an assumed precise orbit is generated using ODEM is compared against varying 'square' potential terms in DSST. Currently, the ODEM offers to include geopotential model up to 120×120 and the DSST can use up to 50×50 Fonte (1993).

In the following experiment, the test satellite PROBA-V's epoch conditions are propagated to generate the position and velocity ephemerides for the arc of seven days. The DSST is used to generate a reference trajectory with $m \times m$ geopotential terms, while keeping all the other perturbation forces turned off. The short-periodic generator was set to achieve the best possible accuracy in the recovery of osculating elements from mean elements. The orbit

Table 5.4 Test cases for comparing the force models within DSST and the ODEM numerical propagator

Test Case	Geo-potential [m× n]	RMS_{pos} [m]	Comments
CASE 1	2×0	0.88	Demonstrates compatibility between ODEM and DSST of the numerical integration and coordinate systems required for J_2 potential
CASE 2	2×2	3.16	Demonstrates compatibility for the 2x2 potential. This case requires modeling the rotation of the Earth.
CASE 3	8×8	6.82	Demonstrates compatibility for the 8x8 potential. This case requires the rotation of the Earth and also demonstrates the recursions for the geo potential.
CASE 4	50×50	11.08	Demonstrates compatibility for the 50x50 potential terms. For the considered 14.2 rev/day orbit, and it is reasonable to expect shallow resonance effects which are captured. Tesseral resonance terms included are (14,14) through (50,14) and (28,28) through (50,28)

was then fitted with the numerical orbit, generated using ODEM, which was initialised with 50×50 geopotential terms and all the other perturbations turned off. The final fit residual in terms of RMS_{pos} is then compared for each values of $m \times m$ ($m = \{2,3,4,...,50\}$) for DSST.

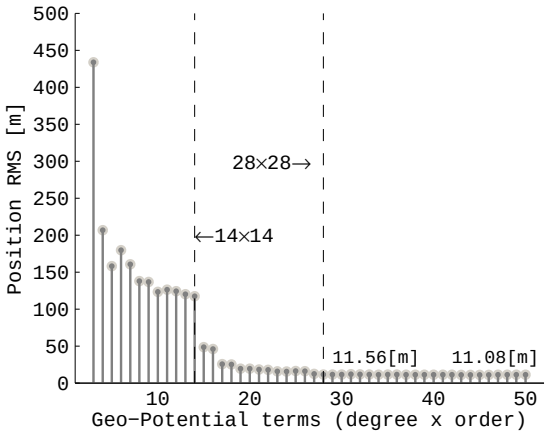

Fig. 5.6 DSST-OD fit accuracy to numerically generated data with different geopotential terms

Figure 5.6 shows the residuals from the fit in terms of RMS_{pos} to DSST generated observations. The plot shows a jump at 14×14, and further change in the accuracy after 28×28 shows almost constant behaviour with increase in geopotential terms inclusion. A shallow resonance effect on a satellite with approximately 14 revolutions per day was driving the accuracy of the propagation. Even if one increases the degree and the order of geopotential terms beyond this point, the RMS_{pos} remained within certain bound, and no drastic improvements were observed. This showed that the second and third resonant harmonic effects were smaller than the DSST's truncation errors. Therefore, as a rule of thumb, in order to capture all the resonant terms one has to include geopotential terms up to a degree and an order of $2 \times n$ [rev/day].

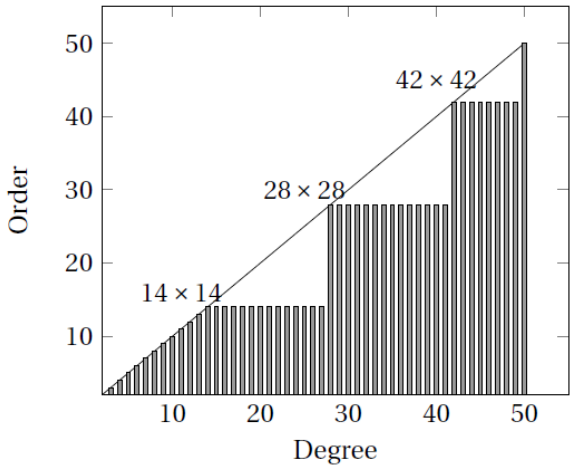

Fig. 5.7 Geo-potential harmonics - degree and order. Area under the diagonal line presents the coefficients included in ODEM and the vertical bars present the coefficients included in DSST while propagating an orbit with 14 revolutions per day.

On the other hand, it is important to understand how to include the sectorial and tesseral terms within the equations of motions to discern the truncation errors within DSST. In ODEM when the propagation is initialised with $m \times n$ geopotential terms, it includes all the coefficients within the considered range. That is, if one initialises ODEM with 50×50 terms, it includes all 1275 coefficients to evaluate Equation 5.2. On the other hand, DSST includes only the selected columns of geopotential terms Green (1979) as depicted in Figure 5.7. In PROBA-V example with 14 rev/day, DSST included all the terms up to 14×14, terms between 28 through 50, and 42 though 50 geopotential terms. In summary, DSST encompassed 1029 terms rather than all the 1275 terms within the 50×50 model. This selection of coefficient inclusion gives the DSST an added advantage of reducing its computational burden, but comes with the cost of reduced prediction accuracy. Although, the savings from the evaluation of ~ 200 coefficients might not contribute towards overall computational efforts, the overall SO catalogue maintenance system will have considerable effects when performing a few hundred thousand propagations per day. The reduced accuracy is well within the set limits for the purpose of catalogue maintenance, and it is considered as an advantage rather than a limitation.

Influence of third body models on propagation accuracy

The influence of third body accelerations are felt on the satellites in all Earth bound orbital regions. From the Figure 3.2 in chapter 3, it can be observed that the effects of third body perturbations are more dominant in MEO and GEO regions than in LEO orbits.

In LEO, drag acceleration is more dominating for the spacecraft orbiting below ~ 550 km. In GEO regions, the magnitude of the perturbing acceleration due to 2×2 ($J_{2,2}$) aspherical gravity terms are a few orders greater than the magnitude of the accelerations from subsequent geopotential terms in GEO regime. The same can be observed in figure 5.8, which is a snippet from figure 3.2. Also, it can be observed that the third body accelerations, from the Sun and the moon, are of the same magnitude as 2×0 (J_2) term. Similar to previous test cases, ODEM generated orbits were compared against DSST orbits. Below is the list of six different test cases

description, and Table 5.5 shows the position RMS for the comparison runs. A geostationary satellite with semi-major axis at 41,165 km and near circular eccentricity at zero inclination is considered for all the test cases.

Test 1 Keplerian orbit

Test 2 J_2, without higher order zonal terms and without solar and lunar perturbations

Test 3 8×8, without solar and lunar perturbations

Test 4 $8 \times 8 + J_2^2$, without solar and lunar perturbations

Test 5 $8 \times 8 + J_2^2$, and with solar and lunar perturbation as time-independent formulation

Test 6 $8 \times 8 + J_2^2$, and with solar and lunar perturbations as weak-time-dependent formulation

Table 5.5 Position RMS of DSST for GEO orbits with different short-periodic effects

	Test 1	Test 2	Test 3	Test 4	Test 5	Test 6
RMS_{pos}	1455.7 m	944.0 m	582.66 m	433.10 m	102.8 m	1.99 m

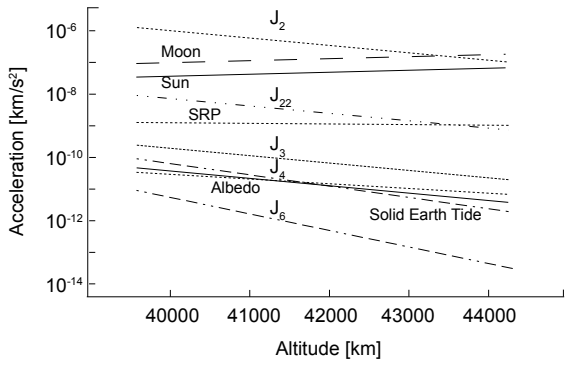

Fig. 5.8 Magnitude of different perturbing accelerations in GEO altitudes

It is clearly seen that the inclusion of geopotential model terms has a significant effect on the accurate prediction of a GEO satellite. Also, as shown in the previous chapter 4.3, the importance of including the time dependent formulation of third body perturbations on the accuracy of the high altitude objects (in MEO and GEO) is obvious from comparing RMS_{pos} of Test 5 and Test 6.

The limitation of the present test methodology is that, the propagators, ODEM and DSST, both included point mass approximations using Newcomb and JPL planetary ephemeris. This is not demonstrating the long term evolution of the differences. But for the purpose of SOs cataloguing, where the assumed propagation time lengths are in the order of days, the test cases and results can be assumed to be sufficient.

Drawing the inference from above test cases, one can say that it is important to include the perturbing forces as in Test 6 for the purpose of using DSST within a catalogue maintenance system.

Similar to the test cases presented in table 5.4 for PROBA-V satellite, CASE 5 was extended to include third body, Sun and moon, accelerations were included together with the 50×50 geopotential terms. Table 5.6 summarizes the test case.

The position RMS for the seven day orbit arc comparison shows $\text{RMS}_{pos} = 11.57$m. This demonstrated that the DSST standalone was able to propagate with higher order terms and include the third body perturbations without discrepancies for a LEO.

Table 5.6 Test cases for comparing the force models within DSST and the ODEM numerical propagator

Test case	Force Models	RMS_{pos} [m]	Comments
CASE 5	50×50 geopotential terms + Sun + Moon	11.57	Demonstrates ability to propagate with higher order terms and third body perturbation.

Influence of solid Earth tides and non-conservative forces

The solid Earth tides are mainly caused by the redistribution of the mass of the earth due to luni-solar gravitational pull. The perturbation is modelled by a second degree zonal harmonics which lags the Earth-Sun and Earth-Moon direction by a certain angle. The test case which included the solid Earth tide effect along with the geo terms and third body perturbations shows the RMS_{pos} to be 11.75m, confirming the propagators are aligned for all the conservative perturbation effects. Comparing the RMS_{pos} with and without solid Earth tides, the difference is found to be 0.18 m.

Table 5.7 Test cases for comparing the force models within DSST and the ODEM numerical propagator

Test case	Force Models	RMS_{pos} [m]	Comments
CASE 6	50×50 geopotential terms + Sun + Moon + solid Earth tides	11.75	Demonstrates the compatibility of all conservative forces – geopotential, solid Earth tide and third body (sun andmoon) in LEO orbit.
CASE 7	50×50 geopotential terms + Sun + Moon + solid Earth tides + Drag	14.30	The residuals derive from the method of averaging employed within DSST for modelling atmospheric drag.
CASE 8	50×50 geopotential terms + Sun + Moon + solid Earth tides + Drag + SRP	14.35	Demonstrates the ability to include solar radiation pressure with the other force models.

Finally, non-conservative effects such as drag due to upper atmospheric density and solar radiation pressure (SRP) were tested and aligned.

Atmospheric forces represent the strongest non-conservative perturbations action on LEO satellites and HEO satellites with perigee heights lower than ~ 600 km. Accurate modelling of aerodynamic forces is difficult because of the low accuracy of predictions of the atmospheric density, spacecraft and atmospheric particle interaction, and varying attitude of non-spherical satellites with respect to the atmospheric molecular flux. The magnitude of the force is directly proportional to the surface area to mass ratio of the SO. The surface interactions are captured via the coefficient of drag (C_D). In circular orbits the effect of atmospheric drag is directly observed on the secular decrease of semi-major axis, while on eccentric orbits the major effect is observed on the circularistaion of the orbits. King-Hele (1987) presents the effect of atmospheric drag on orbits in detail. Uncertainties in non-conservative forces are time varying and cannot be approximated in the same way as uncertainties in conservative forces for the purpose of realistic covariance estimation. Uncertainties in acceleration due to drag is further investigated in detail in chapter 6.

The direct solar radiation pressure depends on the optical properties of the satellite surface together with the surface area to mass ratio of the satellite. The surface characteristics are captured within the parameter C_R, reflectivity coefficient of the spacecraft. The SRP causes periodic variations in all of the orbital elements. The other form of radiation pressure experienced from the orbiting SOs is due to the radiation emitted by the Earth (albedo forces). The typical magnitude of the albedo acceleration for LEO SO is 5 – 25% of the acceleration due to SRP. For the catalogue maintenance system this force is neglected to reduce the computational burden.

The comparison results for orbits including drag and SRP are observed to be RMS_{pos} = 14.30m and 14.35m respectively. Both propagators used Jacchia-Gill upper atmospheric density models to compute the atmospheric densities; both propagators approximate the effect using a cylindrical shadow model and spherical spacecraft model. Table 5.7 summarises the results for the above test cases.

The averaging effect and short-periodic modelling approximations within DSST are responsible for the existing error. The implementation and other approximation errors were either smaller than the other truncation errors or seemed not to affect the propagation accuracy.

5.2.1 Input model selection for optimal DSST propagation

After estimating the inaccuracies induced from different perturbing forces, and understanding the achievable accuracy in propagation with different perturbation forces modelled in a semi-analytical way, the information is used to set the propagator with proper initialising conditions. A recommendation for the initial setup file (PMEF file described in Appendix A which allows the user to configure for DSST) is presented in table 5.8. Using these settings, further investigations on propagation and prediction accuracies are carried out.

Table 5.8 DSST standalone settings ('Y' included, 'N' not included, '-' not available). AOG: Average Orbit Generator for propagating the mean elements, and SPG: Short Periodic Generator for retrieving the osculating elements.

Parameter	LEO setting		MEO setting		HEO setting		GEO setting	
	AOG	SPG	AOG	SPG	AOG	SPG	AOG	SPG
Zonal	Y	Y	Y	Y	Y	Y	Y	Y
Tesseral harmonics (8 X 8)	Y	Y	Y	Y	Y	Y	Y	N
J_2^2 terms	Y	Y	Y	N	Y	N	Y	N
M-Daily terms	-	Y	-	Y	-	Y	-	N
J_2 M-Daily coupling term	-	Y	-	N	-	Y	-	N
Third body	Y	N	Y	Y	Y	Y	Y	Y
Atmospheric drag	Y	-	N	-	Y	-	N	-
Solar radiation pressure	Y	-	Y	-	Y	-	Y	-

5.3 Results from Orbit Propagation Tests

Following the methodology presented in section 5.1 and the scheme presented in Figure 5.4 the orbit fit comparison and prediction comparisons are carried out.

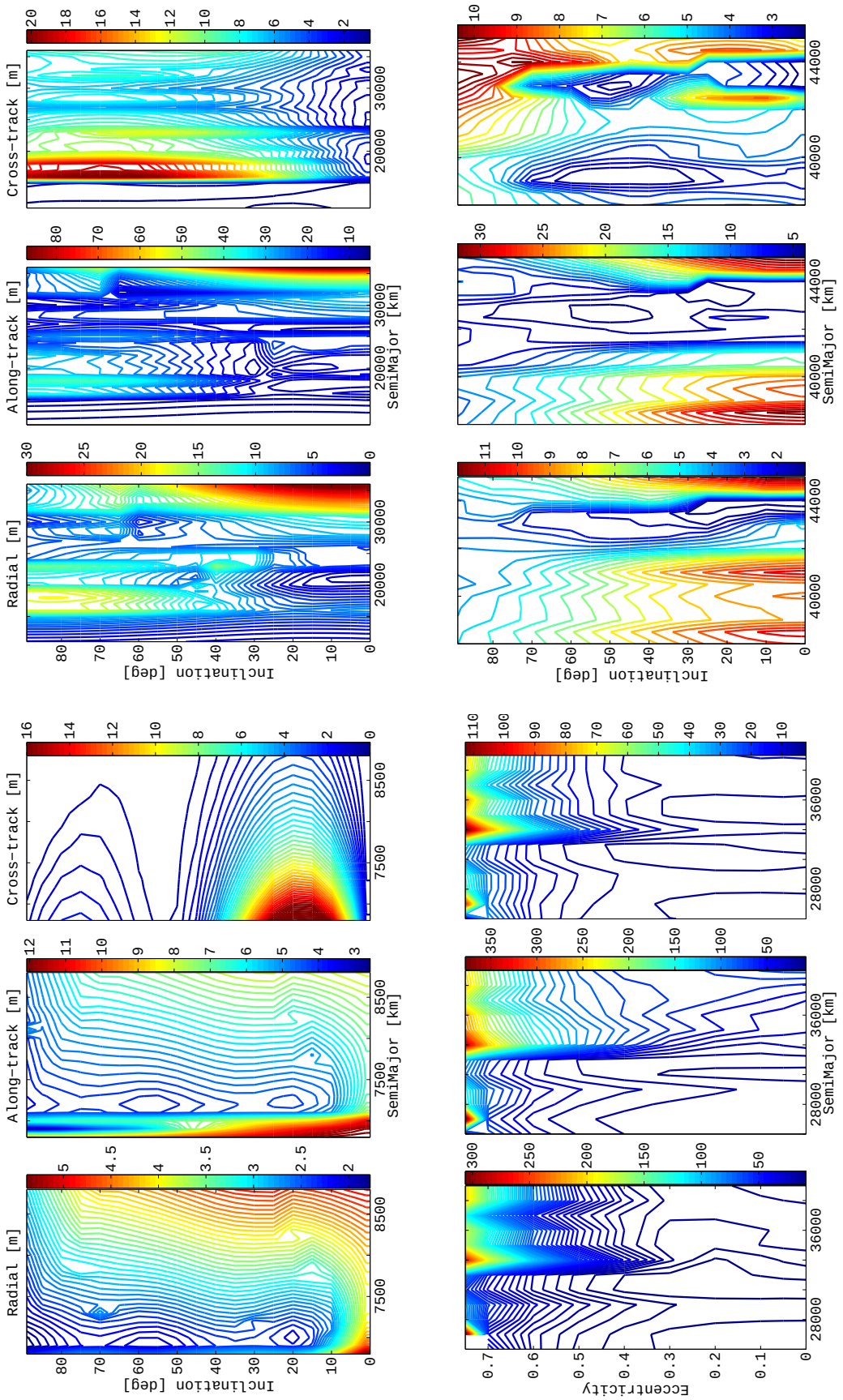

Fig. 5.9 Numerical fit accuracy with DSST generated orbit in LEO (top left), MEO (top right), HEO (bottom left), and GEO region (bottom right). All the simulations used $\Omega = 30^\circ$, $\omega = 30^\circ$ and $M = 0^\circ$ with varying semi-major axis, inclination, and eccentricity (refer Table 5.1 for the grid description).

5.3.1 Orbit Fit Comparison

Plots in Figure 5.9 show the RMS residuals from orbit fits in the R-T-N directions. In total, over 200,000 orbit fits and predictions were performed to asses the DSST's performance. From the plots for the LEO region within Figure 5.9 there are observable variations between semi-major axis and radial direction, and inclination and cross-track direction residuals.

When the drag is considered in the AOG (to generate averaged motion within DSST), sixth order Gaussian quadrature is used to evaluate the drag terms in the equation of motions. Due to this, the semi-analytical method suffered a bit to capture the fast variations of densities at lower altitudes. The sixth order Gaussian quadrature uses 13^{th} degree (2n-1, where n is the order of quadrature) polynomial to represent the density function. The detailed examination of density variations during the analysis period showed that the polynomial used within the numerical quadrature is not sufficient to capture the existing variations at lower altitudes. Figure 5.10 shows the differences between the density variations and the approximated polynomial at different altitudes. Although both scenarios have two orders of magnitude differences, the magnitude of difference at 6500 km is four orders higher than the difference at 7200km. Due to this reason, higher position RMS values in radial and along-track directions at semi-major axes lower than 6700 km are observed.

In the LEO region the results presented show the RMS values while including Izsak's height correction terms Green (1979) and analytical drag-J_2 effects. Without the height correction terms, the drag induced error in radial direction was observed to raise up to 1200 m for seven days of orbit propagation.

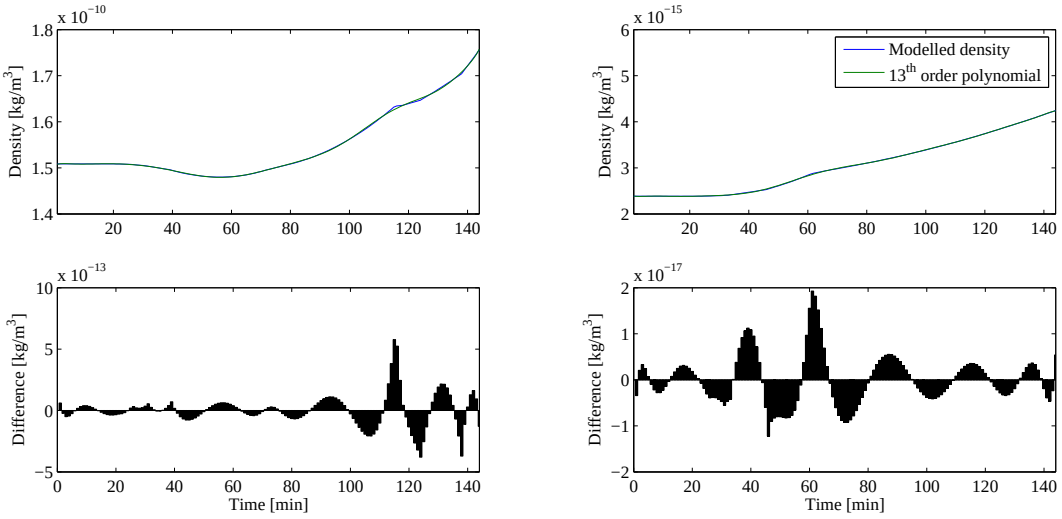

Fig. 5.10 Differences between Jacchia-Gill modelled density and the 13^{th} degree polynomial for the satellite with semi-major axis at 6550 km (right plot) and 7200 km (left plot), with near circular eccentricity of 0.02.

In cross-track component the errors increase between $i = 5°$ and $35°$. To analyse the direct link between inclination and reduction in propagation accuracy, additional simulations were carried out using individual perturbing forces. From the test results it was observed that by evaluating higher order SPG equations for J_2 m-daily coupling terms, the magnitude of errors decreased. The description of the coupling term is discussed in equation 4.17 of section 4.3. Increasing the order of J_2 M-daily tesseral coupling term eventually contribute towards the

increase in computational runtime of DSST. A trade off was made with accuracy such that, the propagation accuracy is within the set limit for SO catalogue maintenance (50m pos, 10m radial; refer Table 2.6), and computational times are kept low.

For the MEO region, the propagator performed better than the set requirement. The deviations between DSST in comparison to ODEM are large at higher altitudes. This is due to third body perturbations, and the optimization used to truncate the WTD terms for MEO satellites. When the degree of series expansion used for WTD terms were increased for GEO satellites the errors were reduced significantly. Since the the requirement for the catalogue maintenance permits to be liberal on the accuracy of propagated orbits, that is to be within the specified requirements, it was decided to keep the optimized settings for MEO space objects. Orbits with an orbital period greater than one day have reduced accuracy in comparison to the rest of the GEO regime.

In HEO the largest error is appearing in the highly eccentric orbits at lower altitudes. This is due to the very low perigee height and consequently the increased atmospheric drag effects. The present derivation of the WTD corrections in mean longitudes employs partial derivatives of the Fourier coefficients in the eccentric longitude expansion for the time independent short periodic motion (details presented in Section 4.3). This assumption holds good for the MEO and GEO regions, but shows decreasing accuracy in the HEO region.

The overall RMSs from the ODEM least squares fits in the different orbital regimes are summarized in Table 5.9. The values show that DSST propagates orbits within the limits of the defined requirements for SSA tasks mentioned Section 2.5.

Table 5.9 DSST propagation accuracy in different orbital regimes in comparison to numerical propagator. The RMS of RMSs are computed for each region to provide distribution of errors in R-T-N directions.

Orbital class	Radial [m]	Along-track [m]	Cross-track [m]	RMS (Position RMS) [m]
LEO	3.54	7.11	4.92	9.35
MEO	9.87	20.45	7.95	24.06
HEO	15.84	71.10	18.95	75.26
GEO	6.56	15.81	5.80	18.07

5.3.2 Orbit Prediction Testing

In the previous subsection the test results from the fit accuracy of the DSST in comparison to ODEM is presented. The emphasis is given on the prediction accuracy of the DSST in comparison to numerically integrated orbits. The method for testing follows the diagram 5.4 and the steps are as follows:

1. A reference trajectory is generated using DSST propagator for seven plus N number of days.

2. ODEM is used to estimated epoch state elements for the first seven days' reference trajectory.

3. Estimated osculating elements are then propagated using the numerical integrator with high-fidelity force models.

4. The propagated ephemerides are compared against the reference ephemeris for N number of days.

5. Position differences are computed to be used as comparison metrics.

Figure 5.11 shows the radial, tangential, and normal direction differences for the fit length and the orbit degradation for the prediction length. For illustrative example cases, two different objects orbiting at different altitudes of 6700 km and 7800 km with inclinations of 5° and 85° respectively are considered.

It can be observed that the tangential direction degrades in a secular fashion along with the prediction time, and the radial and the normal directions have oscillations with increasing amplitudes with time. The sample satellite at 6700 km semi-major axis, in plots 5.11 show faster degradation of accuracy in tangential direction. The effect observed is mainly due to the higher drag perturbations. In addition to the higher drag effect, DSST and ODEM includes the acceleration due to drag in a different way during propagation. Within DSST the perturbing acceleration due to drag are captured through numerical quadratures. While the method reduces the burden on the propagator to estimate the drag acceleration at every time step, it approximates the drag accelerations by smoothing over the considered large integration time steps. It is observed in fit-accuracy test cases that the method is suitable for propagating SO in orbits with semi-major axes greater than 6700 km and with near circular eccentricities. The errors induced due to the smoothing of non-conservative accelerations are prominent at lower altitudes.

The bottom plots of Figure 5.11, for higher LEO with a semi-major axis at 7800 km and near polar inclination show different signatures in the fit and propagation residuals. The truncation in geopotential models might be the reason for observing periodic effects on the axis of orbital momentum. Also, for the inclination of 85 degrees the solar radiation pressure will have drag and lift effects. Which could be the reason for dominating once per orbit superimposed with the twice per day frequencies are observed in tangential direction.

It is difficult to characterize the orbit prediction errors as a single quantity for the entire orbital regime, mainly due to its altitude and inclination dependencies. To summarize, the positions at hourly steps were computed and visualized. Figure 5.12 shows the position differences of DSST against numerical orbits for different prediction lengths and at increasing altitudes, for a polar orbit inclination. These tests provide the insight on the degradation of orbits while propagating the mean element sets. Intuitively, the position accuracy is lower and degrades faster at the semi-major axis below 6900 km due to higher drag perturbations in lower altitudes.

Prediction accuracies in LEO region were below 50 m position metric for the orbits with semi-major axis greater than 6900 km. For the orbits which are below 6900 km (experiencing higher densities) the prediction accuracies were greater than a kilometre after one day of propagation. Similar tests performed in MEO and GEO regions showed that the position differences remained below 15 metres for the prediction lengths of up to 21 days.

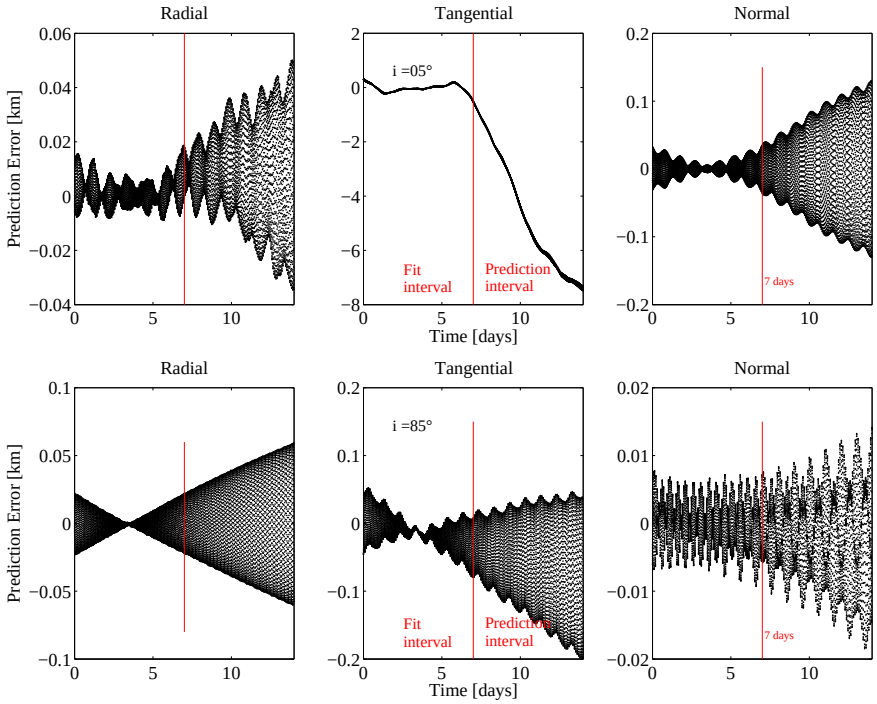

Fig. 5.11 Residual plots, in RTN coordinate frame, of DSST orbits compared with ODEM orbits. Top plots: a = 6700 km, e=0.001, i= 5°; bottom plots: a=7800 km, e=0.001, i=85°. After the separating red line the plots show the RTN position degradation from DSST in comparison with ODEM during the prediction arc.

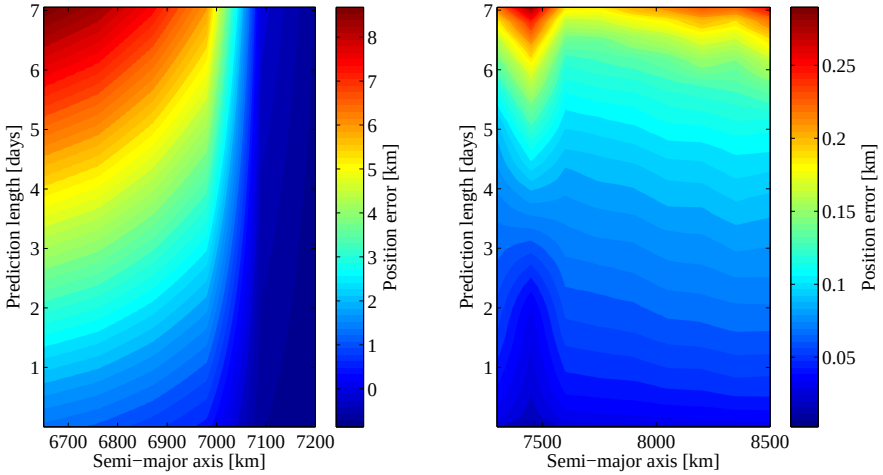

Fig. 5.12 Position differences at each epoch between DSST and Cowell orbits at different altitudes and prediction lengths in LEO regime

5.4 Testing Orbit Determination Routine

In the previous section DSST was used as a propagator and ODEM is used to fit to the DSST generated trajectories. In the present section, the implementation of DSST-OD, a batch least squares program which uses DSST for orbit modeling and estimates epoch mean elements, is tested extensively for its performance. The evaluation was carried out using simulated data and a set of high accuracy GPS observations from PROBA-V. The simulated data was used to test the best accuracy achievable at ideal conditions in all orbital regimes, and the real data, under both continuous and sparse conditions, were used to test DSST-OD's capability to process different cataloguing scenarios.

Similar to the testing of DSST as a propagator in previous section, DSST-OD was also tested on an imaginary grid of satellites. Here, ODEM is used as a propagator to generate equally spaced observations for an imaginary satellite on a grid point presented in Table 5.1. These ephemerides are then fit using DSST-OD batch least squares program. Plots in Figure 5.13 give an overview of the RMS of the residuals from semi-analytical BLSQ orbital fits.

Theoretically, fitting ODEM to DSST generated observations and the fitting DSST to ODEM generated observations with the same models and partial derivative matrices should give identical results. That is to say we should have identical patterns and order of magnitude for the R-T-N residuals. However, there are differences in patterns observed between Figures 5.9 and 5.13. This is due to the differences in the solve-for parameters, estimated epoch state elements, in ODEM and DSST-OD. In ODEM the least squares program estimates osculating state vectors and uses the respective partial derivatives matrices $\left(\frac{\partial \boldsymbol{X}}{\partial \boldsymbol{Y}_0}\right)$, where $\boldsymbol{X}$ is the observation vector and $\boldsymbol{Y}_0$ is the osculating epoch state vector). On the other hand, DSST-OD estimates epoch mean equinoctial elements using $\left(\frac{\partial \boldsymbol{X}}{\partial \bar{\boldsymbol{\epsilon}}_0}\right)$ partial derivative matrices. The two manifolds which are used in ODEM and DSST-OD will be identical only if there are no truncations within the averaging method employed. Due to this effect of different manifolds which direct the convergence of least squares fit, the R-T-N components do not have the same values between DSST-OD and ODEM OD. Rather it is observed that both produced similar pattern and order of magnitude in the fit residuals.

The presented simulation test cases showed that DSST-OD, which makes use of semi-analytical J_2 partial derivative matrices, is capable of processing orbital data in different regimes. During the simulations it was also observed that, DSST-OD converged with a smaller number of iterations than that of the ODEM OD.

The convergence is dependent on the type of observations processed, type of epoch elements estimated, and a-priori elements used to initialize the least squares orbit determination program. During the simulation tests equally spaced position and velocity state vectors, in terrestrial reference frame, are used as observations for both DSST-OD and ODEM OD. But the major difference is in a-priori element space and the estimated elements. An illustrative example case comparing the RMS values at different iteration steps are presented in Table 5.10.

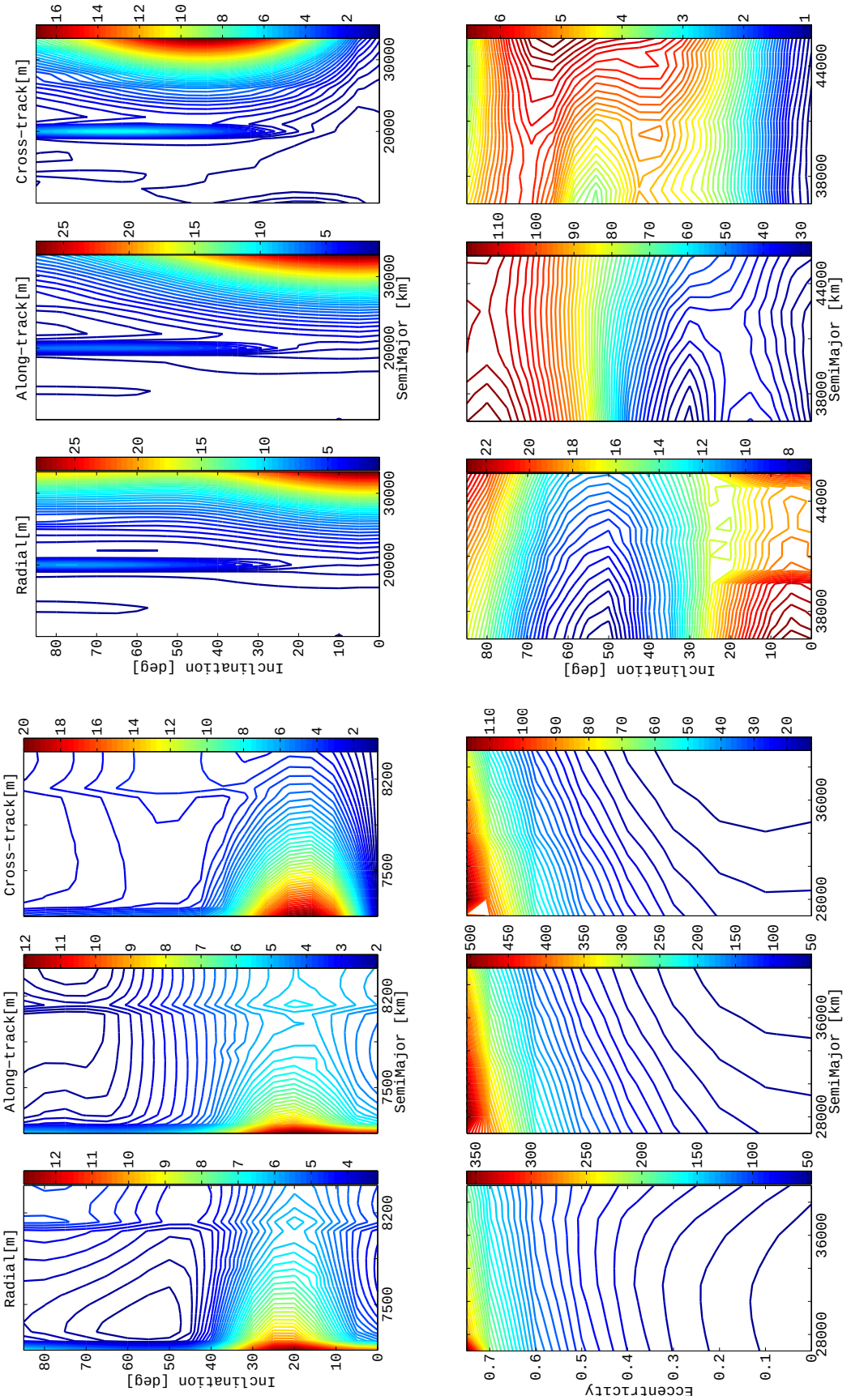

Fig. 5.13 DSST fit accuracy with numerically generated orbit in LEO (top left), MEO (top right), HEO (bottom left), and GEO region (bottom right). All the simulations used $\Omega = 30^\circ$, $\omega = 30^\circ$ and $M = 0^\circ$ with varying semi-major axis, inclination, and eccentricity (refer Table 5.1 for the grid description).

Table 5.10 Batch least square estimator performance when estimating epoch elements in different coordinate systems on the PROBA-V test case

Coordinate type	Initial RMS [m]	Iteration 2 RMS [m]	No. of iterations	Converged RMS [m]
Osculating Cartesian elements	25350	14200	7	9.13
Mean Equinoctial elements	25350	593	4	9.13

It is observed that while estimating the mean element sets, the differences between the updated orbits are two orders of magnitude better than while estimating the osculating elements set. The advantage comes from the fact that the mean elements behave as a linear oscillators, reducing the non-linear dynamics within the modelled system. This provides a better estimate at each iteration. The factor appends the usability of DSST as a satellite theory for the purpose of a SO catalogue maintenance system.

Testing Mean Element Estimator with Real Data

Testing DSST-OD with trajectories generated from ODEM for the SOs on the assumed grid points showcase the correctness of its implementation, and validate the estimation capabilities using semi-analytical partial derivatives. The test methodology assists in understanding the influence of semi-analytical modelling versus numerical modelling. Employing the same force models does not reveal the modelling capabilities in real world scenarios. For example, both OP and OD methods made use of Jacchia-Gill density models for computing the accelerations due to drag and SRP was computed using equivalent radiation pressure models. Test cases under this condition revealed the propagator induced errors, but do not provide the actual information on real world orbit modelling abilities. Real observations are the backbone of SO catalogue maintenance system. To demonstrate the DSST's capability to represent real orbit and DSST-OD's capability to process real observations, dedicated test cases are presented in the following.

Keeping the consistency in the selection of a test satellite, PROBA-V observation data is chosen. PROBA-V carries GPS receivers on-board, for its attitude control and autonomous navigation functions (Mellab et al., 2011). A subset of the observations dating between January 1 - 8, 2014 are used for the present analysis. The observations within the orbit determination routine are used in the form of position vectors in inertial geocentric reference frame. The position vectors for the spacecraft are derived using the combination of code and carrier-phase measurements from the GPS receivers.

DSST-OD and ODEM used 36×36 geopotential terms, Jacchia-Gill atmospheric density model, third body point-masses, and cylindrical shadow model. Respective six orbital elements and the drag coefficient are estimated during the orbit determination runs.

Figure 5.14 shows the DSST fit residuals in radial, tangential and normal directions. The Figure presents fit residuals from the below three observation sets:

- "cont. obs" - continuous data of GPS observations for the span of seven days with one minute interval (7721 observations)
- "sparse obs 1" - sparse data set includes 450 observations over the seven day arc which are observed once per revolution, and

- "sparse obs 2" - sparse data set includes 150 observations which are observed from the same station on uneven intervals over the span of seven days.

These data sets were designed to mirror the SSA-type tracking conditions. That is five to ten minutes of tracking per orbit, and repeatability is not homogeneous which might be due to observability conditions. The fit statistics for these cases are presented in Table 5.11 in comparison with ODEM fits.

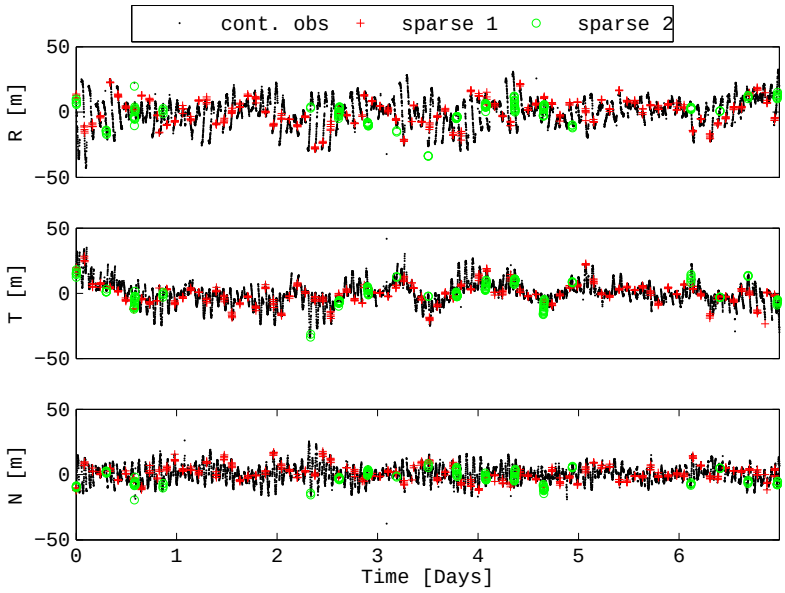

Fig. 5.14 R-T-N fit residuals from DSST-OD to PROBA-V's GPS observations. The observation epoch starts at 00:00:30, Jan 1. 2014. Figure shows fit residuals for both orbit determination with continuous data (7721 obs), sparse 1 data (450 obs), and with sparse 2 data (150 obs)

The GPS navigation solution for the observation arc has 3.5 m position RMS errors which affect the actual orbit. The RMS error of approximately 7 m in ODEM fit includes other factors which are influencing the performance of ODEM. To verify the same, we performed the orbit determination with the full fidelity model available in ODEM, namely the 120×120 geopotential terms, and this did not affect the end result significantly. To test the influence of drag, we considered a data set from a different time interval during which the geo-magnetic indices were smoother. For the new data set, the ODEM fit RMS was reduced to approximately 5 m. A plausible association of the discrepancy in the ODEM fit was made to the atmospheric drag model. Mainly the short term variations in the atmospheric density are responsible for these errors.

The association of errors to short periodic density fluctuations is derived from the theoretical understanding of the Jacchia density model. Here the model makes use of solar flux values which are separated by 3 hours, and it interpolates the data between two actual F10.7 data points. On the other hand, it is shown that upper atmospheric densities fluctuate on the order of minutes to hours; semi-empirical density models often do not capture these abrupt changes (Lechtenberg et al., 2013). From the above understanding the 5m error in ODEM orbit determination run is associated to the limitation of the density model to capture short-term variations in the environment.

Table 5.11 DSST and ODEM orbit determination statistics for PROBA-V GPS observations

Obs type		Radial [m]	Along-track [m]	Cross-track [m]	Position RMS [m]
DSST-OD					
cont. obs	RMS	10.83	8.79	6.20	15.26
	Mean	0.03	0.12	0.55	
sparse obs 1	RMS	10.22	8.17	6.08	14.43
	Mean	0.25	-0.36	1.11	
sparse obs 2	RMS	8.69	8.70	7.44	13.79
	Mean	-0.36	-0.09	-3.12	
ODEM					
cont. obs	RMS	2.59	6.92	1.56	7.79
	Mean	1.77	0.01	0.79	
sparse obs 1	RMS	2.76	6.44	1.58	7.62
	Mean	1.86	0.08	0.25	
sparse obs 2	RMS	2.46	7.01	1.23	7.53
	Mean	1.91	0.08	0.93	

For DSST-OD the residuals are larger, differentiating between measurement (GPS) and model induced errors is difficult. But, from the OD statistics one could say that the performance of DSST-OD is within the limits of SSA applications and the performance is two orders in magnitude better than that of the SGP4 method. SGP4 has the fit accuracy for the same orbit in the order of 10^3 m. The accuracy of the NORAD catalogue and SGP4 is discussed by Aida and Kirschner (2013).

On the other hand, estimation of the right set of mean elements from the observations which are representatives of osculating elements depends on the available observation points where mean elements model will be fitted. To have a proper estimation of mean elements it requires one of the two criteria.

1. To have observations which are evenly distributed over a complete averaging period, that is one orbital revolution. (or)

2. To have accurate short periodic recovery to perform mean to osculating element transformations.

In the present SO cataloguing scenario it is not possible to obtain evenly distributed observations for one complete orbit. Hence DSST must be able to perform accurate mean to osculating element transformations. The above test cases check this criteria for DSST.

In the above test cases, the estimated epoch mean elements are not significantly influenced by sparse data sets. Even though the estimated parameters deviate slightly from zero-mean residuals, as seen in Table 5.11, the final orbits are very close to each other. This statement holds true for the considered three test cases. The estimated mean element sets using three different observation data were propagated for the arc length of seven days and the osculating positions and velocities were compared. This comparison showed that the position deviation from each other were in the range of 50 m position RMS. To infer from the above tests, we could say that the unevenly distributed observation sets did not significantly influence the estimation of mean elements. Here, it is assumed that several tracks of

observations are available for a SO for the catalogue maintenance system. If a single or a few short arc observations are used within DSST-OD, the estimated mean orbital elements suffer significantly from truncations in the short-periodic models.

5.5 Computational Runtime Comparisons

To justify the selection of SST for catalogue maintenance purposes, computational run-times are compared between DSST and ODEM for both OP and OD scenarios.

Figure 5.15 shows the CPU usage times in different scenarios. To evaluate general possible combinations of propagator settings, three different comparisons were conducted. The first, was to compare the load against the propagation arc length. The second test set was to compare different degree and order of geo-potential terms used in propagation. The last test set was to compare computational load when the outputs were requested at different step-sizes. For an objective comparison, both propagators were implemented in FORTRAN and compiled with the IFORT compiler. Testing was carried out on a Open-Suse Linux machine with an i5 processor and 4GB RAM.

Similar time comparisons were conducted for a single geostationary satellite, where the propagators used settings from Table 5.8 to include third body perturbations (WTD terms) and exclude drag forces and m-daily coupling terms. From the simulations, it is observed that ODEM took 0.76 seconds when generating outputs at every 100 s interval for the span of seven days, and DSST took 0.24 seconds for the same.

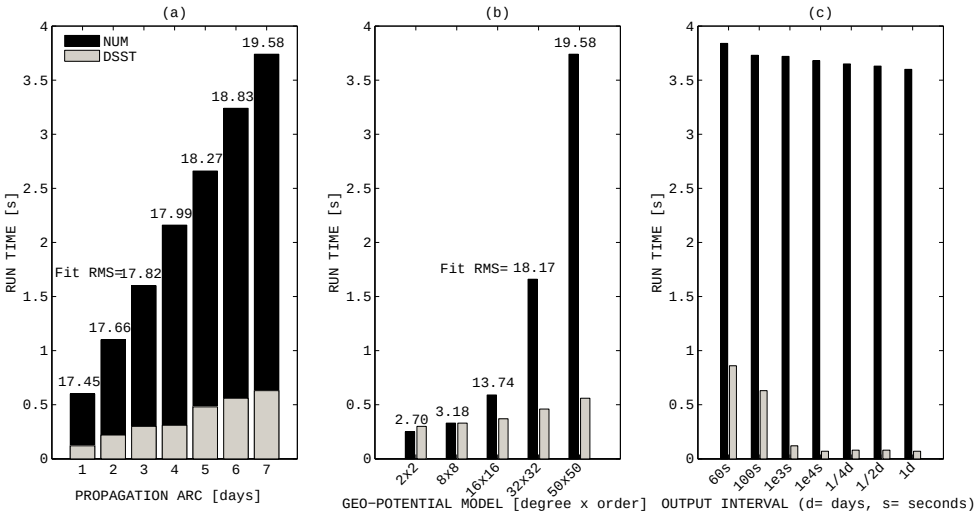

Fig. 5.15 (a) Computational runtime comparison, on PROBA-V test case, between the numerical and DSST propagator for different propagation arc-lengths, with output requested at one minute intervals and using 50×50 geopotential terms. (b) Runtimes for propagators with different geopotential terms and orbits predicted for a seven day time interval. (c) Runtimes for the duration of seven days when the outputs were requested at different time steps with 50×50 geopotential terms.

Comparisons on PROBA-V test case showed that DSST offers approximately an 80% savings in runtime against numerical propagation when using full force models (50 × 50 geo potential terms, third bodies, atmospheric drag and solar radiation pressure). The same is

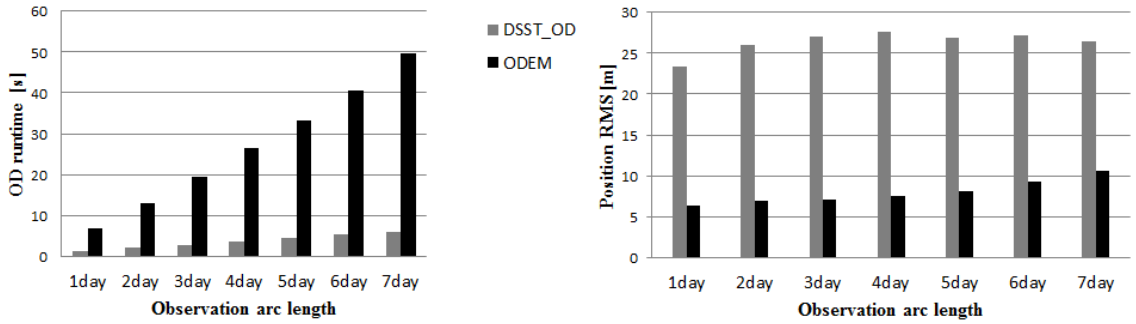

Fig. 5.16 a) Orbit determination programs' CPU time for fitting the orbit for PROBA-V GPS observations for increasing number of days. b) OD performance comparison in terms of position RMS after fitting the orbit over different observation arcs. Both DSST-OD and ODEM used 50×50 geo-potential models, along with the third body perturbations.

observed in the Figure 5.15a, where the numbers on top of the bar indicate the difference in DSST propagation with the SP. Figure 5.15b shows the comparison of computation times when using different geo-potential terms. From the plot it is clear that the initialization cost from DSST pays off only when including geo-potential terms higher than 8×8. The last Figure 5.15c shows the influence of observation steps on propagation runtime. The numerical method consumes almost same amount of CPU time to propagate the orbit over seven days, irrespective of number of outputs requested. On the contrary, DSST's CPU time decreased by two orders of magnitude when outputs were requested every 60 seconds and one day intervals. The difference is mainly from the size of integration step sizes between the numerical method and DSST.

Figure 5.16a shows the computation runtimes for orbit determination procedures. GPS observations of the PROBA-V satellite for the arc of seven days were used in OD. The fit qualities are compared in terms of position RMS, and presented in Figure 5.16b. The main contribution to the savings in computation time in DSST-OD results from the semi-analytical way of establishing partial derivative matrices at the observation time epochs.

Also, if one considers the SSA situation (sparse observation rather than continuous observations), it is more likely that one needs to bridge larger time intervals between observations. Then DSST offers higher percentage of savings in computation time in comparison to the SP method.

CHAPTER 6

ATMOSPHERIC DENSITY MODEL: UNCERTAINTY ESTIMATION

Orbital uncertainty or covariance plays an important role in both catalogue maintenance and applications of the SO catalogue. The implications of unrealistic uncertainties are discussed in section 3.3. Within the same discussion, Figure 3.5 presented the structure of the most plausible uncertainties which influence the accuracy of an orbit prediction. Uncertainties in propagated orbital states are due to: initial state uncertainties, force model uncertainties, and model specific simplifications or propagator uncertainty. Previously, chapter 5 established the propagator specific uncertainties, in comparison to an accurate numerical propagator. The source of initial orbit uncertainty lies in the method of estimation and errors within the observations. Generally, initial state errors are handled by employing non-linear uncertainty propagation techniques. The force model uncertainties are prominent and affect the accuracy of predicted states significantly. Analysing and quantifying model induced prediction errors are complicated problems, due to the diffusion of initial errors and coupling of model errors with them.

Model uncertainties are broadly classified into two different categories (Tardioli and Vasile, 2015):

- Random variability in the environment, which cannot be captured in a physical model, and
- Error due to lack of understanding in certain physical processes.

The classification is dependent on factors on which the modelling of the forces rely on, and how well one can capture the variations within the factors affecting the model. For example, modelling third body perturbations depends on knowing the mass of the body and the precise location with respect to the orbiting object. Physical and mathematical models are capable of estimating the mass and trajectories of the celestial bodies to an accuracy where the uncertainties induced from them can be neglected. In this particular example, periodic observations or dedicated experimental missions could increase the knowledge on third body models. Contrary to the above example, the goodness of a solar radiation pressure depends on the surface area and thermal property modelling capabilities. During the time of the present research, it is still not possible to predict the erratic behaviour on the surface of the Sun. This limitation, together with the randomness within the factors affecting the SRP, makes uncertainties within the predictions stochastic in nature.

In the case of conservative gravitational perturbations, the temporal variability is small. That is to say that the magnitude of spherical harmonic coefficients do not change quickly over time. With precise measurements, one can reduce the level of uncertainties from these

perturbations. In other words, one can reduce the uncertainty due to conservative models on orbit predictions by increasing the knowledge. Currently, the spherical harmonic coefficients are determined from a wide range of measurement techniques, dedicated satellite missions including surface gravity missions and satellite altimetery data (Poore et al., 2016). This increase in knowledge reduces the prediction uncertainty to the order of sub-meter position differences. Non-conservative perturbations such as atmospheric drag and solar radiation pressure are second in line, by magnitude, after the conservative forces. The temporal and spatial variations of such forces are far greater and influenced by factors which cannot be modelled yet in detail. The time variations of these forces depend on different factors such as geomagnetic fluctuations and solar flux variations. Hence these uncertainties can only be modelled as a random noise.

In the the current space environment scenario, ~ 80% of the man-made Earth orbiting objects reside in the LEO region. In LEO orbits, atmospheric drag is the most dominating non-conservative force, and at the same time it is the least accurate among all the modelled perturbations. This chapter addresses the problem of the uncertainty in atmospheric drag. A brief introduction to the atmospheric drag model and different parameters affecting the computation of acceleration due to drag is discussed in section 6.1. By reviewing the literature, which are presented in the following section, it has been established that the upper atmospheric density model is the main source of uncertainty in the drag computations. Hence, this chapter is dedicated to understanding and modelling the density induced uncertainty in orbit predictions. Section 6.2 provides a method for modelling the stochastic uncertainties within the density models. The established density noise model is employed within a set of stochastic differential equations to evaluate the uncertainty induced in propagated orbital states. Also, the established model is implemented to simulate the density noise for the purpose of testing later results. Within the same section, the derived closed form solution is presented. The established solution is quantified with an example test case which is discussed in section 6.3.The final section 6.4 presents a way to make use of the solution within a SO catalogue maintenance system is presented. Test results are discussed which compare the established analytical solution to the precise orbital data. In the end, the complete model can be used independently of the selected orbit propagator.

6.1 Atmospheric Drag Uncertainty

Atmospheric drag, $\boldsymbol{a}_d$ [m/s^2], is considered to be the dominating perturbation for satellites with perigee altitudes between 120 km to 600 km, and its effects are felt up to the altitudes of 2000 km (King-Hele, 1987). The acceleration due to atmospheric drag is modelled as

$$\boldsymbol{a}_d = -\frac{1}{2}\rho C_d \frac{A}{m}\frac{\boldsymbol{v_r}^3}{v_r} \tag{6.1}$$

where C_d is the coefficient of drag for a satellite with cross sectional area A [m^2] projected in the direction of velocity, and mass m[kg]. The relative velocity, $\boldsymbol{v}_r$ [m/s^2], of the satellite with respect to the atmosphere is the difference between the SO's velocity and the velocity of the upper atmosphere.

Equation 6.1 is the simplest description of accelerations due to atmospheric drag, commonly referred to as the cannon-ball model. Depending on the application and requirements,

the above model can be extended to more complex models which consider the attitude variations and the shape of the spacecraft.

From equation 6.1, one can identify three main error sources, which are further discussed below. The subcomponents of the error sources are also presented in Figure 6.1.

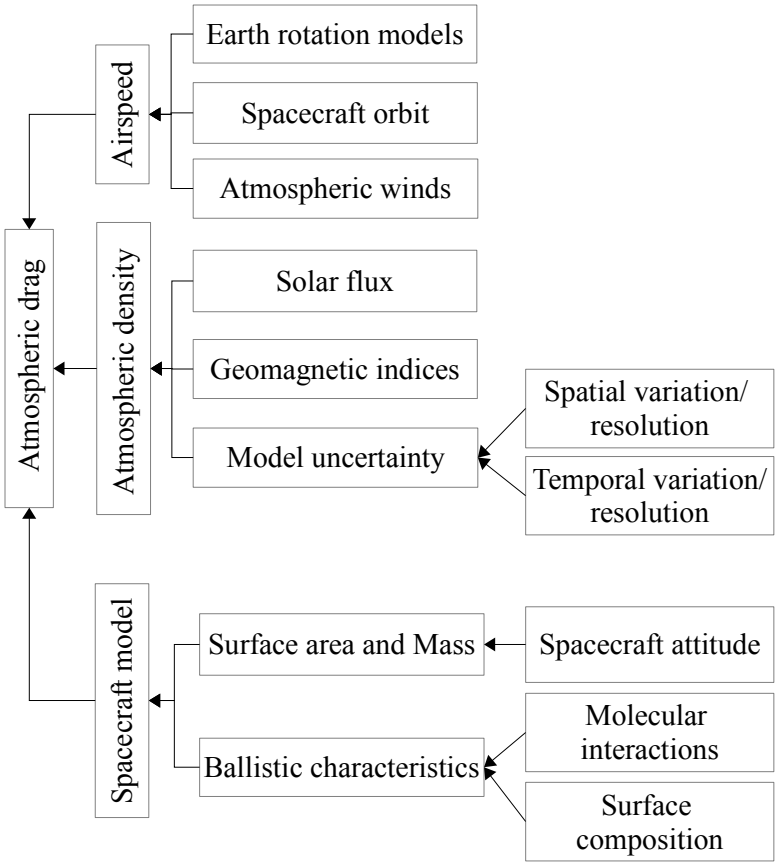

Fig. 6.1 Parameters which influence the modelling and estimation of atmospheric drag acceleration

Spacecraft model errors: These model related errors are due to quantities such as mass, surface area, and spacecraft shape and material. These spacecraft model errors are all dependent on the SO's physical characteristics. The mass, once estimated, is generally assumed constant. But thrusting and ablation can change this quantity. The cross sectional area is related to the configuration of the satellite or the attitude dynamics of the SO, and the variability of cross-sectional area is dependent on different factors such as shape, attitude stabilisation, etc. Although, the variability in A is estimated to go as high as a factor of ten, generally within a catalogue maintenance system a cannon ball model is used for approximating the drag accelerations with a constant cross-sectional area over time. The coefficient of drag, C_D, is related to the shape as well as the material. The dimensionless C_D quantity is hard to model and involves complex interactions between the air molecules and the SO (Gaposchkin, 1994). The quantity C_D varies depending on the composition of the atmosphere and external temperatures of the atmosphere. These variations are generally assumed to be constant over short propagation arcs. In the context of SO cataloguing, the short period of propagation is

the orbital arc lengths of a few days (less than seven days). The combination of A, m, and C_D is termed as the ballistic coefficient of the spacecraft, which is defined as

$$B_C \equiv C_d \frac{A}{m} \tag{6.2}$$

With the above definition, equation 6.1 is reduced to three multipliers (ρ, B_C, and $\boldsymbol{v_r}$). Uncertainty within any of these terms will have similar effect on the end computation of drag accelerations. Using this feature, the quantity B_C is generally used as a solve for parameter while estimating an orbit. That is any uncertainty within any of the model parameters will be assumed to be the error within B_C.

Density model errors: The thermospheric density variations are driven in large part by variations in solar ultraviolet irradiance (King-Hele, 1987). Other factors which influence the mass densities of the upper atmosphere are solar winds, waves from the lower atmosphere, fluctuations in the magnetosphere, etc. It is well understood and established that the density decreases exponentially with altitude with a scale height of 25 km to 75 km. But due to the above mentioned factors influencing the density variations, thermospheric density varies horizontally together with its vertical dependencies. Vallado and Finkleman (2008), Doornbos (2012a), Emmert (2015), and many other researchers have analysed the existing density models and mechanisms for establishing such physical models. $F_{10.7}$ and K_p or A_P proxy indices are used in most of the density models. $F_{10.7}$ is the solar irradiance value at 10.7 cm wavelength, and K_p or A_P values indicate the strength of the geo-magnetism. The use of proxies itself introduces an uncertainty into the modelled density. Several researchers have evaluated the accuracy of individual models by comparing the modelled density against available real observations (Lechtenberg et al., 2013; Vallado and Finkleman, 2008; Yurasov et al., 2005b). The upper atmospheric density is a function of position and time, that is $\rho = f(\boldsymbol{r}, t)$. Because of the spatial and temporal correlation of the density, formulating an uncertainty model for density errors is difficult (Wilkins and Alfriend, 2000). The above studies have also shown that the currently available density models are uncertain between 10% at low altitudes (< 200 km) to 70% at higher altitudes in LEO (> 600 km). The errors vary on a broad range of spatial and temporal scales. Most of these variations are not captured or could not be captured by the physical models.

Relative velocity errors: The relative velocity ($\boldsymbol{v}_r$) is the sum of SO velocity in its orbit ($\boldsymbol{v}_s$), velocity by the co-rotating atmosphere ($\boldsymbol{v}_e$), and velocity of the winds ($\boldsymbol{v}_w$)

$$\boldsymbol{v}_r = \boldsymbol{v}_s + \boldsymbol{v}_e + \boldsymbol{v}_w \tag{6.3}$$

The cross product between the Earth's angular rotation vector, $[0,\ 0,\ 0.7292115 \cdot 10^{-4}]\ \frac{\text{rad}}{s}$, and the satellite's orbital velocity provides the corotation velocity. The velocity relative to the atmosphere depends on the SO's orbit. That is, uncertainty within the computation of the corotation velocity mainly depends on the known initial state of the SO, whereas the Earth rotation models are quite well established and can be neglected for any uncertainty within it. There exist several high altitude wind models (HWM) which provide the zonal and meridonial wind speeds (Doornbos, 2012a). The models are based on gradient winds within a neutral density model, data collected from sounding rockets, and scatter radar data. Contributions from the wind models are much smaller

than the a-priori uncertainties. Considering the knowledge existing in computing these factors, for the present chapter the effects due to $\boldsymbol{v_r}$ are neglected, and assumed to be negligible. Magnitudes of the cross winds can be found within the work carried out by Doornbos (2012b).

After the brief investigation of different components of the drag model, and from the equation 6.1 it is seen that errors within C_D and ρ are the major uncertainty contributors. Several research works have been dedicated to characterise the behaviour of C_D. Vallado and Finkleman (2008) provide a list of literature relating to molecular interaction with the spacecraft's surface. Also, it is observed that the interactions are not completely random, rather deterministic in nature. The uncertainties within the upper atmospheric density models are stochastic in nature and can only be captured as a random variability in the environment. Influence of these random errors, in density models, on orbit predictions will be the main focus of the present research.

From a SOs catalogue's application point, estimating the probability of collision is where the accuracy of the covariance is important. This computation is generally carried out in the satellite centred, Radial (R), Tangential (T), and Normal (N) coordinate frame. Therefore it would be useful to understand the error propagation due to density fluctuations in the R-T-N reference frame.

The following section discusses modelling of density noise and incorporating the noisy model within the drag model. Later part of the section establishes the stochastic differential equations in relative orbital dynamics.

6.2 Propagation of Density Noise to Relative Orbital Motion

The main objective is to formulate a method to capture both the spatial and the temporal variations of the densities. Due to the time dependant orbital motion, the physical forces which are temporally correlated are also spatially correlated. This allows us to formulate the noise which is just correlated in time to capture the spatial disturbances too. Akella et al. (1998) have shown that the density perturbation can be modelled by a stationary Gauss-Markov stochastic process. Following this work Wilkins and Alfriend (2000) developed a density noise model which included zero mean white noise with constant covariance. Using the model, Wilkins and Alfriend made an effort to capture and propagate uncertainty due to density noise. They compared the established model against the B_C variations which are estimated using a sequential orbital filter. More recently, Emmert et al. (2017) represented density noise as a Brownian motion for propagating the orbital uncertainties. Emmert focused on propagation of density uncertainty to orbital mean motion and mean anomaly. A similar approach to model in upper atmospheric density is employed within this research, and the noise model for density is given by equation 6.5 as below:

$$\rho(\boldsymbol{r},t) = \rho_m(\boldsymbol{r},t) + \zeta_\rho(\boldsymbol{r},t) \tag{6.4}$$

$$\rho(\boldsymbol{r},t) = \rho_m(\boldsymbol{r},t)[1+\epsilon_\rho(t)] \tag{6.5}$$

where

$$\begin{aligned} \rho_m(\boldsymbol{r},t) &= \text{model estimated density} \\ \zeta_\rho(\boldsymbol{r},t) &= \text{deviation of true density from the modelled density} \\ \epsilon_\rho(t) &= \frac{\zeta_\rho(\boldsymbol{r},t)}{\rho_m(\boldsymbol{r},t)} = \text{relative density error} \end{aligned}$$

In Equation 6.4, $\zeta_\rho(\boldsymbol{r},t)$ is the quantity which captures the differences between the density model and the actual density. To represent the error relative to the modelled density, parameter $\epsilon_\rho(t)$ is defined as the ratio between the deviation and the actual density. The modelled densities are capable of capturing the attitude variations and density variations due to solar activities up to certain extent. Thus considering the relative error is a more relevant quantity to describe the uncertainties within the modelled densities. Also, it has previously been shown that the variances of relative errors are temporally more uniform than that of the total error (Emmert, 2015). The uniformity in the error statistics allows one to model the relative noise either as a white noise or as Brownian motion. In the present research, the relative error is treated as Brownian motion. Formally, white noise (W_t) is described as the derivative of Brownian motion (Lawler (2006); Pg: 33), which is given as

$$\begin{aligned} \epsilon_\rho(t,\tau) &\equiv \frac{1}{\tau}\int_0^t W_s ds \\ W_t &\equiv \tau\frac{\mathrm{d}\epsilon_\rho(t,\tau)}{\mathrm{d}t} \end{aligned} \tag{6.6}$$

where τ is the characteristic timescale of a given system, and W_t is the uncorrelated white noise with below properties:

$$\begin{aligned} E\{W_t\} &= 0 \\ E\{(W_t - E\{W_t\})^2\} &= \sigma_\rho^2 \text{ ; is constant over time} \end{aligned} \tag{6.7}$$

where σ_ρ^2 is the variance of the relative density error (ϵ_ρ).

Yurasov et al. (2005a,b) present an elaborate study on estimating the fluctuations between the actual atmospheric density and a chosen atmospheric density model. Using the TLE of active satellites and debris objects, the study presents the time series for the density corrections for GOST and NRLMSISE-00 density models. The analysis involved SOs from different altitudes, which shows the altitude and time variations of the models. Within the results it is shown that the altitude variations of the density model errors have a linear trend from 6% at 150 km altitude to 26% at 650 km altitude. This number considers different solar activity periods and seasonal variations, but does not consider a complete 11 year solar cycle. For simulation purposes the variance of the relative errors is set to 15%. That is the relative noise errors (ϵ_ρ) are generated with one sigma value of 0.15.

Using equation 6.5 in 6.1 together with the definition of B_C, the acceleration due to drag is rewritten in its stochastic form as

$$\begin{aligned} \boldsymbol{a}_d &= \frac{B_C}{2}\left[\rho_m(\boldsymbol{r},t) + \zeta_\rho(\boldsymbol{r},t)\right]\frac{\boldsymbol{v_r}^3}{v_r} \\ &= \boldsymbol{a}_{d,model} + \frac{B_C}{2}\rho_m(\boldsymbol{r},t)\cdot\epsilon_\rho(t)\,\frac{\boldsymbol{v_r}^3}{v_r} \\ &= \boldsymbol{a}_{d,model} + \delta\boldsymbol{a}_{d,stoc} \end{aligned} \tag{6.8}$$

The deterministic acceleration due to drag $\boldsymbol{a}_{d,model}$ is computed based on the densities according to a density model, and $\delta\boldsymbol{a}_{d,stoc}$ is the stochastic acceleration which is due to the relative random variations, ϵ_ρ, in the modelled density.

The established $\delta\boldsymbol{a}_{d,stoc}$ captures the relative accelerations to the modelled acceleration. Relative orbital dynamics are considered to evaluate the effect of $\delta\boldsymbol{a}_{d,stoc}$. Since the analysis concentrates on the uncertainty in the positions due to uncertainty in the density models, the effects of cross winds (atmospheric winds) are neglected. With the previously mentioned, circular orbit cases, the R and N components of the drag acceleration can be assumed to be zero, which leads to the components of the stochastic acceleration in the RTN frame

$$\delta\boldsymbol{a}_{d,stoc} = \begin{pmatrix} 0 \\ \delta a_{d,stoc,T} \\ 0 \end{pmatrix} \tag{6.9}$$

Relative orbital dynamics with random acceleration

The relative motion development has been applied in designing the formation flying spacecraft orbits. Alfriend (2010) presents the details on the development and discusses the various existing forms of relative equations of motions. The representation offers direct and relevant characteristics of the bounded relative motion in terms of chaser orbits departing from the target orbit. This is advantageous to study the deviation in predicted orbits due to uncertainty in the force models.

Here, it is assumed that the target orbit is the central orbit which is not affected by any noisy perturbing forces, and the target spacecraft is affected only through the forces which are captured by the modelled perturbing accelerations ($\boldsymbol{a}_{model}$). The differential acceleration, ($\delta\boldsymbol{a}$ - either random or deterministic), will be acting on the chaser spacecraft making it move in a different orbit than the target orbit. In the present analysis, the chaser spacecraft is assumed to experience stochastic drag acceleration, ($\delta\boldsymbol{a}_{d,stoc}$), due to density noise. Understanding the relative motion of the chaser orbit with respect to the target orbit will assist in estimating the deviation in orbit due to the stochastic differential acceleration. For this purpose, the Clohessy-Wiltshire-Hill (CWH) set of equations are considered, and are given in 6.10, 6.11, and 6.12.

$$\delta\ddot{e}_R = \quad 3n^2\delta e_R + 2n\delta\dot{e}_T \quad + \delta a_{e_R} \tag{6.10}$$

$$\delta\ddot{e}_T = \quad -2n\delta\dot{e}_R \quad + \delta a_{e_T} \tag{6.11}$$

$$\delta\ddot{e}_N = \quad -n^2\delta e_N \quad + \delta a_{e_N} \tag{6.12}$$

Where n is the mean motion of the satellite. A vectorised form of the above set of equations can be written as

$$\delta\dot{\boldsymbol{e}} = \boldsymbol{G}\delta\boldsymbol{e}(t) + \boldsymbol{D}\begin{pmatrix} 0_{[3\times1]} \\ \delta\boldsymbol{a}_e(t) \end{pmatrix} \tag{6.13}$$

where $\delta\boldsymbol{a}_e$ is the difference between the (deterministic) perturbing accelerations acting upon the target and chaser spacecraft, and $\delta\boldsymbol{e}$ is the difference in position of the chaser represented in the target spacecraft centred reference frame. The matrix form of the force functions are

given as

$$\boldsymbol{G} = \begin{pmatrix} 0 & 0 & 0 & 1 & 0 & 0 \\ 0 & 0 & 0 & 0 & 1 & 0 \\ 0 & 0 & 0 & 0 & 0 & 1 \\ 3n^2 & 0 & 0 & 2n & 0 & 0 \\ 0 & 0 & 0 & -2n & 0 & 0 \\ 0 & 0 & -n^2 & 0 & 0 & 0 \end{pmatrix} \text{ and } \boldsymbol{D} = \begin{pmatrix} 0 & 0 & 0 & 0 & 0 & 0 \\ 0 & 0 & 0 & 0 & 0 & 0 \\ 0 & 0 & 0 & 0 & 0 & 0 \\ 0 & 0 & 0 & 1 & 0 & 0 \\ 0 & 0 & 0 & 0 & 1 & 0 \\ 0 & 0 & 0 & 0 & 0 & 1 \end{pmatrix} \tag{6.14}$$

The CWH equations describes the chaser spacecraft motion in the target spacecraft centred coordinate system. These sets of equations are particularly valid for circular orbit about a central body. Alfriend (2010) has shown that the equations are valid for near circular orbits. The actual limit on eccentricity has to be evaluated when real observational data is available, and it is not further analysed within this research work.

From the CWH equations, equation 6.12 is a simple harmonic oscillator, and equation 6.10 and 6.11 are coupled oscillators. It is also observed that the N-component is independent of the R and T components. The homogeneous part of the equation (with $\delta \boldsymbol{a}_e = 0$) has a solution in closed form and for the given initial condition $\delta \boldsymbol{e}(t_0) = \delta \boldsymbol{e}_0$ at $t_0 = 0$, which is given in the form of the state transition matrix, $\boldsymbol{\phi}_{CWH}$, as below

$$\delta \boldsymbol{e}(t) = \boldsymbol{\phi}_{CWH} \cdot \delta \boldsymbol{e}_0 \tag{6.15}$$

Expanding the state transition matrix, the complete solution is given as

$$\delta \begin{pmatrix} e_R(t) \\ e_T(t) \\ e_N(t) \\ \dot{e}_R(t) \\ \dot{e}_T(t) \\ \dot{e}_N(t) \end{pmatrix} = \begin{pmatrix} 4-3\mathtt{C} & 0 & 0 & \frac{1}{n}\mathtt{S} & \frac{2}{n}(1-\mathtt{C}) & 0 \\ 6(\mathtt{S}-nt) & 1 & 0 & -\frac{2}{n}(1-\mathtt{C}) & \frac{1}{n}(4\mathtt{S}-3nt) & 0 \\ 0 & 0 & \mathtt{C} & 0 & 0 & \frac{1}{n}\mathtt{S} \\ 3nt \cdot \mathtt{S} & 0 & 0 & \mathtt{C} & 2\mathtt{S} & 0 \\ -6n(1-\mathtt{C}) & 0 & 0 & -2\mathtt{S} & 4\mathtt{C}-3 & 0 \\ 0 & 0 & -n\mathtt{S} & 0 & 0 & \mathtt{C} \end{pmatrix} \cdot \delta \begin{pmatrix} e_{R_0} \\ e_{T_0} \\ e_{N_0} \\ \dot{e}_{R_0} \\ \dot{e}_{T_0} \\ \dot{e}_{N_0} \end{pmatrix} \tag{6.16}$$

where $\mathtt{C} = \cos(nt)$ and $\mathtt{S} = \sin(nt)$, and the mean motion $n = n_0$ (Alfriend, 2010).

The errors due to drag acting on satellite orbits are assumed to be small within the analysis interval, in comparison to the main or target orbit. With this assumption, and formulating the above CWH equations with stochastic drag, leads to a set of Stochastic Differential Equations (SDE) of the form.

$$\delta \dot{\boldsymbol{e}} = \boldsymbol{G} \delta \boldsymbol{e}(t) + \boldsymbol{D} \cdot \begin{pmatrix} 0_{[3\times 1]} \\ \delta \boldsymbol{a}_{d,stoc} \end{pmatrix} \tag{6.17}$$

Considering the equation 6.9 within the second term on the right hand side

$$\boldsymbol{D} \cdot \begin{pmatrix} 0_{[3\times 1]} \\ \delta \boldsymbol{a}_{d,stoc} \end{pmatrix} = \begin{pmatrix} 0 \\ 0 \\ 0 \\ 0 \\ \delta a_{d,stoc,T} \\ 0 \end{pmatrix} \tag{6.18}$$

For circular orbital cases and in the absence of all other perturbing forces, SO velocity is given as $v_T^2 = \frac{\mu}{a}$. Where μ is the mass of the central body times the gravitational constant and a is the semi-major axis. Using the expression for circular orbital velocity and separating the random parameter, the above equation is written in the form

$$\begin{pmatrix} 0 \\ 0 \\ 0 \\ 0 \\ \delta a_{d,stoc,T} \\ 0 \end{pmatrix} = \begin{pmatrix} 0 \\ 0 \\ 0 \\ 0 \\ \frac{B_c}{2}\rho_m \frac{\mu}{a} \\ 0 \end{pmatrix} \cdot \epsilon_\rho(t) = \boldsymbol{L}_{RTN} \cdot \epsilon_\rho(t) \tag{6.19}$$

The new force function acting on the stochastic parameter is labelled as $\boldsymbol{L}_{RTN}$. Using equation 6.19 in 6.17, the complete linearised SDE in RTN position and velocity vectors is represented as

$$\delta \dot{\boldsymbol{e}} = \boldsymbol{G}(t, \boldsymbol{e}) + \boldsymbol{L}_{RTN} \cdot \epsilon_\rho(t) \tag{6.20}$$

An SDE will have an infinite number of solutions, a unique solution is obtained with each realisation of the random variable. Each realisation of the stochastic CWH equation will generate a unique trajectory. Since we are not interested in the complete solution for the equation 6.20, we aim to derive the time evolution of the mean and the covariance of the established stochastic differential equation.

Mean and Variance of a linear SDE

The general form of an SDE is given by

$$\begin{aligned} \dot{\boldsymbol{x}}_t &= \boldsymbol{f}(t)\boldsymbol{x}(t) + \boldsymbol{L}(t;\boldsymbol{x}_t)W(t) \\ \mathrm{d}\boldsymbol{x}_t &= \boldsymbol{f}(t)\boldsymbol{x}(t)\mathrm{d}t + \boldsymbol{L}(t;\boldsymbol{x}_t)\mathrm{d}B_t \end{aligned} \tag{6.21}$$

where the initial conditions are $\boldsymbol{x}(t_0) \sim \boldsymbol{N}(\boldsymbol{m_0}, \boldsymbol{P_0})$, $\boldsymbol{f}(t)$ and $\boldsymbol{L}(t)$ are matrix valued functions of time, and $\mathrm{d}B_t = W(t)\mathrm{d}t$, where $W(t)$ is the uncorrelated white noise with diffusion matrix $\boldsymbol{Q}$. The solution of the above equation with given initial conditions is given by Klebaner (2005)(Section 3.1) as

$$\boldsymbol{x}(t) = \boldsymbol{\psi}(t, t_0)\boldsymbol{x}(t_0) + \int_{t_0}^{t} \boldsymbol{\psi}(t, t')\boldsymbol{L}(t;\boldsymbol{x}_t)\mathrm{d}B(t') \tag{6.22}$$

where $\boldsymbol{\psi}$ is the state transition solution for $\boldsymbol{f}(t)$. In case of Brownian motion, the integrand has to be integrated twice (from the definition in equation 6.6). For zero initial uncertainty, $\boldsymbol{P}_0 = 0$, the time variance of $\boldsymbol{m}(t) = \boldsymbol{\psi}(t, t_0)\boldsymbol{m}(t_0)$. That is, the mean of the equation is the solution of the deterministic part of the differential equation, where as the variance of $\boldsymbol{x}(t)$ is evaluated by computing the variance of the equation 6.22

$$\mathrm{var}\left[\boldsymbol{x}(t)\right] = \mathrm{var}\left[\int_{t_0}^{t} \boldsymbol{\psi}(t, t')\boldsymbol{L}(t;\boldsymbol{x}_t)\mathrm{d}B(t')\right] \tag{6.23}$$

Equation 6.23 will provide the base for establishing the closed form solution for our problem of estimating prediction uncertainty due to density model uncertainty. The solution

to the above equation depends on evaluating the second integral of white noise. Steps involved in evaluating the right hand side of the above equation and estimating the variance of $\boldsymbol{x}(t)$ is given in Appendix B.1.

Deriving closed form solution for R-T components

The solution provided in the equation 6.23 is employed to derive time variances of the R and T components. Using the state transition matrix for CWH system, given in equation 6.16, together with the stochastic force function $\boldsymbol{L}_{RTN}$ in the equation 6.19, $\delta\boldsymbol{e}(t)$ is written as

$$\delta\boldsymbol{e}(t) = \boldsymbol{\phi}_{CWH}(t,t_0)\cdot\delta\boldsymbol{e}(t_0) + \int_{t_0}^{t}\boldsymbol{\phi}_{CWH}(t,t')\boldsymbol{L}_{RTN}\epsilon_\rho(t')\mathrm{d}t' \tag{6.24}$$

To evaluate the variances of each component separately, $\mathrm{var}[\delta e_R] = P_{\delta e_R}$ and $\mathrm{var}[\delta e_T] = P_{\delta e_T}$ are evaluated for $t_0 = 0$ and $\boldsymbol{P}_0 = 0$. The first two diagonal elements of $\boldsymbol{P}_{RTN}(t)$ are given by

$$P_{\delta e_R} = \mathrm{var}\left[\int_0^t\left[\frac{2}{n}(1-\cos(nt'))\right]\cdot\left[\frac{B_c}{2}\rho_m\frac{\mu}{a}\right]\cdot\epsilon_\rho(t')\mathrm{d}t'\right] \tag{6.25}$$

$$P_{\delta e_T} = \mathrm{var}\left[\int_0^t\left[\frac{1}{n}(4\sin nt' - 3nt')\right]\cdot\left[\frac{B_c}{2}\rho_m\frac{\mu}{a}\right]\cdot\epsilon_\rho(t')\mathrm{d}t'\right] \tag{6.26}$$

Depending on the requirement, one can numerically integrate the above equation to find the deviation due to prediction uncertainty.

For catalogue maintenance, the accuracy of the propagator is selected and chosen in the order of 10 m. From the point of the present application, it will be sufficient if the solution of the above equation includes the uncertainty magnitudes greater than the prediction accuracy of the propagator. Also, for the purpose of catalogue maintenance computational efficiency, it will be advantageous to form a closed form solution. In order to simplify the problem and establish an analytical solution, the following additional assumptions are made:

- The influence on change in mean-motion is small within the uncertainty prediction arc-lengths (3 to 7 days) and for altitudes greater than 350 km. Thus the time variation of mean motion is neglected.
- For the considered circular orbital case, the variation of modelled densities ($\mathrm{d}(\rho_m)$) is assumed to be much smaller than the relative noise/error (ϵ_ρ).
- The SO is under the influence of central body gravitational force and drag accelerations, the rest of the perturbations are neglected.

With the above assumptions the constant terms are brought together and assigned with $I_\rho = B_c\cdot\rho_m(t_0)(\mu n_0)^{1/3}$ and using the derivation method presented in Appendix B.1, the solutions for the Equations 6.25 and 6.26 are found to be

$$P_{\delta e_R} = \sigma_\rho^2\cdot I_\rho\cdot\frac{4}{\tau^4 n^2}\left[\frac{t^4}{4} - \frac{3t^2}{n^2} - \frac{6}{n^4}[\cos nt - 1]\right] \tag{6.27}$$

$$P_{\delta e_T} = \sigma_\rho^2\cdot I_\rho\cdot\frac{1}{\tau^5 n}\left[\frac{t^5}{20} - \frac{t^3}{8} - \frac{4t}{n^3} + \frac{22t\cos nt}{n^2} - \frac{22\sin nt}{n^5} + \frac{7t^2\sin nt}{n^3}\right] \tag{6.28}$$

The solutions to $P_{\delta e_R}$ and $P_{\delta e_T}$ show that both variances increase at some powers of time and with periodic terms which depend on the mean motion of the orbiting object. It can be readily observed from the above equations that the uncertainty in radial direction increases with the fourth power of time. On the other hand, the uncertainty in tangential direction increases with the fifth power of time.

6.3 Testing the Closed Form Solution

To test the solution, initially it was compared with simulated test cases. Appendix B discusses the method for simulating the density noise and the implementation of the same. Each run of the density noise model realises a random trajectory for the given noise characteristics. From the understanding of the spatial variation of the upper atmospheric density (latitude and longitude variations) in section 6.1 the time correlation factor τ is set to one tenth of the orbital period and a relative uncertainty of 15% was used. Similar to Montecarlo simulations, 1000 orbit trajectories were realised for the arc length of 7 days. Figure 6.2 shows the variances at each time step from the ensemble of 1000 stochastic trajectories. A spacecraft with an altitude of 450 km, inclination of 87°, and eccentricity representing a near circular orbit ($e = 0.001$) was set.

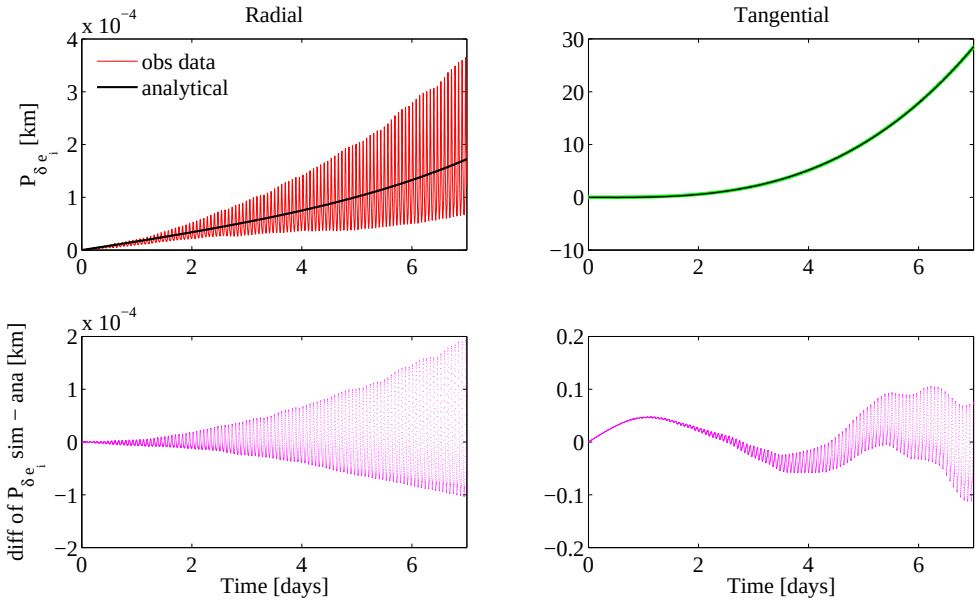

Fig. 6.2 Top row: Propagated uncertainties as variances in R-T directions from the ensemble of 1000 Brownian paths for a SO (see text). Black lines show the analytical fit using the time series. Bottom row: Differences between simulated uncertainty and the analytical solution.

In the Figure 6.2, the colour plots in the top row show the uncertainties in the radial and tangential directions from the simulated orbits. The black curves show the results from the analytical evaluation of equations 6.27 and 6.28. As it is observed in the figure, the analytical solution (without periodic terms) captures the secular growth of the uncertainty to the extent that captures the shape of the simulated curves.

From the simulations, it is observed that the variance in radial direction grows less steeper than the tangential direction. The most prominent term in the radial direction will thus be

the in orbit fluctuations, which has a frequency equal to once per orbit. The amplitude is increasing with time, which is not captured from the analytical solution which neglects the periodic variations. The most prominent effect of density uncertainty on the orbit predictions will be in the tangential (T) directions. In comparison to simulated data, the analytical solution captured the effects to the extent of reducing the error in variance predictions by two orders of magnitude for the orbital arc of seven days.

In the above example, a single satellite was considered and compared against the known time correlation value for the noise. In reality, the value for τ is not well known and is hard to establish for the actual upper atmosphere. Hence a parametric approach is developed and proposed for the purpose of catalogue maintenance system. Also, orbits of different altitudes are examined with the developed theory.

6.4 Parametrization and Application to Catalogue Maintenance

The final goal is to estimate the uncertainty in the tangential direction with sufficient accuracy to represent the realistic covariances. Also, to remove the requirement for the propagator to compute $P_{\delta e_i}$, the following six parameters were adopted.

$$\begin{aligned} P_{\delta e_R} &= A_R t^4 + B_R t^2 + C_R t \\ P_{\delta e_T} &= A_T t^5 + B_T t^3 + C_T t \end{aligned} \tag{6.29}$$

Where the coefficients $[A_R, B_R, C_R]$ and $[A_T, B_T, C_T]$ capture the time correlation, density, and mean motion effects of the orbits on the variance propagation. As seen from the figure 6.2, the periodic oscillations in tangential direction are two to three orders of magnitude smaller than the secular increase in the prediction error. Hence, the in orbit variations which are present in equations 6.27 and 6.28 are neglected within the parametrised approximation.

As discussed earlier, in reality it might not be possible to accurately determine the τ value for density fluctuations. Instead, one can estimate these coefficients using precise orbital data when available, or make use of the coefficients while estimating them using simulated data.

To analyse the coefficients, SWARM-C satellite data for the year of 2016 is used. SWARM-C has a semi-major axis of 6814 km and its orbits in a near circular orbit with inclination of ~ 87 degrees.

Differences between the numerically predicted orbit (ODEM orbits) and the precise orbital data are computed to estimate the deviation in the predicted orbits. To isolate the effect of the density model in the propagation, the epoch state elements are estimated from a one day precise orbit. Then, the estimated elements are propagated using ODEM, with the Jacchia-Gill density model (without noise) for a period of seven days to compare against the data. Figure 6.3 shows the steps followed in the testing procedure.

When predicting LEO orbits, the most dominant perturbing force is due to drag acceleration, with all the conservative perturbing forces assumed to be well modelled. The same was discussed in the beginning of this chapter. Hence, the uncertainty in predicted orbits due to gravitational perturbations are assumed to be negligible when computing the orbits in the LEO region. This assumption makes the differences obtained by comparing the propagated orbit and precise orbital data to be mainly due to the uncertainty in atmospheric drag.

The parameters in equation 6.29 represent the variances in radial and tangential directions over time. The precise SWARM-C orbital arc is compared against the predicted orbit to evaluate the error growth in time. Following the loop given in the flowchart for the test procedure

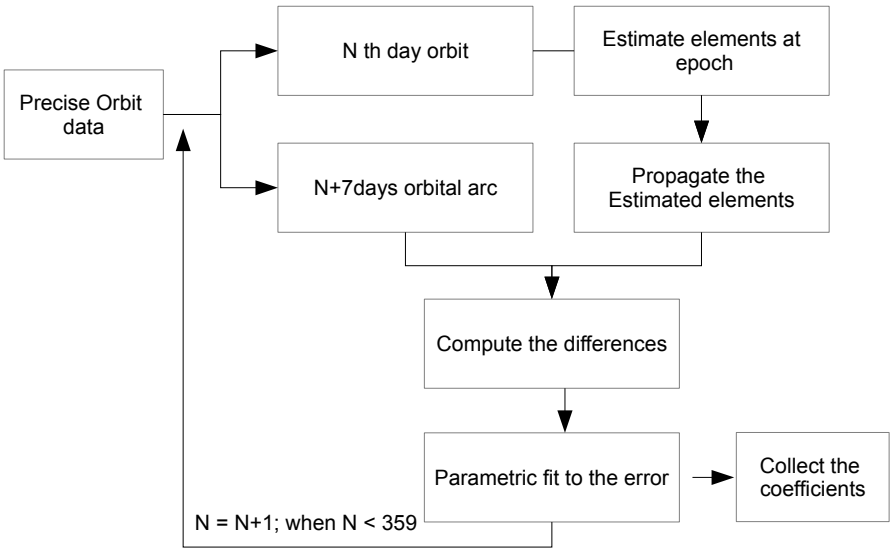

Fig. 6.3 Estimating the deviation in prediction in orbit propagator while comparing to precise orbital arc

in Figure 6.3 the coefficients were estimated for each day of the year 2016. This presents the variations in coefficients over a period of time. The distribution of coefficients over one year is analysed to understand the dispersion of the coefficients. In the end, the behaviour of the coefficients with different altitude is established with simulated data. Following the empirical understanding, a secondary model to compute the coefficients is established.

Figure 6.4 shows the differences between the estimated and then predicted orbits of the SWARM-C satellite and the precise orbits from the periods between 01 and 08 January 2016. The plots are for the analytical fit, which is performed using the estimated A_i, B_i, and C_i coefficients over the residuals. It shows that the radial and tangential direction deviations are well approximated with the derived time trends. The estimated coefficients captures the prediction uncertainty for the given analysis period. Figure 6.5 shows the deviations in R and T directions which are propagated for seven days.

Figure 6.6 shows the daily variation of the individual coefficients, and Figure 6.7 shows the distribution of the coefficients for the examined year. The fluctuations in the estimated coefficients are associated to the variations in the density values. Further examinations showed a correlation of 0.68 with F10.7 flux variations during the period of analysis. The behaviour is expected from the derived analytical solutions for the time variation of variances in both R and T directions. Due to this dependency, one requires to establish an understanding of the time coefficients behaviour with different level of solar activities, or re-calibrate the coefficients with observed values.

Figure 6.8 shows A_i, B_i, and C_i coefficients estimated for imaginary SOs orbiting at different altitudes. All the coefficients in either components showed a systematic exponential decrease in magnitudes. This behaviour too can be associated with the presence of $\rho_m(t_0)$ term in the analytical solution. Exponential decrease of density over increasing altitude drives the coefficients to behave similarly.

The behaviour of the coefficients are directly used for extracting the values of the time power coefficients for the given altitude. Exponential curves with a modelled equation 6.30

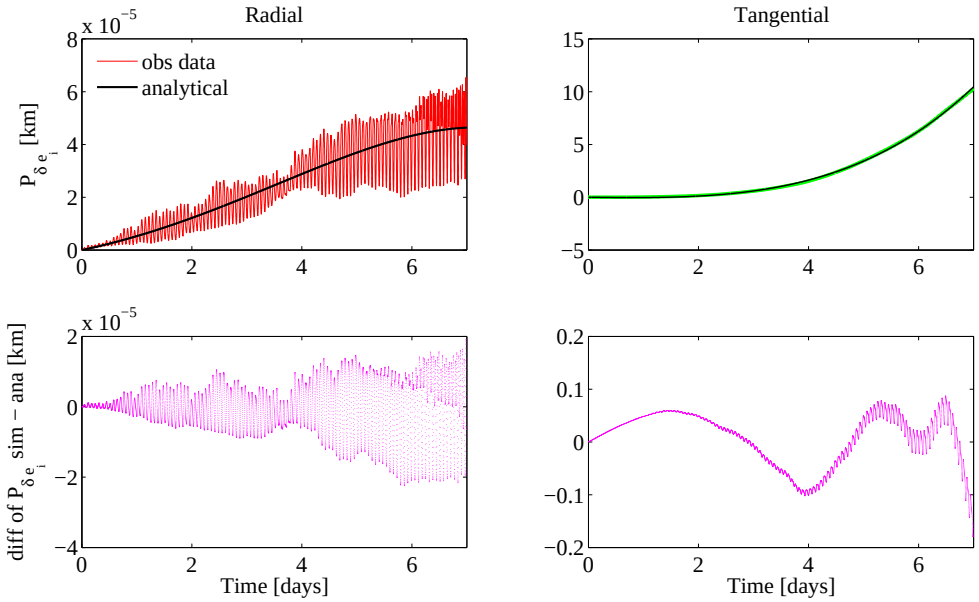

Fig. 6.4 Top row: Propagated uncertainties as variances in R-T directions from the precise orbital data of SWARM-C satellite. Black lines show the analytical fit using the time series. Bottom row: Differences between simulated uncertainty and the analytical solution.

are fitted to the coefficients computed

$$J_i = L_{J_i} \cdot \exp\left(\left(1 - \frac{a}{R_e}\right) \cdot K_{J_i}\right) \; ; \; J = \{A, B, C\} \; ; \; i = \{R, T\} \tag{6.30}$$

where a is the semi-major axis and R_e is the radius of the Earth. For the purpose of estimating exponent coefficients, the semi-major axis is normalised with the Earth's radius. The estimated L_{J_i}s and K_{J_i}s are presented in the below Table 6.1.

Table 6.1 L and K exponent model coefficients for estimating the polynomials with varying semi-major axis as per equation 6.30.

	A		B		C	
Components	L	K	L	K	L	K
Radial	1E-20	139.53	1.3E-9	140.28	2.5E-2	154.92
Tangential	1E-23	138.29	1E-12	137.56	5E-2	132.68

The intrinsic rate of decrease of $\{A_i, B_i, C_i\}$ coefficients with an increase in the semi-major are approximately of the same magnitude. This shows that the behaviour is directly correlated to the density variation with increasing altitude. This was also observed when the simulations are repeated with different periods of solar activity. The L coefficients are related to the assumed time correlation factor in generating the density noise. Difficulty in predicting both τ and F10.7 values are the major reason to have a stochastic approach to capture the density fluctuations. The simulation model can be calibrated using the available precise orbital data in order to use the model for practical applications.

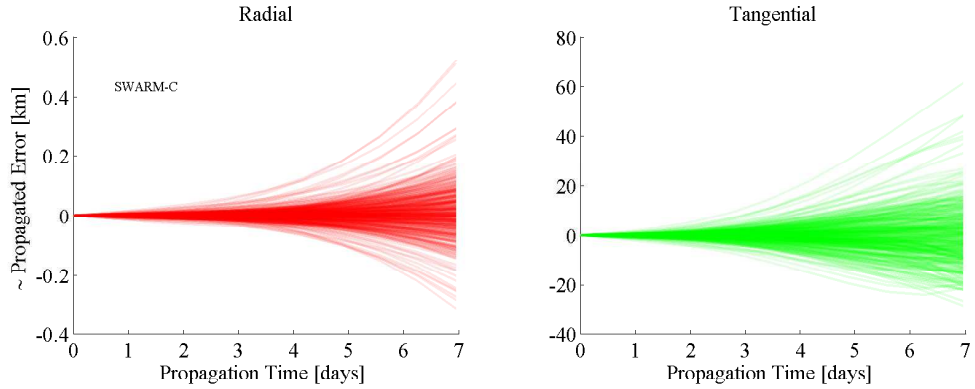

Fig. 6.5 Propagating the estimated prediction uncertainty using A_i, B_i, and C_i time coefficients for variances of radial and tangential components. The coefficients are estimated using the precise SWARM-C data for the year of 2016

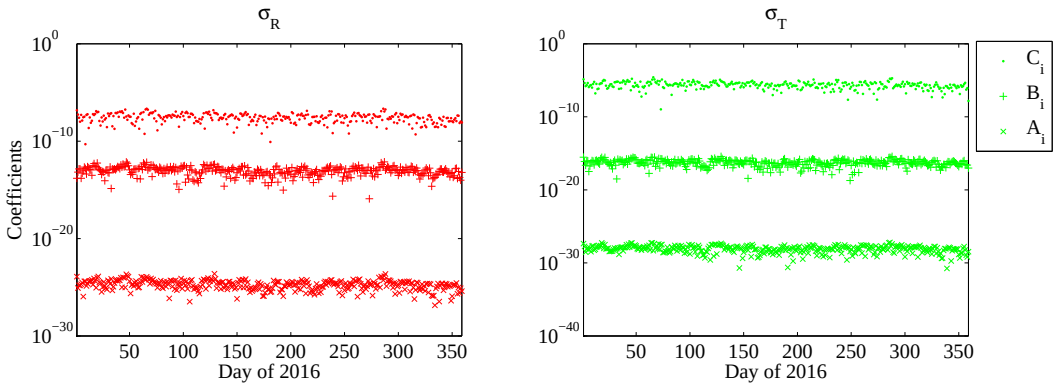

Fig. 6.6 Absolute values of A_i, B_i, and C_i time coefficients estimated for SWARM-C satellite for the year of 2016. See text for the details on the estimation procedure.

A two step approach allows one to estimate the prediction uncertainty due to modelled density errors without using an orbit propagator or evaluating density models:

1. For the given semi-major of the SO estimate $\{A_i, B_i, C_i\}$ coefficients using equation 6.30 and Table 6.1.

2. Compute variances in radial and tangential directions using equation 6.29.

This will enable the catalogue maintenance system to save a large amount of computational resources while evaluating the drag model uncertainties.

The validity of the present model will be tested in the next chapter together with the covariance propagation analysis.

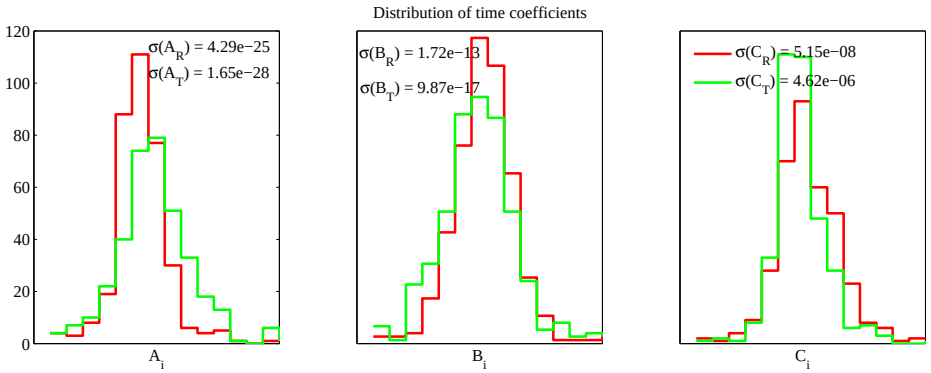

Fig. 6.7 Distribution of A_i, B_i, and C_i time series daily coefficients estimated for SWARM-C satellite for the year of 2016. See text for the details on the estimation procedure.

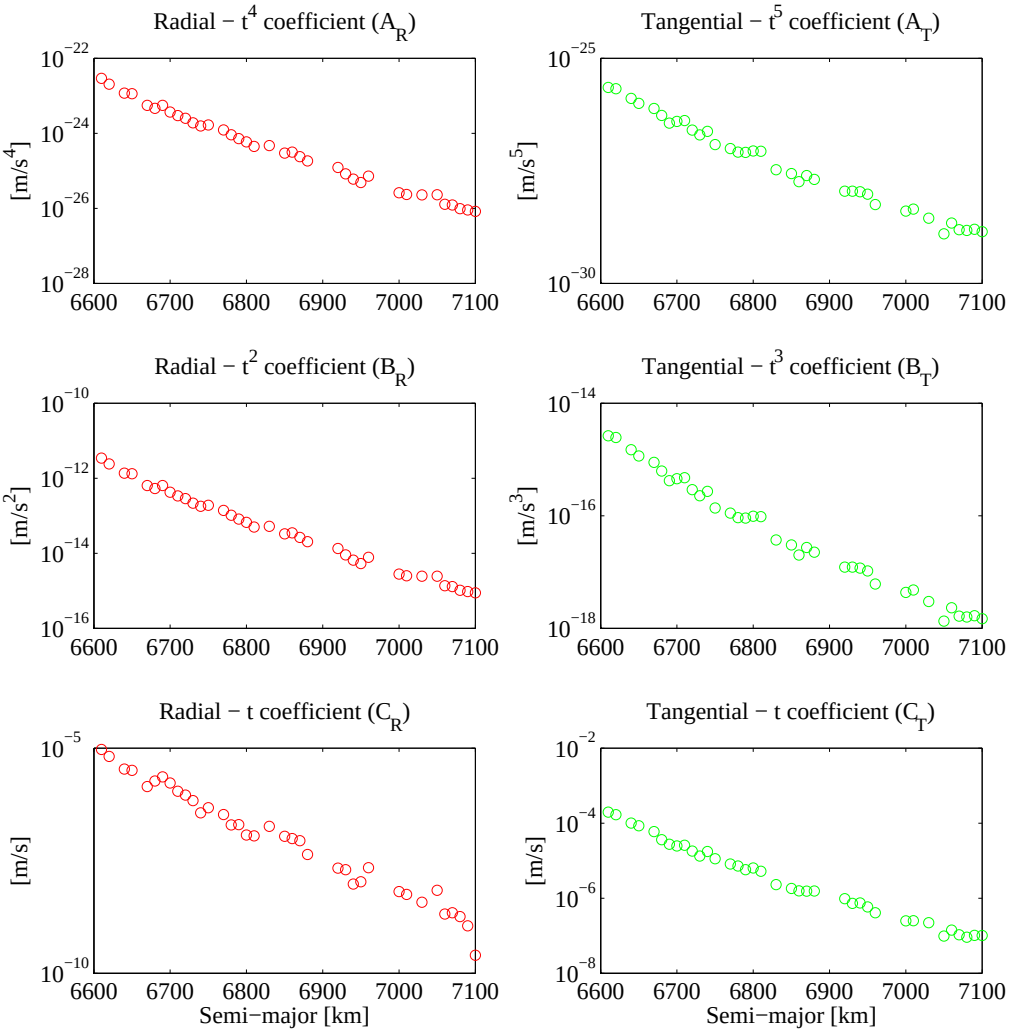

Fig. 6.8 Variation of A_i, B_i, and C_i time series coefficients for variances of radial and tangential components compared against increasing semi-major axis

CHAPTER 7

UNCERTAINTY PROPAGATION QUANTIFICATION

While the concept of statistical representation of orbital uncertainty is straightforward and well understood, propagating the covariance under linear assumptions comes with limitations due to non-linear nature of the orbital dynamics. If the initial or estimated uncertainties are sufficiently small and the statistics can be represented by Gaussian assumptions, linear error propagation theory, discussed in the Chapter 3, is applied to propagate the representative error ellipsoid volumes centred at the propagated state. The error ellipsoid is the iso-valued surface representing the variance of the three dimensional Guassian distribution. Non-linearities behave differently depending on the equations of motion of the chosen set of position and velocity state space or element space for representing an orbit.

Quantification of propagated covariances is generally carried out by comparing the statistics against Monte-Carlo simulations. One such study carried out by Sabol (2010) compares the linear covariance propagation in Cartesian ECI positions, osculating and mean Keplerian elements, and osculating and mean equinoctial elements. These results demonstrated that a mean equinoctial element based formulation maintains a Gaussian distribution better than the osculating element and Cartesian position representations.

Sabol mentions that improved performance of the equinoctial variables was due to geometry, and the mean equinoctial elements' better performance over osculating variables are due to the more linear nature of the mean element set.

In this section, Monte-Carlo simulations are carried out to reproduce the results to confirm the findings from Sabol. In addition, a method is presented to improve the initial and propagated mean equinoctial covariance by incorporating the atmospheric model uncertainty.

7.1 Covariance Propagation in Mean Element Space

The covariance matrix $\boldsymbol{P}_t$ is an uncertainty or a covariance matrix describing the confidence region of the propagated state at time t. For a given true state, $\boldsymbol{y}_t$ is expected to be within the region represented by $\boldsymbol{P}_t$; this implies that the true state is inside the numerically predicted probability region. This concept is used as the basis for quantifying the propagated covariance using equations 3.19 and 3.21 for the linear EKF and UKF methods, respectively.

6-D Monte-Carlo simulations were carried out using ODEM for propagating the Cartesian states and the DSST was used for propagating the Keplerian and the equinoctial elements (in both osculating and mean elements). The orbits propagated within Monte-Carlo runs are designated with superscript MC, as in $\boldsymbol{y}_t^{MC}$. To check if $\boldsymbol{y}_t^{MC}$ is within the propagated $\boldsymbol{P}_t$, a

metric commonly known as Mahalanobis distance is calculated with respect to propagated mean $\boldsymbol{y}_t^{est}$. The equation below gives the definition for calculating the Mahalanobis distance (k) (Mahalanobis, 1936):

$$k = \sqrt{(\boldsymbol{y}^{est} - \boldsymbol{y}^{MC})^\top \boldsymbol{P}^{-1} (\boldsymbol{y}^{est} - \boldsymbol{y}^{MC})} \tag{7.1}$$

By calculating the distance k for each propagated MC state, the number of MC points within the propagated covariance ellipsoid is calculated. That is the number of points with $k \leq 1$ for a 1-sigma ellipsoid, $k \leq 3$ for 3-sigma ellipsoid, and so on, is used to compute the percentage of points within the required sigma ellipsoids. Figure 7.1 illustrates the two dimensional case for MC sigma points and the 3-sigma ellipse at an initial state. The initial ellipse should contain 95% of the MC sigma points (probability mass in 2D).

For the purpose of simulation, the initial covariance matrices were estimated using sparsely spaced GPS observations within the BLSQ OD system. This in turn resulted in estimating a conservative (tight / very optimistic) covariance at the initial epoch. The intention is to demonstrate the degradation of the propagated ellipsoid over time, as the ellipsoid does not capture the propagation and model inaccuracies caused by the orbital theory. Figure 7.2 shows the percentage of sigma points contained within the ellipsoid for Cartesian states and mean equinoctial elements. In the figure, the UKF performs better than the EKF propagation, by an enlarged covariance propagation from the UKF method. The determinant of the error matrix provides the volume of the Gaussian ellipsoid. The same can be observed from the volume comparisons presented in the Figure 7.3. The volumes of the UKF propagated covariance matrices are a few orders of magnitude greater than that of the volumes of EKF propagated position uncertainty ellipsoids. From careful examination of the eigenvalues and eigenvectors of the covariance matrix, it was found that the magnitude of the eigenvectors in tangential and radial directions were much larger in the UKF propagated covariance matrix than the EKF propagated ellipsoids. Further detailed analysis of propagated UKF ellipsoids showed that the R-T-N components of transformed covariances did not represent the MC simulations.

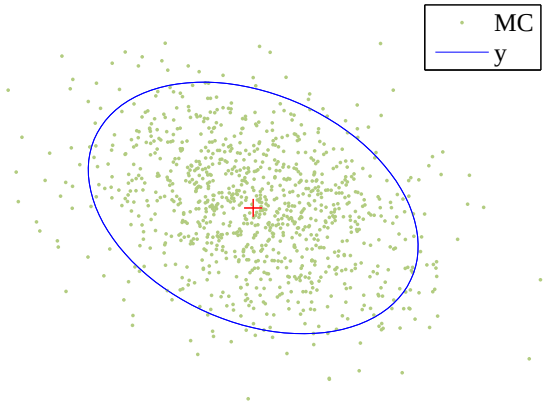

Fig. 7.1 Showing the Gaussian ellipsoid centred at mean state $\boldsymbol{y}$ together with the Monte-Carlo points.

The two primary purposes of propagating covariances into future epochs are for the application of observation correlation and conjunction assessment. The enlarged covariances from the UKF leads to an increase in false positives in correlating the catalogued objects with survey observations, and also causes over estimation of the probability of collision leading to degradation of orbital lifetime of an operating satellite. On the other hand, EKF covariance may underestimate the real uncertainty, which might lead to false negatives. More importantly this might lead to an under estimation of the probability of collision, which might be fatal to missions.

For the catalogue to provide proper support to space operations, it is important to have realistic covariances at the time of interest. From the simulations, it is understood that UKF is

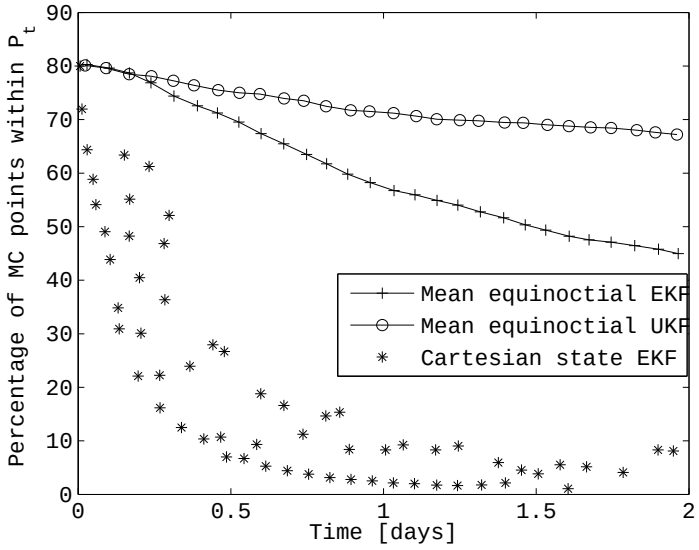

Fig. 7.2 Percentage of Monte-Carlo points within EKF propagated six dimensional covariance in Cartesian state, and EKF and UKF propagated covariances in mean equinoctial element space. PROBA-V test satellite epoch conditions were used for the simulation.

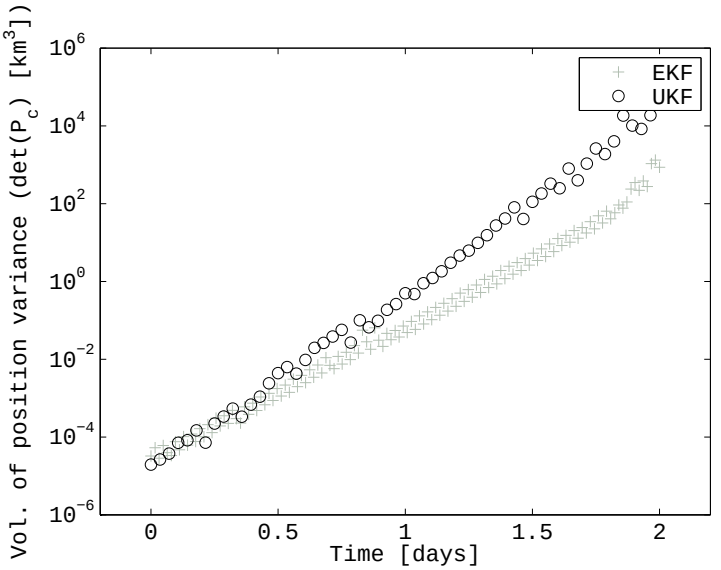

Fig. 7.3 Volume of covariance matrices propagated using EKF and UKF methods for the test simulation specified in figure 7.2.

overestimating and EKF is underestimating the propagated covariance matrices. It is relatively straight forward to estimate the difference between the underestimated covariance matrix and enlarge the ellipsoid, rather than shrinking the overly estimated ellipsoids. Together with the above limitation, the UKF consumes 13 times more computational time than the EKF. Hence, for the purpose of catalogue maintenance, it is recommended to make use of the EKF linearised approximation together with further improvements.

The above simulations verified the study from Sabol (2010), together it provides an understanding of the behaviour of UKF and EKF propagated covariance volumes together with linearity regions. The next section discusses improvements for covariance propagation which include the atmospheric model uncertainty.

7.2 Realistic Covariance Computation

The probability confidence within $\boldsymbol{P}$ has a size and shape associated with the components of the matrix. A crucial component of the correlation or collision probability estimation is the evolution of the likelihood distribution. This evolution is dictated by variations captured within $\boldsymbol{\phi}(t_0, t_i)$. If there is an uncertainty in $\boldsymbol{\phi}$, that uncertainty can be modelled as a process noise consisting of the propagation errors $\boldsymbol{Q}_p$ and model errors $\boldsymbol{Q}_m$. Propagation errors result more from deterministic errors and can be calibrated using real observations or precise orbits when available. The model noise is assumed to have a Gaussian distribution with zero mean. With this model, the propagated covariance $\hat{\boldsymbol{P}}_t$ is given as

$$\hat{\boldsymbol{P}}_t = \left[\boldsymbol{\phi}^\top \boldsymbol{P}_0 \boldsymbol{\phi}\right] + \boldsymbol{Q}_p + \boldsymbol{Q}_m \tag{7.2}$$

From the previous analysis in chapter 5, a coarse empirical generalisation can be applied for evaluating the propagator induced uncertainty for the DSST based orbit propagation. Results obtained from orbit prediction tests, where the propagator differences over time at different altitudes are presented, can be used as a base for enlarging the covariance matrices accordingly. Neglecting the periodic variations, a linear curve can be used to inflate the diagonal elements of the covariance matrix.

$$Q_{p,ii} = \mathscr{E}_i \cdot t \; ; \; i = 1...6 \tag{7.3}$$

where $\mathscr{E}_i$ is the slope of the error in the corresponding equinoctial elements.

In chapter 6, it has been discussed that the uncertainty of conservative forces are well understood and are modelled up to an extent where they could be comfortably neglected. Using the equations established for propagating the error due to density model uncertainty, we can use the time dependent polynomials to capture the error in radial and tangential directions given by

$$\begin{aligned} q_R &= A_R t^4 + B_R t^2 + C_R t \\ q_T &= A_T t^5 + B_T t^3 + C_T t \end{aligned} \tag{7.4}$$

thus the model induced errors (for LEO objects) are included within the propagated covariances as

$$\boldsymbol{Q}_m = \frac{\partial \boldsymbol{c}}{\partial \bar{\boldsymbol{c}}} \frac{\partial \boldsymbol{Y}_{RTN}}{\partial \boldsymbol{c}} \begin{bmatrix} q_R & 0 & 0 & \dots & 0 \\ 0 & q_T & 0 & \dots & 0 \\ 0 & 0 & 1 & \dots & 0 \\ & \cdots & & & \\ 0 & 0 & 0 & \dots & 1 \end{bmatrix} \frac{\partial \boldsymbol{Y}_{RTN}}{\partial \boldsymbol{c}}^{\top} \frac{\partial \boldsymbol{c}}{\partial \bar{\boldsymbol{c}}}^{\top} \tag{7.5}$$

The above equation transforms the R-T-N prediction uncertainty to an osculating equinoctial elements set before transforming the process noise into final mean equinoctial elements. The partial derivative matrices within the equation 7.5 are the two body transformation matrix from satellite centred coordinates to equinoctial elements and osculating to mean element transformation partial derivatives. Both matrices are computed while an orbit propagation is carried out and hence it does not add extra computational times in evaluating the model noise in mean equinoctial elements.

To validate the covariance matrix which includes process noise, the previous Monte-Carlo simulation with the PROBA-V satellite was carried out. Together with testing, the process noise propagated covariances were also transformed into the satellite centred R-T-N reference frame. Figure 7.4 shows the percentage of Monte-Carlo points which are within the propagated three sigma covariance ellipsoidal volumes. The effect of transformed covariance matrices are not significant and the same can be observed by comparing EKF curves in Figure 7.2.

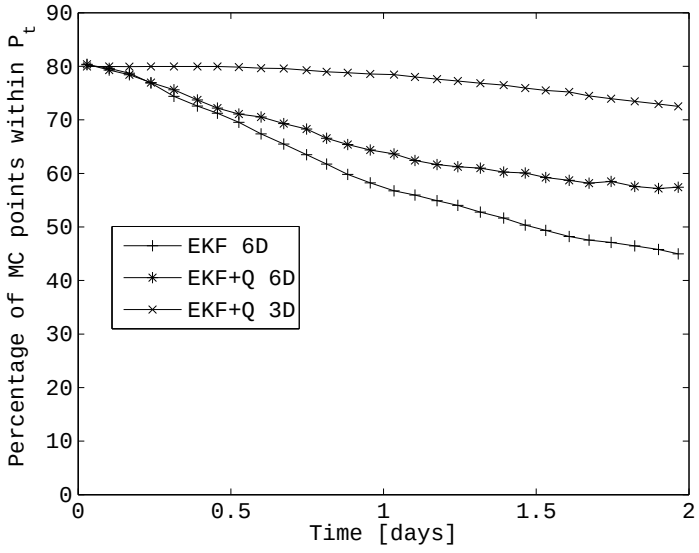

Fig. 7.4 Percentage of MC points contained within the propagated covariance ellipsoids using EKF with and without process noise, for PROBA-V. The plot also includes the comparison of points contained in ellipsoids when the Mahalanobis distance is estimated for full 6×6 covariance matrix against position only 3×3 covariance matrix.

Detailed inspection revealed that inclusion of $\boldsymbol{Q}_m$ inflated the covariance in magnitude such that the uncertainty envelope was able to capture the errors to the geometric limit. The linearised Gaussian ellipsoids do not bend with the orbital curvature. Enlarging the covariance matrix with the right set of values did not blow up the volume to increase the

empty space within it. Contrary to the case of UKF, where the mean was shifted from the propagated state, $\hat{\boldsymbol{P}}_t$ was centred at the predicted mean.

The force-model uncertainties are modelled in radial and tangential directions. The effect of these uncertainties is observed in Figure 7.4. The MC points are well contained within the position uncertainty volume, while the complete six dimensional comparison shows that the MC points are drifting out of the covariance ellipsoid.

7.3 Comparison with Precise Orbits

Although the simulation revealed that including the process noise was beneficial in terms of estimating realistic covariances at propagated times, it has to be noted that the estimation of $\{A_i, B_i, C_i\}$ coefficients were computed using the available precise orbital data for the PROBA-V satellite within the analysis interval. This will not be the case for the maintenance system of SO catalogue with a few hundred thousand objects. Another limitation of the experiment is that it is validated for a single satellite orbiting at the altitude of ~ 730 km. In the following section, satellites with available precise orbital data at different altitudes are analysed.

Table 7.1 provides the altitudes of the considered five satellites, whose precise orbital data were available for the year 2016. To test the established method for covariance propagation, given in equation 7.2, which includes the model errors, as in equation 7.5, from the atmospheric density uncertainties, as in equation 7.4, the following test methodology was employed:

1. Estimate the orbit using DSST-OD with one day precise orbital arc as observations. The observations are selected with 300 seconds step-sizes.
2. Propagate the estimated position state vector (y_t) and covariance (P_t) forward in time for N days.
3. Compute the Mahalanobis distance between y_t and precise orbital data using the propagated covariance.
4. Repeat Steps 1-3 for all the available days with precise orbits.
5. Compute the percentage of precise orbital points which are within the propagated covariance using equation 7.5.

Table 7.1 Satellites with precise orbits used in testing covariance propagation with process noise formulation.

Satellite	Semi-major axis [km]	Data availability [no. of days in 2016]
GRACE-A	6754	365
PROBA-V	7192	353
PROBA-2	7090	300
SENTINEL-3A	7181	280
SWARM-C	6813	365

To compute the q_R and the q_T terms within the process noise matrix, the exponential model established in chapter 6 is used. Table 6.1 provides the required coefficients to compute

the radial and the tangential direction coefficients, to directly evaluate the time evolution of variances in respective directions due to atmospheric drag. The estimated coefficients based on the test satellites' semi-major axis are given in Table 7.2.

Table 7.2 Coefficients for the test satellites to estimate drag uncertainty in orbit propagation

Satellite	Radial Coefficients			Tangential Coefficients		
	A_r	B_r	C_r	A_t	B_t	C_t
GRACE-A	2.22E-24	2.04E-13	8.78E-7	2.40E-27	2.53E-16	1.68E-5
PROBA-V	1.51E-28	1.26E-17	2.07E-11	1.79E-31	2.01E-20	1.82E-9
PROBA-2	1.41E-27	1.20E-16	2.47E-10	1.64E-30	1.81E-19	1.53E-8
SENTINEL-3A	1.92E-28	1.60E-17	2.70E-11	2.27E-31	2.54E-20	2.29E-9
SWARM-C	6.12E-25	5.53E-14	2.09E-7	6.68E-28	7.11E-17	4.90E-6

Figure 7.5 shows the residuals from comparing the propagated orbits and precise orbits for the duration of seven days. The propagated covariances from the EKF and EKF together with model uncertainties are also presented. It can be observed that, including model uncertainty to enlarge the covariance ellipsoid volume captures the uncertainties better than the EKF linear propagation of covariance matrix. Since the enlargement of the covariance matrices are carried out in the radial and the tangential direction, it does not affect the volume as much as it would have in the case of UKF covariance propagation.

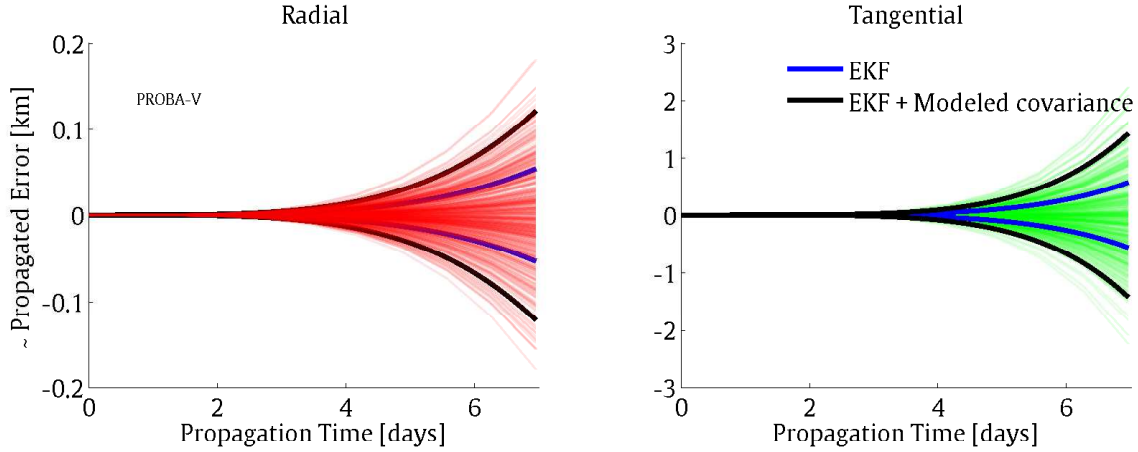

Fig. 7.5 Residuals in radial and tangential directions from comparing propagated orbits and precise orbits for PROBA-V satellite for the year 2016. Blue and black curves represents the EKF propagated covariance and EKF+density uncertainty estimated using the exponential model respectively.

Figure 7.6 shows the estimated and computed $\{A_i, B_i, C_i\}$ coefficients for the PROBA-V satellite. It can be seen that the exponential model provided coefficients on the same order as the coefficients which were computed from fitting the time-powered polynomials to the residuals.

Using the Mahalanobis distance to estimate the percentage of orbits, which are within the propagated one sigma 3D covariance ellipsoids, are compared to quantify the realistic estimation of covariances. Table 7.3 presents the percentage in radial and tangential directions for the year of 2016. The initial covariances are estimated using DSST-OD on the first day of the year 2016.

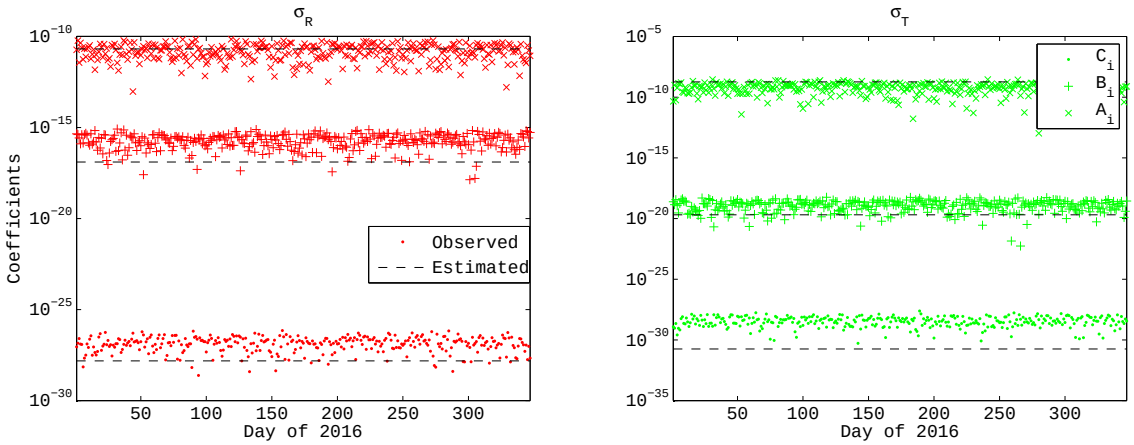

Fig. 7.6 Observed coefficients for radial and tangential variance growth due to atmospheric drag uncertainty, which are obtained from comparing PROBA-V precise orbits for the year 2016. Dashed lines show the exponential model estimated coefficient values for both radial and tangential direction uncertainty growth.

Table 7.3 Percentage of the differences between propagated and precise orbits, which are within the propagated covariances after seven days of propagation. The initial covariances are estimated by DSST-OD.

Satellite	EKF	EKF + $\boldsymbol{Q}_m$
GRACE-A	42%	81%
PROBA-V	32%	84%
PROBA-2	56%	80%
SENTINEL-3A	30%	77%
SWARM-C	59%	76%

Including the model uncertainty shows a clear trend in better containment of the propagated uncertainties for the above five test satellites. Comparing the volumes of these covariances after seven days against the volumes of the covariances from UKF showed that EKF $+\boldsymbol{Q}_m$ are smaller than UKF ellipsoids. Also, the major advantage of the EKF $+\boldsymbol{Q}_m$ propagation method is that the mean is retained within the true mean of the orbital states.

The major limitation of the above experiment is the overly optimistic estimation of the initial covariance (using BLSQ OD). This is the direct result of using continuous and long observation arcs. Also, using precise orbital ephemerides as observations provide very good estimation of the orbits. This is not the case in a real world scenario where observations are sparse and covariance resulting from an OD is sufficiently large. This poses as a limitation to propagate with linear approximation for the period of seven days. To over come this limitation, it requires intense analysis using real observational data, which will be left as part of the future work.

Having a realistic covariance will have a large impact on both catalogue maintenance and its application systems. Keeping the main objective in mind, it is recommended to employ linear covariance propagation which makes use of state transition matrices for propagating uncertainties together with analytical approximation for model uncertainty. The method offers benefits in both realistic estimation of the future uncertainties together with lower computational costs, when compared to other methods of uncertainty propagation or a Monte-Carlo method.

CHAPTER 8

CONCLUSIONS AND FUTURE WORK

This research addresses the algorithmic design of the SSA catalogue for a large number of space objects. Different astrodynamical techniques are combined to tackle the problems of orbit propagation, orbit determination, and uncertainty propagation. Current challenges and major constraints when designing such a catalogue are outlined. The problem is elaborated in Chapter 1 and a five point objective is given. In this chapter, the solution or recommendation for each of the five objectives is summarised. In the end, notes on future work are presented.

8.1 Summary

The contributions and results for each of the five objectives are presented:

1. *Establish the requirements for the orbital theory that is to be employed in the catalogue maintenance system.*

A thorough literature study of the present and the future space object population was carried out in Chapter 2. By the year 2050, the number of space objects, with sizes ≥ 10 cm, will be on the order of 10^5. Accidental collisions, explosions, and planned large constellations are the main contributors to the increase of SO population. Better sensor technology, to observe fainter and smaller objects, will also increase the number of SOs that are identified. This provides an estimation of the number of objects to be maintained in the catalogue. Reviewing the present SOs observation technologies highlighted the limitations in terms of frequency of re-observation and accuracy of observations.

Using the above information, the goal for an orbit propagator was set as:

- Average propagation arc length to be seven days.
- Prediction accuracy of the propagator must be less than 50 m in position error, while keeping the radial error below 10 m for the arc length of seven days.
- Relative computational load of the propagator must be an order of magnitude smaller than a numerical propagator treating the same force models.

An orbital theory that employs the mean element space is beneficial for SOs cataloguing. An averaged element set behaves more linearly, and this makes formulation and implementation easier than the theory in osculating element space. Other favourable characteristics of a theory are elaborated in section 2.4. Having a common orbital theory for cataloguing purpose

is advantageous, which makes a theory in non-singular orbital elements more favourable over a theory formulated in classical orbital elements.

Following these requirements and reviewing several existing analytical and semi- analytical satellite theories in Chapter 3, the Draper Semi-analytical Satellite Theory (DSST) was selected for further analysis. DSST is formulated in non-singular equinoctial elements. DSST uses the generalised method of averaging technique to obtain mean element variational equations and the mean element equations of motion for modelling the perturbing forces. The recursive formulation allows the theory to be implemented in a modular form, making it suitable for efficient propagation of SOs in different orbital regions.

2. *Develop a generic test methodology for evaluating the performance of an orbit propagation method for the various orbital regions.*

After selecting DSST as a candidate propagator, it has been rigorously tested to establish its accuracy. Two sets of test cases were established during this research work:

The first set is to evaluate the significance of each perturbing force on the prediction accuracy and to test the correctness of the implementation of the force models. This method employed brute force testing of each perturbing forces to understand the residual signature and magnitude of the residuals from the least squares fit. The frequencies within the fit residuals highlights the missing perturbing forces. The test methods allowed force models in the different orbit propagators to be aligned.

The second set of test cases are to over come the lack of observations to test DSST in various orbital regions. A new test methodology was established, according to which a grid of imaginary satellites are distributed across the orbital space around the Earth. Each point on the grid is evaluated individually for testing the selected orbit propagator's accuracy in comparison with a numerical orbit integrator. This method of testing evaluated DSST thoroughly for most possible orbits from LEO to GEO together with HEO regions. Chapter 5 presents a complete description of the test methodologies and results. Multiple test procedures are employed, in which:

a) the semi-analytical theory is used to generate a perturbed trajectory. This trajectory is taken as the 'truth' to which a numerical trajectory is fit using least squares. The residuals demonstrate the numerical propagator's ability to replicate the semi-analytical truth ephemeris.

b) the numerical trajectory is taken as the 'truth' and the semi-analytical trajectory is fit to it. This procedure demonstrates both the semi-analytical theory and the semi-analytical partial derivatives within the least squares orbit determination.

c) independently generated ephemerides for a satellite equipped with a GPS receiver are used as the truth data. Both the numerical and the semi-analytical orbits were fit to the GPS data to compare the fit RMS.

3. *Study, evaluate, and propose a suitable satellite theory for the catalogue maintenance system. Extend the selected theory to make it suitable, in case of close match.*

The theoretical evaluation of DSST demonstrated that it is a close alternative for the numerical propagator. The theory includes extensive force models, and the standalone orbit propagator is implemented in a modular fashion. The established testing methods brought out the artefacts due to model truncations, series approximations, and missing perturbation models within the standalone DSST orbit propagator. From the initial results, several software

bugs were resolved. The coupling terms such as J_2/m-Daily tesseral terms are identified to be important in short periodic generator; they are essential for reaching the required orbit propagator accuracy. The time independent formulation of third body short periodic perturbations was insufficient to achieve the propagation accuracy of ≤ 50 m requirement in MEO and GEO regions. The absence of J_2 - Drag coupling contributes more to the LEO propagation error than the solid Earth tides and the third body perturbations.

These missing perturbation models were implemented, and the correctness of the orbit propagator was extensively tested. A weak time dependent formulation was derived in eccentric longitude and implemented to reach the accuracy of ≤ 10 m in higher altitudes. After the improvements and modifications, the standalone propagator has the following propagation accuracies:

Table 8.1 DSST propagation accuracy, for seven day orbital arc, in different orbital regimes in comparison to numerical propagator (ODEM).

Orbital class	Radial [m]	Along-track [m]	Cross-track [m]	Position RMS [m]
LEO	3.54	7.11	4.92	9.35
MEO	9.87	20.45	7.95	24.06
HEO	15.84	71.10	18.95	75.26
GEO	6.56	15.81	5.80	18.07

The goal of having propagation accuracy of less than 50 m position RMS, over the propagation arc of seven days, was fulfilled in LEO, MEO, and GEO regions. DSST suffered slightly higher inaccuracies in propagating highly eccentric orbits. The propagation RMS in HEO regime is around 75 m for seven day arc lengths. The main cause of the error for highly eccentric orbits with low perigee altitudes is from averaging of the drag forces. Also the eccentric longitude approximation in evaluating the weak time dependent terms for third body perturbations failed to capture the time dependent effects in eccentric orbits. Future efforts should be made on deriving a closed form approximation for the time dependent corrections in the mean longitude.

In SSA, where object observations are carried out either once per revolution, day, or on irregular intervals, the DSST outperforms numerical techniques by three to four orders in magnitude of computational runtime. Overall, the advantage from using a semi-analytical theory for the purpose of catalogue maintenance is in terms of the lower computational load and the compactness of information exchange. The advantage is at the cost of orbit prediction accuracies. However, deviations of predictions from DSST are within the acceptable range.

4. *Optimize computation of partial derivatives to allow use of the selected orbit propagator in a differential correction (i.e. orbit determination) process to assist the catalogue maintenance system.*

After testing DSST for its propagation accuracy, it is employed within a least squares orbit determination system. New functionalities of a semi-analytical way of computing the partial derivative matrix are implemented and successfully tested. The grid testing method evaluated the capabilities of the DSST orbit determination programs in different orbital regimes. DSST-OD performs very close in terms of accuracy to the numerical BLSQ. DSST-OD's computation

times are approximately 70% to 90% less than the ODEM run times in LEO, MEO and GEO orbital regimes. Test cases using PROBA-V GPS observation data, which were also used to replicate SSA type observation scenarios (sparse and very sparse observation sets) highlights the importance of recovery of short periodic effects within a SST. The a-priori radius of convergence for DSST-OD is an order of magnitude larger, in semi-major axis, than the radius of convergence for ODEM. Provided the a-priori is within this larger radius of convergence, the estimated orbit from DSST-OD is able to converge on the right set of orbital elements. Due to the precise transformations employed for mean to osculating conversion in DSST, the estimated orbits are without biases even when observations are very sparse.

Having the J_2 force model in the partial derivative matrices is sufficient for achieving the required convergence. As DSST-OD was estimating the orbits in mean equinoctial element space, the number of iterations were less than that of the ODEM when initialised with similar conditions. Extensive test cases carried out in Chapter 5 shows the benefits in different orbital regions. The lesser steps to convergence adds towards the advantages in saving the computational resources.

5. *Develop a method for estimating the model uncertainty in orbit predictions, and a method for realistic covariance propagation.*

The stochastic differential equation (SDE) method is employed together with the process noise formulation to estimate the effect of density model uncertainties on the orbit prediction uncertainty. From the literature review, it was established that the upper atmospheric densities vary both spatially and with time. This subtle effect, which can be called horizontal turbulence, is not captured within the current generation of atmospheric density models. An interpolated Gauss-Markov process was employed for characterising the density noise over the modelled atmosphere. Implementation of the same is used to test the closed form analytical solution obtained in relative R-T-N reference frame. The Clohessy-Wiltshire-Hill equations and their solution for the two body case is used in deriving the time dependencies of the position variances. The solution reaffirmed that the tangential direction is the most affected due to the noise in density. Conventionally in space operations, the square root of the variance in tangential direction is propagated using a quadratic time series (t^2). From the analytical solution it is observed that the variances behave more as a complete fifth order polynomial (t^5) (neglecting the one orbital periodic variations). The coefficients of these time polynomials are dependent on different factors, but mainly attributable to the temporal variation of the horizontal turbulence and the altitude.

It requires precise orbital information at different altitudes and various time periods to empirically capture the time correlation effects due to spatial variations in the densities. For the purpose of a catalogue maintenance system it is sufficient to capture the effects down to the order of propagation accuracy. The density noise model was used to estimate the time series polynomial coefficients for propagating density uncertainty in RTN states. In the end, the variations of the coefficients with altitude are approximated with parametric exponential models. This provides a simplistic means for evaluating the propagation uncertainty due to model uncertainty without using an orbit propagator. The method has shown that it is capable of efficiently capturing the variances in the satellite centred state frame. The established models are tested with precise orbital data. This shows that the combination of exponential model and the time polynomials is able to capture propagation uncertainties due to density uncertainties with the accuracy of 2%. This is on the order of a few meters for the propagation arc length of seven days.

In the final chapter 7, two different uncertainty propagation techniques were compared against Monte-Carlo simulations. The comparisons show that EKF together with process noise and density model uncertainty provides the most realistic covariances for the propagation arc length of seven days. Beyond which, both the UKF and the EKF uncertainty propagation methods did not represent the actual orbital uncertainty. The tests are also identified to be having a conservative view on the established methods, as it suffered from using very optimistic initial covariances.

8.2 Future Work

Despite the thorough analysis and research, there remains room to improve and build on the concept for the space object catalogue maintenance system. Together with the technical limitations, this work was impacted by arbitrary policies, with respect to real observation and orbital data. These policies come from both national and commercial entities. Three areas of future research, directly related to orbit and uncertainty propagation, suggest themselves.

- **Data and observations**

Having the capability to fuse different sensor information in correlation and orbit determination will greatly facilitate the usage of different observational techniques. Currently, NORAD and other national systems, ISON, SEESAT amateur observations, etc., are not cumulatively being considered for the purpose of cataloguing. Also, multi-sensor networks can remove the need for high accuracy, high cost, single observation sites. An ability to use sensor fusion techniques will push towards utilising low cost, low accuracy multi sensor tracking methods.

The problem of maximizing the number of catalogued objects while maintaining the quality of observation is a multi-variable optimization problem. Solution to this will provide an optimized observation scheduler. Although there are efforts being made to make use of neural networks and fuzzy logic to optimize the scheduler, this remains one of the important aspects to be tackled for the SOs cataloguing.

Space Situational Awareness should be viewed as a transnational programme. Improving the policy to facilitate international collaboration for data sharing will greatly improve the input to the catalogue system. The most desirable feature is to have continuous tracking of all debris, but it is beyond the present technical and economical capabilities of any single entity. Having a shared platform for different countries, agencies, or institutes would be an initial step towards achieving continuous tracking.

- **Drag, solar radiation pressure, and covariance realism**

The physical knowledge for predicting the geomagnetic storms, solar storms, or coronal mass ejections (CME) still is not completely understood. Orbits of satellites will be disturbed beyond recovery from most general procedures after such events. Figure 8.1 shows the number of satellites lost after a geomagnetic storm event in 1989 (NOAA, 2017). More than half the catalogued satellites were not found in the orbits where they were expected to be found. Although a Nature web publication (CNRS, 2018) claimed to predict the Sun's activity, these predictions are confined to a few hours before any major solar eruptions. If it happens that a CME is directed towards the Earth, all the SOs orbits will be disturbed. To handle such an event and to recover the catalogued objects it is important have a mechanisms to safeguard

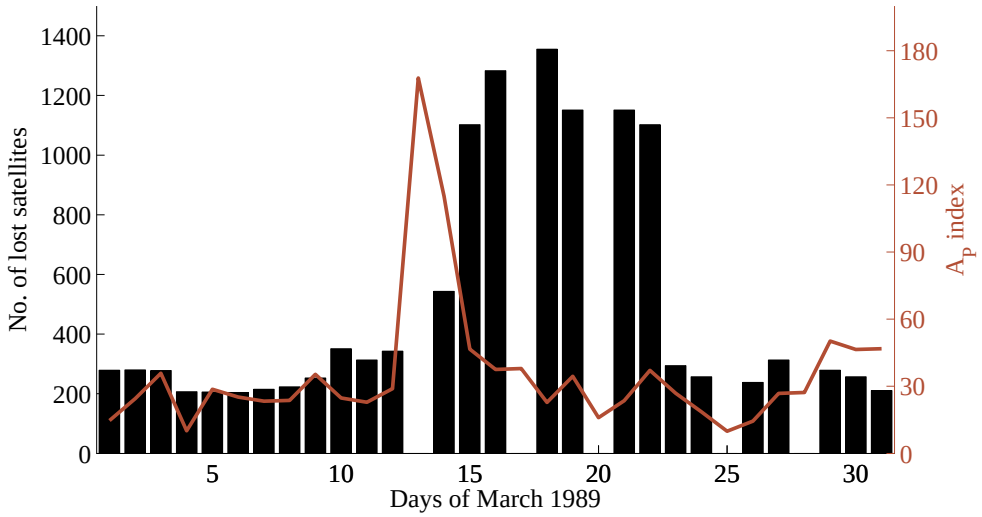

Fig. 8.1 Number of satellites lost from the NORAD catalogue following a geomagnetic storm. Data is extracted from (NOAA, 2017).

the collected information. This requires a procedure in place to recalibrate the catalogue after a solar storm and a method to handle the lost and found objects.

The developed density uncertainty model requires further investigation and quantification with real observational data. Within the proposed exponential model, the coefficients can be calibrated using the immediate past (few days before the present epoch) orbital data. The method requires additional study before it could be used for capturing the density uncertainties in orbit predictions. Needlessly to say, the effect of estimated covariance matrices on the space operations (probability of collision estimation) and observation correlation must be studied. The understanding will facilitate longer re-observation time lengths and reducing the required number of sensors. The approach presented for drag needs to be extended to treat solar radiation pressure as a stochastic system. This will improve the uncertainty estimation for MEO, GEO, and HEO objects.

Most cataloguing systems makes use of canon ball model to compute drag and SRP accelerations. It is required to understand the discrepancies of the spacecraft model simplification with actual space craft model.

Having the right size and orientation of covariance has an immense effect on a cataloguing system and catalogue's application. Methods for estimating and capturing different aspects of orbit uncertainty are a non-trivial challenge. A future study must elaborate on estimating a realistic covariance.

- **Improving the DSST and parallelization**

During this research work, considerable amount of effort was dedicated in improving the propagation accuracy of the DSST. There is still room for improving and optimising the semi-analytical propagator. The present weak-time dependent eccentric longitude approximation is capable of predicting third body perturbations for the orbits with eccentricities below 0.2. This problem must be further investigated to extend the capabilities to higher eccentricities. The atmospheric drag makes use of numerical quadratures to evaluate the averaged effect on a SO. It has been observed in the test results that this method is fast but fails to predict the orbits under high densities or with high eccentricities. Improving the quadrature method or

deriving an analytical formulation might facilitate the propagator in handling high density scenarios. The input on model selection for the DSST can be further optimized to deliver better accuracy vs computational time efficiency.

Most importantly, exploiting the present computational resources can be achieved better through parallel computing methods. Currently, the standalone DSST is free from common modules architecture and facilitates the vectorization of the propagation. But one might consider exploiting the modern coding paradigms together with concepts like Picard-Chebyshev methods to port the existing FORTRAN 77 version of the DSST standalone propagator to an advanced high level programming language.

In-line with the previously proposed exchanging observations on an open platform, it will be useful to have the open-source concept provide access to common software tools. This type of effort will facilitate the seamless data exchange from observatories to space operators and other users.

REFERENCES

Aida, S. and Kirschner, M. (2013). Accuracy assessment of sgp4 orbit information conversion into osculating elements. In *6th European Conference on Space Debris*.

Akella, M. R., Junkins, J. L., and Alfriend, K. T. (1998). Some consequences of force model uncertainty on probability of collision with orbital debris. *Journal of the Chinese Society of Mechanical Engineers, Transactions of the Chinese Institute of Engineers, Series C/Chung-Kuo Chi Hsueh Kung Ch'eng Hsuebo Pao*, 19(1):1–7.

Akim, E. L. and Golikov, A. R. (1993). Numeric-analytical satellite theory. *NASA STI/Recon Technical Report A*, 95:955–962.

Alby, F., Lansard, E., and Michal, T. (1997). Collision of cerise with space debris. In *Second European Conference on Space Debris*.

Alfano, S. (2003). Relating position uncertainty to maximum conjunction probability. In *AAS/AIAA Astrodynamics Specialists Conference*, San Diego, CA. AAS Publications Office.

Alfriend, K. T. (2010). *Spacecraft formation flying: Dynamics, control and navigation*. Elsevier astrodynamics series. Elsevier/Butterworth-Heinemann, Amsterdam and Boston and London, 1st ed. edition.

Barker, W. N., Casali, S. J., and Wallner, R. N. (1995). The accuracy of general perturbations and semi-analytical satellite ephemeris theories. In *AAS/AIAA Astrodynamics Conference*.

Battin, R. H. (1999). *An introduction to the mathematicsand methods of astrodynamics*. AIAA education series. American Institute of Aeronautics and Astronautics, isbn:1–56347–342–9 edition.

Berger, J. M., Moles, J. B., and Wilsey, D. G. (1992). *An Analysis of USSPACECOM's Space Surveillance Network (SSN) Sensor Tasking Methodology*. Master thesis, Air Force Institute of Technology, Faculty of the School of Engineering.

Berry, M. M. (2004). *A Variable Step Double Integration Numerical Integrator*. Doctor of philosophy, Faculty of the Aerospace Engineering, Virginia Polytechnic Institute and State University.

Beutler, G., Mervart, L., and Verdun, A. (2005). *Methods of celestial mechanics: Physical, mathematical, and numerical principles*, volume 1. Springer, Berlin and London.

Bezděk, A. and Vokrouhlický, D. (2004). Semianalytic theory of motion for close-earth spherical satellites including drag and gravitational perturbations. *Planetary and Space Science*, 52(14):1233–1249.

Boikov, V. F., Makhonin, G. N., Testov, A. V., Khutorovsky, Z. N., and Shogin, A. N. (2009). Prediction procedures used in satellite catalog maintenance. *Journal of Guidance, Control, and Dynamics*, 32(4):1179–1199.

Boyle, D. R., Mortari, D., and Pollock, T. (2006). Use of star trackers for space situational awareness. In *Space Control Conference (Classified), 2-4 May 2006, MIT Lincoln Laboratory, Lexington, MA*.

Brouwer, D. (1959). Solution of the problem of artificial satellite theory without drag. *The Astronomical Journal*, 64:378–376.

Brouwer, D. and Hori, G.-I. (1961). Theoretical evaluation of atmospheric drag effects in the motion of an artificial satellite. *The Astronomical Journal*, 66:193.

Cefola, P. J., Long, A., and Holloway, JR., G. (1974). The long-term prediction of artificial satellite orbits. In *12th Aerospace Sciences Meeting*.

Cefola, P. J. and Slutsky, M. S. (1981). Zonal harmonic short periodic model developed for the precision orbit propagation.

CNRS (2018). Towards a better prediction of solar eruptions. www2.cnrs.fr/sites/en/fichier/cp_eruptions_solaires_vd_anglais_web.pdf.

Coffey, S. and Deprit, A. (1982). Third-order solution to the main problem in satellite theory. *Journal of Guidance, Control, and Dynamics*, 5(4):366–371.

Coffey, S. L. and Alfriend, K. T. (1984). An analytic orbit prediction program generator. *Journal of Guidance, Control, and Dynamics*, 7(5):575–581.

Collins, S. K. (1981). *Long Term Prediction of High Altitude Orbits*. Doctor of philosophy, Department of Aeronautics and Astronautics, Massachusetts Institute of Technology.

Correia Da Costa, B., Bernardini, M., Cerf, M., Fessard, M., and Reynaud, S. (2012). Long-term semi-analytical orbit propagation tool for future european launchers design. In *AIAA/AAS Astrodynamics Specialist Conference*.

Crawford, M. (1991). NSOC precise orbits and atmospheric effects. Astrodynamics Conference, Dahlgren, VA.

Curry, G. R. (2005). *Radar system performance modeling*. Artech House radar library. Artech House, Boston, 2nd ed. ISB: 9781580538176 edition.

Danielson, D. A., Sagovac, C. P., and Snider, J. R. (1990). Satellite motion around an oblate planet: a perturbation solution for all orbital parameters. In *The Theory of Orbits in the Solar System and in Stellar Systems*, AIAA paper 90-2885.

Dell'Elce, L., Arnst, M., and Kerschen, G. (2015). Probabilistic assessment of the lifetime of low-earth-orbit spacecraft: Uncertainty characterization. *Journal of Guidance, Control, and Dynamics*, 38(5):900–912.

DeMars, K. J. (2010). *Nonlinear Orbit Uncertainty Prediction and Rectification for Space Situational Awareness*. Doctor of philosophy, Department of Aerospace Engineering, The University of Texas, Austin, Texas.

Doornbos, E. (2012a). Empirical modelling of the thermosphere. In Doornbos, E., editor, *Thermospheric Density and Wind Determination from Satellite Dynamics*, Springer Theses, pages 21–57. Springer Berlin Heidelberg, Berlin, Heidelberg.

Doornbos, E. (2012b). *Thermospheric Density and Wind Determination from Satellite Dynamics*. Phd thesis, Delft, Netherlands.

Eckstein, M., Shi, Y., and Kevorkian, J. (1966). Satellite motion for all inclinations around an oblate planet. In Kontopoulos, G. I., editor, *The Theory of Orbits in the Solar System and in Stellar Systems*, volume 25 of *IAU Symposium*, page 291.

Egan, M. P., Price, S. D., Wright, C. O., and Mizuno, D. R. (2003). The midcourse space experiment point source catalog version 2.3 explanatory guide. Air Force Research Laboratory, AFRL-VS-TR-2003-1589.

Emmert, J. T. (2015). Thermospheric mass density: A review. *Advances in Space Research*, 56(5):773–824.

Emmert, J. T., Warren, H. P., Segerman, A. M., Byers, J. M., and Picone, J. M. (2017). Propagation of atmospheric density errors to satellite orbits. *Advances in Space Research*, 59(1):147–165.

ESA (2016a). Copernicus sentinal-1a satellite hit by space particle. https://www.esa.int/Our_Activities/Observing_the_Earth/Copernicus/Sentinel-1/Copernicus_Sentinel-1A_satellite_hit_by_space_particle.

ESA (2016b). Space surveillance and tracking-sst segment. http://www.esa.int/Our_Activities/Operations/Space_Situational_Awareness/Space_Surveillance_and_Tracking_-_SST_Segment.

Fiedler, H., Weigel, M., Herzog, J., Schildknecht, T., Prohaska, M., Ploner, M., and Montenbruck, O. (2015). Smartnet: First experience of setting up a telescope system to survey the geostationary ring. In *25th International Symposium on Space Flight Dynamics*.

Finkleman, D. and Cefola, P. J. (2012). Progress in solving the unsolved problems in satellite theory. In *63rd International Astronautical Congress*.

Flegel, S. K., Krisko, P., Gelhaus, J., Wiedemann, C., Moeckel, M., Krag, H., Klinkrad, H., Xu, Y.-L., Horstman, M., Matney, M., and Vörsmann, P. (2010). Modeling the space debris environment with MASTER-2009 and ORDEM2010. In *38th COSPAR Scientific Assembly*, volume 38 of *COSPAR Meeting*.

Folcik, Z. J. and Cefola, P. J. (2012). A general solution to the second order j2 contribution in a mean equinoctial element semianalytic satellite theory. In *Advanced Maui Optical and Space Surveillance Technologies Conference*.

Folcik, Z. J., Lue, A., and Vatsky, J. (2011). Reconciling covariances with reliable orbital uncertainty. In *Advanced Maui Optical and Space Surveillance Technologies Conference*.

Fonte, D. J. (1993). *Implementing a 50x50 Gravity Field Model in an Orbit Determination System*. Master thesis, Department of Aerospace Engineering, Massachusetts Institute of Technology.

Fonte, D. J., Neta, B., Sabol, C., Danielson, D. A., and Dyar, W. R. (1995). Comparison of orbit propagators in the research and development goddard trajectory determination system - part 1: Simulated data. In *AAS/AIAA Astrodynamics Conference*.

Fonte, D. J. and Sabol, C. (1995). Optimal dsst input decks for various orbit types. Phillips Laboratory, PL-TR-95-1072.

Fraysse, H., Morand, V., Deleflie, F., Lamy, A., and Martin, T. (2011). Long term orbit propagation techniques developed in the frame of the french space act. In *Internation Symposium on Space Flight Dynamics*.

Fujimoto, K. and Scheeres, D. J. (2012). Rapid non linear uncertainty propagation via analytical techniques. In *Advanced Maui Optical and Space Surveillance Technologies Conference*.

Gaposchkin, E. M. (1994). Calculation of satellite drag coefficients. Lincoln Laboratory, Lexington, Massachusetts, 94-31038.

Gedeon, G. S. (1969). Tesseral resonance effects on satellite orbits. *Celestial Mechanics*, 1(2):167–189.

Gill, E. (2005). Mathematical descripton of the odem orbit determination software. German Aerospace Center, FDS-MTH-3020.

Goericke (1999). *Technical report on space debris: Text of the report adopted by the Scientific and Technical Subcommittee of the United Nations Committee on the Peaceful Uses of Outer Space*. United Nations, New York.

Golikov, A. R. (2012). Theona—a numerical-analytical theory of motion of artificial satellites of celestial bodies. *Cosmic Research*, 50(6):449–458.

Goodliff, K., Cornelius, D., and Sasamoto, W. (2006). Stochastic orbital lifetime analysis. *AIAA/USU Conference on Small Satellites*.

Green, A. J. (1979). *Orbit Determination and Prediction Processes for Low Altitude Satellites*. Doctor of philosophy, Massachusetts Institute of Technology, The Charles Stark Draper Laboratory, Inc., Boston, Massachusetts , USA.

Hairer, E., Nørsett, S. P., and Wanner, G. (2009). *Solving ordinary differential equations I: Nonstiff problems*, volume 8 of *Springer series in computational mathematics, 0179-3632*. Springer, Heidelberg and London, 2nd rev. ed. edition.

Herriges, D. L. (1988). *NORAD General Perturbation Theories an Independent Analysis*. Master of science, Massachusetts Institute of Technology, Boston, Massachusetts , USA.

Herzog, J. (2013). *Cataloguing of Objects on High and Intermediate Altitude Orbits*. Doctor of philosophy, Bern, Switzerland.

Hill, K., Sabol, C., and Alfriend, K. T. (2012). Comparison of covariance based track association approaches using simulated radar data. *Journal of the Astronautical Sciences*, 59(1-2):281–300.

Hill, K., Sydney, P., Hamada, K., Cortez, R., Luu, K., Jah, M. K., Schumacher, P. W., Coulman, M., Houchard, J., and Naho'olewa, D. (2010). Covariance-based network tasking of optical sensors. In *AAS/AIAA Space Flight Mechanics Meeting*.

Hoots, F. R. and France, R. G. (1984). Performance of an analytic satellite theory in a real-world environment. *Advances in the Astronautical Sciences*, 54:1067.

Hoots, F. R. and France, R. G. (1987). An analytic satellite theory using gravity and a dynamic atmosphere. *Celestial Mechanics*, 40(1):1–18.

Hoots, F. R. and Roehrich, R. L. (1980). SPACETRACK REPORT NO. 3 : Models for Propagation of NORAD Element Sets.

Hori, G.-I. (1971). Theory of general perturbations for non-canonical systems. *Publications of the Astronomical Society of Japan*, 23:567.

Horwood, J. T., Aristoff, J. M., Singh, N., and Poore, A. B. (2014). A comparative study of new non-linear uncertainty propagation methods for space surveillance. In *SPIE Defense and Security*, SPIE Proceedings, page 90920H. SPIE.

Horwood, J. T. and Poore, A. B. (2014). Gauss von Mises distribution for improved uncertainty realism in space situational awareness. *SIAM/ASA Journal on Uncertainty Quantification*, 2(1):276–304.

Hujsak, R. S. (1979). A Restricted Four Body Solution for Resonating Satellites Without Drag: Project Space Track: Special Astrodynamic Report No. 1. Aerospace Defence Command, United States Air Force.

IADC (2011). Space Debris: IADC Assessment Report for 2011. https://www.iadc-online.org/Documents.

Jakhu, R. S., Jasani, B., and McDowell, J. C. (2018). Critical issues related to registration of space objects and transparency of space activities. *Acta Astronautica*, 143:406–420.

Jenkin, A. B., Sorge, M. E., Peterson, G. E., McVey, J. P., and Yoo, B. B. (2015). Predicting the future of the space debris environment. https://www.aerospace.org/crosslinkmag/fall-2015/predicting-the-future-space-debris-environment.

Jones, B., Doostan, A., and Born, G. H. (2012). Nonlinear propagation of orbit uncertainty using non-intrusive polynomial chaos. *Journal of Guidance, Control, and Dynamics*.

Julier, S. J. and Uhlmann, J. K. (2004). Unscented filtering and nonlinear estimation. *Proceedings of the IEEE*, 92(3):401–422.

Kamel, A. A. (1982). Geosynchronous satellite perturbations due to earth's triaxiality and luni-solar effects. *Journal of Guidance, Control, and Dynamics*, 5(2):189–193.

Kamel, A. A. (1983). New nonsingular forms of perturbed satellite equations of motion. *Journal of Guidance, Control, and Dynamics*, 6(5):387–392.

Kaufman, B. (1981). First order semianalytic satellite theory with recovery of the short period terms due to third body and zonal perturbations. *Acta Astronautica*, 8(5-6):611–623.

Kaula, W. M. (1966). Theory of satellite geodesy. applications of satellites to geodesy. In *Waltham, Mass.: Blaisdell, 1966*.

Khutorovsky, Z. N. (2004). Techniques and algorithms for determination of orbits of leo satellites using measurements acquired during one penetration to the field of view of detection radar: Phase 1 and 2. KIA Systems, Moscow, Russia.

King-Hele, D. (1987). *Satellite orbits in an atmosphere. Theory and applications*. Glasgow : Blackie, ISBN 978-0-216-92252-5, Second edition.

Klebaner, F. C. (2005). *Introduction to stochastic calculus with applications*. Imperial College Press, London, Imperial College Press, ISBN: 1-86094-555-4, 2nd. edition.

Klinkrad, H. (2006). *Space Debris: Models and Risk Analysis*. Springer-Praxis books in astronautical engineering. Berlin, Springer-Praxis books in astronautical engineering, ISBN: 9783540254485, 1st edition.

Kozai, Y. (1959). The motion of a close earth satellite. *The Astronomical Journal*, 64:367.

Kragel, B., Herman, S., and Roseveare, N. (2012). A comparison of methods for estimating track-to-track assignment probabilities. *IEEE Transactions on Aerospace and Electronic Systems*, 48(3).

Kubo-oka, T., Fuse, T., and Kunimori, H. (2015). Optical survey of geosynchronous satellite. In *33rd International Communications Satellite Systems Conference*.

Lane, M. (1965). The development of an artificial satellite theory using a power-law atmospheric density representation. In *2nd Aerospace Sciences Meeting*.

Lara, M., San-Juan, J. F., and Hautesserres, D. (2018). Heosat: a mean elements orbit propagator program for highly elliptical orbits. *CEAS Space Journal*, 10(1):3–23.

Lawler, G. F. (2006). *Introduction to stochastic processes*. Chapman & Hall/CRC, Boca Raton, Chapman & Hall/CRC, ISBN: 978-1584886518, 2nd edition.

Lechtenberg, T., McLaughlin, C. A., Locke, T., and Krishna, D. M. (2013). Thermospheric density variations: Observability using precision satellite orbits and effects on orbit propagation. *Space Weather*, 11(1):34–45.

Lee, B.-S., Lee, J. S., Yoon, J. C., and Choi, K.-H. (1997). A new analytical ephemeris solution for the geostationary satellite and its application to koreasat. *Space Technology*, 17:299.

Lin, Q., Lai, J., Li, Z., and Xiong, Z. (2007). Simulation analysis of space debris environment and threat pre-warning: Interactive session on space debris. In *58th International Astronautical Congress*, volume IAC-07-A6.I.01.

Liou, J. C. (2018). Overview of the orbital debris environment. In *Space Traffic Management Conference*.

Liou, J. C. and Johnson, N. L. (2007). A sensitivity study of the effectiveness of active debris removal in leo. In *58th International Astronautical Congress*, volume IAC-07-A6.3.05.

Liu, J. J. F. and Alford, R. L. (1979). A semi-analytic theory for the motion of a close-earth artificial satellite with drag. In *17th Aerospace Sciences Meeting*.

Liu, J. J. F. and Alford, R. L. (1980). Semianalytic theory for a close-earth artificial satellite. *Journal of Guidance, Control, and Dynamics*, 3(4):304–311.

Mahalanobis, P. C. (1936). On the generalized distance in statistics. In *Proceedings of the National Institute of Sciences*.

McClain, W. D. (1977). A recursively formulated first-order semianalytic artificial satellite-theory: Volume 1: The generalized method of averaging applied to artificial satellite problem. Computer Sciences Corporation, CSC/TR-77/6010.

McClain, W. D. (1978). A recursively formulated first-order semianalytic artificial satellite theory based on the generalized method of averaging: Volume 2: The explicit development of the first-order averaged equations of motion for the nonspherical gravitaional and nonresonant third-body perturbations. Computer Sciences Corporation, CSC/TR-78/6001.

Mehrholz, D., Leushacke, L., Flury, W., Jehn, R., Klinkrad, H., and Landgraf, M. (2002). Detecting, tracking and imaging space debris. ESA, Ref: 109-Feb2002.

Mellab, K., Galano, D., Santandrea, S., and Teston, F. (2011). The PROBA-V mission. In *International Academy of Astronautics Symposium on Small Satellites for Earth Observation, Berlin, Germany, 2011*.

Mersman, W. A. (1970). A new algorithm for the lie transformation. *Celestial Mechanics*, 3(1):81–89.

Milani, A., Nobili, A. M., and Farinella, P. (1987). *Non-gravitational perturbations and satellite geodesy*. Hilger, Bristol, Hilger-Bristol, ISBN: 0-85274-538-9, 1st edition.

Miller, J. G. (2007). A new sensor allocation algorithm for the space surveillance network. *Military Operations Research*, 12(1):57–70.

Minihold, R. and Bues, D. (2012). Introduction to radar system and component tests: White paper. Rohde & Schwarz, 08-2012-1MA207-0e.

Molotov, I., Agapov, V., Titenko, V., Khutorovsky, Z., Burtsev, Y., Guseva, I., Rumyantsev, V., Ibrahimov, M., Kornienko, G., Erofeeva, A., Biryukov, V., Vlasjuk, V., Kiladze, R., Zalles, R., Sukhov, P., Inasaridze, R., Abdullaeva, G., Rychalsky, V., Kouprianov, V., Rusakov, O., Litvinenko, E., and Filippov, E. (2008). International scientific optical network for space debris research. *Advances in Space Research*, 41(7):1022–1028.

Montenbruck, O. and Gill, E. (2001). *Satellite Orbits: Models, Methods, and Applications*. Springer, Springer, ISBN:978-3-642-58351-3, 1st edition.

Morrison, J. A. (1965). Generalized method of averaging and the von zeipel method. In *Thermophysics Specialist Conference*.

Morton, M. M. and Roberts, T. (2011). Joint space operations center (jspoc) mission system (jms). In *Advanced Maui Optical and Space Surveillance Technologies Conference*.

Mueller, A., Scheifele, G., and Starke, S. (1979). An analytical orbit predictor for near-earth satellites. In *AIAA, Aerospace Sciences Meeting*.

Naka, R. F., Walter, L. G., Pensa, A. F., Tennant, S. M., and Judd, O. P. (1997). Report on Space Surveillance, Asteroids and Comets, and Space Debris. Volume 1: Space Surveillance. United States Air Force Scientific Advisory Board, Ref: SAB-TR-96-04.

NASA-ODPO (2016). NASA Orbital Debris Office: Quaterly News, October Issue 4. National Aeronautics and Space Administration.

Nazarenko, A. I. (2014). Prediction of the space debris spatial distribution on the basis of the evolution equations. *Acta Astronautica*, 100:47–56.

Nechak, L., Berger, S., and Aubry, E. (2010). Uncertainty propagation using polynomial chaos and center manifold theories. *Recent Advances in Signal Processing, Robotics and Automation*, pages 46–51.

Neelon, JR., J. G., Cefola, P. J., and Proulx, R. J. (1997). Current development of the draper semianalytical satellite theory standalone orbit propagator package. In *Astrodynamics Conference*.

No, T. S. and Jung, O. C. (2005). Analytical solution to perturbed geosynchronous orbit. *Acta Astronautica*, 56(7):641–651.

NOAA (2017). Space weather prediction center: Satellite drag. https://www.swpc.noaa.gov/impacts/satellite-drag.

O'Brien, R. and Sang, J. (2004). Semianalytic satellite theory using the method of multiple scales. In *AIAA/AAS Astrodynamics Specialist Conference and Exhibit*.

Oltrogge, D. and Alfano, S. (2015). COMSPOC Update and Operational Benefits. In *31st Space Symposium, Colorado Springs, Colorado*.

Poore, A. B., Aristoff, J. M., and Horwood, J. T. (2016). Covariance and uncertainty realism in space surveillance and tracking. Numerica Corporation, Fort Collins, CO.

Proulx, R. J. (1982). Mathematical description of the tesseral resonance and resonant harmonic coefficient solve-for capabilities. Charles Stark Draper Laboratory, Ref: NSWC-001-15Z-RJP.

Proulx, R. J., McClain, W. D., Early, L. W., and Cefola, P. J. (1981). A theory for the short-periodic motion due to the tesseral harmonic gravity field. In *AAS/AIAA Astrodynamics Specialists Conference*, San Diego, CA. AAS Publications Office.

Sabol, C. A. (2010). Linearized orbit covariance generation and propagation analysis via simple monte carlo simulations. Air Force Research Laboratory.

Seago, J. H., Griesbach, J., Woodburn, J. W., and Vallado, D. A. (2011). Sequential orbit-estimation with sparse tracking. In *AAS/AIAA Space Flight Mechanics Meeting*, pages 281–299.

Setty, S. J., Cefola, P. J., Fiedler, H., and San-Juan, J. F. (2016a). Attributes affecting the accuracy of a batch least square orbit determination using semi-analytical satellite theory. In *AMOS 2016 – Advanced Maui Optical and Space*, Maui, USA.

Setty, S. J., Cefola, P. J., Montenbruck, O., and Fiedler, H. (2014). Prediction accuracies of draper semi-analytical satellite theroy in leo, meo ahd heo regime for space object catalogue maintenance. In *AAS/AIAA Space Flight Mechanics Meeting*, San Diego, CA. AAS Publications Office.

Setty, S. J., Cefola, P. J., Montenbruck, O., and Fiedler, H. (2016b). Application of semi-analytical satellite theory orbit propagator to orbit determination for space object catalog maintenance. *Advances in Space Research*, 57(2016):2218–2233.

Setty, S. J., Cefola, P. J., Montenbruck, O., Fiedler, H., and Lara, M. (2013). Investigation the suitability of analytical and semi-analytical satellite theories for space object catalogue maintenance in geosynchronous tegime. In *AAS/AIAA –Astrodynamics Specialist Conference*.

Sharifi, M. A. and Seif, M. R. (2011). Dynamic orbit propagation in a gravitational field of an inhomogeneous attractive body using the lagrange coefficients. *Advances in Space Research*, 48(5):904–913.

Singer, Y. and Warmuth, M. K. (1998). A new parameter estimation method for gaussian mixtures. *Advances in Neural Information Processing Systems*, 11.

Skolnik, M. I. (1981). *Introduction to radar systems*. McGraw-Hill International, Auckland and Singapore, 2nd ed., international student ed. edition.

Slutsky, M. S. (1983). The first-order short-periodic motion of an artificial satellite due to third body perturbations - numerical evaluation. *Advances in the Astronautical Sciences*, 54:1001–1022.

Slutsky, M. S. and McClain, W. D. (1981). The first-order short-periodic motion of an artificial satellite due to third body perturbations. In *AAS/AIAA Astrodynamics Specialists Conference*, San Diego, CA. AAS Publications Office.

Space News (2015). OneWeb Taps Airbus to Build 900 Internet Smallsats. http://spacenews.com/airbus-wins-oneweb-contract/.

Sproll, F., Hampf, D., Riede, W., Eckl, J., Riepl, S., Schreiber, U., Bamann, C., Hugentobler, U., Kirchner, G., and Koidl, F. (2016). Two-color and multistatic space debris laser tracking. In *20th International Workshop on Laser Ranging*.

Sridharan, R. and Seniw, W. (1980). *ANODE: An Analytic Orbit Determination System*. Number v. 1. MIT Lexington Lincoln Lab. and Defense Technical Information Center.

Tapley, B., Bettadpur, S., Watkins, M. M., and Reigber, C. (2003). The gravity recovery and climate experiment: Mission overview and early results. Geophys. Res. Lett., 31, L09607, doi:10.1029/2004GL019920.

Tapley, B. D., Schutz, B. E., and Born, G. H. (2004). *Statistical orbit determination*. Elsevier Academic Press, ISBN: 9781281018939, Amsterdam and Boston.

Tardioli, C. and Vasile, M. (2015). Collision and re-entry analysis under aleotory and epistemic uncertainty. In *AIAA/AAS Astrodynamics Specialist Conference and Exhibit*.

Taylor, S. P. (1982). *Semianalytical Satellite Theory and Sequential Estimation*. Master of science, Department of Mechanical Engineering, Massachusetts Institute of Technology.

US General Accounting Office (1997). Space Surveillance: DOD and NASA Need Consolidated Requirements and a Coordinated Plan.

Valk, S., Lemaître, A., and Anselmo, L. (2008). Analytical and semi-analytical investigations of geosynchronous space debris with high area-to-mass ratios. *Advances in Space Research*, 41(7):1077–1090.

Valk, S., Lemaître, A., and Deleflie, F. (2009). Semi-analytical theory of mean orbital motion for geosynchronous space debris under gravitational influence. *Advances in Space Research*, 43(7):1070–1082.

Vallado (2018). Satellite Catalogue (SAT CAT). https://celestrak.com/satcat.

Vallado, D. A. (1997). *Fundamentals of Astrodynamics and Applications*. Space technology series. McGraw-Hill, Space technology series, ISBN: 0-07-066829-9.

Vallado, D. A. (2005). An analysis of state vector propagation using differing flight dynamics programs. In *AAS/AIAA Space Flight Mechanics Meeting*.

Vallado, D. A., Ackermann, M. R., Cefola, P. J., and Kiziah, R. R. (2016). Orbital strategies to mitigate the solar exclusion effect on space-based observation of geo. In *AAS/AIAA Astrodynamics Specialists Conference 2016*.

Vallado, D. A. and Alfano, S. (2011). Curvilinear coordinates for covariance and relative motion operations. In *AAS/AIAA Astrodynamics Specialists Conference*.

Vallado, D. A., Crawford, P., Hujsak, R. S., and Kelso, T. S. (2006). Revisiting spacetrack report no. 3. In *AIAA/AAS Astrodynamics Specialist Conference 2006*.

Vallado, D. A. and Finkleman, D. (2008). A critical assessment of satellite drag and atmospheric density modeling. In *AAS/AIAA Astrodynamics Specialists Conference*.

Vetter, J. R. (2007). Fifty years of orbit determination: Development of modern astrodynamics methods. *Johns Hopkins Apl Technical Digest*, 27(3):239–252.

Vinti, J. P. (1961). Theory of an accurate intermediary orbit for satellite astronomy. National Bureau of Standards, USA.

Wagner, E. A. (1986). The extended semianalytical kalman filter and its application to synchronous orbits. *Journal of the Astronautical Sciences*, 34:147–159.

Walsh, D. W. (2013). A survey of radars capable of providing small debris measurements for orbit prediction. https://pdfsecret.com/download/a-survey-of-radars-capable-of-providing-small-debris_5a31f03dd64ab212338fd807_pdf.

Weigel, M. and Patyuchenko, A. (2011). Orbit determination error analysis for a future space debris tracking radar. In *European Space Surveillance Conference*.

Wilkins, M. P. and Alfriend, K. T. (2000). Characterizing orbit uncertainty due to atmospheric uncertainty. In *AIAA/AAS Astrodynamics Specialist Conference*.

Wnuk, E. (2002). Prediction of artificial satellite positions on the basis of the second order theory of motion. *Advances in Space Research*, 30(2):321–330.

Yurasov, V. S. (1996). Universal semianalytic satellite motion propagation method. In *Second US-Russian Space Surveillance Workshop*.

Yurasov, V. S., Nazarenko, A. I., Cefola, P. J., and Alfriend, K. T. (2005a). Application of the arima model to analyze and forecast the time series of density corrections for nrlmsis-00. In *AAS/AIAA Astrodynamics Specialists Conference*.

Yurasov, V. S., Nazarenko, A. I., Cefola, P. J., and Alfriend, K. T. (2005b). Density corrections for the nrlmsis-00 atmosphere model. In *AAS/AIAA Space Flight Mechanics Meeting*.

Zadunaisky, P. E. (1976). On the estimation of errors propagated in the numerical integration of ordinary differential equations. *Numerische Mathematik*, 27(1):21–39.

Zeis, E. G. (1977). *A computerized Algebraic Utility for the Construction of Non-singular Satellite Theories*. Master of science, Department of Mechanical Engineering, Massachusetts Institute of Technology.

APPENDIX A

DSST STANDALONE PROGRAM

The DSST standalone offers the access to the Draper Semi-analytical Satellite theory as both orbit propagator and orbit determination package. The output from the standalone software is via text files, and the output can be tailored to the very specific requirements of a calling program. Currently, the standalone consists of three calling routines:

1. Orbit propagator services
2. Orbit determination services
3. Uncertainty propagator services

Flowcharts A.1 and A.2 presents the high-level input and output flow for the above three services. The charts also present different output requests available in propagator services and observation models within orbit determination services.

The propagator is called via the linking script "dsst_orbsim.com". The script processes the link for data files, some of them are in binary format; attaches the "pmef.txt", which is the propagator settings file; and points to the dsst executable. The list of required physical model files are:

- Solar flux and geo-magnetic indices for Jacchia- Roberts and Jacchia- Gill density models
- Geopotential models
- Solar Lunar Planetary and timing coefficients
- Coordinate system constants
- Modified Newcomb operators (Hansen coefficients used in the tesseral resonance and tesseral linear combination short-periodic models)
- International Earth Rotation and Reference Systems (IERS)

Except the IERS tables all the other files are provided in binary format. Using binary format has proven efficient in terms of computational runtime. Section A.1 provides the complete list of available keywords to tailor the propagator and orbit determination runs.

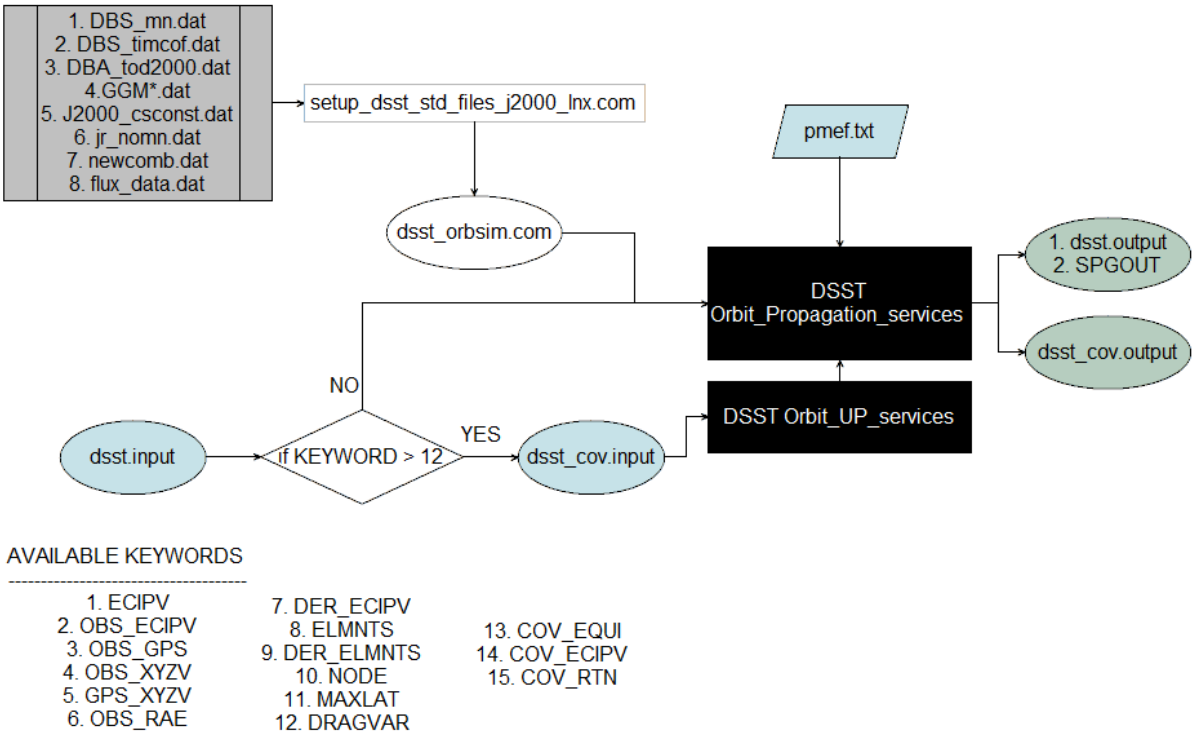

Fig. A.1 High level input and output flow for DSST standalone orbit propagator services and uncertainty propagator services together with the list of available output keyword options.

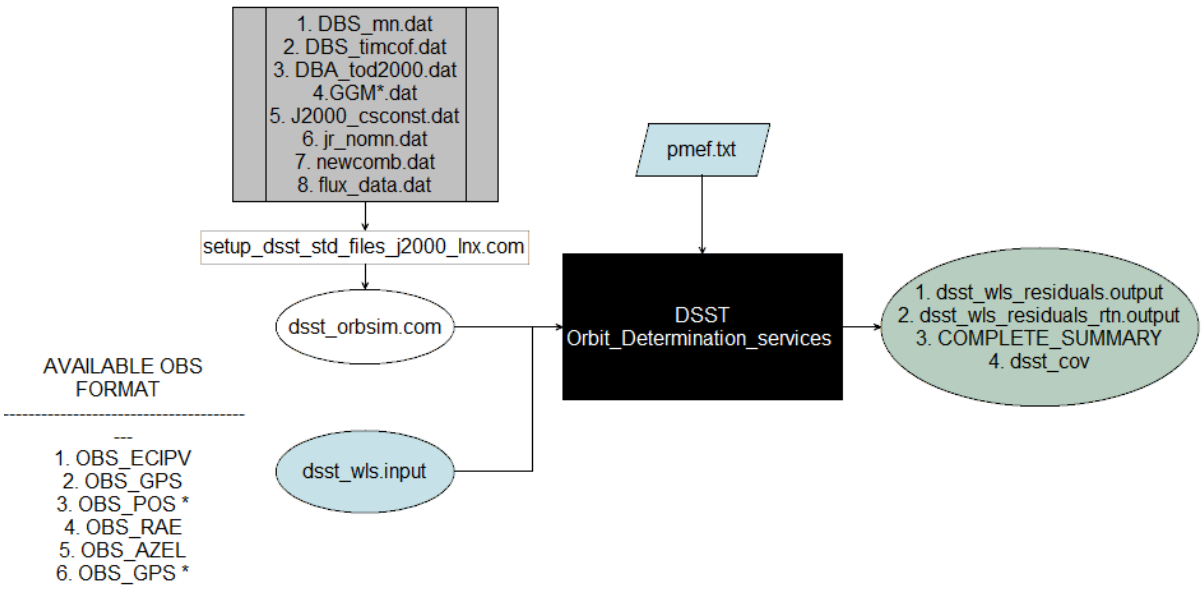

Fig. A.2 High level input and output flow for DSST standalone orbit determination services together with the list of observations which are able to be processed within the current software.

A.1 DSST Input Settings and Outputs

Parameter		Description
Epoch of mean elements file		
PME_DATE	1	YYYYMMDD
PME_TIME	2	HHMMSS.SSSS
Mean Kepler element set at Epoch time		
ELS_KEP(1)	3	Mean semi-major axis (km)
ELS_KEP(2)	4	Mean eccentricity
ELS_KEP(3)	5	Mean inclination (deg)
ELS_KEP(4)	6	Mean right ascension (deg)
ELS_KEP(5)	7	Mean argument of Perigee (deg)
ELS_KEP(6)	8	Mean mean anomaly (deg)
Mean Equinoctial element set at Epoch time		
ELS_EQUIN(1)	9	Mean semi-major axis (km)
ELS_EQUIN(2)	10	Mean eccentricity vector h
ELS_EQUIN(3)	11	Mean eccentricity vector k
ELS_EQUIN(4)	13	Mean inclination vector p
ELS_EQUIN(5)	14	Mean inclination vector q
ELS_EQUIN(6)	15	Mean mean longitude (deg)
Mean Position and Velocity set at Epoch time		
POSVEL(1)	16	x position component (km)
POSVEL(2)	17	y position component (km)
POSVEL(3)	18	z position component (km)
POSVEL(4)	19	x' velocity component (km/s)
POSVEL(5)	20	y' velocity component (km/s)
POSVEL(6)	21	z' velocity component (km/s)
Spacecraft parameters		
PME_CD	22	Drag coefficient to be used with mean elements (DSST assumes a spherical spacecraft model)
PME_CR	23	Solar radiation pressure coefficient to be used with mean elements (DSST assumes a spherical spacecraft model)
PME_RHO_ONE	24	Currently not used in standalone
SMA_SIGMA	25	Currently not used in standalone
INC_SIGMA	26	Currently not used in standalone
ASC_SIGMA	27	Currently not used in standalone
PME_SCMASS	28	Spacecraft mass (kg)
PME_SCAREA	29	Spacecraft surface area (km^2)
ODEG integration		
PME_STEPSIZE	30	Integrator stepsize (suggested value: 43200 s)
DP_SPARE1	31	Currently not used in standalone
DP_SPARE2	32	Currently not used in standalone

Parameter		Description
DP_SPARE3	33	Currently not used in standalone
DP_SPARE4	34	Currently not used in standalone
DP_SPARE5	35	Currently not used in standalone
DP_SPARE6	36	Currently not used in standalone
RESPRD	37	Period tolerance for tesseral resonance from central body spherical harmonics in seconds (Default : 864000 s [10 days])
RESORB	38	Period tolerance for tesseral resonance from central body spherical harmonics in satellite revolutions (Default : 10 Days, Minimum allowed is 3 days)
Equinoctial retrograde factor		
PME_RETRO	38	Equinoctial retrograde factor value: 1= Direct elements value: -1= Retrograde elements
Reference frames		
PME_KEP_SYS	39	Coordinate systems for Keplerian elements value: 1= Mean of 1950 value: 2= True of reference (1950) value: 11= Mean of J2000 value: 12= True of reference (J2000)
POS_VEL_SYS	40	Coordinate systems for Cartesian elements value: 1= Mean of 1950 value: 2= True of reference (1950) value: 11= Mean of J2000 value: 12= True of reference (J2000)
Atmospheric density model		
GEN_METHOD	41	Currently not used in standalone
ATMOS_MODEL	42	Atmospheric density model selection value: 1= Jacchia-Roberts value: 2= Harris-Priester value: 3= Jacchia 64 (stub) value: 4= Jacchia 70 (stub) value: 5= MSIS (stub) value: 20= JAcchia-Gill
JACRB_DATE	43	Creation date (YYMMDD) Jacchia file, value: 840401
JACRB_SSS	44	Seq number of Jacchia file, value: 123
SLP1950_DATE	45	Creation date (YYMMDD) SLP1950 file, value: 840401
SLP1950_SSS	46	Seq number of SLP1950 file, value: 456
SLPTOD_DATE	47	Creation date (YYMMDD) SLPTOD file, value: 840401
SLPTOD_SSS	48	Seq number of SLPTOD file, value: 789
TIMECF_DATE	49	Creation date (YYMMDD) TIMECF file, value: 840401
TIMECF_SSS	50	Seq number of SLPTOD file, value: 123
HARRIS_MODEL	51	Harris-Priester model number (F10.7 value selection) value: 1 = F10.7 =65 value: 2 = F10.7 =75

Parameter		Description
		value: 3 = F10.7 =100 value: 4 = F10.7 =125 value: 5 = F10.7 =150 value: 6 = F10.7 =175 value: 7 = F10.7 =200 value: 8 = F10.7 =225 value: 9 = F10.7 =250 value: 10 = F10.7 =275
Potential model selection		
POTNTL_MODEL	52	Gravity model selection value: 1 = Not used in DSST value: 2 = Grace Gravity Model GGM01S value: 3 = Not used in DSST value: 4 = Not used in DSST
PME_NMAX	53	Max degree of central body field used (≤ 50)
PME_MMAX	54	Max order of central body field used (≤ 50)
PME_IZONAL	55	Central body zonal harmonic included in averaged orbit generator value: 1 = Analytical averaging value: 3 = Off
PME_IJ2J2	56	J_2^2 effect included in averaged orbit generator value: 1 = On value: 3 = Off
PME_NMAXRS	57	Max degree of resonant terms used in ODEG (≤ 50)
PME_MMAXRS	58	Max order of resonant terms used in ODEG (≤ 50)
PME_ITHIRD	59	Third body averaging option inclusion flag value: 1 = Analytical averaging value: 3 = Off
PME_INDDRG	60	Atmospheric drag inclusion flag value: 1 = Yes, included value: 3 = No, not included
PME_ISZAK	61	Iszak J_2 height correction inclusion flag value: 1 = Yes, included value: 3 = No, not included
PME_INDSOL	62	Solar radiation pressure inclusion flag value: 1 = Yes, included value: 3 = No, not included
PME_JSHPER	63	Changed the settings (to be removed in future)
PME_JZONAL	64	Changed the settings (to be removed in future)
PME_JMDALY	65	Changed the settings (to be removed in future)
Co-ordinates and reference frames		
PME_INP_TYPE	66	Type of element input value: 1 = Position/Velocity value: 2 = Keplerian elements

Parameter		Description
		value: 3 = Equinoctial
PME_EQUI_SYS	67	Coordinate systems for Equinoctial elements value: 1= Mean of 1950 value: 2= True of reference (1950) value: 11= Mean of J2000 value: 12= True of reference (J2000)
INTEG_FRAME	68	Integration frame value: 11= Mean of J2000 value: 12= True of reference (J2000)
OUTPUT_FRAME	69	Output reference frame value: 1= Mean of 1950 value: 2= True of reference (1950) value: 8= NORAD value: 11= Mean of J2000 value: 12= True of reference (J2000)
PME_NSTATE	70	Changed the settings (to be removed in future)
Short periodic model selection		
PME_SPSHPER	71	Preset Short-periodic model used by the semianalytic orbit generator value: 1= Mean Elements only value: 2= Low altitude, near circular orbit (moderate accuracy option) value: 3= Low altitude, near circular orbit (improved accuracy option) value: 4= 24 Hour Geosynchronous Orbit (moderate accuracy option) value: 5= 12 Hour high eccentricity Molniya Orbit (moderate accuracy option) value: 6= Manual selection. Settings from line 101 to 132 be used value: 7= Low altitude, Eccentric orbit (moderate accuracy option) value: 8= Low altitude, Eccentric orbit (improved accuracy option) value: 9= Medium altitude(MEO) (moderate accuracy option) value: 10= Medium altitude(MEO) (improved accuracy option) value: 11= Highly elliptical orbit (HEO) (improved accuracy option) value: 12= Geosynchronous orbits (GEO) (improved accuracy option)
PME_KSPCF	72	Print the short periodic coefficients in the SPGOUT file

Parameter		Description
PME_INDSET	73	Solid Earth tide indicator value: 1 = Solar and Lunar tidal effects value: 2 = Solar tidal effects only value: 3 = Lunar tidal effects only value: 4 = No tidal effects
INT_SPARE1	74	Currently not used in standalone
INT_SPARE2	75	Currently not used in standalone
INT_SPARE3	76	Currently not used in standalone
INT_SPARE4	77	Currently not used in standalone
INT_SPARE5	78	Currently not used in standalone
INT_SPARE6	79	Currently not used in standalone
INT_SPARE7	80	Currently not used in standalone
INT_SPARE8	81	Currently not used in standalone
INT_SPARE9	82	Currently not used in standalone
INT_SPARE10	83	Currently not used in standalone
Partial derivative options		
PD_IANAL	84	Compute partial derivatives by analytical method (only for state transition matrix) value: 1 = Yes value: 3 = No
PD_IDIFF	85	Compute partial derivatives by finite differencing method (only for sensitivity matrix) value: 1 = Yes value: 3 = No
PD_IQDRT	86	Currently not used in standalone
PD_SHORT	87	Currently not used in standalone
PD_ICBVAR	88	Currently not used in standalone
PD_J22VAR	89	Currently not used in standalone
PD_ITBVAR	90	Currently not used in standalone
PD_IDRVAR	91	Currently not used in standalone
PD_ISRVAR	92	Currently not used in standalone
PD_KGRAVP	93	Currently not used in standalone
PD_KPRTB1	94	Print the partial derivatives in the SPGOUT file
PD_KPRTB2	95	Print the partial derivatives in the SPGOUT file
PD_KPRTB3	96	Print the partial derivatives in the SPGOUT file
PD_KPRTB4	97	Print the partial derivatives in the SPGOUT file
Orbit determination settings		
PD_NSTATE	98	Number of state parameters to be estimated at Epoch in DSST_OD (Default = 6)
PD_NDYNAM	99	Number of dynamic parameters to be estimated (Default is 0 and maximum allowed is 2)

Parameter		Description
PD_NSOLVE	100	Total number of parameters to be estimated in DSST_OD (NSOLVE = NSTATE+NDYNAM) (currently redundant input parameter)

Manual short periodic flags

SP_ZONALS	101	Zonal short periodic inclusion value: 1 = Yes, included value: 3 = No, not included
SP_MDAILY	102	M Daily short periodic inclusion value: 1 = Yes, included value: 3 = No, not included
SP_J2MDLY	103	J_2 - M Daily coupling terms inclusion value: 1 = Yes, included value: 3 = No, not included
SP_TESSLC	104	Tesseral short periodic inclusion value: 1 = Yes, included value: 3 = No, not included
SP_J2SQ	105	J_2^2 short periodic inclusion value: 1 = Yes, included value: 3 = No, not included
SP_LUNSOL	106	Third body short periodic inclusion value: 1 = Yes, included value: 3 = No, not included

Manual short expansion settings

SP_NZN	107	Maximum degree of high frequency (Linear Combination) zonal harmonic expansion
SP_LZN	108	Maximum order of high frequency (Linear Combination) zonal harmonic expansion
SP_JZN	109	Maximum frequency in central-body longitude (θ) expansion
SP_NMD	110	Maximum degree of high frequency (Linear Combination) M-daily expansion
SP_MMD	111	Maximum order of high frequency (Linear Combination) M-daily expansion
SP_LMD	112	
SP_NJ2MD	113	Maximum degree of high frequency (Linear Combination) J_2 - M-daily coupling terms
SP_MJ2MD	114	Maximum order of high frequency (Linear Combination) J_2 - M-daily coupling terms
SP_LJ2MD	115	
SP_IDRMD	116	Flag to include drag terms in J_2 - M daily coupling term
SP_NTS	117	Maximum degree of high frequency (Linear Combination) tesseral harmonic expansion

Parameter		**Description**
SP_MTS	118	Maximum order of high frequency (Linear Combination) tesseral harmonic expansion
SP_LTS	119	Maximum d'Alembert of high frequency (Linear Combination) tesseral harmonic expansion
SP_LTSHAN	120	Maximum power of e^2 in series for Hansen coefficients
SP_JMINTS	121	Maximum frequency in mean longitude (λ) for tesseral harmonic expansion
SP_JMAXTS	122	Minimum frequency in mean longitude (λ) for tesseral harmonic expansion
SP_LUN_NTH	123	Short periodic setting; currently not in use
SP_LUN_JMX	124	Short periodic setting; currently not in use
SP_LUN_LTH	125	Short periodic setting; currently not in use
SP_LUN_ITD	126	Short periodic setting; currently not in use
SP_LUN_NTD	127	Short periodic setting; currently not in use
SP_SOL_NTH	128	Short periodic setting; currently not in use
SP_SOL_JMX	129	Short periodic setting; currently not in use
SP_SOL_LTH	130	Short periodic setting; currently not in use
SP_SOL_ITD	131	Short periodic setting; currently not in use
SP_SOL_NTD	132	Short periodic setting; currently not in use

Name	dsst.output file (ELMNTS request)
EPOCH_YMD	Output request time
ELEMENTS (1)	Semimajor axis (km) at the output request time
ELEMENTS (2)	Eccentricity at the output request time
ELEMENTS (3)	Inclination (deg) at the output request time
ELEMENTS (4)	Ascending node (deg) at the output request time
ELEMENTS (5)	Argument of perigee (deg) at the output request time
ELEMENTS (6)	Mean anomaly (deg) at the output request time
ELEMENTS (7)	Equinoctial element h at the output request time
ELEMENTS (8)	Equinoctial element k at the output request time
ELEMENTS (9)	Equinoctial element p at the output request time
ELEMENTS (10)	Equinoctial element q at the output request time
ELEMENTS (11)	Mean longitude (deg) at the output request time
ELEMENTS (12)	Mean semimajor axis rate (km/s) at the output request time
ELEMENTS (13)	h rate (1/s) at the output request time
ELEMENTS (14)	k rate (1/s) at the output request time
ELEMENTS (15)	p rate (1/s) at the output request time
ELEMENTS (16)	q rate (1/s) at the output request time
ELEMENTS (17)	Mean mean longitude rate (deg/s) at the output request time

Name	dsst.output file (ECIPV request)
EPOCH_YMD	Output request time
ECIPV (1)	X position (km) at the output request time
ECIPV (2)	Y position (km) at the output request time
ECIPV (3)	Z position (km) at the output request time
ECIPV (4)	X Velocity (km) at the output request time
ECIPV (5)	Y Velocity (km) at the output request time
ECIPV (6)	Z Velocity (km) at the output request time

Sample pmef.txt file

This file is same for both propagation and orbit determination calls

```
C
C
C      SAMPLE PMEF TEXT FILE
C
C234567890123456789012345678901234567890123456789012345678901234567890123456789012
   0.20130425000000000D+08 PME_DATE        1
   0.13000000000000000D+06 PME_TIME        2
C
   0.42164980000000000D+05 ELS_KEP(1)      3
   0.00099754570000000D+00 ELS_KEP(2)      4
   0.64299810000000000D-05 ELS_KEP(3)      5
   0.12182730000000000D+03 ELS_KEP(4)      6
   0.24905660000000000D+03 ELS_KEP(5)      7
   0.34939100000000000D+03 ELS_KEP(6)      8
C
   0.00000000000000000D+04 ELS_EQUIN(1)    9
   0.00000000000000000D+00 ELS_EQUIN(2)   10
   0.00000000000000000D+00 ELS_EQUIN(3)   11
   0.00000000000000000+00 ELS_EQUIN(4)    12
   0.00000000000000000D+00 ELS_EQUIN(5)   13
   0.00000000000000000D+00 ELS_EQUIN(6)   14
C
   0.00000000000000000D+00 POSVEL(1)      15
   0.00000000000000000D+00 POSVEL(2)      16
   0.00000000000000000D+00 POSVEL(3)      17
   0.00000000000000000D+00 POSVEL(4)      18
   0.00000000000000000D+00 POSVEL(5)      19
   0.00000000000000000D+00 POSVEL(6)      20
C
   0.23000000000000000D+01 PME_CD         21
   0.12000000000000000D+01 PME_CR         22
   0.00000000000000000D+00 PME_RHO_ONE    23
   0.50000000000000000D-04 SMA_SIGMA      24
   0.50000000000000000D-04 INC_SIGMA      25
   0.50000000000000000D-04 ASC_SIGMA      26
   0.14000000000000000D+03 PME_SCMASS     27
   0.00000000000000000D-06 PME_SCAREA     28
C
   0.43200000000000000D+05 PME_STEPSIZE   29
C
   0.00000000000000000D+00 DP_SPARE1      30
   0.00000000000000000D+00 DP_SPARE2      31
   0.00000000000000000D+00 DP_SPARE3      32
   0.00000000000000000D+00 DP_SPARE4      33
   0.00000000000000000D+00 DP_SPARE5      34
   0.00000000000000000D+00 DP_SPARE6      35
C
   0.20000000000000000D+06 RESPRD         36
```

```
   0.02300000000000000D+02 RESORB          37
C
           1               PME_RETRO       38
          11               PME_KEP_SYS     39
          11               POS_VEL_SYS     40
           1               GEN_METHOD      41
           2               ATMOS_MODEL     42
      840401               JACRB_DATE      43
         123               JACRB_SSS       44
      840401               SLP1950_DATE    45
         456               SLP1950_SSS     46
      840401               SLPTOD_DATE     47
         789               SLPTOD_SSS      48
      840401               TIMECF_DATE     49
         123               TIMECF_SSS      50
           2               HARRIS_MODEL    51
           2               POTNTL_MODEL    52
C
           2               PME_NMAX        53
           0               PME_MMAX        54
           1               PME_IZONAL      55
           1               PME_IJ2J2       56
           2               PME_NMAXRS      57
           0               PME_MMAXRS      58
C
           1               PME_ITHIRD      59
           3               PME_INDDRG      60
           3               PME_ISZAK       61
           3               PME_INDSOL      62
           1               PME_JSHPER      63
           1               PME_JZONAL      64
           1               PME_JMDALY      65
           2               PME_INP_TYPE    66
          11               PME_EQUI_SYS    67
          11               INTEG_FRAME     68
          11               OUTPUT_FRAME    69
           0               PME_NSTATE      70
           4               PME_SPSHPER     71
           1               PME_KSPCF       72
           1               PME_INDSET      73
C
           0               INT_SPARE1      74
           0               INT_SPARE2      75
           0               INT_SPARE3      76
           0               INT_SPARE4      77
           0               INT_SPARE5      78
           0               INT_SPARE6      79
           0               INT_SPARE7      80
           0               INT_SPARE8      81
           0               INT_SPARE9      82
```

```
             0              INT_SPARE10    83
C
             1              PD_IANAL       84
             0              PD_IDIFF       85
             0              PD_IQDRT       86
             0              PD_SHORT       87
             1              PD_ICBVAR      88
             0              PD_J22VAR      89
             0              PD_ITBVAR      90
             0              PD_IDRVAR      91
             0              PD_ISRVAR      92
             0              PD_KGRAVP      93
             2              PD_KPRTB1      94
             1              PD_KPRTB2      95
             2              PD_KPRTB3      96
             2              PD_KPRTB4      97
C
             6              PD_NSTATE      98
             0              PD_NDYNAM      99
             6              PD_NSOLVE     100
C
             1              SP_ZONALS     101
             1              SP_MDAILY     102
             3              SP_J2MDLY     103
             3              SP_TESSLC     104
             1              SP_J2SQ       105
             1              SP_LUNSOL     106
C
            12              SP_NZN        107
             4              SP_LZN        108
            16              SP_JZN        109
            12              SP_NMD        110
            12              SP_MMD        111
             4              SP_LMD        112
             4              SP_NJ2MD      113
             4              SP_MJ2MD      114
             2              SP_LJ2MD      115
             1              SP_IDRMD      116
             8              SP_NTS        117
             8              SP_MTS        118
             4              SP_LTS        119
             2              SP_LTSHAN     120
           -12              SP_JMINTS     121
            12              SP_JMAXTS     122
             1              SP_LUN_NTH    123
             1              SP_LUN_JMX    124
             1              SP_LUN_LTH    125
             1              SP_LUN_ITD    126
             1              SP_LUN_NTD    127
             1              SP_SOL_NTH    128
```

```
1               SP_SOL_JMX    129
1               SP_SOL_LTH    130
1               SP_SOL_ITD    131
1               SP_SOL_NTD    132
```

Sample dsst_wls.input file

This file will be the observations file for standalone least square orbit determination program (DSST_OD)

```
EPOCH
OBS_ECIPV     0.0000D+00     0.66902D+04     0.1818D-05     -0.4109D-02     ...
OBS_ECIPV     0.1000D+03     0.66457D+04     0.7711D+03     -0.4128D-02     ...
OBS_ECIPV     0.2000D+03     0.65126D+04     0.1531D+04     -0.4318D-02     ...
OBS_ECIPV     0.3000D+03     0.62929D+04     0.2272D+04     -0.4673D-02     ...
OBS_ECIPV     0.4000D+03     0.59893D+04     0.2982D+04     -0.5182D-02     ...
OBS_ECIPV     0.5000D+03     0.56061D+04     0.3653D+04     -0.5828D-02     ...
OBS_ECIPV     0.6000D+03     0.51482D+04     0.4275D+04     -0.6591D-02     ...
OBS_ECIPV     0.7000D+03     0.46218D+04     0.4840D+04     -0.7445D-02     ...
OBS_ECIPV     0.8000D+03     0.40339D+04     0.5340D+04     -0.8362D-02     ...
OBS_ECIPV     0.9000D+03     0.33924D+04     0.5770D+04     -0.9311D-02     ...
OBS_ECIPV     0.1000D+04     0.27058D+04     0.6123D+04     -0.1025D-01     ...
EXIT
```

Name	dsst.output file (ECIPV request)
EPOCH	Requests the initialization of orbit determination services
OBS_ECIPV	Specifies the type of observation (here, it refers to position and velocities in ITRF co-ordinate frame)
DATA (1)	Time of the observation after Epoch in seconds
DATA (2)	X position (km) at time t
DATA (3)	Y position (km) at time t
DATA (4)	Z position (km) at time t
DATA (5)	X Velocity (km) at time t
DATA (6)	Y Velocity (km) at time t
DATA (7)	Z Velocity (km) at time t

Note: the data field and spacing between the fields can be of any length (with maximum of 35 characters per field)

APPENDIX B

SIMULATING AND INTEGRATING BROWNIAN MOTION

In chapter 6 a method for capturing the impact of upper atmospheric density model errors is presented. Equation 6.5 presented the employed density model with relative noise together with the modelled density. To support the evaluation of established method, while over coming the lack of real observations in various altitudes, a simulation model was implemented. The details on approximating the Brownian noise and its implementation is presented in section B.2.

In the same chapter, stochastic differential equation (SDE) is employed together with the relative orbital equations of motion. To support the evaluation of the time variation of the variance of SDE, section B.1 presents a derivation of the variance of the processes given in equation 6.25.

B.1 Covariance of the integral function of a Brownian motion

The mathematical foundation for Brownian motion as a stochastic process was done by **?**, and this process is also called as Wiener Process or Random Walk.

The Brownian motion $\epsilon(t)$ serves as a basic model for the cumulative effect of pure noise. If $\epsilon(t)$ denotes the position of a particle at time t, then the displacement $\epsilon(t)-\epsilon(0)$ is the effect of the purely stochastic noise over time t.

Basic properties of Brownian Motion, which is a stochastic process, are given be Klebaner (2005), which are presented below:

1. Independent of increments: $\epsilon(t)-\epsilon(s)$, for $t > s$, is independent of the past.
2. Normal increments: $\epsilon(t)-\epsilon(s)$ has Normal distribution with mean 0 and variance $t-s$. This implies that $\epsilon(t)-\epsilon(0)$ has $N(0,t)$ distribution.
3. Continuity of paths: $\epsilon(t)$, $t \geq 0$ are continuous functions of t.
4. A Brownian motion is a Gaussian process with zero mean function, and covariance function min(t,s) (Klebaner, 2005, Theorem 3.3)

$$E[\epsilon(t),\epsilon(s)] = \min(t,s)$$

From the definition of Brownian motion presented in the equation 6.6, it is seen that multiple integration of white noise has to be performed. Here in this section, we present a

derivation of the variance of the process, that is the first, second, and the third integral of white noise, with the characteristic time scale τ.

The covariance of white noise is given by

$$\mathrm{cov}\left[W_0(t), W_0(t')\right] = \sigma^2 \delta(t - t') \tag{B.1}$$

where $\delta(\cdot)$ is the Dirac delta function. In the following derivation an integer subscript (z) in the (W_z) representation of the white noise is used to specify the order of integration performed on the white noise. That is: $W_0(t)$ will be the white noise, and $W_1(t) = \epsilon(t)$ represents the Brownian motion.

The covariance of the W_1 is given by

$$\mathrm{cov}\left[W_1(t), W_1(t')\right] = E\left[\left(\frac{1}{\tau}\int_0^{t'} W_0(s')\mathrm{d}s'\right)\left(\frac{1}{\tau}\int_0^{t} W_0(s)\mathrm{d}s\right)\right] \tag{B.2}$$

Here, the time scaling factor (τ) is constant over time. Using the rules of Expectation operator, the above equation can be written as

$$\mathrm{cov}\left[W_1(t), W_1(t')\right] = \frac{1}{\tau^2}\, E\left[\left(\int_0^{t'} W_0(s')\mathrm{d}s'\right)\left(\int_0^{t} W_0(s)\mathrm{d}s\right)\right] \tag{B.3}$$

For the ease of understanding the derivation, in further steps a unit time scaling factor $(\tau = 1)$ will be considered. With that, the covariance of Brownian motion or the first integral of white noise is given as

$$\begin{aligned}
\mathrm{cov}\left[W_1(t), W_1(t')\right] &= E\left[\left(\int_0^{t'} W_0(s')\mathrm{d}s'\right)\left(\int_0^{t} W_0(s)\mathrm{d}s\right)\right] \\
&= \int_0^t \int_0^{t'} E\left[W_0(s')W_0(s)\right]\mathrm{d}s'\mathrm{d}s \\
&= \int_0^t \int_0^{t'} \sigma^2 \delta(s' - s)\mathrm{d}s'\mathrm{d}s \\
&= \begin{cases} \int_0^t \sigma^2 \mathrm{d}s \,;\, t' \geq t \\ \int_0^{t'} \sigma^2 \mathrm{d}s' \,;\, t' \leq t \end{cases}
\end{aligned} \tag{B.4}$$

Following the similar steps, the covariance of the integral of Brownian motion is then given by

$$\begin{aligned}
\mathrm{cov}\left[W_2(t), W_2(t')\right] &= E\left[\left(\int_0^{t'} W_1(s')\mathrm{d}s'\right)\left(\int_0^{t} W_1(s)\mathrm{d}s\right)\right] \\
&= \int_0^t \int_0^{t'} E\left[W_1(s')W_1(s)\right]\mathrm{d}s'\mathrm{d}s \\
&= \int_0^t \int_0^{t'} \sigma^2 \min(s, s')\mathrm{d}s'\mathrm{d}s
\end{aligned} \tag{B.5}$$

Taking $t' \geq t$ and splitting the inner integral of equation B.5 into two, as in $s' \leq s$ and $s' \geq s$

$$\begin{aligned}\int_0^{t'} \min(s', s)\mathrm{d}s' &= \int_0^{s} s'\mathrm{d}s' + \int_0^{t'} s\mathrm{d}s \\ &= \frac{1}{2}s^2 + s(t' - s) \\ &= st' - \frac{1}{2}s^2 \end{aligned} \tag{B.6}$$

Taking the outer integral of equation B.5, is then evaluated as

$$\begin{aligned}\mathrm{cov}\left[W_2(t), W_2(t')\right] &= \sigma^2 \int_0^{t} \left(st' - \frac{1}{2}s^2\right)\mathrm{d}s \\ &= \sigma^2 \left(\frac{1}{2}t^2 t' - \frac{1}{6}t^3\right) \\ &= \sigma^2 \frac{t^2}{6}\left(3t' - t\right) \end{aligned} \tag{B.7}$$

From which $\mathrm{var}[W_2(t)] = \frac{1}{3}\sigma^2 t^3$, for unit time scale factor. Including the time scale factor τ, as in equation B.3, and following the same procedure it can be shown that the variance of the integral of Brownian motion is

$$\mathrm{var}[W_2(t)] = \frac{1}{3}\sigma^2 \left(\frac{t}{\tau}\right)^3 \tag{B.8}$$

B.2 Implementation of Density Noise Model

For the present study the characteristic time length $\tau = T/10$ is considered (T is the orbital period in seconds). Much shorter fluctuations are neglected by assuming that the cumulative uncertainty is smaller than the ability of a density model to capture such effects. Also, empirically analysing the variations in ballistic coefficients, a Lagrange polynomial of the order three showed to be sufficient; the same is used within the implementation. Interpolating the noise within the certain time intervals is assumed to provide the correlated noise.

Figure B.1 shows the schematic diagram for density noise modelling with the above method. Figure B.2 shows an arc of densities computed using Jacchia-Gill model together with interpolated Gauss- Markov noise added to it. The example considers the attitude of 400 km, $\sigma_\rho = 15\%$ relative density uncertainty, and time correlation factor $\tau = T/n$.

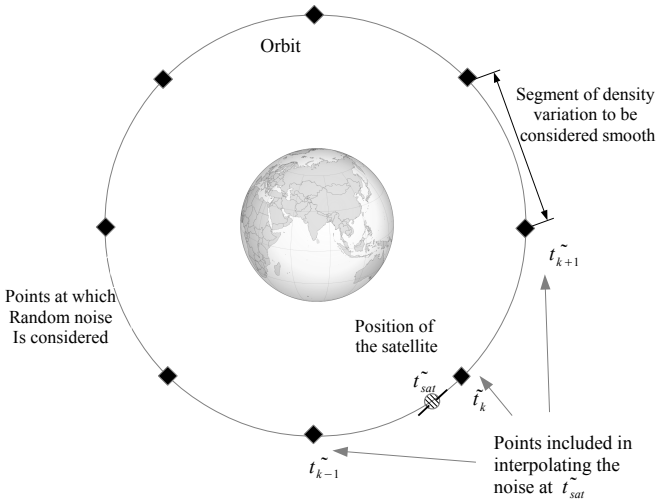

Fig. B.1 Schematic representation of polynomial interpolation of random density noise.

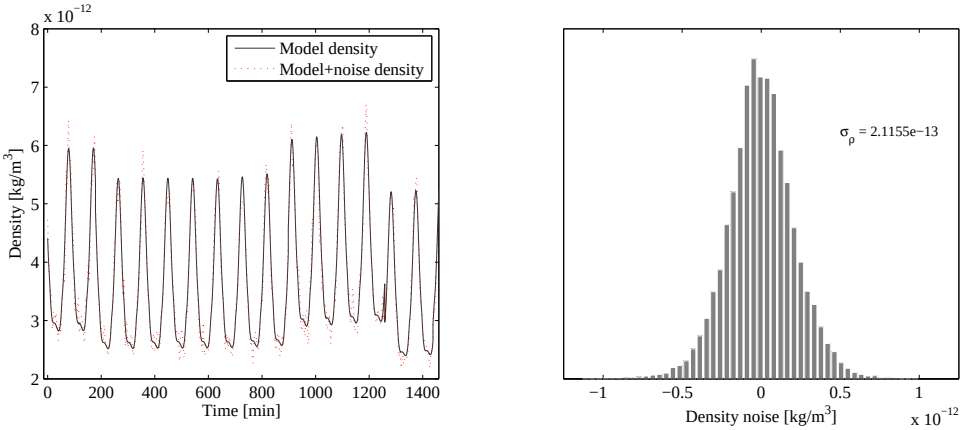

Fig. B.2 (Left) Modelled densities from Jacchia-Gill model for an object at 400 km altitude on Jan 1, 2016, and the dotted red line shows the density with the added relative noise of $\sigma_\rho = 0.15$, and with the time correlation factor of $\tau = T/10$ seconds. (Right) Histogram of the density differences between Jacchia-Gill model and the density with noise.

APPENDIX C

SOFTWARE MODULES

Generally, complete models for the equations of motion for the precision mean elements were implemented early on in the DSST Standalone development. However, only limited modelling of the smaller short-periodic terms was implemented. For example, the short-periodic models for the J2-squared terms and for the J_2 secular/tesseral m-daily coupling terms were not implemented in the DSST Standalone. The Weak-Time-Dependent (WTD) terms in the lunar-solar short-periodic motion are not implemented in the DSST Standalone. Modelling limitations in the DSST Standalone may also be due to the more recent development of the terms such as the solid Earth tides contributions to the precise mean element equations of motion.

The SPSHPER key word currently provides accuracy options for LEO, MEO, HEO, and GEO orbits. Previously, the improved accuracy option was only available for LEO near circular orbits. The options available via the SPSHPER keyword in the PMEF file were incomplete with respect to supporting the options required for the current study, which were extended during the course of this research work.

This appendix provides the FORTRAN 77 modules which are implemented to improve the standalone version of the DSST. The code structure follows the standalone version programming paradigm. Figure C.1 shows the software design for the orbit propagation services down to the level of short periodic routines. The overall architecture of the standalone, Fortran 77 code, follows the steps:

- Initialisation of constants: through the subroutines *GetEnv, MP_read_PMEF, Get_CSCons*, and *Read_EPOT*.
- Initialisation of quantities that depend on the initial epoch: *IntAnl*.
- Initialisation of quantities which depend on the epoch orbital elements: *BegAnl*. This step is reinitialised at each iteration step within DSST-OD.
- Generate output the request epoch: *OrbAnl*

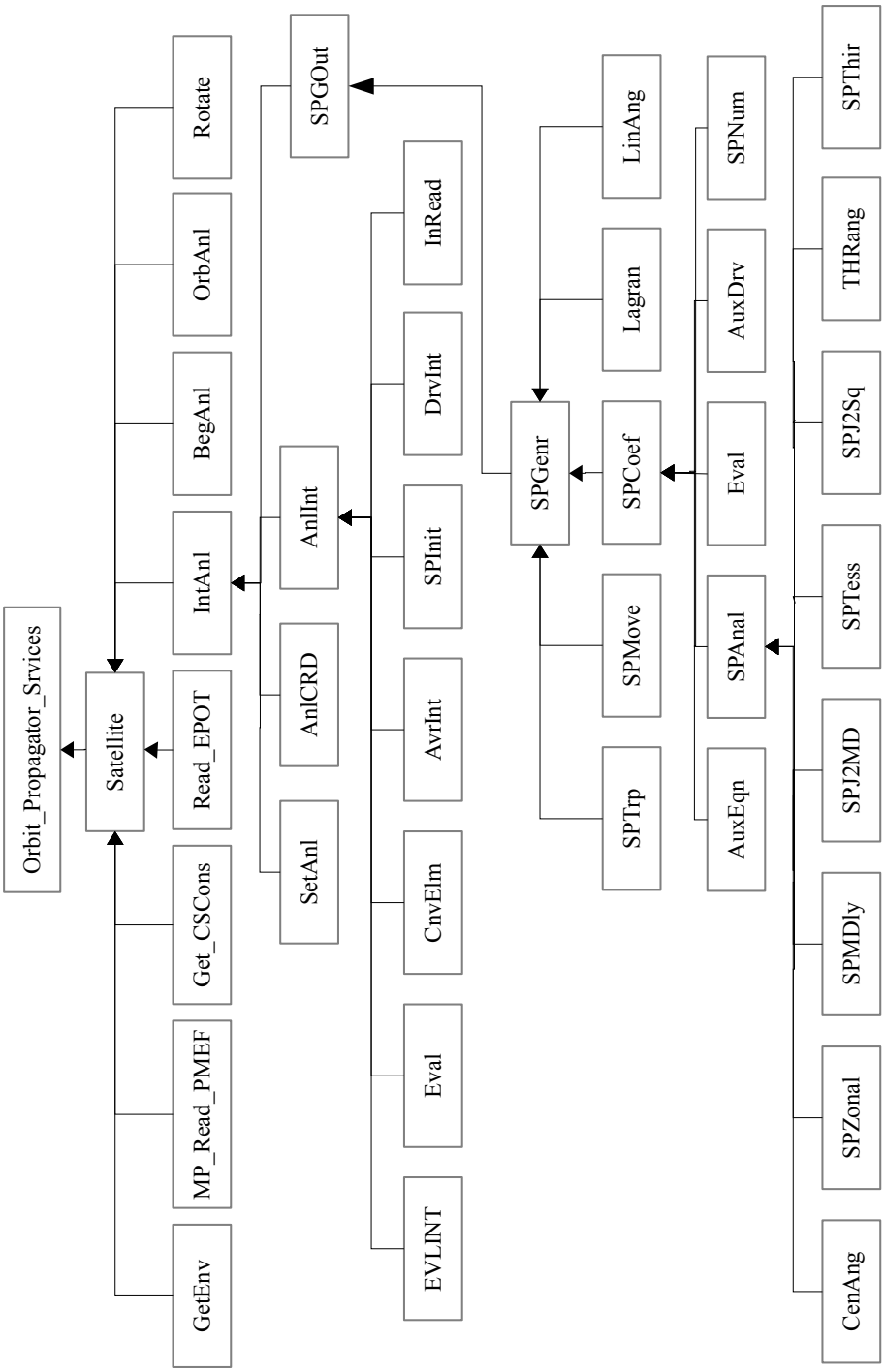

Fig. C.1 Software architecture of DSST standalone software program for short periodic generator.

The short periodic development: J_2 squared, J_2 M-Daily coupling, WTD for low eccentricities, and semi-analytical batch filter were implemented into DSST standalone. The necessary switches and flags used in order to exercise different options were set in initialisation routines, and corresponding header files, 'INIT_PMERN' , and 'INIT_PMEF_KEYS' subroutines.

C.1 J_2 squared - Subroutine

This subroutine computes the Fourier coefficients of the J2-squared short-periodic perturbation in the equinoctial elements. This version implements the algorithm in the DSST Fortran 77 Standalone. In this algorithm, there is an expansion in the eccentricity and terms proportional to J2-squared times eccentricity squared are neglected.

```
      SUBROUTINE SPJ2SQ (CCOEF,SCOEF)
C
C     Parameters ************************************
C
C          CCOEF  O   Fourier Series Cosine Coefficients
C
C             (I, J)    Coefficient of Cos (J* Lambda) for
C                              element I
C
C          SCOEF  O   Fourier Series Sine Coefficients
C
C             (I, J)    Coefficient of Cos (J* Lambda) for
C                              element I
C
C     I/O from included header files *********************
C
C          /SATELM/
C
C               A
C               XH
C               XK
C               P
C               Q
C               RETRG
C
C          /FRC/
C
C               FRC_MAXBOD
C               FRC_MAXGRAV
C
C               CS
C               ICENT
C               RADIUS
C
C
C     NO SUBROUTINES CALLED
C
C***************** DECLARATIONS ************************
C
      IMPLICIT         NONE
C
C
C     I/O from included header files ********************
C
      INCLUDE 'satelm.h'
      INCLUDE 'frc.h'
C
C    Local variables ***********************************
C
```

```
C          INTEGER*4          ICENT
C
C
C          REAL*8             A
C          REAL*8             AB(FRC_MAXBOD)
C
C          REAL*8             P
C          REAL*8             Q
C
C          REAL*8             CS(FRC_MAXGRAV,(FRC_MAXGRAV+3))
C          REAL*8             RETRG
C
      REAL*8             PP
      REAL*8             PPP
      REAL*8             PPPP
C
      REAL*8             C
      REAL*8             CC
      REAL*8             CCC
      REAL*8             CCCC
C
      REAL*8             PQ
      REAL*8             PPQQ
C
      REAL*8             XJ2RA
C
      REAL*8             FAC
      REAL*8             TEM1
      REAL*8             TEM2
      REAL*8             TEM3
      REAL*8             TEM4
      REAL*8             TEM5
C
      REAL*8             CCOEF(6,5)
      REAL*8             SCOEF(6,5)

C
C***************** BEGIN PROGRAM *************************
C
C                  COMPUTE AUXILIARY QUANTITIES.
C
   10 PP   = SATELM.P * SATELM.P
      PPP  = SATELM.P * PP
      PPPP = SATELM.P * PPP
C
      C    = PP + SATELM.Q * SATELM.Q
      CC   = C*C
      CCC  = C*CC
      CCCC = C*CCC
C
      PQ   = SATELM.P * SATELM.Q
      PPQQ = PP - SATELM.Q * SATELM.Q
C
C                  The following line of code was modified on
C                  20 May 2013 to be compatible with the GTDS
C                  subroutine of same name
C
   20 XJ2RA = FRC.RADIUS(FRC.ICENT) / (SATELM.A*(C + 1.D0))
C
      XJ2RA = FRC.CS(2) * XJ2RA * XJ2RA
      XJ2RA = XJ2RA * XJ2RA
C
C                  COMPUTE THE FOURIER COEFFICIENTS OF THE J2-SQUARED
C                  SHORT-PERIODIC PERTURBATIONS.
C
C                  SEMIMAJOR AXIS
C
   30 FAC  = 3.D0 * SATELM.A * XJ2RA
      TEM2 = 10.D0*CC - 52.D0*C + 10.D0
C
      CCOEF (1,1) = 0.D0
      SCOEF (1,1) = 0.D0
```

```
C
      CCOEF (1,2) = FAC * (5.D0*CCC - 26.D0*CC + 5.D0*C - TEM2*PP)
      SCOEF (1,2) = FAC * (TEM2*PQ) * SATELM.RETRG
C
      CCOEF (1,3) = 0.D0
      SCOEF (1,3) = 0.D0
C
      CCOEF (1,4) = FAC * (32.D0*PPPP - 32.D0*C*PP + 4.D0*CC)
      SCOEF (1,4) = FAC * (16.D0*C - 32.D0*PP)*PQ * SATELM.RETRG
C
      CCOEF (1,5) = 0.D0
      SCOEF (1,5) = 0.D0
C
C                  H
C
   40 FAC  = XJ2RA / 8.D0
      TEM5 = 240.D0 - 168.D0*C
      TEM3 = 144.D0 - 72.D0*C
      TEM1 = 18.D0*CCC + 36.D0*CC - 342.D0*C + 108.D0
C
      CCOEF (2,1) = FAC * (TEM1*PQ) * SATELM.RETRG
      SCOEF (2,1) = FAC * (TEM1*PP + 27.D0*CCCC - 186.D0*CCC +
     *   447.D0*CC - 234.D0*C + 36.D0)
C
      CCOEF (2,2) = 0.D0
      SCOEF (2,2) = 0.D0
C
      CCOEF (2,3) = FAC * (TEM3*PP + 18.D0*CCC - 128.D0*CC + 498.D0*C
     *   - 92.D0)*PQ * SATELM.RETRG
      SCOEF (2,3) = FAC * (TEM3*PPPP + (18.D0*CCC - 92.D0*CC + 426.D0*C
     *   - 92.D0)*PP - 9.D0*CCCC + 73.D0*CCC - 267.D0*CC + 46.D0*C)
C
      CCOEF (2,4) = 0.D0
      SCOEF (2,4) = 0.D0
C
      CCOEF (2,5) = FAC * (TEM5*(PP - C/2.D0)*PQ) * SATELM.RETRG
      SCOEF (2,5) = FAC * (TEM5*(PPPP - C*PP) - 21.D0*CCC + 30.D0*CC)
C
C                  K
C
   50 CCOEF (3,1) = FAC * (- TEM1*PP + 45.D0*CCCC - 150.D0*CCC +
     *   105.D0*CC - 126.D0*C + 36.D0)
      SCOEF (3,1) = CCOEF (2,1)
C
      CCOEF (3,2) = 0.D0
      SCOEF (3,2) = 0.D0
C
      CCOEF (3,3) = FAC * (- TEM3*PPPP + (18.D0*CCC - 236.D0*CC +
     *   714.D0*C - 92.D0)*PP - 9.D0*CCCC + 91.D0*CCC - 303.D0*CC +
     *   46.D0*C)
      SCOEF (3,3) = FAC * (TEM3*PP - 18.D0*CCC + 200.D0*CC - 642.D0*C +
     *   92.D0)*PQ * SATELM.RETRG
C
      CCOEF (3,4) = 0.D0
      SCOEF (3,4) = 0.D0
C
      CCOEF (3,5) =   SCOEF (2,5)
      SCOEF (3,5) = - CCOEF (2,5)
C
C                  P
C
   60 FAC  = 3.D0 * (CC - 1.D0) * XJ2RA / 16.D0
      TEM4 = 12.D0*C + 20.D0
      TEM2 = 3.D0*CC + 5.D0*C
C
      CCOEF (4,1) = 0.D0
      SCOEF (4,1) = 0.D0
C
      CCOEF (4,2) = FAC * (60.D0*C* SATELM.P - 72.D0*PPP)
      SCOEF (4,2) = FAC * (72.D0*PP - 24.D0*C)* SATELM.Q * SATELM.RETRG
C
      CCOEF (4,3) = 0.D0
```

```
      SCOEF (4,3) = 0.D0
C
      CCOEF (4,4) = FAC * (TEM4*PPP - 3.D0*TEM2* SATELM.P)
      SCOEF (4,4) = FAC * (- TEM4*PP + TEM2)* SATELM.Q * SATELM.RETRG
C
      CCOEF (4,5) = 0.D0
      SCOEF (4,5) = 0.D0
C
C                 Q
C
   70 CCOEF (5,1) = 0.D0
      SCOEF (5,1) = 0.D0
C
      CCOEF (5,2) = FAC * (12.D0*C - 72.D0*PP)* SATELM.Q
      SCOEF (5,2) = FAC * (48.D0*C* SATELM.P - 72.D0*PPP) * SATELM.RETRG
C
      CCOEF (5,3) = 0.D0
      SCOEF (5,3) = 0.D0
C
      CCOEF (5,4) =   SCOEF (4,4) * SATELM.RETRG
      SCOEF (5,4) = - CCOEF (4,4) * SATELM.RETRG
C
      CCOEF (5,5) = 0.D0
      SCOEF (5,5) = 0.D0
C
C                 LAMBDA
C
   80 FAC  = 3.D0 * XJ2RA
      TEM4 = 3.D0*CC + 10.D0*C - 45.D0
      TEM2 = 13.D0*CC - 13.D0*C + 7.D0
C
      CCOEF (6,1) = 0.D0
      SCOEF (6,1) = 0.D0
C
      CCOEF (6,2) = FAC * (PQ*TEM2) * SATELM.RETRG
      SCOEF (6,2) = FAC * (PPQQ*TEM2/2.D0)
C
      CCOEF (6,3) = 0.D0
      SCOEF (6,3) = 0.D0
C
      CCOEF (6,4) = FAC * (PQ*PPQQ*TEM4/4.D0) * SATELM.RETRG
      SCOEF (6,4) = FAC * (TEM4*(CC - 8.D0*PQ*PQ)/16.D0)
C
      CCOEF (6,5) = 0.D0
      SCOEF (6,5) = 0.D0
C
C
      RETURN
      END
```

C.2 J_2 M-Daily coupling - Subroutine

To compute the second order M-Daily coefficients due to the coupling between the first order M-Daily coefficients, and the first order J_2 and Drag mean element rates. The formulation of the coupling effect is from Cefola and Slutsky (1981).

Through finite differencing, the partial derivatives of the first order M-Daily coefficients are evaluated. Later by calling J_2Part subroutine for the partial derivatives of the J_2 average element rates are obtained.

```
      SUBROUTINE SPJ2MD(C,S,NCUP,MCUP,LCUP, IDRMD)
C
C     Parameters ****************************************
C
C        C      O      Fourier Series Cosine Coefficients
C          (I, J)         Coefficient of Cos (J* Theta) for
C                         element I
C        S      O      Fourier Series Sine Coefficients
C          (I, J)         Coefficient of Sin (J* Theta) for
C                         element I
C
C       NJ2MD     I    MAX DEGREE FOR THE COUPLED M-DAILIES
C       MJ2MD     I    MAX ORDER FOR THE COUPLED M-DAILIES
C       LJ2MD     I    MAX D'ALEMBERT CHARACTERISTIC FOR THE
C                      COUPLED M-DAILIES
C     I/O from included header files ********************
C
C               Y
C               Y
C     Subroutines Called ********************************
C          SPMDLY    J2PART    AUXEQN    CENANG

      IMPLICIT          NONE
C     HEADER FILES **************************************
      INCLUDE          'frc.h'
      INCLUDE          'satelm.h'
      INCLUDE          'spintg.h'
      INCLUDE          'estflg.h'
C***************** DECLARATIONS *************************

      INTEGER*4         NCUP
      INTEGER*4         MCUP
      INTEGER*4         LCUP
      INTEGER*4         IDRMD
      INTEGER*4         IDIFF, IDUMS
      INTEGER*4         NSOLAR, NDRAG, NSOLVE
      INTEGER*4         I, J, II, JJ
      INTEGER*4         K, L, XL
      REAL*8            C(6,MCUP)
      REAL*8            S(6,MCUP)
      REAL*8            DELMDT(6)
      REAL*8            CCCOEF(6,MCUP)
      REAL*8            CSCOEF(6,MCUP)
      REAL*8            BCCOEF(6,MCUP)
      REAL*8            BSCOEF(6,MCUP)
      REAL*8            FCCOEF(6,MCUP)
      REAL*8            FSCOEF(6,MCUP)
      REAL*8            CPART
      REAL*8            SPART
      REAL*8            RECIP
      REAL*8            CON
      REAL*8            A(6,6), AJ2(6,6)
      REAL*8            AMAT(6,6)
      REAL*8            VPELMT(6)
      REAL*8            FACTOR
      REAL*8            RATE(6)
      REAL*8            ABTEMP, DELTA, TWODEL
```

```
C***************** BEGIN PROGRAM *************************
C    INITIALIZE THE SINE AND COSINE COEFFICIENT ARRAYS

      DO 6 II = 1,6
           DO 5 JJ = 1,MCUP
                CCCOEF(II,JJ) = 0.D0
                CSCOEF(II,JJ) = 0.D0
                BCCOEF(II,JJ) = 0.D0
                BSCOEF(II,JJ) = 0.D0
                FCCOEF(II,JJ) = 0.D0
                FSCOEF(II,JJ) = 0.D0
                C (II, JJ)    = 0.D0
                S (II, JJ)    = 0.D0

    5      CONTINUE
    6 CONTINUE

C       GET THE ELEMENTS
        VPELMT(1)= SATELM.A
        VPELMT(2)= SATELM.XH
        VPELMT(3)= SATELM.XK
        VPELMT(4)= SATELM.P
        VPELMT(5)= SATELM.Q
        VPELMT(6)= SATELM.XLAMDA

C  GET THE FIRST ORDER M-DAILY SHORT PERIODIC VARIATIONS

        CALL SPMDLY(CCCOEF,CSCOEF,NCUP,MCUP,LCUP)

C    TEST ON DRAG / M-DAILY FLAG
        IF (IDRMD.EQ.1) GO TO 20

C    GET PARTIALS OF THE J2-MEAN RATES
        CALL J2PART (AMAT)

C    ACCUMULATE THE PARTIALS
        DO 33 I = 1,6
             DO 34 J = 1,6
             A(I,J) =   AMAT(I,J)
   34        CONTINUE
   33   CONTINUE

C    CONSTRUCT THE J2-MEAN RATES
        FACTOR = -2.D0 *VPELMT(1)/7.D0
C
        DO 15 I =1,6
          RATE(I) = FACTOR*A(I,1)
   15   CONTINUE
C
        GO TO 70
C
   20   CONTINUE

C  LOGIC FOR DRAG PARTIALS AND FULL AOG RATES IF
C  DRAG / M-DAILY COUPLING IS TO BE INCLUDED.
C  SAVE THE ESTSET FLAGS IN IDUMS AND THEN TURN OFF
C  THESE FLAGS
        IDUMS = ESTFLG.IDIFF

C  SET UP FOR DRAG PARTIALS
        ESTFLG.IDIFF = 1

C  COMPUTE DRAG PARTIALS
        CALL ADIFF    ( AMAT )

C  ACCUMULATE THE PARTIALS
        DO 35 I = 1,6
            DO 30 J = 1,6
             A(I,J) =   AMAT(I,J)
  30       CONTINUE
  35   CONTINUE
```

```
        CALL    AVRAGE    (DELMDT, FRC.FRCTIM, VPELMT,    .FALSE.)

        RATE = DELMDT
        RATE(6) = RATE(6) - SATELM.XMEAN

  70  CONTINUE

C   CONSTRUCT THE M-DAILY COEFFICIENT PARTIALS

        DO 110 K = IDRMD, 5
                  ABTEMP = DABS(VPELMT(K))
                  DELTA = 1.D-05*ABTEMP
                        IF(DELTA.LT.1.D-20) DELTA = 1.D-5

                  TWODEL = 2.D0*DELTA

C   FORWARD STEP
                  VPELMT(K) = VPELMT(K) + DELTA

C   CONSTRUCT AUXILLIARY INPUT TO SPMDLY
                  CALL AUXEQN    (VPELMT,SATELM.RETRG, FRC.GM)
                  CALL CENANG    (SPINTG.ISPBOD(1),1)

                  CALL SPMDLY(FCCOEF,FSCOEF,NCUP,MCUP,LCUP)

C   BACKWARD STEP
                  VPELMT(K) = VPELMT(K) - TWODEL

C   CONSTRUCT AUXILLIARY INPUT TO SPMDLY
                  CALL AUXEQN    (VPELMT,SATELM.RETRG, FRC.GM)
                  CALL CENANG    (SPINTG.ISPBOD(1),1)

                  CALL SPMDLY(BCCOEF,BSCOEF,NCUP,MCUP,LCUP)

C   RESET VPELMT(K) TO PROPER SETTING.
                  VPELMT(K) = VPELMT(K) + DELTA


        DO 100 I = 1,6
          DO 90  L = 1,MCUP

            CPART=(FCCOEF(I,L) - BCCOEF(I,L))/TWODEL
            SPART=(FSCOEF(I,L) - BSCOEF(I,L))/TWODEL

C   ACCUMULATE SUMS
            C(I,L) = C(I,L) + A(I,K)*CSCOEF(K,L) - RATE(K)*SPART
            S(I,L) = S(I,L) + A(I,K)*CCCOEF(K,L) - RATE(K)*CPART
  90      CONTINUE

  100   CONTINUE
  110  CONTINUE

C   RESET ALL AUXILLIARY PARAMETERS

        CALL AUXEQN    (VPELMT,SATELM.RETRG, FRC.GM)
        CALL CENANG    (SPINTG.ISPBOD(1),1)

C   ADJOIN ROTATION FACTOR
       DO 151 L=1,MCUP

          XL = L
          RECIP = 1.D0/(XL*FRC.OMEGA(1))

       DO 140 I = 1,6

            C(I,L) =  -RECIP * C(I,L)
            S(I,L) =   RECIP * S(I,L)

  140 CONTINUE
  151 CONTINUE

C   MEAN LONGITUDE COUPLING
```

```
      IF (IDRMD.EQ.2) GO TO 900
         CON = 1.5D0 * SATELM.XMEAN / ( FRC.OMEGA(1) * VPELMT(1))

      DO 160 L = 1, MCUP
             XL = L
             C(6,L) = C(6,L) + CON * S(1,L) / XL
             S(6,L) = S(6,L) - CON * C(1,L) / XL
160   CONTINUE

900   CONTINUE

      RETURN
      END SUBROUTINE SPJ2MD
```

C.3 WTD for low eccentricities - Subroutine

This subroutine computes the corrections for C and S Fourier coefficients for the weak time dependent corrections for third body short periodic terms. The equations which are followed here are discussed in chapter 4.

```
      SUBROUTINE   SPWTD_LOWECC   (C, S, NTH, LTH, JMAXTH, K, TIME  )
C
C     PARAMETERS ***************************************************
C
C          C          O    COSINE COEFFICIENTS CORRECTIONS
C          S          O      SINE COEFFICIENTS CORRECTIONS
C          NTH        I
C          LTH        I
C          JAMXTH     I
C          K          I    BODY NUMBER
C     SUBROUTINES CALLED *******************************************
C
C        SPTHIR
C
C***************** DECLARATIONS ************************************
C
      IMPLICIT          NONE
C
C     HEADER FILES *****************************************************
C
      INCLUDE          'anavin.h'
      INCLUDE          'anlprm.h'
      INCLUDE          'frc.h'
      INCLUDE          'satelm.h'
      INCLUDE          'switch.h'
      INCLUDE          'spintg.h'
C
C     LOCAL VARIABLES **************************************************
C
      INTEGER*4         II, JJ, I, L, J
      INTEGER*4         NTH
      INTEGER*4         LTH
      INTEGER*4         JMAXTH
      INTEGER*4         KTHR
      INTEGER*4         K
      INTEGER*4         IARRAY(9)

      REAL*8            VPELMT (6)

      REAL*8            C     (6,NTH+1)
      REAL*8            S     (6,NTH+1)
      REAL*8            CCCOEF(6,NTH+1)
      REAL*8            CSCOEF(6,NTH+1)
      REAL*8            BCCOEF(6,NTH+1)
      REAL*8            BSCOEF(6,NTH+1)
      REAL*8            FCCOEF(6,NTH+1)
      REAL*8            FSCOEF(6,NTH+1)

      REAL*8            DCPART
      REAL*8            DSPART
      REAL*8            D2CPART
      REAL*8            D2SPART

      REAL*8            ONEN
      REAL*8            ONEN2
      REAL*8            ONENL
      REAL*8            ONEN2L
      REAL*8            DELTA
      REAL*8            DELTA2
      REAL*8            TWODEL
      REAL*8            SEMI32
```

```
      REAL*8            DELMDT (6)
      REAL*8            TIME
      REAL*8            TIME_KEEP
      REAL*8            TSTEP
      REAL*8            TEMP(6*3)


Ccccccccccccccccccccccccccccccccccccccccccccccccccccccccccccccccccccccccc

       DELTA     = 3600.D0    ! TIME STEP FOR FINET DIFFERENCES
       TWODEL    = 2.0*DELTA
       DELTA2    = DELTA*DELTA

       KTHR      = K  - 1

       VPELMT(1)= SATELM.A
       VPELMT(2)= SATELM.XH
       VPELMT(3)= SATELM.XK
       VPELMT(4)= SATELM.P
       VPELMT(5)= SATELM.Q
       VPELMT(6)= SATELM.XLAMDA

       SEMI32    = 1.5/VPELMT(1)
       IARRAY(1)= 1
       IARRAY(2)= 2
       IARRAY(3)= 3


       TIME_KEEP      = FRC.FRCTIM
       FRC.FRCTIM     = TIME

C           INITIALIZE THE SINE AND COSINE COEFFICIENT ARRAYS
C
      DO 6 II = 1,6
C
           DO 5 JJ = 1,NTH+1
C
                CCCOEF(II,JJ) = 0.D0
                CSCOEF(II,JJ) = 0.D0
                BCCOEF(II,JJ) = 0.D0
                BSCOEF(II,JJ) = 0.D0
                FCCOEF(II,JJ) = 0.D0
                FSCOEF(II,JJ) = 0.D0
                C     (II,JJ) = 0.D0
                S     (II,JJ) = 0.D0

    5      CONTINUE
C
    6 CONTINUE
C
C      GET THE CENTER C AND S COEFFICIENTS
C
         CALL   SPTHIR   (CCCOEF,CSCOEF,   NTH,LTH,JMAXTH)

C
C      COMPUTE THE PARTIALS OF C AND S COEFFICIENTS
C
C           CONSTRUCT THE WTD  COEFFICIENT PARTIALS

         TSTEP  = FRC.FRCTIM
         TSTEP  = FRC.FRCTIM  - DELTA
C
C        RESET THE EQUATIONS FOR NEW TIME

         CALL   EVAL (TSTEP,1,2,2,1,2,IARRAY,TEMP)
         CALL   AVRAGE   (DELMDT,   TSTEP , VPELMT,   .TRUE.)
         CALL   THRANG   (FRC.POSVEL(1,KTHR),SPINTG.ISPBOD(1),SPINTG.ISPBOD(K),1)

C        GET COEFFICIENTS FOR F(X-H)
C
         CALL   SPTHIR   (BCCOEF,BSCOEF,   NTH,LTH,JMAXTH)
```

```
C
         TSTEP  = TSTEP +  TWODEL
C
C        RESET THE EQUATIONS FOR NEW TIME

         CALL   EVAL (TSTEP,1,2,2,1,2,IARRAY,TEMP)
         CALL   AVRAGE   (DELMDT,   TSTEP , VPELMT,   .TRUE.)
         CALL   THRANG   (FRC.POSVEL(1,KTHR),SPINTG.ISPBOD(1),SPINTG.ISPBOD(K),1)
C
C        GET COEFFICIENTS FOR F(X-H)

         CALL   SPTHIR   (FCCOEF,FSCOEF,   NTH,LTH,JMAXTH)
C
C        RESET THE TIME AND RESET TO PROPER SETTINGS
C

         FRC.FRCTIM = TIME_KEEP
         CALL   EVAL (TIME,1,2,2,1,2,IARRAY,TEMP)
         CALL   AVRAGE   (DELMDT,   TIME , VPELMT,   .TRUE.)
         CALL   THRANG   (FRC.POSVEL(1,KTHR),SPINTG.ISPBOD(1),SPINTG.ISPBOD(K),1)
C

        DO 100 I = 1,6
C
          DO 90  J = 1,NTH+1

                    L         = J
                    ONEN      = 1.D0 / ( SATELM.XMEAN *L)
                    ONEN2     = 1.D0 / ( SATELM.XMEAN *SATELM.XMEAN *L *L)

C
C        SINGLE TIME DERIVATIVE PARTIALS
C
                    DCPART = (FCCOEF(I,L) -BCCOEF(I,L)) / TWODEL
C
                    DSPART = (FSCOEF(I,L) -BSCOEF(I,L)) / TWODEL
C
C        DOUBLE TIME DERIVATIVE PARTIALS
C
                    D2CPART= (FCCOEF(I,L) -(2*CCCOEF(I,L)) +BCCOEF(I,L)) /DELTA2
C
                    D2SPART= (FSCOEF(I,L) -(2*CSCOEF(I,L)) +BSCOEF(I,L)) /DELTA2

C        ACCUMULATE SUMS FOR C AND S CORRECTIONS
C
                    C  (I,L) = 2.3 *(+(ONEN*DSPART) -(ONEN2*D2CPART))
C
                    S  (I,L) = 2.3 *(-(ONEN*DCPART) +(ONEN2*D2SPART))
C
  90       CONTINUE
C
  100    CONTINUE
C
        DO L = 1,NTH+1
                    ONEN    =  1.D0 / ( SATELM.XMEAN *L *L)
                    C  (6,L) =  C  (6,L) -(SEMI32 *ONEN *DCPART)
                    S  (6,L) =  S  (6,L) -(SEMI32 *ONEN *DSPART)
        END DO

       END SUBROUTINE SPWTD_LOWECC
```

C.4 Orbit Determination Services - Main program

This procedure invokes DSST based orbit determination routine. The computation of matrix inversions are handled through Linear Algebra PACkage (LAPACK).

```
      PROGRAM   ORBIT_DETERMINATION_SERVICES
C
C     INPUT ============================================================
C
C          SYS$INPUT    User commands from default input channel
C
C
C     OUTPUT ===========================================================
C
C          SYS$OUTPUT   Output data to the default output channel
C
C     SUBROUTINES CALLED ===============================================
C
C          INIT_HEADERS           - Initializes the header files
C          SATELLITE              - Propagates using DSST
C          MP_WRITE_PMEF          - Writes a updated pmef file
C          SETPMERNUPDATE         - Sets the updated state/element in DP_BLOCK
C
C       from LAPACK library
C
C          DGELSY                 - Real linear least square solver
C
C     RESTRICTIONS =====================================================
C
C          None.
C
C     Implicit Types ===================================================
C
      IMPLICIT     NONE
C
C
C     Data Items =======================================================
C
      REAL*8                 ELEMENTS,       TIME,          BURN_DELTA_V,
     2                       EPOCH_YMD,      EPOCH_HMS,     POSVEL
C
      REAL*8                 SEMIMAJOR,      ECCENTRICITY,    PERIGEE,
     2                       BETA,           E_ANOMALY,       M_ANOMALY,
     3                       ANOMALY,        DELTA_M,         DELTA_T
C
      REAL*8                 MU,             DEGREES,         RADIANS
C
      REAL*8                 ELEMENTS_DER,  POSVEL_DER, OBS_ECIPV_STATE
      REAL*8                 OBS_RAE, OBS_GPS, OBS_SLR
      REAL*8                 AMATRIX, BMATRIX, BBAR_MATRIX
      REAL*8                 INITIAL_STATE
C
C
      REAL*8                 RHO_ONE_HIGH      / 0.0 D0 /
      REAL*8                 RHO_ONE_LOW       / 0.0 D0 /
C
      REAL*8                 WORK(9999999*8), RCOND
      REAL*8                 RMSP, STATE (6), POSVEL_DER_EPOCH,RMSP_DIFF
      REAL*8                 KEP(6), DYDA0(6,6), RTN(3), RTN_A, RES_POSVEL

      REAL*8                 TEMP_MAT_VEC
      REAL*8                 UPDATESTATE_TOT, PM_ST_FIRST, PM_ST_UPDT
      REAL*8                 HWH5(6,6), HWH6(6,6)
      REAL*8                 DEV_APRIORI, ITERATION_EPSILON
      REAL*8                 TEMP_1, TEMP_2, TEMP_3
      REAL*8                 CD_FIRST, CD_UPDATE, CR_FIRST, CR_UPDATE
      REAL*8                 VAR_RESIDUALS, MEAN_RESIDUALS

      REAL*8                 UPDATED_CD_TOTAL,UPDATED_CR_TOTAL
```

```
      REAL*8                  CD_SIGMA, CR_SIGMA

      REAL*8                  TIME_ARRAY
      REAL*8                  TT1(6)

      REAL*8,ALLOCATABLE,DIMENSION(:,:) :: HWH_ACC, HWH, H, TEMP_MAT, HTRANS
      REAL*8,ALLOCATABLE,DIMENSION(:,:) :: WEIGHT
      REAL*8,ALLOCATABLE,DIMENSION(:)   :: HWB, BBAR_MATRIX_ACC, STATE_UPDATE_LSQ
      REAL*8,ALLOCATABLE,DIMENSION(:)   :: TEMP_VEC
C
      REAL*8                  DSTATE_DEQUI_EPOCH(6,6)
      REAL*8                  P_STATE(6,6)
      REAL*8                  T_M1(6,6), T_M2(6,6)
      REAL*8                  RFCTR

      REAL*8                  EST_KEP(6), EST_STATE(6), EST_EQUI(6)
      REAL*8                  POS(3), VEL(3), U(3,3)

      REAL*8                  YMD, HMS
      REAL*8                  DYJUL0, SJUL0, ETIME0, ETIME, DYJ, SCJ

      REAL*8                  LTC_MAT (3,3), ROT_E_MAT(3,3), DADS(3,3)
      REAL*8                  AZ, EL, RHO

      INTEGER*4               INVERSE, K

      INTEGER*4               TSET, LDA, LWORK, INFO, RANK, JPVT(6)
      INTEGER*4               IATMOS_PREBURN   / 1      /
      INTEGER*4               IATMOS_POSTBURN  / 1      /
C
      INTEGER*4               MAX_LIST_LENGTH, BURN_NUMBER
      INTEGER*4               INDEX1,   I,    J
      INTEGER*4               ITR_IDX, NO_OBS, SYS_PMERN
C
      INTEGER*4               BLENGTH,       SATELLITE,      STATUS,
     2                        NORMAL, SATELLITE_DUB, IER
C
C
      INTEGER*4               NSTATE_DER, NDYNAM_DER, NSOLVE_
C
      INTEGER*4               CLOCK(8)
CRJP      INTEGER*4               LIB$ESTABLISH, ERROR_HANDLER
C
      LOGICAL                 FIRST_PASS, ITR_LOOP
      LOGICAL                 INIT_FLAG,      UPDATED_STATE
C
C     Constants  ============================================================
C
C     Service request buffer length
      PARAMETER    (   BLENGTH         =       512    )
C
C     Maximum number of burns which can be passed in a burn list
      PARAMETER    (   MAX_LIST_LENGTH     =       10      )
C
C     Normal return status from function SATELLITE
      PARAMETER    (   NORMAL          =       0      )
C
      PARAMETER    (  DEGREES  =  0.017453292519943296 D00 )
      PARAMETER    (  RADIANS  =  1.D0/DEGREES             )
      PARAMETER    (  MU       =  398600.8              D00 )
C
C     Character Variables ========================================
C
      CHARACTER               BLANK           /                 ' ' /
C
      CHARACTER * (BLENGTH)   ALINE
C
      CHARACTER * (12)        REQUEST

      CHARACTER * ( 9)        EPOCH           /       'OS_EPOCH ' /
      CHARACTER * ( 9)        ECIPV           /       'OS_ECIPV ' /
      CHARACTER * (12)        ELMNTS          /       'OS_ELEMENTS ' /
```

```
      CHARACTER * (10)       NODE            /       'OS_ASCEND␣'    /
      CHARACTER * (10)       MAXLAT          /       'OS_MAXLAT␣'    /
      CHARACTER * (11)       DRAGVAR         /       'OS_DRAGVAR␣'   /
C
C
      CHARACTER * (13)       DER_ELMNTS      /       'OS_DER_ELMNTS␣'/
      CHARACTER * (13)       DER_ECIPV       /       'OS_DER_ECIPV␣␣'/
C
      CHARACTER * (12)       ERROR           /       'OS_ERROR␣'     /
C
      CHARACTER * ( 5)       PMERN           /       'pmern'         /
C
      CHARACTER * (72)       MESSAGE
      CHARACTER * (12)       FILENAME
      CHARACTER * (12)       YEAR_,TIME_,DAY_
      CHARACTER * (3 )       STATION
C
C     Dimensions ============================================================
C
      DIMENSION         BURN_DELTA_V(4,MAX_LIST_LENGTH)
      DIMENSION         ELEMENTS   (17)
      DIMENSION         POSVEL     (6)
C
      DIMENSION         ELEMENTS_DER (6,300)
      DIMENSION         POSVEL_DER   (6,300),POSVEL_DER_EPOCH(6,6)
      DIMENSION         OBS_ECIPV_STATE(6)
      DIMENSION         OBS_GPS(6)
      DIMENSION         OBS_RAE(6)
      DIMENSION         AMATRIX(999999,6)
      DIMENSION         BMATRIX(999999,1)
      DIMENSION         BBAR_MATRIX(999999,1)
      DIMENSION         INITIAL_STATE(6)
      DIMENSION         RES_POSVEL(999999,6), RTN_A(999999,3)
      DIMENSION         TEMP_MAT_VEC(6)

      DIMENSION         UPDATESTATE_TOT(6), PM_ST_FIRST(6), PM_ST_UPDT(6)
      DIMENSION         VAR_RESIDUALS(6), MEAN_RESIDUALS(6)

      DIMENSION         TIME_ARRAY(999999)

C
C     Functions =============================================================
C
      EXTERNAL          SATELLITE
C
C
C     Data Statements ===============================================
C
      DATA              FIRST_PASS    /.TRUE./
C
      STATIC            FIRST_PASS
C
C***************** BEGIN PROGRAM ************************************

C     Open standard input and standard output, residuals in ECI and RTN frames

      OPEN ( UNIT=6, FILE='dsst_wls.output', STATUS='OLD')
      OPEN ( UNIT=338,FILE='dsst_wls_residuals.output', STATUS='OLD')
      OPEN ( UNIT=339,FILE='dsst_wls_residuals_rtn.output', STATUS='OLD')
      OPEN ( UNIT=340,FILE='COMPLETE_SUMMARY', STATUS='OLD')

C     INITIALIZE LOOP PARAMETERS
        ITR_IDX= 1
        ITR_LOOP= .TRUE.

      DO WHILE(ITR_LOOP)
C     Do the observation loop

         write(99,*) 'got␣to␣first␣pass␣'


         IF ( FIRST_PASS ) THEN
```

```
            CALL INIT_HEADERS ()
            FIRST_PASS = .FALSE.
            PMERN = 'pmern'
         ENDIF

         OPEN ( UNIT=5, FILE='dsst_wls.input',  STATUS='OLD')

         NO_OBS= 1
         BBAR_MATRIX = 0

         DO WHILE (.TRUE.)

C           READ request from SYS$INPUT
            READ (5,'(A)') ALINE
            REQUEST = ALINE (1:12)

C           CASEOF request
C           IF epoch data
            IF ( REQUEST(1:5).EQ."EPOCH" ) THEN
               write(99,*) 'request is epoch'//EPOCH

C              Set defaults for request time and burn list
               TIME             = 0.D0
               BURN_NUMBER      = 0
               DO I=1,MAX_LIST_LENGTH
                  BURN_DELTA_V(1,I) = 0.D0
                  BURN_DELTA_V(2,I) = 0.D0
                  BURN_DELTA_V(3,I) = 0.D0
                  BURN_DELTA_V(4,I) = 0.D0
               END DO

C           Extract request time and burn list from request
            INDEX1 = INDEX(ALINE,BLANK)
            READ (ALINE(INDEX1:),*,IOSTAT=STATUS)
     2        TIME,BURN_NUMBER,((BURN_DELTA_V(I,J),I=1,4),
     3        J=1,BURN_NUMBER)
C
            write(99,*) 'about to call SATELLITE'
C           CALL SATELLITE to obtain state at request time
654           STATUS = SATELLITE ( PMERN,           TIME,
     2                             BURN_DELTA_V,    BURN_NUMBER,
     3                             IATMOS_PREBURN,  IATMOS_POSTBURN,
     4                             RHO_ONE_HIGH,    RHO_ONE_LOW,
     5                             EPOCH_YMD,       EPOCH_HMS,
     6                             POSVEL,          ELEMENTS,
     7                             ELEMENTS_DER,    POSVEL_DER,
     8                             NSTATE_DER,      NDYNAM_DER,
     9                             MESSAGE,         FILENAME )


C             IF normal return
              IF ( STATUS .EQ. NORMAL ) THEN

C                 KEEPING THE PARTIALS FOR COVARIANCE TRANSFORMATION
                  DSTATE_DEQUI_EPOCH(1:6,1:6) = POSVEL_DER(1:6,1:6)

C                 WRITE data record to SYS$OUTPUT
                  WRITE (ALINE,'(A,4X,2D25.16)') EPOCH,EPOCH_YMD,EPOCH_HMS
                  WRITE (6,'(A)')  ALINE

                  CALL JULPAK (DYJUL0,SJUL0,EPOCH_YMD,EPOCH_HMS)
C
              ELSE

C                 WRITE error record to SYS$OUTPUT
                  GOTO 654
                  WRITE (ALINE,'(A,1X,A,1X,A)')  ERROR, MESSAGE, FILENAME
                  WRITE (6,'(A)')  ALINE
C
              END IF

                IF(ITR_IDX.EQ.1) THEN  ! ALLOCATE and INITIALIZE BLOCK
```

```
                NSOLVE_ = NSTATE_DER + NDYNAM_DER
                WRITE(*,*) 'DSST-OD : RUNNING'

                ALLOCATE(HTRANS(NSOLVE_, NSOLVE_))
                ALLOCATE(H(NSOLVE_, NSOLVE_))
                ALLOCATE(TEMP_MAT(NSOLVE_,NSOLVE_))
                ALLOCATE(HWH(NSOLVE_,NSOLVE_))
                ALLOCATE(HWH_ACC(NSOLVE_,NSOLVE_))
                ALLOCATE(HWB(NSOLVE_))
                ALLOCATE(BBAR_MATRIX_ACC(NSOLVE_))
                ALLOCATE(STATE_UPDATE_LSQ(NSOLVE_))
                ALLOCATE(WEIGHT(NSOLVE_,NSOLVE_))
                ALLOCATE(TEMP_VEC(NSOLVE_))

                CALL GET_PMERN_STATE(PM_ST_FIRST, CD_FIRST, CR_FIRST)

C               Initialize Weighting matrix
                WEIGHT = 0.00
                DO I = 1,3
                  WEIGHT(I,I) =  1 !1/100
                  WEIGHT(I+3,I+3) = 0.1 !1/1E6 ! km/s  for velocity
                END DO

                IF (NSOLVE_ .GT. 6) THEN
                 DO I = 7,NSOLVE_
                  WEIGHT(I,I) = 100.00
                 END DO
                ENDIF

              ENDIF ! ALLOCATE and INITIALIZE BLOCK

C           ELSE IF position and velocity data at request time
            ELSE IF ( REQUEST(1:9).EQ."OBS_ECIPV" ) THEN

C             Set defaults for request time and burn list

              TIME             = 0.D0
              BURN_NUMBER      = 0
              DO I=1,MAX_LIST_LENGTH
                 BURN_DELTA_V(1,I) = 0.D0
                 BURN_DELTA_V(2,I) = 0.D0
                 BURN_DELTA_V(3,I) = 0.D0
                 BURN_DELTA_V(4,I) = 0.D0
              END DO

C             EXTRACT TIME AND OBSERVATION FROM THE ALINE
              INDEX1 = INDEX(ALINE,BLANK)
              READ (ALINE(INDEX1:),*,IOSTAT=STATUS)
     2        YMD, HMS,OBS_ECIPV_STATE

              CALL JULPAK(DYJ, SCJ, YMD, HMS)
              TIME  = ( DYJ - DYJUL0 )*86400.D0  + (SCJ-SJUL0)

C             CALL SATELLITE to obtain state at request time
              STATUS = SATELLITE ( PMERN,           TIME,
     2                             BURN_DELTA_V,    BURN_NUMBER,
     3                             IATMOS_PREBURN,  IATMOS_POSTBURN,
     4                             RHO_ONE_HIGH,    RHO_ONE_LOW,
     5                             EPOCH_YMD,       EPOCH_HMS,
     6                             POSVEL,          ELEMENTS,
     7                             ELEMENTS_DER,    POSVEL_DER,
     8                             NSTATE_DER,      NDYNAM_DER,
     9                             MESSAGE,         FILENAME )

C             IF normal return
              IF ( STATUS .EQ. NORMAL ) THEN

                TIME_ARRAY (NO_OBS) = TIME

                CALL TRNASFORM_ECI_RTN ( U,POSVEL )
```

```
C               ASSEMBLE H MATRIX AND B MATRIX
C               H - PARTIAL DERIVATIVE MATRIX FOR ELEMENTS
C               B - DIFFERENCE BETWEEN THE OBESRVATION AND PROP

                H          = 0.00
                H(1:6,1:NSOLVE_) = POSVEL_DER(1:6,1:NSOLVE_)

                IF (NSOLVE_ .GT. 6) THEN
                  DO I = 7,NSOLVE_
                   H (I,I) = 1.00
                  END DO
                ENDIF
C
                HTRANS     = TRANSPOSE(H)                                  ! H transpose

                CALL MATMAT(TEMP_MAT,HTRANS,WEIGHT,NSOLVE_,NSOLVE_,NSOLVE_)   ! HtW

                CALL MATMAT(HWH,TEMP_MAT,H,NSOLVE_,NSOLVE_,NSOLVE_)        ! HtWH

                TEMP_VEC (1:6) = OBS_ECIPV_STATE - POSVEL                     ! B (
                    residuals)
                RES_POSVEL(NO_OBS,1:6) = TEMP_VEC (1:6)

                IF (NSOLVE_ .GT. 6) THEN
                   TEMP_VEC (7) = 0.0
                ENDIF
                IF (NSOLVE_ .GT. 7) THEN
                   TEMP_VEC (8) = 0.0
                ENDIF

                CALL MATMAT(HWB,TEMP_MAT,TEMP_VEC,NSOLVE_,NSOLVE_,1)          ! HtWB
C
                CALL  LSQ_ACC_OBS (NO_OBS, HWH_ACC, BBAR_MATRIX_ACC, HWH, HWB, NSOLVE_)

C               RTN residual computation
                CALL MATMAT(RTN,U,TEMP_VEC(1:3),3,3,1)
                RTN_A(NO_OBS,1:3) = RTN(1:3)

              END IF
C
C           ELSE IF ONLY POSITION measurements
            ELSE IF ( REQUEST(1:7).EQ."OBS_POS" ) THEN

              TIME             = 0.D0
              BURN_NUMBER      = 0
              DO I=1,MAX_LIST_LENGTH
                 BURN_DELTA_V(1,I) = 0.D0
                 BURN_DELTA_V(2,I) = 0.D0
                 BURN_DELTA_V(3,I) = 0.D0
                 BURN_DELTA_V(4,I) = 0.D0
              END DO

C             EXTRACT TIME AND OBSERVATION FROM THE ALINE
              INDEX1 = INDEX(ALINE,BLANK)
              READ (ALINE(INDEX1:),*,IOSTAT=STATUS)
     2        YMD, HMS,OBS_ECIPV_STATE

              CALL JULPAK(DYJ, SCJ, YMD, HMS)
              TIME  = ( DYJ - DYJUL0 )*86400.D0  + (SCJ-SJUL0)

C             CALL SATELLITE to obtain state at request time
              STATUS = SATELLITE ( PMERN,          TIME,
     2                             BURN_DELTA_V,   BURN_NUMBER,
     3                             IATMOS_PREBURN, IATMOS_POSTBURN,
     4                             RHO_ONE_HIGH,   RHO_ONE_LOW,
     5                             EPOCH_YMD,      EPOCH_HMS,
     6                             POSVEL,         ELEMENTS,
     7                             ELEMENTS_DER,   POSVEL_DER,
     8                             NSTATE_DER,     NDYNAM_DER,
     9                             MESSAGE,        FILENAME )

C             IF normal return
```

```
              IF ( STATUS .EQ. NORMAL ) THEN

                TIME_ARRAY (NO_OBS) = TIME

                CALL TRNASFORM_ECI_RTN ( U,POSVEL )

C               ASSEMBLE H MATRIX AND B MATRIX
C               H - PARTIAL DERIVATIVE MATRIX FOR ELEMENTS
C               B - DIFFERENCE BETWEEN THE OBESRVATION AND PROP

                H          = 0.00
                H(1:6,1:NSOLVE_) = POSVEL_DER(1:6,1:NSOLVE_)

                IF (NSOLVE_ .GT. 6) THEN
                  DO I = 7,NSOLVE_
                   H (I,I) = 1.00
                  END DO
                ENDIF
C
                HTRANS     = TRANSPOSE(H)                                    ! H transpose

                WEIGHT(4:6,4:6) = 0.D0
                CALL MATMAT(TEMP_MAT,HTRANS,WEIGHT,NSOLVE_,NSOLVE_,NSOLVE_)! HtW

                CALL MATMAT(HWH,TEMP_MAT,H,NSOLVE_,NSOLVE_,NSOLVE_)         ! HtWH

                TEMP_VEC (1:3) = OBS_ECIPV_STATE(1:3) - POSVEL(1:3)         ! B (residuals
                    )
                RES_POSVEL(NO_OBS,1:3) = TEMP_VEC (1:3)

                IF (NSOLVE_ .GT. 6) THEN
                   TEMP_VEC (7) = 0.0
                ENDIF
                IF (NSOLVE_ .GT. 7) THEN
                   TEMP_VEC (8) = 0.0
                ENDIF

                CALL MATMAT(HWB,TEMP_MAT,TEMP_VEC,NSOLVE_,NSOLVE_,1)          ! HtWB
C
                CALL  LSQ_ACC_OBS (NO_OBS, HWH_ACC, BBAR_MATRIX_ACC, HWH, HWB, NSOLVE_)

C               RTN residual computation
                CALL MATMAT(RTN,U,TEMP_VEC(1:3),3,3,1)
                RTN_A(NO_OBS,1:3) = RTN(1:3)

              END IF
C           ELSE IF range and angle measurements
              ELSE IF ( REQUEST(1:7).EQ."OBS_RAE" ) THEN

                TIME             = 0.D0
                BURN_NUMBER      = 0
                DO I=1,MAX_LIST_LENGTH
                   BURN_DELTA_V(1,I) = 0.D0
                   BURN_DELTA_V(2,I) = 0.D0
                   BURN_DELTA_V(3,I) = 0.D0
                   BURN_DELTA_V(4,I) = 0.D0
                END DO

C               EXTRACT TIME AND OBSERVATION FROM THE ALINE
                INDEX1 = INDEX(ALINE,BLANK)
                READ (ALINE(INDEX1:),*,IOSTAT=STATUS)
     2          YMD, HMS, STATION, OBS_RAE

                OBS_RAE(2:3) = OBS_RAE(2:3)*DEGREES

                CALL JULPAK(DYJ, SCJ, YMD, HMS)
                TIME  = ( DYJ - DYJUL0 )*86400.D0  + (SCJ-SJUL0)

C               CALL SATELLITE to obtain state at request time
                STATUS = SATELLITE ( PMERN,           TIME,
     2                               BURN_DELTA_V,    BURN_NUMBER,
     3                               IATMOS_PREBURN,  IATMOS_POSTBURN,
```

```
     4                              RHO_ONE_HIGH,    RHO_ONE_LOW,
     5                              EPOCH_YMD,       EPOCH_HMS,
     6                              POSVEL,          ELEMENTS,
     7                              ELEMENTS_DER,    POSVEL_DER,
     8                              NSTATE_DER,      NDYNAM_DER,
     9                              MESSAGE,         FILENAME )

C             IF normal return
              IF ( STATUS .EQ. NORMAL ) THEN

                TIME_ARRAY (NO_OBS) = TIME

                CALL TRNASFORM_ECI_RTN ( U,POSVEL )

C               ASSEMBLE H MATRIX AND B MATRIX
C               H - PARTIAL DERIVATIVE MATRIX FOR ELEMENTS
C               B - DIFFERENCE BETWEEN THE OBESRVATION AND PROP

                H  = 0.00
                H(1:6,1:NSOLVE_) = POSVEL_DER(1:6,1:NSOLVE_)

C               CONVERT ITRF POSITION TO ICRF FRAME
                CALL ICRF2ITRF (OBS_GPS, ROT_E_MAT, POSVEL, TIME)

                CALL OBSITE(OBS_GPS, STATION, AZ, EL, RHO, DADS, LTC_MAT)
                CALL MATMAT(T_M1(1:3,1:3),DADS, LTC_MAT,3,3,3)
                CALL MATMAT(T_M2(1:3,1:3), T_M1(1:3,1:3), ROT_E_MAT,3,3,3)

                TEMP_MAT = 0.D0
                CALL MATMAT(TEMP_MAT(1:6,1:6), T_M2(1:6,1:6), H(1:6,1:6),6,6,6)
                H = TEMP_MAT

                TEMP_MAT = 0.D0
                IF (NSOLVE_ .GT. 6) THEN
                  DO I = 7,NSOLVE_
                   H (I,I) = 1.00
                  END DO
                ENDIF
C
                HTRANS     = TRANSPOSE(H)

                WEIGHT(1,1) = 1000.D0
                WEIGHT(2,2) = 0.1D0
                WEIGHT(3,3) = 0.1D0
                WEIGHT(4:6,4:6) = 0.D0
                CALL MATMAT(TEMP_MAT(1:6,1:3),HTRANS(1:6,1:3),WEIGHT(1:3,1:3),6,3,3)! HtW

                CALL MATMAT(HWH(1:6,1:6),TEMP_MAT(1:6,1:3),H(1:3,1:6),6,3,6)        !
                    HtWH

                ! B (residuals)
                TEMP_VEC(1)    =  OBS_RAE(1) - RHO
                TEMP_VEC(2)    =  OBS_RAE(2) - AZ
                TEMP_VEC(3)    =  OBS_RAE(3) - EL

                TEMP_VEC(4:6)  =  0.D0

                RES_POSVEL(NO_OBS,1) = TEMP_VEC(1)
                RES_POSVEL(NO_OBS,2:3) = TEMP_VEC(2:3)/DEGREES

                IF (NSOLVE_ .GT. 6) THEN
                   TEMP_VEC (7) = 0.0
                ENDIF
                IF (NSOLVE_ .GT. 7) THEN
                   TEMP_VEC (8) = 0.0
                ENDIF

                CALL MATMAT(HWB,TEMP_MAT(1:6,1:3),TEMP_VEC(1:3),6,3,1)          ! HtWB
C
C
                CALL  LSQ_ACC_OBS (NO_OBS, HWH_ACC, BBAR_MATRIX_ACC, HWH, HWB, 6)
```

```
C               RTN residual computation
                TEMP_VEC(1:3) = 0.D0

              END IF
C           ELSE IF we want to exit
            ELSE IF (REQUEST(1:4).EQ."EXIT") THEN

               EXIT

C           ELSE
            ELSE

C           Pass the request through to SYS$OUTPUT
            WRITE (6,'(A)')  ALINE
C
            END IF
C           END CASE

          END DO

C
C         COMPUTE MEAN, VARIANCE and WEIGHTS
          MEAN_RESIDUALS(1) = SUM(RES_POSVEL(1:NO_OBS,1))/NO_OBS
          MEAN_RESIDUALS(2) = SUM(RES_POSVEL(1:NO_OBS,2))/NO_OBS
          MEAN_RESIDUALS(3) = SUM(RES_POSVEL(1:NO_OBS,3))/NO_OBS
          MEAN_RESIDUALS(4) = SUM(RES_POSVEL(1:NO_OBS,4))/NO_OBS
          MEAN_RESIDUALS(5) = SUM(RES_POSVEL(1:NO_OBS,5))/NO_OBS
          MEAN_RESIDUALS(6) = SUM(RES_POSVEL(1:NO_OBS,6))/NO_OBS

          VAR_RESIDUALS(1) = SUM((RES_POSVEL(1:NO_OBS,1)-MEAN_RESIDUALS(1))**2)/NO_OBS
          VAR_RESIDUALS(2) = SUM((RES_POSVEL(1:NO_OBS,2)-MEAN_RESIDUALS(2))**2)/NO_OBS
          VAR_RESIDUALS(3) = SUM((RES_POSVEL(1:NO_OBS,3)-MEAN_RESIDUALS(3))**2)/NO_OBS
          VAR_RESIDUALS(4) = SUM((RES_POSVEL(1:NO_OBS,4)-MEAN_RESIDUALS(4))**2)/NO_OBS
          VAR_RESIDUALS(5) = SUM((RES_POSVEL(1:NO_OBS,5)-MEAN_RESIDUALS(5))**2)/NO_OBS
          VAR_RESIDUALS(6) = SUM((RES_POSVEL(1:NO_OBS,6)-MEAN_RESIDUALS(6))**2)/NO_OBS


C         BEGINING OF THE LEAST SQUARES - FIRST ITR (which is outside the loop)
C
C                   Take the Inverse of (HtWH) = (HtWH)^-1

           CALL F06DBF(NSOLVE_,0,JPVT,1)
           CALL DGETRF(NSOLVE_,NSOLVE_,HWH_ACC,NSOLVE_,JPVT,WORK(1:NSOLVE_), INFO)    ! LU
               - factorization
           CALL DGETRI(NSOLVE_,HWH_ACC,NSOLVE_,JPVT,WORK(1:NSOLVE_), NSOLVE_, INFO)   !
               Compute the inverse of the matrix


C         Get the initilization vector to call DGELSY
          CALL F06DBF(NSOLVE_,0,JPVT,1)

C         INITIALIZATION OF REDUNDANT VARIABLES FOR LEAST SQUARES
          RCOND             = 0.01D0
          TSET              = NSOLVE_+1
          LDA               = TSET
          LWORK             = NSOLVE_*NSOLVE_
          WORK(1:NSOLVE_)   = 0
          STATE_UPDATE_LSQ  = 0

C         CALLING THE LEAST SQUARE SOLVER
          CALL MATMAT(STATE_UPDATE_LSQ,HWH_ACC,BBAR_MATRIX_ACC,NSOLVE_,NSOLVE_,1)

C         COLLECT THE TOTAL UPDATE AFTER EACH ITRERATION
          UPDATESTATE_TOT(1:2) = UPDATESTATE_TOT(1:2)+STATE_UPDATE_LSQ(1:2)
          UPDATESTATE_TOT(3:6) = UPDATESTATE_TOT(3:6)+STATE_UPDATE_LSQ(3:6)*180/3.14217

          IF ( NSOLVE_ .GT. 6) THEN
          UPDATED_CD_TOTAL     = UPDATED_CD_TOTAL + STATE_UPDATE_LSQ (7)
          ENDIF
          IF ( NSOLVE_ .GT. 7) THEN
          UPDATED_CR_TOTAL     = UPDATED_CR_TOTAL + STATE_UPDATE_LSQ (8)
          ENDIF
```

```
C         ITERATION CONTROL

          ITERATION_EPSILON = 1E-8
          IF ( ITR_IDX .EQ. 1) THEN
          TEMP_3  = 0.D0
          ENDIF

          RMSP=SQRT(VAR_RESIDUALS(1)*VAR_RESIDUALS(1)+VAR_RESIDUALS(2)*VAR_RESIDUALS(2)+
              VAR_RESIDUALS(3)*VAR_RESIDUALS(3))

C         COMPARE WITH RMS OF PREVIOUS ITERATION
          RMSP_DIFF =  ABS(TEMP_3 - RMSP)
          TEMP_3    = RMSP


C         SET ITR FLAG FOR NEXT ITERATION
          IF(ABS(RMSP_DIFF).LE.ITERATION_EPSILON .OR. ITR_IDX.GE.20) THEN
              ITR_LOOP = .FALSE.
          END IF

C
C         UPDATE THE WEIGHT MATRIX
C
          TEMP_2 = 0.D0

          DO I = 1,NSOLVE_
            WEIGHT(I,I) = 1/HWH_ACC(I,I)
            TEMP_1  = 1/HWH_ACC(I,I)
            TEMP_2 = MAX(TEMP_2, TEMP_1)
          END DO

          DO I = 1,NSOLVE_
            WEIGHT(I,I) = WEIGHT(I,I) * 1E2 / TEMP_2
          END DO

          DO I = 1,6
            WEIGHT(I,I) = 1/VAR_RESIDUALS(I)
          END DO
C
C         SET THE MEAN EQUINICTIAL ELEMENT UPDATE INTO PMERN BLOCK
C
          IF(NDYNAM_DER .GE. 1)THEN
            CD_UPDATE = CD_FIRST+STATE_UPDATE_LSQ(7)
            CR_UPDATE = CR_FIRST
          END IF

          IF(NDYNAM_DER .GE. 2)THEN
            CR_UPDATE = CR_FIRST+STATE_UPDATE_LSQ(8)
          END IF

          IF (NDYNAM_DER .LE. 0) THEN
            CD_UPDATE = CD_FIRST
            CR_UPDATE = CR_FIRST

          END IF
C
          OPEN ( UNIT=2999, FILE='pmern',  STATUS='OLD')
          CALL   SETPMERNUPDATE (STATE_UPDATE_LSQ(1:6), CD_UPDATE, CR_UPDATE, EST_KEP,
              RFCTR)

C         CONVERT UPDATED ELEMENT TO EQUINOCTIAL
          CALL EQNKEP   (EST_EQUI,RFCTR,EST_KEP, .TRUE.)

C         CONVERT UPDATED ELEMENT TO STATE VECTOR
          CALL  CARTES   (POS,VEL, EST_EQUI, RFCTR, 3.9860044D5)
          EST_STATE(1:3) = POS
          EST_STATE(4:6) = VEL

C         WRITE THE UPDATED PMEF FILE
          CALL MP_WRITE_PMEF(2999, IER)
          CLOSE ( UNIT=2999 )
```

```
          CLOSE ( UNIT=5    )


C         WRITE THE SUMMARY FILE ( added 2014.11.10 SJS)
C ----------------------------------COMPLETE_SUMMARY
    ----------------------------------------

          IF (ITR_IDX .EQ. 1) THEN
             ! header
             WRITE(340,'(A)') 'DSST_OD␣Iteration␣Summary'

             ! date and time info
             CALL DATE_AND_TIME(YEAR_,TIME_,DAY_,CLOCK)
             WRITE(340, *) '␣␣␣␣␣␣␣␣',YEAR_(1:4),'/',YEAR_(5:6),'/',YEAR_(7:8)
             WRITE(340, *) '␣␣␣␣␣␣␣␣',TIME_(1:2),':',TIME_(3:4),':',TIME_(5:6)
             WRITE(340, *)
             WRITE(340, *)
          END IF ! header writing


          IF (  NSOLVE_ .GT. 6 ) THEN
          CD_SIGMA    = SQRT(HWH_ACC(7,7))
          ELSE
          CD_SIGMA    = 0.D0
          ENDIF

          IF (  NSOLVE_ .GT. 7 ) THEN
          CR_SIGMA    = SQRT(HWH_ACC(8,8))
          ELSE
          CR_SIGMA    = 0.D0
          ENDIF

          ! Iteration number
          WRITE(340,'(A,␣I)') 'Iteration', ITR_IDX
          WRITE(340,*)
          WRITE(340,'(A,␣I)') 'No␣of␣Obs␣Processed', NO_OBS
          WRITE(340,*)

          ! Estimated parameters info
          WRITE(340,'(A)') 'Estimated␣Parameters:'
          WRITE(340,'(A)')

          ! Dr/dA convariance matrix
          WRITE(340,'(A)') 'Mean␣Equinoctial␣Elements␣covariance␣Matrix'
          WRITE(340,'(A)')
          WRITE(340,'(A10,6A20)') 'mean-->','semimajor␣axis','h','k','p','q','lambda'
          WRITE(340,'(A10,6D20.12)') 'SMA'  ,HWH_ACC(1,1:6)
          WRITE(340,'(A10,6D20.12)') 'h'    ,HWH_ACC(2,1:6)
          WRITE(340,'(A10,6D20.12)') 'k'    ,HWH_ACC(3,1:6)
          WRITE(340,'(A10,6D20.12)') 'p'    ,HWH_ACC(4,1:6)
          WRITE(340,'(A10,6D20.12)') 'q'    ,HWH_ACC(5,1:6)
          WRITE(340,'(A10,6D20.12)') 'lam'  ,HWH_ACC(6,1:6)
          WRITE(340,*)

          T_M1 = TRANSPOSE(DSTATE_DEQUI_EPOCH)
          CALL MATMAT(T_M2,HWH_ACC(1:6,1:6),T_M1,6,6,6)
          CALL MATMAT(P_STATE,DSTATE_DEQUI_EPOCH,T_M2,6,6,6)
          ! Dr/dA convariance matrix
          WRITE(340,'(A)') 'State␣covariance␣Matrix'
          WRITE(340,'(A)')
          WRITE(340,'(A10,6A20)') 'd/d()-->','X','Y','Z','VX','VY','VZ'
          WRITE(340,'(A10,6D20.12)') 'X'    ,P_STATE(1,1:6)
          WRITE(340,'(A10,6D20.12)') 'Y'    ,P_STATE(2,1:6)
          WRITE(340,'(A10,6D20.12)') 'Z'    ,P_STATE(3,1:6)
          WRITE(340,'(A10,6D20.12)') 'VX'   ,P_STATE(4,1:6)
          WRITE(340,'(A10,6D20.12)') 'VY'   ,P_STATE(5,1:6)
          WRITE(340,'(A10,6D20.12)') 'VZ'   ,P_STATE(6,1:6)
          WRITE(340,*)

          WRITE(340,'(A)') 'ESTIMATED␣MEAN␣EQUINOCTIAL␣ELEMENTS␣(SIGMA␣VALUES␣ARE␣STILL␣IN
              ␣EQUINOCTIAL␣SPACE)'
          WRITE(340,'(A)')
```

```
          WRITE(340,'(A10,␣2A20)') 'Element', 'Estimate␣Value', 'sigma'
          WRITE(340,'(2A10,1F20.12,␣1D15.5)') 'SMA' , '[km]' , EST_EQUI(1), SQRT(HWH_ACC
              (1,1))
          WRITE(340,'(2A10,1F20.12,␣1D15.5)') 'h␣␣' , '␣'    , EST_EQUI(2), SQRT(HWH_ACC
              (2,2))
          WRITE(340,'(2A10,1F20.12,␣1D15.5)') 'k␣␣' , '␣'    , EST_EQUI(3), SQRT(HWH_ACC
              (3,3))
          WRITE(340,'(2A10,1F20.12,␣1D15.5)') 'p␣␣' , '␣'    , EST_EQUI(4), SQRT(HWH_ACC
              (4,4))
          WRITE(340,'(2A10,1F20.12,␣1D15.5)') 'q␣␣' , '␣'    , EST_EQUI(5), SQRT(HWH_ACC
              (5,5))
          WRITE(340,'(2A10,1F20.12,␣1D15.5)') 'Lam' , '[deg]', EST_EQUI(6), SQRT(HWH_ACC
              (6,6))* RADIANS
          WRITE(340,'(A)')
          WRITE(340,'(2A10,1F20.12,1D15.5)')  'C_D' , '␣'    ,  CD_UPDATE   , CD_SIGMA
          WRITE(340,'(2A10,1F20.12,1D15.5)')  'C_R' , '␣'    ,  CR_UPDATE   , CR_SIGMA
          WRITE(340,'(A)')
          WRITE(340,'(A)') 'ESTIMATED␣MEAN␣KEPLERIAN␣ELEMENTS'
          WRITE(340,'(A)')
          WRITE(340,'(A10,␣1A20)') 'Element', 'Estimate␣Value'
          WRITE(340,'(2A10,1F20.12␣)') 'SMA' , '[km]' , EST_KEP(1)
          WRITE(340,'(2A10,1F20.12␣)') 'ECC' , '␣'    , EST_KEP(2)
          WRITE(340,'(2A10,1F20.12␣)') 'INC' , '[deg]', EST_KEP(3)* RADIANS
          WRITE(340,'(2A10,1F20.12␣)') 'RAAN', '[deg]', EST_KEP(4)* RADIANS
          WRITE(340,'(2A10,1F20.12␣)') 'AOP' , '[deg]', EST_KEP(5)* RADIANS
          WRITE(340,'(2A10,1F20.12␣)') 'M'   , '[deg]', EST_KEP(6)* RADIANS
          WRITE(340,'(A)')
          WRITE(340,'(A)') 'ESTIMATED␣MEAN␣POS␣/␣VEL'
          WRITE(340,'(A)')
          WRITE(340,'(A10,␣2A20)') 'Element', 'Estimate␣Value', 'sigma'
          WRITE(340,'(2A10,1F20.12,␣1D15.5␣)') 'X' , '[km]'  , EST_STATE(1), SQRT(P_STATE
              (1,1))
          WRITE(340,'(2A10,1F20.12,␣1D15.5␣)') 'Y' , '[km]'  , EST_STATE(2), SQRT(P_STATE
              (2,2))
          WRITE(340,'(2A10,1F20.12,␣1D15.5␣)') 'Z' , '[km]'  , EST_STATE(3), SQRT(P_STATE
              (3,3))
          WRITE(340,'(2A10,1F20.12,␣1D15.5␣)') 'VX', '[km/s]', EST_STATE(4), SQRT(P_STATE
              (4,4))
          WRITE(340,'(2A10,1F20.12,␣1D15.5␣)') 'VY', '[km/s]', EST_STATE(5), SQRT(P_STATE
              (5,5))
          WRITE(340,'(2A10,1F20.12,␣1D15.5␣)') 'VZ', '[km/s]', EST_STATE(6), SQRT(P_STATE
              (6,6))
          WRITE(340,'(A)')
          WRITE(340,*) '
              --------------------------------------------------------------------------------
              '
          WRITE(340,'(A)')

          CD_FIRST    = CD_UPDATE
          CR_FIRST    = CR_UPDATE
C ---------------------------------END WRITING COMPLETE_SUMMARY
     ---------------------------------------
C         UPDTE THE ITERATION NUMBER
          ITR_IDX=ITR_IDX+1
          FIRST_PASS = .TRUE.
          HWH_ACC = 0.00D8
          BBAR_MATRIX_ACC = 0.00D8

C      END OF THE ITERATION LOOP
       END DO
       WRITE(340,*)

C      RELEASE THE ALLOCATABLES
       DEALLOCATE(H)
       DEALLOCATE(HTRANS)
       DEALLOCATE(HWH)
       DEALLOCATE(HWH_ACC)
       DEALLOCATE(HWB)
       DEALLOCATE(BBAR_MATRIX_ACC)
       DEALLOCATE(STATE_UPDATE_LSQ)

C ---------------------------------WRITING BLOCK----------------------------------------
```

```
      K=1
C     Print the last itiration number in the residual file
      WRITE(338,'(A)') 'ITR NUMBER'
      WRITE(338,*)  ITR_IDX-1
      WRITE(338,*)

C     Print the last itiration residuals in both ECI and RTN frame in different files
      DO WHILE(K .LE. NO_OBS-1)
          WRITE(338,'(1D35.16, 6D35.16)')  TIME_ARRAY(K), RES_POSVEL(K,1:6)
          WRITE(339,'(1D35.16, 3D35.16)')  TIME_ARRAY(K), RTN_A(K,1:3)
          K = K+1
      END DO

      CLOSE (UNIT= 338)
      CLOSE (UNIT= 339)
      CLOSE (UNIT= 340)

C     WRITING COVARIANCE FILE
      OPEN ( UNIT=341,FILE='dsst_od_cov.output', STATUS='OLD')

      WRITE(341,'(A)')'C     DSST OD GENERATED COVARIANCE FILE'
      WRITE(341,'(A)')'C'
      WRITE(341, '(1D25.16, 1X, A)') P_STATE(1,1),'CX_X          1'
      WRITE(341,'(A)')'C'
      WRITE(341, '(1D25.16, 1X, A)') P_STATE(2,1),'CY_X          2'
      WRITE(341, '(1D25.16, 1X, A)') P_STATE(2,2),'CY_Y          3'
      WRITE(341,'(A)')'C'
      WRITE(341, '(1D25.16, 1X, A)') P_STATE(3,1),'CZ_X          4'
      WRITE(341, '(1D25.16, 1X, A)') P_STATE(3,2),'CZ_Y          5'
      WRITE(341, '(1D25.16, 1X, A)') P_STATE(3,3),'CZ_Z          6'
      WRITE(341,'(A)')'C'
      WRITE(341, '(1D25.16, 1X, A)') P_STATE(4,1),'CX_DOT_X      7'
      WRITE(341, '(1D25.16, 1X, A)') P_STATE(4,2),'CX_DOT_Y      8'
      WRITE(341, '(1D25.16, 1X, A)') P_STATE(4,3),'CX_DOT_Z      9'
      WRITE(341, '(1D25.16, 1X, A)') P_STATE(4,4),'CX_DOT_X_DOT  10'
      WRITE(341,'(A)')'C'
      WRITE(341, '(1D25.16, 1X, A)') P_STATE(5,1),'CY_DOT_X      11'
      WRITE(341, '(1D25.16, 1X, A)') P_STATE(5,2),'CY_DOT_Y      12'
      WRITE(341, '(1D25.16, 1X, A)') P_STATE(5,3),'CY_DOT_Z      13'
      WRITE(341, '(1D25.16, 1X, A)') P_STATE(5,4),'CY_DOT_X_DOT  14'
      WRITE(341, '(1D25.16, 1X, A)') P_STATE(5,5),'CY_DOT_Y_DOT  15'
      WRITE(341,'(A)')'C'
      WRITE(341, '(1D25.16, 1X, A)') P_STATE(6,1),'CZ_DOT_X      16'
      WRITE(341, '(1D25.16, 1X, A)') P_STATE(6,2),'CZ_DOT_Y      17'
      WRITE(341, '(1D25.16, 1X, A)') P_STATE(6,3),'CZ_DOT_Z      18'
      WRITE(341, '(1D25.16, 1X, A)') P_STATE(6,4),'CZ_DOT_X_DOT  19'
      WRITE(341, '(1D25.16, 1X, A)') P_STATE(6,5),'CZ_DOT_Y_DOT  20'
      WRITE(341, '(1D25.16, 1X, A)') P_STATE(6,6),'CZ_DOT_Z_DOT  21'
      WRITE(341,'(A)')'C'
      WRITE(341, '(I16     ,10X, A)')    11     ,   'COV_SYS       22'
      WRITE(341, '(I16     ,10X, A)')     3     ,   'COV_INP_TYPE  23'

      CLOSE (UNIT= 341)

C     END OF THE PROGRAM ORBIT_DETERMINATION_SERVICES
      END
```

LIST OF FIGURES

LIST OF TABLES

ACKNOWLEDGEMENTS

First and foremost, my greatest gratitude is to my supervisor Dr. Oliver Montenbruck. Thank you for taking me by hand and teaching me just not the technical aspects of orbital mechanics, but also to think and state a scientific problem in a clear manner. I cannot thank enough for the patience Dr. Montenbruck have shown in making sure I got the fundamentals right, and for the time and patience put during the preparation of this thesis. Second, I would like to thank Dr. Hauke Fidler for giving the opportunity to work in Space Situational Awareness group at GSOC, for the valuable discussions and for the support, and for proof reading the thesis. Also, I would like to thank Dr. Paul Cefola, who unofficially supervised me through out this work, from explaining the math concepts to helping in scientific writing and introducing to the astrodynamics community. Dr. Cefola provided not only the technical expertise, but also huge opportunity for personal and professional development. I am humbled and extremely honoured to have been given the opportunity to work with all three. Any number of thanking words would not justify the time and effort they have given me.

I want to thank Prof. Dr. Felix Huber for being my Doktorvater, at the Bundeswehr University Munich, for constructive comments during the graduate seminars at GSOC and for the careful reading of my thesis. I would like to thank my former colleagues Johannes Herzog, Sonya Spiridonova, Mauricio Andres, and specially to Jan Siminski and Andreas Hinze. Thank you all for the fruitful discussions, assists, and support during this thesis work at GSOC and later. Being associated with this group has been enjoyable, greatly fruitful, and has culminated in a strong sense of fulfilment.

I would like to convey my thanks to Prof. Juan Felix San Juan for his unconditional support and reviewing the thesis, and to Mr. David Vallado for thoroughly reading the thesis and providing the constructive comments.

The work in this thesis was supported by Munich Aerospace funding, I would like to thank all involved in providing the scholarship.

The final and largest thank-you is to my parents and family, I would have never made it without your support and patience through the years.